



## **University of Huddersfield Repository**

Totea, Ana-Maria

Characterisation of smectite clay-drug complexes in polymer matrices using isothermal titration calorimetry and evaluation of drug release

### **Original Citation**

Totea, Ana-Maria (2020) Characterisation of smectite clay-drug complexes in polymer matrices using isothermal titration calorimetry and evaluation of drug release. Doctoral thesis, University of Huddersfield.

This version is available at <http://eprints.hud.ac.uk/id/eprint/35195/>

The University Repository is a digital collection of the research output of the University, available on Open Access. Copyright and Moral Rights for the items on this site are retained by the individual author and/or other copyright owners. Users may access full items free of charge; copies of full text items generally can be reproduced, displayed or performed and given to third parties in any format or medium for personal research or study, educational or not-for-profit purposes without prior permission or charge, provided:

- The authors, title and full bibliographic details is credited in any copy;
- A hyperlink and/or URL is included for the original metadata page; and
- The content is not changed in any way.

For more information, including our policy and submission procedure, please contact the Repository Team at: [E.mailbox@hud.ac.uk](mailto:E.mailbox@hud.ac.uk).

<http://eprints.hud.ac.uk/>

**CHARACTERISATION OF SMECTITE CLAY-DRUG COMPLEXES IN  
POLYMER MATRICES USING ISOTHERMAL TITRATION CALORIMETRY  
AND EVALUATION OF DRUG RELEASE**

**ANA-MARIA ȚOTEA**

A thesis submitted to the University of Huddersfield in partial fulfillment of the  
requirements for the degree of Doctor of Philosophy

The University of Huddersfield

09 January 2020

## **Copyright statement**

- i. The author of this thesis (including any appendices and/ or schedules to this thesis) owns any copyright in it (the “Copyright”) and s/he has given The University of Huddersfield the right to use such Copyright for any administrative, promotional, educational and/or teaching purposes.
- ii. Copies of this thesis, either in full or in extracts, may be made only in accordance with the regulations of the University Library. Details of these regulations may be obtained from the Librarian. Details of these regulations may be obtained from the Librarian. This page must form part of any such copies made.
- iii. The ownership of any patents, designs, trademarks and any and all other intellectual property rights except for the Copyright (the “Intellectual Property Rights”) and any reproductions of copyright works, for example graphs and tables (“Reproductions”), which may be described in this thesis, may not be owned by the author and may be owned by third parties. Such Intellectual Property Rights and Reproductions cannot and must not be made available for use without permission of the owner(s) of the relevant Intellectual Property Rights and/or Reproductions.

## **Declaration**

Chapter 3 of this report has been published in the International Journal of Pharmaceutics

<https://doi.org/10.1016/j.ijpx.2018.100003>

Ana-Maria Totea was the first author of this publication with her supervisor Dr Kofi Asare-Addo the reviewer of the manuscript.

Chapter 4 of this report has been published in the Journal of Pharmaceutical Analysis

<https://doi.org/10.1016/j.jpha.2019.12.001>

Ana-Maria Totea was the first author of this publication with her supervisor Dr Kofi Asare-Addo the reviewer of the manuscript.

## **Abstract**

This thesis investigated the process of adsorption of three cationic drugs having different molecular weights and therapeutic effects (propranolol hydrochloride (PPN), diltiazem hydrochloride (DIL) and metformin hydrochloride (MET)) onto a smectite clay (magnesium aluminium silicate (MAS)) and the effects of this process on extending the release of such drugs. Furthermore, two different polymers (xanthan gum (XG) and polyethylene oxide (PEO)) were used in the study in combination with the formulated clay-drug complexes.

The process of adsorption of the three drugs onto MAS was explored using isothermal titration calorimetry (ITC) along with attenuated total reflectance Fourier transform infrared spectroscopy (ATR-FTIR), scanning electron microscopy with energy dispersive X-ray spectroscopy (SEM/EDX), high-performance liquid chromatography (HPLC), microscopy and small angle X-ray scattering (SAXS). The calorimetric results confirmed the binding between MAS and the drugs at various pHs and temperatures. In all cases, an overall change in enthalpy was found to be exothermic with a comparatively small entropic contribution to the total change in Gibbs free energy. However, the binding profiles were different, one binding event being observed upon binding of PPN and MET onto MAS. The binding of DIL onto MAS exhibited two binding events and were attributed to DIL binding to montmorillonite and saponite. The findings suggest that the binding process was enthalpically driven and entropically unfavourable (lower affinity) suggesting hydrogen bonding and electrostatic interactions dominate the interaction.

The latter part of this thesis aimed to investigate the capacity of the formed MAS-PPN complexes combined with XG and PEO, compared to MAS-PPN physical mix combined with the same polymers to control the release of PPN. Bulk compaction behaviour was studied for the formulations prepared as plots of relative density vs. upper punch pressure measured during loading to 130 MPa (10 kN) and unloading. The compaction curves of all the samples tested followed roughly similar trends: the compaction behaviour was dominated by plastic recovery during the loading stage following non-reversible deformation, movement and fragmentation of the particles. Compacts were further tested for their dissolution properties in pH 1.2 hydrochloric acid and pH 6.8 buffer. Results showed that PEO was able to provide controlled PPN release in both acid and buffer at very low

polymer concentrations in tablets (5% w/w), whereas burst effects were observed upon dissolution of compacts containing the same amount of XG which may be as a result of its anionic nature. Overall, a more controlled PPN release rate from the tablets containing MAS-PPN complexes compared to those containing MAS-PPN physical mixture was observed which is a result of the MAS-PPN binding and adds important benefits to drug release.

This information therefore provides a better understanding of the mechanisms of adsorption of PPN, DIL and MET onto MAS, and demonstrates the promising potential of MAS-cationic drug (drugs with short half-life) complexes as drug reservoirs in polymeric matrices to modulate drug release.

### **Dedication**

This thesis is dedicated to my husband George, my children Katie, Nicholas and the little one we are expecting, and to my parents. You are my greatest achievement, my whole world.

## **Acknowledgements**

I would firstly like to thank my main supervisor, Dr Kofi Asare-Addo for all his help, encouragement and support, and for the multitude of opportunities you have provided me. Your honesty and patience inspired me to become a better person and your encouragement gave me the confidence I needed to overcome all challenges I encountered during my PhD.

I would also like to thank my second supervisor, Professor Laura Waters for her support, for being an inspirational woman in science.

To every member of my research group, thank you for your positive attitude, kindness and for being awesome. To all the technical staff in the School of Applied Sciences, thank you for your assistance and friendship.

I would personally like to thank Dr Peter Laity for his unconditional support and for sharing his wealth of knowledge.

# Contents

<b>Chapter 1: General introduction to the thesis.....</b>	<b>2</b>
<b>1.1. Introduction .....</b>	<b>2</b>
<b>1.2. Oral dosage forms .....</b>	<b>3</b>
<b>1.3. Minerals in the pharmaceutical industry .....</b>	<b>5</b>
<b>1.4. Magnesium aluminium silicate .....</b>	<b>8</b>
<b>1.4.1. Characterisation .....</b>	<b>8</b>
<b>1.4.2. Chemical analysis .....</b>	<b>12</b>
<b>1.5. Applications and published studies .....</b>	<b>14</b>
<b>1.6. Active ingredients.....</b>	<b>17</b>
<b>1.6.1. Propranolol hydrochloride (PPN).....</b>	<b>17</b>
<b>1.6.2. Diltiazem hydrochloride (DIL).....</b>	<b>20</b>
<b>1.6.3. Metformin hydrochloride (MET).....</b>	<b>22</b>
<b>1.7. Polymers used in controlling drug release .....</b>	<b>24</b>
<b>1.7.1. Xanthan gum (XG) .....</b>	<b>26</b>
<b>1.7.2. Polyethylene oxide (PEO) .....</b>	<b>28</b>
<b>1.8. Isothermal titration calorimetry (ITC) .....</b>	<b>30</b>
<b>1.9. Aims and objectives of current study.....</b>	<b>34</b>
<b>1.10. References .....</b>	<b>35</b>
<b>Chapter 2: Materials and methods.....</b>	<b>43</b>
<b>2.1. Materials.....</b>	<b>43</b>
<b>2.2. Methods .....</b>	<b>43</b>
<b>2.2.1. Formulation of single and double drug loaded MAS-drug complexes.....</b>	<b>43</b>
<b>2.2.2. Characterisation of MAS-drug complexes .....</b>	<b>44</b>
<b>2.2.3. Tablet formulation and characterisation.....</b>	<b>53</b>
<b>2.3. References .....</b>	<b>57</b>
<b>Chapter 3: Adsorption of propranolol hydrochloride onto magnesium aluminium silicate .....</b>	<b>60</b>
<b>3.1. Methodology .....</b>	<b>60</b>
<b>3.1.1. Formulation of single and double drug loaded MAS-PPN complexes .....</b>	<b>60</b>
<b>3.1.2. Characterisation of MAS-PPN complexes.....</b>	<b>60</b>
<b>3.2. Results and discussion .....</b>	<b>63</b>
<b>3.2.1. Attenuated total reflectance Fourier transform infrared spectroscopy (ATR-FTIR).....</b>	<b>63</b>
<b>3.2.2. Powder X-ray diffractometry (PXRD) .....</b>	<b>64</b>
<b>3.2.3. Differential scanning calorimetry (DSC) .....</b>	<b>70</b>
<b>3.2.4. Scanning electron microscopy with energy dispersive X-ray spectroscopy (SEM/EDX)....</b>	<b>71</b>
<b>3.2.5. High performance liquid chromatography (HPLC).....</b>	<b>77</b>
<b>3.2.6. Small angle X-Ray scattering (SAXS).....</b>	<b>79</b>
<b>3.2.7. Microscopy .....</b>	<b>85</b>
<b>3.2.8. Calorimetric binding studies .....</b>	<b>87</b>

<b>3.3. Conclusions .....</b>	<b>107</b>
<b>3.4. References .....</b>	<b>108</b>
<b>Chapter 4: Adsorption of diltiazem hydrochloride onto magnesium aluminium silicate .....</b>	<b>113</b>
<b>    4.1. Methodology .....</b>	<b>113</b>
<b>4.1.1. Formulation of single and double drug loaded MAS-PPN complexes .....</b>	<b>113</b>
<b>4.1.2. Characterisation of MAS-PPN complexes.....</b>	<b>113</b>
<b>    4.2. Results and discussion .....</b>	<b>118</b>
<b>4.2.1. Attenuated total reflectance Fourier transform infrared spectroscopy (ATR-FTIR).....</b>	<b>118</b>
<b>4.2.2. Powder X-ray diffractometry (PXRD) .....</b>	<b>119</b>
<b>4.2.3. Differential scanning calorimetry (DSC) .....</b>	<b>120</b>
<b>4.2.4. Scanning electron microscopy with energy dispersive X-ray spectroscopy (SEM/EDX)....</b>	<b>121</b>
<b>4.2.5. High performance liquid chromatography (HPLC).....</b>	<b>126</b>
<b>4.2.6. Small Angle X-ray Scattering .....</b>	<b>130</b>
<b>4.2.7. Microscopy .....</b>	<b>134</b>
<b>4.2.8. Calorimetric binding studies .....</b>	<b>136</b>
<b>    4.3. Conclusions .....</b>	<b>149</b>
<b>    4.4. References .....</b>	<b>150</b>
<b>Chapter 5: Adsorption of metformin hydrochloride onto magnesium aluminium silicate .....</b>	<b>153</b>
<b>    5.1. Methodology .....</b>	<b>153</b>
<b>5.1.1. Formulation of single and double drug loaded MAS-MET complexes.....</b>	<b>153</b>
<b>5.1.2. Characterisation of MAS-MET complexes .....</b>	<b>153</b>
<b>    5.2. Results and discussion .....</b>	<b>156</b>
<b>5.2.1. Attenuated Total Reflectance Fourier Transform Infrared Spectroscopy (ATR-FTIR) ....</b>	<b>156</b>
<b>5.2.2. Powder X-Ray Diffractometry (PXRD).....</b>	<b>157</b>
<b>5.2.3. Differential Scanning Calorimetry (DSC) .....</b>	<b>158</b>
<b>5.2.4. Scanning Electron Microscopy with Energy Dispersive X-Ray Spectroscopy (SEM/EDX)</b> .....	<b>159</b>
<b>5.2.5. High Performance Liquid Chromatography (HPLC).....</b>	<b>163</b>
<b>5.2.6. Small Angle X-Ray Scattering.....</b>	<b>165</b>
<b>5.2.7. Microscopy .....</b>	<b>169</b>
<b>5.2.8. Calorimetric binding studies .....</b>	<b>170</b>
<b>    5.3. Conclusions .....</b>	<b>180</b>
<b>    5.4. References .....</b>	<b>181</b>
<b>Chapter 6: Tablet formulation and dissolution testing studies.....</b>	<b>185</b>
<b>    6.1. Methodology .....</b>	<b>185</b>
<b>6.1.1. Bulk compaction behaviour and tablet porosity .....</b>	<b>185</b>
<b>6.1.2. Dissolution testing and kinetics of drug release .....</b>	<b>185</b>
<b>    6.2. Results and discussion .....</b>	<b>185</b>
<b>6.2.1. Formulation codes .....</b>	<b>185</b>
<b>6.2.2. Bulk compaction behaviour and tablet porosity .....</b>	<b>186</b>
<b>6.2.3. Dissolution testing and kinetics of drug release .....</b>	<b>192</b>

<i>6.3. Conclusions</i> .....	216
<i>6.4. References</i> .....	217
<b>Chapter 7: General discussions and conclusions .....</b>	<b>220</b>
<i>7.1. Introduction</i> .....	220
<i>7.2. Binding between Propranolol hydrochloride (PPN) and Magnesium Aluminium Silicate (MAS)</i> .....	220
<i>7.3. Binding between Diltiazem hydrochloride (DIL) and Magnesium Aluminium Silicate (MAS)</i> .....	223
<i>7.4. Binding between Metformin hydrochloride (MET) and Magnesium Aluminium Silicate (MAS)</i> .....	225
<i>7.5. Challenges of current study</i> .....	226
<i>7.6. Future work</i> .....	227
<i>7.7. References</i> .....	228

## **List of Figures**

**Fig. 1.1.** The widespread use of minerals in pharmaceutical industry and medicine: adapted from (Carretero and Pozo, 2009)

**Fig. 1.2.** (1.) Alumina octahedron; (2.) Alumina sheet composed of alumina octahedron structures joined together; (3.) Silica tetrahedron; (4.) Silica sheet composed of silica tetrahedron structures joined together; joined together in different proportions the alumina sheet and the silica sheet make up the structure of clay minerals: adapted from (K.G. Theng, 2012)

**Fig. 1.3.** Classification of clay minerals based on their layered structure, either 1:1 (alternating octahedral and tetrahedral sheets), 2:1 (one octahedral sheet sandwiched between two tetrahedral sheets) or 2:1:1 for Chlorite group (one octahedral sheet sandwiched between two tetrahedral sheets 2:1 structure plus an additional brucite- or gibbsite- like sheet ) adapted from (Barton and Karathanasis, 2002; Khurana *et al.*, 2015)

**Fig 1.4.** Montmorillonite (a) and saponite (b) clays structure showing the magnesia or alumina octahedral sheet trapped between two tetrahedral silicate sheets: adapted from (Vanderbilt Minerals, 2014b)

**Fig 1.5.** Alumina or magnesia sheet composed of octahedron structures joined together and sandwiched between two silica sheets composed of silica tetrahedron structures joined together: adapted from (Vanderbilt Minerals, 2014b)

**Fig. 1.6.** Delamination of MAS in water achieved by the diffusion of counter ions from platelet faces towards water molecules by osmosis: adapted from (Vanderbilt Minerals, 2014b, 2014a)

**Fig. 1.7.** MAS colloidal structure in water – “house of cards” following the attraction between the weakly positive platelet edges the platelet faces that are negatively charged: adapted from (Vanderbilt Minerals, 2014b, 2014a)

**Fig. 1.8.** Diffuse double layer formation following the addition of excess water and water miscible solvents which destabilizes the “house of cards” structure: adapted from (Vanderbilt Minerals, 2014b, 2014a)

**Fig 1.9.** Behaviour of PPN with varying pH which can lead to protonation of the amine group, deprotonation of the hydroxyl group or make no change: adapted from (*ACD I-Lab*, 2018)

**Fig. 1.11.** Behaviour of DIL with varying pH which can lead to protonation of the amine group: adapted from (*ACD I-Lab*, 2018)

**Fig. 1.12.** Behaviour of MET with varying pH which can lead to protonation of the amine group: adapted from (*ACD I-Lab*, 2018)

**Fig. 1.13.** Representation of polymer formation via polymerisation through the formation of covalent bonds between monomeric units

**Fig. 1.14.** Schematic demonstration of drug release from hydrophilic, swellable polymer matrix systems, determined by gel layer formation and its time dependent dynamics: adapted from (Varma *et al.*, 2004; Ghori and Conway, 2015)

**Fig. 1.15.** Chemical structure of Xanthan Gum: adapted from (CPKelco, 2008)

**Fig. 1.16.** Polyethylene oxide (PEO) synthesis

**Fig. 1.17.** Simple one binding site model where A is the ligand in the syringe and M is the macromolecule in the sample cell; upon binding these form a 1:1 complex

**Fig. 1.18.** Competitive ligand binding where A is the ligand in the syringe and M and B are the macromolecule and competitive ligand respectively, both present in the sample cell

**Fig. 1.19.** VP-ITC micro calorimeter (a) (MicroCal, 1998); Schematic diagram of the VP-ITC micro calorimeter

**Fig 2.1.** MAS-drug flocculated complex dispersions

**Fig. 2.2.** Bragg's Law showing the scattering of x-rays from a crystal lattice

**Fig. 2.3.** HPLC system showing analysis steps involving mobile phase pumping, sample injection and sample passage through column, detector and finally into waste

**Fig. 2.4.** Nanostar system from Bruker

**Fig. 2.5.** SAXS analysis setup showing: (a) Nanostar chamber with the sample holder; (b) sample holder image showing empty borosilicate glass capillary tube (1) and filled capillary tubes with MAS (2), MAS-PPN (3), MAS-DIL (4) and MAS-MET (5) in powder form, particle size 63 – 125 µm; (c) nanography to detect sample coordinates for the analysis showing capillaries (1) to (5)

**Fig. 2.6.** SAXS analysis setup showing MAS-drug flocculated complex dispersion placed into a metal cell fitted with a glass capillary sealed at both ends (1 mm diameter)

**Fig. 2.7.** Tablet press powder compaction described step by step: die fill stage, compaction and ejection

**Fig. 3.1.** ATR-FTIR spectra of PPN, MAS and single and double drug loaded MAS-PPN complex particles

**Fig. 3.2.** PXRD patterns of MAS, PPN and MAS-PPN single and double drug loaded complexes

**Fig. 3.3.** PXRD successive runs testing variations in the basal distance of MAS-PPN single drug loaded complex following dehydration

**Fig. 3.4.** PXRD successive runs testing variations in basal distance of MAS-PPN single drug loaded complex following dehydration and rehydration

**Fig. 3.5.** PXRD successive runs testing variations in basal distance of MAS-PPN single drug loaded complex following dehydration and rehydration

**Fig. 3.6.** PXRD successive runs testing variations in basal distance of MAS following dehydration

**Fig. 3.7.** Thermograms obtained for MAS, PPN and MAS-PPN single and double drug loaded complex particles

**Fig. 3.8.** Surface characterisation of MAS using SEM/EDX. SEM images at different magnifications  $\times 500$  (a),  $\times 1500$  (b),  $\times 5000$  (c) and  $\times 10\,000$  (d); atomic distribution profile at five different sample locations (Spectrum 1-5)

**Fig. 3.9.** Characterisation of PPN surface using SEM/EDX. SEM images at different magnifications  $\times 500$  (a),  $\times 1500$  (b),  $\times 5000$  (c) and  $\times 10\,000$  (d); atomic distribution profile at two different sample locations (Spectrum 1 and 2)

**Fig. 3.10.** Surface characterisation of MAS-PPN single drug loaded complex using SEM/EDX. SEM images at different magnifications  $\times 500$  (a),  $\times 1500$  (b),  $\times 5000$  (c) and  $\times 10\,000$  (d); atomic distribution profile at five different sample locations (Spectrum 1-5)

**Fig. 3.11.** Surface characterisation of MAS-PPN double drug loaded complex using SEM/EDX. SEM images at different magnifications  $\times 500$  (a),  $\times 1500$  (b),  $\times 5000$  (c) and  $\times 10\,000$  (d); atomic distribution profile at five different sample locations (Spectrum 1-5)

**Fig 3.12.** Calibration curve for PPN (100 to 0.1  $\mu\text{g/ml}$ ) showing linearity ( $R^2=0.9998$ )

**Fig. 3.13.** Typical SAXS data for specimens in powder form: (a and b) 2D-SAXS patterns for MAS and MAS-PPN complexes showing the centre of the beam stop; (c) 1D-SAXS intensity curves for MAS and MAS-PPN complexes (open symbols showing uncorrected

data and line showing data after scaled background subtraction), and scaled background (open black square symbols)

**Fig. 3.14.** Double-logarithmic plot of intensity vs. the scattering vector for MAS and MAS-PPN complexes in powder form (particle size 63 – 125  $\mu\text{m}$ ), showing the slope of the linear part for the data which allows the calculation of the power-law constant  $a$  as -3.63 for MAS and -3.57 for MAS-PPN complexes

**Fig. 3.15.** Guinier plot of MAS dispersion and MAS – PPN complex dispersion showing two linear regions in the high and low  $q$  values

**Fig. 3.16.** Double-logarithmic plot of intensity vs. the scattering vector for MAS and MAS-PPN complexes in liquid form, showing power law behaviour

**Fig. 3.17.** Microscopy images of dilute MAS dispersion (0.037 % w/v) in purified water (pH 5) at different magnifications ( $\times 4$ ,  $\times 10$ ,  $\times 40$  and  $\times 100$ )

**Fig. 3.18.** Microscopy images of single drug loaded MAS-PPN complex dispersion prepared using purified water (pH 5) at different magnifications ( $\times 4$ ,  $\times 10$ ,  $\times 40$  and  $\times 100$ )

**Fig. 3.19.** SIM titration of PPN solution into MAS dispersion at pH 5 (black), pH 7 (red) and pH 9 (blue) (25 °C). The return to the baseline highlighted in black is used determine the most rapid interaction. Results are based on three independent repeats done under similar conditions.

**Fig. 3.20.** SIM calorimetric binding studies evaluating the adsorption of PPN onto MAS at pH 5 (a), pH 7 (c) and pH 9 (e) (25 °C). Data analysed through one set of sites curve fitting showing the enthalpy change (kcal mol<sup>-1</sup> of injectant) obtained from injecting PPN (0.150 % w/v) into MAS (0.037 % w/v). Results are based on three independent repeats done under similar conditions.

**Fig. 3.21.** Multiple injection mode calorimetric titration of 0.150 % w/v PPN solution (pH 5) into 0.037 % w/v MAS dispersion (pH 5) at 25 °C (a) and 37 °C (c). Raw data (top) and integrated heats (bottom) as a function of molar ratio. Control runs suggesting limited interaction between water and PPN or MAS; Thermodynamic profile for binding of PPN onto MAS at 25 °C (b) and 37 °C (d) showing enthalpy ( $\Delta H$ ), entropy( $\Delta S$ ) or Gibbs free energy ( $\Delta G$ ). Results are based on three independent repeats done under similar conditions.

**Fig. 3.22.** Titration of 0.037 % w/v PEO dispersion (pH 5) into 0.037 % w/v MAS dispersion (pH 5) at 25 °C (a) and 37 °C (b). Raw data (top) and integrated heats (bottom) as a function of molar ratio.

**Fig. 3.23.** (a) Titration of 0.037 % w/v PEO dispersion (pH 5) into water (pH 5) at 25 °C; (b) Titration of water (pH 5) into 0.037 % w/v MAS dispersion (pH 5) at 25 °C. Raw data (top) and integrated heats (bottom) as a function of molar ratio

**Fig. 3.24.** Scheme of MAS-PEO intercalated composite formation using MAS dispersed in water and PEO dispersed in water: adapted from. (Gao, 2004) Note: Red lines are PEO polymer

**Fig. 3.25.** Titration of PPN solution (pH 5) into PEO dispersion (pH 5) at 25 °C

**Fig. 3.26.** Titration of 0.150 % w/v PPN solution (pH 5) into MAS-PEO mixture (0.037 % w/v MAS; 0.037 % w/v PEO; pH 5) at 25 °C (a) and 37 °C (c). Raw data (top) and integrated heats (bottom) as a function of molar ratio; Thermodynamic profile for adsorption of PPN onto MAS-PEO complex at 25 °C (b) and 37 °C (d) showing enthalpy ( $\Delta H$ ), entropy( $\Delta S$ ) or Gibbs free energy ( $\Delta G$ ). Results are based on three independent repeats done under similar conditions.

**Fig. 3.27.** Schematic representation using shapes of possible chemical interactions between PPN, MAS and PEO based on isothermal titration calorimetry results

**Fig. 3.28.** Raw data for titration of 0.020 % w/v XG dispersion (pH 5) into 0.037 % w/v MAS dispersion (pH 5) at 25 °C (a) and 37 °C (b). Results are based on three independent repeats done under similar conditions.

**Fig. 3.29.** Scheme of MAS-XG composite formation using MAS dispersed in water and PEO dispersed in water: adapted from. (Gao, 2004) Note: Red lines are XG polymer

**Fig. 3.30.** Calorimetric titration of 0.150 % w/v PPN solution (pH 5) into 0.020 % w/v XG dispersion (pH 5) at 25 °C (a) and 37 °C (c). Raw data (top) and integrated heats (bottom) as a function of molar ratio. Control runs suggesting limited interaction between water and XG

**Fig. 3.31.** Titration of 0.150 % w/v PPN solution (pH 5) into a mixture of MAS and XG (0.037 % w/v MAS; 0.020 % w/w XG; pH 5), at 25 °C (a) and 37 °C (c). Raw data (top) and integrated heats (bottom) as a function of molar ratio; Thermodynamic profile for adsorption of PPN onto MAS-XG mixture at 25 °C (b) and 37 °C (d) showing enthalpy ( $\Delta H$ ),

entropy( $\Delta S$ ) or Gibbs free energy ( $\Delta G$ ). Results are based on three independent repeats done under similar conditions.

**Fig. 3.32.** Schematic representation using shapes of possible chemical interactions between PPN, MAS and XG based on isothermal titration calorimetry results.

**Fig. 4.1.** DIL undergoing dilute acid hydrolysis and product DC-DIL

**Fig 4.2.** Competitive ligand binding where A is the ligand in the syringe (DIL) and M and B are the macromolecule and competitive ligand respectively (montmorillonite and saponite making up the MAS), both present in the sample cell

**Fig 4.3.** Competitive ligand binding where A is the ligand in the syringe (DIL) and M and B are the macromolecule and co-solute respectively (MAS and PEO respectively), both present in the sample cell

**Fig. 4.4.** ATR-FTIR scans on MAS, DIL and MAS – DIL single and double drug loaded complex particles

**Fig. 4.5.** PXRD patterns of MAS, DIL and MAS-DIL single and double drug loaded complexes

**Fig. 4.6.** Thermograms obtained for MAS, DIL and MAS-DIL single and double drug loaded complex particles

**Fig. 4.7.** Characterisation of DIL surface using SEM/EDX. SEM images at different magnifications  $\times 100$  (a),  $\times 1500$  (b),  $\times 5000$  (c) and  $\times 10\,000$  (d); atomic distribution profile at two different sample locations (Spectrum 1 and 2)

**Fig. 4.8.** Surface characterisation of MAS-DIL single drug loaded complex using SEM/EDX. SEM images at different magnifications  $\times 500$  (a),  $\times 1500$  (b),  $\times 5000$  (c) and  $\times 10\,000$  (d); atomic distribution profile at five different sample locations (Spectrum 1-5)

**Fig. 4.9.** Surface characterisation of MAS-DIL double drug loaded complex using SEM/EDX. SEM images at different magnifications  $\times 500$  (a),  $\times 1500$  (b),  $\times 5000$  (c) and  $\times 10\,000$  (d); atomic distribution profile at five different sample locations (Spectrum 1-5)

**Fig 4.10.** Calibration curve for DIL (red) (100 to 0.1  $\mu\text{g}/\text{ml}$ ) showing linearity ( $R^2=0.9999$ ) and for DC-DIL (blue) (82.52 – 0.83  $\mu\text{g}/\text{ml}$ )

**Fig. 4.11.** Typical HPLC chromatograms of: DIL standard solution at 25 °C (a) and DIL recovered from MAS-DIL complex using 2 M HCl (24 h exposure) (b), 2 M HCl (30 min exposure) (c), ultra – pure water (d) and pH 6.8 phosphate buffer (e) showing the presence

of DIL (1) and degradant DC-DIL (2)

**Fig. 4.12.** Typical SAXS data for specimens in powder form: (a and b) 2D-SAXS patterns for MAS and MAS-DIL complexes showing the centre of the beam stop; (c) 1D-SAXS intensity curves for MAS and MAS-DIL complexes (open symbols showing uncorrected data and line showing data after scaled background subtraction), and scaled background (open black square symbols)

**Fig. 4.13.** Double-logarithmic plot of intensity vs. the scattering vector for MAS and MAS-DIL complexes in powder form (particle size 63 – 125  $\mu\text{m}$ ), showing the slope of the linear part for the data which allows the calculation of the power-law constant  $a$  as -3.63 for MAS and -3.62 for MAS-DIL complexes

**Fig. 4.14.** Guinier plot of MAS dispersion (0.25 % w/v) and MAS-DIL complex dispersion (containing 0.25 % w/v MAS and 0.25 % w/v DIL) showing two linear regions in the high and low  $q$  values

**Fig. 4.15.** Double-logarithmic plot of intensity vs. the scattering vector for MAS and MAS-DIL complexes (containing 0.25 % w/v MAS and 0.25 % w/v DIL) in liquid form, showing power law behaviour

**Fig. 4.16.** Scheme of the ‘house of cards’ formed upon MAS dispersion in water: adapted from (Vanderbilt Minerals, 2014) (a); Chemical representation of DIL structure (c); Digital microscopy images of MAS (b) and complexes formed between MAS and DIL at different times of aggregation (d – j)

**Fig. 4.17.** Titration of 0.045 % w/v (1 mM) DIL solution (pH 5) into 0.010 % w/v MAS dispersion pH 5 (black), pH 7 (red) and pH 9 (green) at 25 °C

**Fig. 4.18.** ITC raw data showing: titration of 0.144 % w/v (3.2 mM) DIL into 0.036 % MAS and blank titrations (water into MAS 0.036 % w/v and DIL 0.144 % w/v (3.2 mM) into water) (a); titration of 0.020 % w/v (0.45 mM) DIL into 0.010 % w/v MAS (b). All experiments were undertaken at pH5 and 25 °C.

**Fig. 4.19.** Species distribution plot showing the binding between ligand A (DIL) and macromolecules M and B (MAS mixture of montmorillonite and saponite) reaching saturation point (a); Thermodynamic profile through a competitive curve fitting model for adsorption of DIL solution (0.144 % w/v (3.2 mM)) pH 5 onto MAS dispersion (0.036 % w/v) pH 5 at 25 °C (b)

**Fig. 4.20.** Species distribution plot showing the binding between ligand A (DIL) and macromolecules M and B (MAS mixture of montmorillonite and saponite) reaching saturation point (a); Thermodynamic profile through a competitive curve fitting model for adsorption of DIL solution (0.144 % w/v (3.2 mM)) pH 5 onto MAS dispersion (0.036 % w/v) pH 5 at 37 °C (b)

**Fig. 4.21.** Possible DIL-MAS chemical interaction: cation exchange, hydrogen bonding and water bridging

**Fig. 4.22.** Raw data for titration of 0.037 % w/v PEO dispersion (pH 5) into 0.037 % w/v MAS dispersion (pH 5) at 25 °C; Control run between 0.037 % w/v PEO dispersion solution (pH 5) and water (pH5) at 25 °C and between 0.037 % w/v MAS dispersion solution (pH 5) and water (pH5) at 25 °C.

**Fig. 4.23.** Thermodynamic profile through a competitive curve fitting model for adsorption of DIL solution (0.090 % w/v (2 mM)) pH 5 onto MAS-PEO mixture (0.037 % w/v MAS and 0.020 % w/v PEO mixed together at a ratio of 1:1 v/v) pH 5 at 25 °C

**Fig. 4.24.** Thermodynamic profile through a one set of sites curve fitting model for adsorption of DIL solution (0.090 % w/v (2 mM)) pH 5 onto PEO dispersion (0.020 % w/v) pH 5 at 25 °C

**Fig. 4.25.** Raw data for titration of 0.020 % w/v XG dispersion (pH 5) into 0.037 % w/v MAS dispersion (pH 5) at 25 °C, control run between 0.020 % w/v XG dispersion (pH 5) and water (pH5) at 25 °C and control run between 0.037 % w/v MAS dispersion (pH 5) and water (pH5) at 25 °C

**Fig. 4.26.** Raw data for titration of 0.090 % w/v (2 mM) DIL solution (pH 5) into 0.020 % w/v XG dispersion (pH 5) at 25 °C and control run between (0.144 % w/v (3.2 mM) (pH 5)) DIL solution and water (pH5) at 25 °C

**Fig. 4.27.** Thermodynamic profile through a one set of sites curve fitting model for adsorption of DIL solution (0.090 % w/v (2 mM)) pH 5 onto MAS-XG mixture (0.037 % w/v MAS and 0.020 % w/v XG mixed together at a ratio of 1:1 v/v) pH 5 at 25 °C

**Fig. 5.1.** ATR-FTIR repeated scans on MAS – MET single drug loaded complex

**Fig. 5.2.** PXRD patterns of MAS, MET and MAS-MET single and double drug loaded complexes

**Fig. 5.3.** DSC thermogram of MAS, MET and MAS – MET complexes

**Fig. 5.4.** Characterisation of MET surface using SEM/EDX. SEM images at different magnifications  $\times 100$  (a),  $\times 500$  (b),  $\times 1000$  (c) and  $\times 5\,000$  (d); atomic distribution profile at two different sample locations (Spectrum 1 and 2)

**Fig. 5.5.** Surface characterisation of MAS-MET single drug loaded complexes using SEM/EDX. SEM images at different magnifications  $\times 500$  (a),  $\times 1\,500$  (b),  $\times 5\,000$  (c) and  $\times 10\,000$  (d); atomic distribution profile at five different sample locations (Spectrum 1-5)

**Fig. 5.6.** Surface characterisation of MAS-MET double drug loaded complexes using SEM/EDX. SEM images at different magnifications  $\times 500$  (a),  $\times 1\,500$  (b),  $\times 5\,000$  (c) and  $\times 10\,000$  (d); atomic distribution profile at five different sample locations (Spectrum 1-5)

**Fig. 5.7.** Calibration curve for MET (100 to 0.1  $\mu\text{g}/\text{ml}$ ) showing linearity ( $R^2=0.1$ )

**Fig. 5.8.** Typical SAXS data for specimens in powder form: (a and b) 2D-SAXS patterns for MAS and MAS-MET complexes showing the centre of the beam stop; (c) 1D-SAXS intensity curves for MAS and MAS-MET complexes (open symbols showing uncorrected data and line showing data after scaled background subtraction), and scaled background (open black square symbols)

**Fig. 5.9.** Double-logarithmic plot of intensity vs. the scattering vector for MAS and MAS-MET complexes in powder form (particle size 63 – 125  $\mu\text{m}$ ), showing the slope of the linear part for the data which allows the calculation of the power-law constant  $a$  as  $-3.63$  for MAS and  $-3.57$  for MAS-MET complexes

**Fig. 5.10.** Guinier plot of MAS dispersion and MAS-MET complex dispersion showing two linear regions in the high and low  $q$  values

**Fig. 5.11.** Double-logarithmic plot of intensity vs. the scattering vector for MAS and MAS-MET complexes in liquid form, showing power law behaviour

**Fig. 5.12.** Microscopy images of single drug loaded MAS-MET complex dispersion prepared using purified water (pH 5) at different magnifications:  $\times 4$  (a);  $\times 10$  (b);  $\times 40$  (c); and  $\times 100$  (d)

**Fig. 5.13.** Titration of 0.016 % w/v (1 mM) MET solution (pH 5) into 0.010 % w/v MAS dispersion pH 5 (black), pH 7 (red) and pH 9 (green) at 25 °C

**Fig. 5.14.** Multiple injection mode calorimetric titration of 0.033 % w/v MET solution (pH 5) into 0.037 % w/v MAS dispersion (pH 5) at 25 °C (a) and 37 °C (b). Raw data (top) and

integrated heats (bottom) as a function of molar ratio. Control runs suggesting interaction between water and MET

**Fig. 5.15.** Thermodynamic profile for binding of MET (0.033 % w/v) onto MAS (0.037 % w/v) at 25 °C (a) and 37 °C (b) showing enthalpy ( $\Delta H$ ), entropy( $\Delta S$ ) or Gibbs free energy ( $\Delta G$ ). Results are based on three independent repeats done under similar conditions.

**Fig. 5.16.** Possible MAS-MET chemical interaction: cation exchange, hydrogen bonding and water bridging

**Fig. 5.17.** Titration of 0.300 % w/v MET into 0.020 % w/v PEO dispersion at 25 °C (a) and 37 °C (b). Raw data (top) and integrated heats (bottom) as a function of molar ratio.

**Fig. 5.18.** Titration of 0.300 % w/v MET into MAS and PEO mixture (0.020 % w/v PEO; 0.020 % w/v MAS) at 25 °C (a) and 37 °C (b). Raw data (top) and integrated heats (bottom) as a function of molar ratio.

**Fig. 5.19.** Calorimetric binding studies showing (a) titration of 0.033 % w/v MET solution (pH 5) into 0.020 % w/v XG dispersion (pH 5) at 25 °C (red) and dilution of 0.033 % w/v MET (pH5) into water pH 5 (black): raw data (top) and integrated heats (bottom) as a function of molar ratio, and (b) integrated heats obtained upon subtraction of MET (0.033 % w/v) dilution in water from the data

**Fig. 5.20.** Titration of 0.080 % w/v MET into MAS and XG mixture (0. 020 % w/v XG; 0.020 % w/v MAS) at 25 °C (a) and 37 °C (b). Raw data (top) and integrated heats (bottom) as a function of molar ratio.

**Fig. 5.21.** Titration of 0.080 % w/v MET into MAS and XG mixture (0. 40 % w/v XG dispersion mixed with 0.040 % w/v MAS dispersion at a 1 to 1 ratio v/v): integrated heats (bottom) as a function of molar ratio showing the erroneous fitting of a one set of sites model to the data

**Fig. 6.1.** Compaction behaviour of formulations containing MAS-PPN complexes or MAS-PPN physical mixture and 5% PEO (a) or XG (b) compacted to 130 MPa: plots of measured upper punch pressure vs. relative density

**Fig. 6.2.** Compaction behaviour of formulations containing MAS-PPN complexes or MAS-PPN physical mixture and 10 % PEO (a) or XG (b) compacted to 130 MPa: plots of measured upper punch pressure vs. relative density

**Fig. 6.3.** Compaction behaviour of formulations containing MAS-PPN complexes or MAS-PPN physical mixture and 30 % PEO (a) or XG (b) compacted to 130 MPa: plots of measured upper punch pressure vs. relative density

**Fig. 6.4.** Compaction behaviour of formulations containing MAS-PPN complexes or MAS-PPN physical mixture and 50 % PEO (a) or XG (b) compacted to 130 MPa: plots of measured upper punch pressure vs. relative density

**Fig. 6.5.** PPN release profile from matrices made of MAS-PPN phys. mix and complex particles combined with PEO (5%) in (a) pH 1.2 hydrochloric acid and (b) pH 6.8 buffer over 10 h

**Fig. 6.6.** PPN release profile from matrices made of MAS-PPN phys. mix and complex particles combined with PEO (10%) in (a) pH 1.2 hydrochloric acid and (b) pH 6.8 buffer over 10 h

**Fig. 6.7.** PPN release profile from matrices made of MAS-PPN phys. mix and complex particles combined with PEO (30%) in (a) pH 1.2 hydrochloric acid and (b) pH 6.8 buffer over 10 h

**Fig. 6.8.** PPN release profile from matrices made of MAS-PPN phys. mix and complex particles combined with PEO (50%) in (a) pH 1.2 hydrochloric acid and (b) pH 6.8 buffer over 10 h

**Fig. 6.9.** Proposed release mechanism model of MAS-PPN complexes and MAS-PPN physical mixture in PEO matrix tablets

**Fig. 6.10.** PPN release profile from matrices made of MAS-PPN phys. mix and complex particles combined with XG (5%) in (a) pH 1.2 hydrochloric acid and (b) pH 6.8 buffer over 10 h

**Fig. 6.11.** PPN release profile from matrices made of MAS-PPN phys. mix and complex particles combined with XG (10%) in (a) pH 1.2 hydrochloric acid and (b) pH 6.8 buffer over 10 h

**Fig. 6.12.** PPN release profile from matrices made of MAS-PPN phys. mix and complex particles combined with XG (30%) in (a) pH 1.2 hydrochloric acid and (b) pH 6.8 buffer over 10 h

**Fig. 6.13.** PPN release profile from matrices made of MAS-PPN phys. mix and complex particles combined with XG (50%) in (a) pH 1.2 hydrochloric acid and (b) pH 6.8 buffer over 10 h

**Fig. 6.14.** Proposed release mechanism model of MAS-PPN complexes and MAS-PPN physical mixture in XG matrix tablets

## **List of Tables**

**Table 1.1.** Chemical analysis VEEGUM® F EP/ MAS showing the amount of oxides and carbonates present in the sample as weight (%). Results obtained using IR spectroscopy and a calcimeter.

**Table 1.2.** Chemical structure and physicochemical properties of PPN (Shalaeva *et al.*, 2007; Rojtanatanya and Pongjanyakul, 2010; Sugano, 2012)

**Table 1.3.** Chemical structure and physicochemical properties of DIL

**Table 1.4.** Chemical structure and physicochemical properties of metformin hydrochloride

**Table 3.1.** Compounds and parameters used in ITC SIM and MIM experiments

**Table 3.2.** HPLC method validation for PPN showing linearity range, intermediate and intra assay precision, LOD and LOQ

**Table 3.3.** PPN content in single drug loaded and double drug loaded MAS–PPN complex particles using three different dissolution media: 2M HCl, ultra-pure water (pH 5) and phosphate buffer (pH 6.8)

**Table 3.4.** SIM calorimetric binding studies evaluating the adsorption of PPN onto MAS at pH 5, 7 and pH 9 (25 °C). Data analysed through one set of sites curve fitting using a non-linear least squares model to calculate affinity (K), changes in enthalpy ( $\Delta H$ ), entropy( $\Delta S$ ) or Gibbs free energy ( $\Delta G$ ). Results are based on three independent repeats done under similar conditions.

**Table 3.5.** Multiple injection mode calorimetric binding studies evaluating the adsorption of PPN onto MAS at 25 and 37 °C (pH 5). Data analysed through one set of sites curve fitting using a non-linear least squares model to calculate affinity (K), changes in enthalpy ( $\Delta H$ ), entropy( $\Delta S$ ) or Gibbs free energy ( $\Delta G$ ). Results are based on three independent repeats done under similar conditions.

**Table 3.6.** The binding parameters (affinity, free energy, binding enthalpy and entropy factor) for PPN solution (0.150 % w/v) titration into a MAS and PEO mixture (0.037 % w/v MAS; 0.037 % w/v PEO) at 25 and 37 °C (pH 5).

**Table 3.7.** Multiple injection mode calorimetric binding studies evaluating the binding between PPN (0.150 % w/v) and XG (0.20 % w/v) at 25 and 37 °C (pH 5). Data analysed through one set of sites curve fitting using a non-linear least squares model to calculate

affinity (K), changes in enthalpy ( $\Delta H$ ), entropy (- $T\Delta S$ ) or Gibbs free energy ( $\Delta G$ ). Results are based on three independent repeats done under similar conditions.

**Table 3.8.** Results showing data analysed through competitor binding model to calculate affinity (K) and changes in enthalpy ( $\Delta H$ ) and entropy (- $T\Delta S$ ) for the PPN-MAS binding in the presence of XG following multiple injection calorimetric binding studies between PPN (0.150 % w/v) and XG-MAS mixture (0.037 % w/v MAS; 0.020 % w/w XG) at 25 and 37 °C (pH 5). Results are based on three independent repeats done under similar conditions.

**Table 4.1.** Compounds and parameters used in ITC SIM and MIM experiments

**Table 4.2.** HPLC method validation for DIL and DC-DIL

**Table 4.3.** DIL and DC-DIL content in double drug loaded MAS-DIL complex particles

**Table 4.4.** Multiple injection mode calorimetric binding studies studying the adsorption of DIL (0.144 % w/v (3.2 mM)) onto MAS (0.036% w/v) at 25°C (pH 5). Data analysed through a competitive curve fitting model to calculate affinity (K) and changes in enthalpy ( $\Delta H$ ) and entropy (- $T\Delta S$ ).

**Table 4.5.** Multiple injection mode calorimetric binding studies studying the adsorption of DIL (0.144 % w/v (3.2 mM)) onto MAS (0.036% w/v) at 25°C (pH 5). Data analysed through a competitive curve fitting model to calculate affinity (K) and changes in enthalpy ( $\Delta H$ ) and entropy (- $T\Delta S$ ).

**Table 4.6.** Calorimetric binding studies evaluating the adsorption of DIL (0.090 % w/v (2 mM)) onto MAS (0.036 % w/v) at 25°C (pH 5). Data analysed through a competitive curve fitting model to calculate affinity (K) and changes in enthalpy ( $\Delta H$ ) and entropy (- $T\Delta S$ ).

**Table 4.7.** Multiple injection mode calorimetric binding studies studying the adsorption of DIL (0.090 % w/v (2 mM)) onto MAS-XG mixture (0.037 % w/v MAS and 0.020 % w/v XG mixed together at a ratio of 1:1 v/v) at 25°C (pH 5). Data analysed through a competitive curve fitting model to calculate affinity (K) and changes in enthalpy ( $\Delta H$ ) and entropy (- $T\Delta S$ ).

**Table 5.1.** Compounds and parameters used in ITC SIM and MIM experiments

**Table 5.2.** HPLC method validation for MET showing linearity range, intermediate and intra assay precision, LOD and LOQ

**Table 5.3.** MET content in double drug loaded MAS–MET complex particles using three different dissolution media: 2M HCl, ultra-pure water (pH 5) and phosphate buffer (pH 6.8)

**Table. 5.4.** Multiple injection mode calorimetric binding studies evaluating the adsorption of MET onto MAS at 25 and 37 °C (pH 5). Data analysed through one set of sites curve fitting using a non-linear least squares model to calculate affinity (K), changes in enthalpy ( $\Delta H$ ), entropy( $\Delta S$ ) or Gibbs free energy ( $\Delta G$ ). Results are based on three independent repeats done under similar conditions. Heat of dilution for MET (0.033 % w/v) and water (pH 5) subtracted at both temperatures to correct data.

**Table. 6.1.** Formulation codes for tablets prepared using MAS-PPN complexes or MAS-PPN physical mixture (both containing an equivalent of 40 mg PPN), and PEO or XG in different amounts (5 % w/w, 10 % w/w, 30 % w/w and 50 % w/w)

**Table. 6.2.** Comparison of bulk compaction behaviour and porosity for formulations MAS-PPN complexes or MAS-PPN physical mixture and 5% w/w PEO or XG; all specimens compacted to 130 MPa average upper punch pressure

**Table. 6.3.** Comparison of bulk compaction behaviour and porosity for formulations MAS-PPN complexes or MAS-PPN physical mixture and 10 % PEO or XG; all specimens compacted to 130 MPa average upper punch pressure.

**Table. 6.4.** Comparison of bulk compaction behaviour and porosity for formulations MAS-PPN complexes or MAS-PPN physical mixture and 30 % PEO or XG; all specimens compacted to 130 MPa average upper punch pressure.

**Table. 6.5.** Comparison of bulk compaction behaviour and porosity for formulations MAS-PPN complexes or MAS-PPN physical mixture and 50 % PEO or XG; all specimens compacted to 130 MPa average upper punch pressure.

**Table. 6.6.** Kinetics of drug release of tablets prepared using MAS-PPN complexes of MAS-PPN physical mixture incorporated in 5 % PEO matrices

**Table. 6.7.** Kinetics of drug release of tablets prepared using MAS-PPN complexes of MAS-PPN physical mixture incorporated in 10 % PEO matrices

**Table. 6.8.** Kinetics of drug release of tablets prepared using MAS-PPN complexes of MAS-PPN physical mixture incorporated in 30 % PEO matrices

**Table. 6.9.** Kinetics of drug release of tablets prepared using MAS-PPN complexes of MAS-PPN physical mixture incorporated in 50 % PEO matrices

**Table. 6.10.** Tablets containing MAS-PPN complexes or MAS-PPN physical mixture in PEO matrix: appearance prior to dissolution studies and after dissolution in pH 1.2 hydrochloric acid and pH 6.8 buffer

**Table. 6.11.** Tablets containing MAS-PPN complexes or MAS-PPN physical mixture in XG matrix: appearance prior to dissolution studies and after dissolution in pH 1.2 hydrochloric acid and pH 6.8 buffer

## **Abbreviations**

ATR-FTIR	Attenuated total reflectance Fourier transform infrared spectroscopy
API	Active pharmaceutical ingredient
CEC	Cation exchange capacity
CR	Controlled release
CS	Chitosan
DC-DIL	Desacetyl diltiazem
DIL	Diltiazem hydrochloride
DSC	Differential scanning calorimetry
EDX	Energy dispersive X-ray spectroscopy
ER	Extended release
G	Galactomannan
HPLC	High performance liquid chromatography
HPMC	Hydroxypropyl methylcellulose
ITC	Isothermal titration calorimetry
MAS	Magnesium aluminium silicate
MEC	Minimum effective concentration
MET	Metformin hydrochloride
MIM	Multiple injections mode
MTC	Minimum toxic concentration
MW	Molecular weight
NaCMC	Sodium carboxymethylcellulose
NCT	Nicotine

NMR	Nuclear magnetic resonance
PEO	Polyethylene oxide
PPN	Propranolol hydrochloride
PXRD	Powder X-ray diffractometry
SANS	Small angle neutron scattering
SAXS	Small angle X-ray scattering
SEM	Scanning electron microscopy
SIM	Single injection mode
UV	Ultraviolet
VX	O-ethyl-S-[2-N,N-(diisopropylamino)ethyl] methylphosphonothioate
XG	Xanthan gum

# *Chapter 1:*

## *General Introduction to the Thesis*

## **Chapter 1: General introduction to the thesis**

### **1.1. Introduction**

Minerals are widely used in the pharmaceutical industry and in medicine. The use of minerals by humans dates back to about 2500 BC in Mesopotamia where they demonstrated clays use for therapeutic purposes (Gomes, 2018). Further evidence from Ancient Greece, Roman times and medieval times reported the use of clay for medicinal purposes. Minerals are easily available in nature and are used for their nutritional, cosmetic and therapeutic properties due to their safety and physicochemical properties. Novel practices involve the use of minerals as drug carriers in the formulation of pharmaceutical dosage forms through their capacity to adsorb or reversibly fixate polar compounds onto their structure and form complex dispersions and particles (Carretero and Pozo, 2009). These complexes can modify the release of drugs upon administration, which is desirable for drugs having a short half-life and require frequent administration to maintain adequate drug plasma levels that are used to treat chronic conditions (Rojtanatanya and Pongjanyakul, 2010). However, the physicochemical characteristics of the formed complexes are not entirely understood and understanding them is essential to establishing a successful formulation. The purpose of the presented research was to understand the process of adsorption of cationic drugs onto a smectite clay (magnesium aluminium silicate) and the effects of this process on extending the release of such drugs. The adsorption onto magnesium aluminium silicate of three model drugs having different therapeutic effects was studied. Furthermore, two different polymers were used in the study in combination with the formulated clay-drug complexes. Polymers are of high importance to the pharmaceutical industry as they offer a wide variety of physical and chemical characteristics which can be easily manipulated and are widely used in the formulation of tablets as to improve bioavailability and control drug release (Sinko, 2010). The ability to extend drug release is also essential in improving patient compliance, hence the popularity of polymers and the rapid advances in the pharmaceutical industry since their introduction.

The use of polymers in combination with clay-drug complex particles in the present study offers an in-depth understanding of controlling drug release using a combined system consisting of a natural drug carrier in a polymeric matrix.

## **1.2. Oral dosage forms**

Oral administration represents the cheapest, safest, most common and convenient route of administration among patients and is usually intended for systemic effects. Examples of oral dosage forms are tablets, capsules, emulsions, suspensions and solutions (Aulton, 2007).

The drug is released from the dosage form, penetrates the physiological barriers of the gastrointestinal tract and reaches the blood system. However, oral administration of drugs has many disadvantages too due to the role of the physicochemical properties of the drug (Patrick, 2001). The formulated drug must be physically and metabolically stable and have the right hydrophilic and hydrophobic balance. It is also important to correctly establish the proper dose that will provide a therapeutic effect and will not be toxic in patients. All drug compounds need appropriate use as they are xenobiotics (foreign to the body) and can cause harm instead of healing. “Only the dose makes a thing not a poison”, as Paracelsus, stated (Jambhekar and Breen, 2009).

Most drugs are formulated and marketed as tablet dosage forms, due to patient compliance and reduced costs. Tablets are generally made by compression and contain the active pharmaceutical ingredient (API) and additives (used for specific functions), such as fillers (diluents) to add bulk to the dosage form, binders to aid granule formation from powder ingredients, disintegrants to help tablet break-up in the GI tract, glidants and lubricants to improve flow properties of the granules, as well as coating materials, stabilizers, flavouring and colouring agents and sweeteners (Mahato and Narang, 2012).

Tablets can be classified based on the physicochemical properties of the drug, site, absorption from the GI tract, solubility and stability, biocompatibility with other ingredients, as well as the dose. Therefore, tablets can be administered orally (swallowed) for systemic effects, or via buccal route (placed under the cheek mucosa, or between the lip and the gum) or sublingual route (under the tongue), intended for a rapid absorption or a local effect (Aulton, 2007; Mahato and Narang, 2012). Tablets can also be classified as effervescent, chewable, dispersible and lozenges. Considering drug release, this can be immediate, controlled, extended or delayed and depends on the pharmacokinetic and physicochemical properties of drugs (Rodrigues *et al.*, 2013). Most drugs are formulated to provide immediate drug release. Therefore, following administration significant fluctuations in the drug plasma level can occur and hence, the dose may be ineffective, lower than the minimum effective

concentrations (MEC), or toxic, higher than the minimum toxic concentration (MTC) (Rodrigues *et al.*, 2013).

Controlled-release tablets are of high interest as they display several benefits compared to conventional tablets, such as maintaining a constant drug-plasma concentration for extended periods of time, thereby achieving optimal efficacy in chronic conditions where medication must be administered at constant levels, and a reduced frequency of side effects (Aulton, 2007). There are many terms that are interchangeably used to name this type of formulation, such as controlled release (CR), extended release (ER), prolonged release etc., however the objective is the same (Goyal *et al.*, 2017). Controlled-release tablets are made by adding modified-release excipients to the powder mix during manufacturing. This leads to the drug particles becoming entrapped in a matrix of excipients which further controls the extent at which the drug is released (Moynihan and Crean, 2009). Examples of controlled-release excipients used in the formulation of pharmaceutical dosage forms are minerals, used as carriers of active ingredients to achieve modified release and polymers (Carretero and Pozo, 2009).

### 1.3. Minerals in the pharmaceutical industry

Minerals have a variety of applications in the pharmaceutical industry and in medicine which dates back since prehistory (Carretero and Pozo, 2009). Minerals have physicochemical properties such as chemical inertness, high adsorption capacity and specific area, swelling, water solubility and dispersivity, plasticity, acid-absorbing capacity, as well as colour, opacity and low or no toxicity in patients, which makes them suitable for medical and pharmacological applications (Carretero, 2002; Carretero and Pozo, 2009). In the formulation of pharmaceutical dosage forms, minerals are used as excipients, carriers of active ingredients to achieve modified release, as binders, fillers, disintegrants, lubricants, thickening agents, anticaking agents, flavouring correctors and emulsifying agents (Fig 1.1). The minerals which have their specific properties reported and are used at the moment for therapeutic purposes are clay minerals (Carretero, 2002).

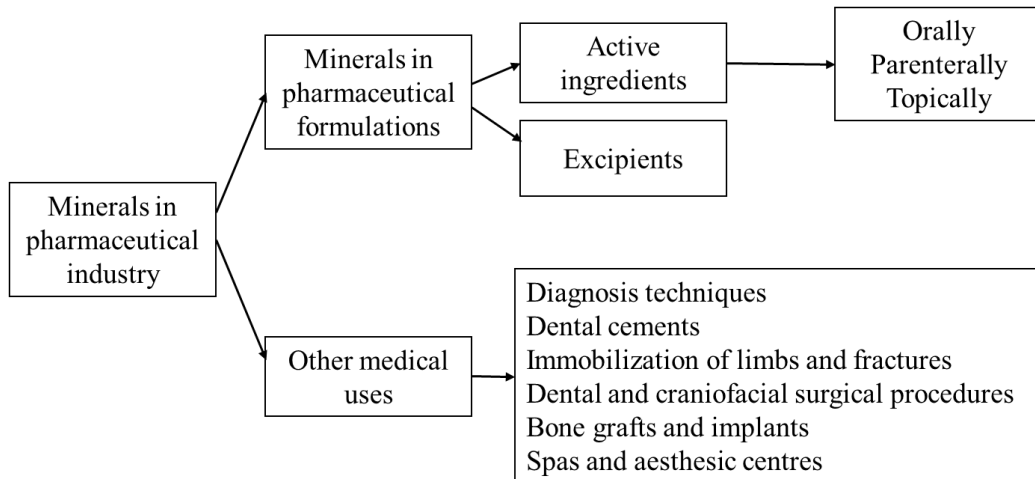
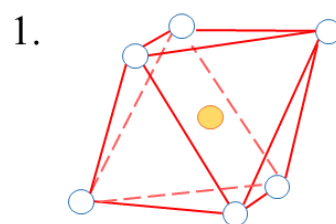


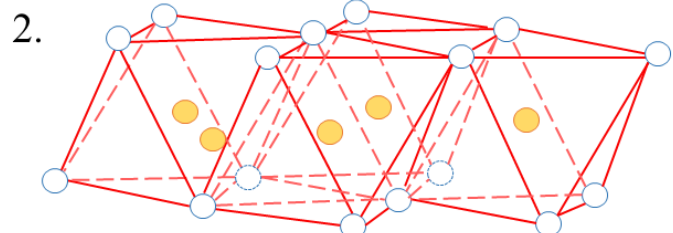
**Fig. 1.1.** The widespread use of minerals in pharmaceutical industry and medicine: adapted from (Carretero and Pozo, 2009)

The terms clay and clay minerals should be distinguished – clay represents the fine-grained inorganic section that make up soils and sediments, which is mainly composed of clay minerals, mostly phyllosilicates (>50%) (Carrado and Bergaya, 2007). Clay minerals are phyllosilicates with a heterogeneous porosity that make up the fine-grained fragments of soils and sediments (Carrado and Bergaya, 2007). They may also be called *layered (hydr)oxides of silicon and aluminium or magnesium* based on their chemical formula (Carrado and Bergaya, 2007).

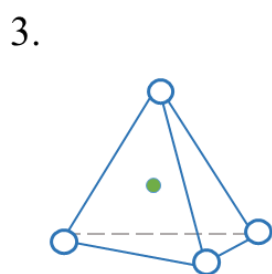
These are composed of one tetrahedral silica sheet and one octahedral alumina sheet that are joined together in different proportions to form an aluminosilicate layer.



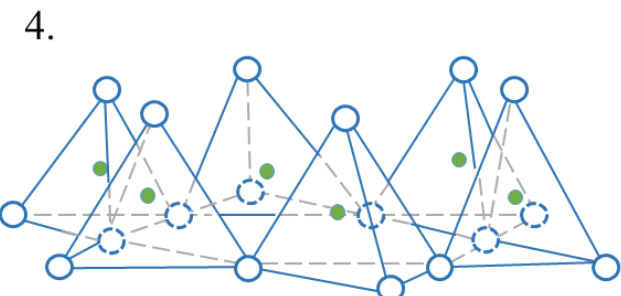
and = Hydroxyls



= Aluminiums, magnesiums, etc



and = Oxygens



= Silicons

**Fig. 1.2.** (1.) Alumina octahedron; (2.) Alumina sheet composed of alumina octahedron structures joined together; (3.) Silica tetrahedron; (4.) Silica sheet composed of silica tetrahedron structures joined together; joined together in different proportions the alumina sheet and the silica sheet make up the structure of clay minerals: adapted from(Theng, 2012)

As shown in Fig. 1.2., the silica tetrahedral sheet is formed of individual tetrahedrons (containing a central  $\text{Si}^{4+}$  ion that is coordinated to four oxygen atoms) linked to share three corners. The basal oxygen atoms in the tetrahedral sheet are therefore almost coplanar and form an open hexagonal network (Theng, 2012). The octahedral sheet is formed of individual alumina octahedrons (containing a central  $\text{Al}^{3+}$  or  $\text{Mg}^{2+}$  ion, coordinated to six hydroxyl groups) linked by sharing edges. When  $\text{Al}^{3+}$  is the predominant cation, only two of every three octahedral positions are occupied in order to maintain the charge balance within the

clay lattice (dioctahedral clay). In contrast, all octahedral positions are filled when the central cation is  $Mg^{2+}$  (trioctahedral clay) (Theng, 2012).

Based on the number and type of layers (tetrahedral and octahedral sheets) present, clays may be classified as shown in Fig. 1.3. Smectites, kaolinite, palygorskite and talc are the clay mineral groups used in the pharmaceutical industry (Carretero and Pozo, 2009).

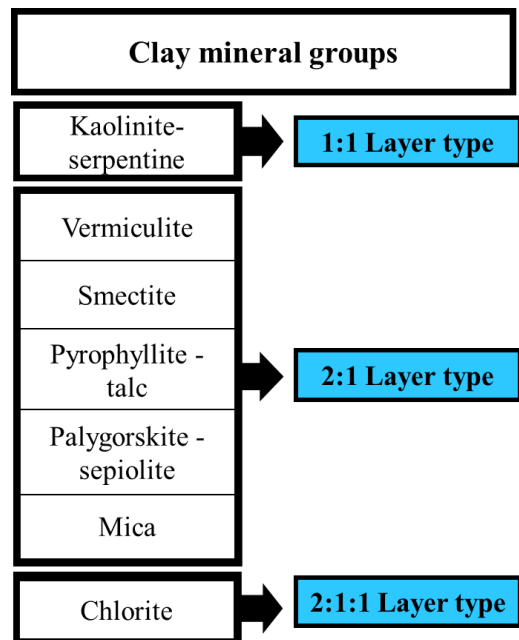


**Fig. 1.3.** Classification of clay minerals based on their layered structure, either 1:1 (alternating octahedral and tetrahedral sheets), 2:1 (one octahedral sheet sandwiched between two tetrahedral sheets) or 2:1:1 for Chlorite group (one octahedral sheet sandwiched between two tetrahedral sheets 2:1 structure plus an additional brucite- or gibbsite- like sheet ) adapted from (Barton and Karathanasis, 2002; Khurana *et al.*, 2015)

The most widely used smectite clays used within the pharmaceutical industry are montmorillonite, saponite and hectorite, often used as excipients within drug formulation. These share structural similarities but have unique chemical composition. Smectites are used as disintegrants due to their high swelling capacity and acid-absorbing capacity, as diluents and binders due to their plasticity, as emulsifying, thickening and anticaking agents due to their colloidal and thixotropic properties and as flavour correctors due to their high sorption capacity. Also, the structure of smectite clays makes it possible for them to interact or form

complexes with drugs in many ways, via cation exchange with cationic drugs, weak anionic exchange with anionic drugs, hydrogen bonding, intercalation between un-delaminated crystals and adsorption by solvent decomposition onto the high surface area of the clay to enhance dissolution rate.

#### 1.4. Magnesium aluminium silicate

##### 1.4.1. Characterisation

Magnesium aluminium silicate (MAS / VEEGUM<sup>®</sup>) is a mixture of natural smectite montmorillonite and saponite clays as shown in Fig. 1.4. They are often used to improve the physical characteristics of drugs and to control their release (Pongjanyakul, Khunawattanakul and Puttipipatkhachorn, 2009; Kanjanakawinkul *et al.*, 2013). It has a high surface area, a very good affinity with cationic drugs and it is not toxic or irritant, therefore making it suitable to be used within drug formulation. MAS has a layered silicate structure, formed of one alumina or magnesia octahedral sheet, sandwiched between two tetrahedral silicate sheets (Kanjanakawinkul *et al.*, 2013).

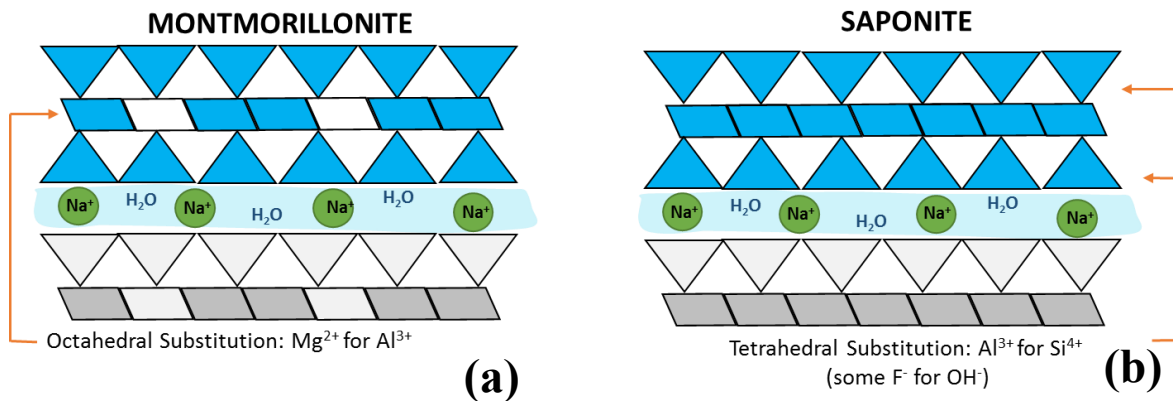


**Fig 1.4.** Montmorillonite (a) and saponite (b) clays structure showing the magnesia or alumina octahedral sheet trapped between two tetrahedral silicate sheets: adapted from(Vanderbilt Minerals, 2014b)

The silica tetrahedral sheet is formed of individual tetrahedrons (containing a central  $Si^{4+}$  ion that is coordinated to four oxygen atoms) linked to share three corners. The basal oxygen atoms in the tetrahedral sheet are therefore almost coplanar and form an open hexagonal network (Kanjanakawinkul *et al.*, 2013). The octahedral sheet is formed of individual alumina octahedrons (containing a central  $Al^{3+}$  or  $Mg^{2+}$  ion, coordinated to six hydroxyl

groups) linked by sharing edges (Fig. 1.5.).

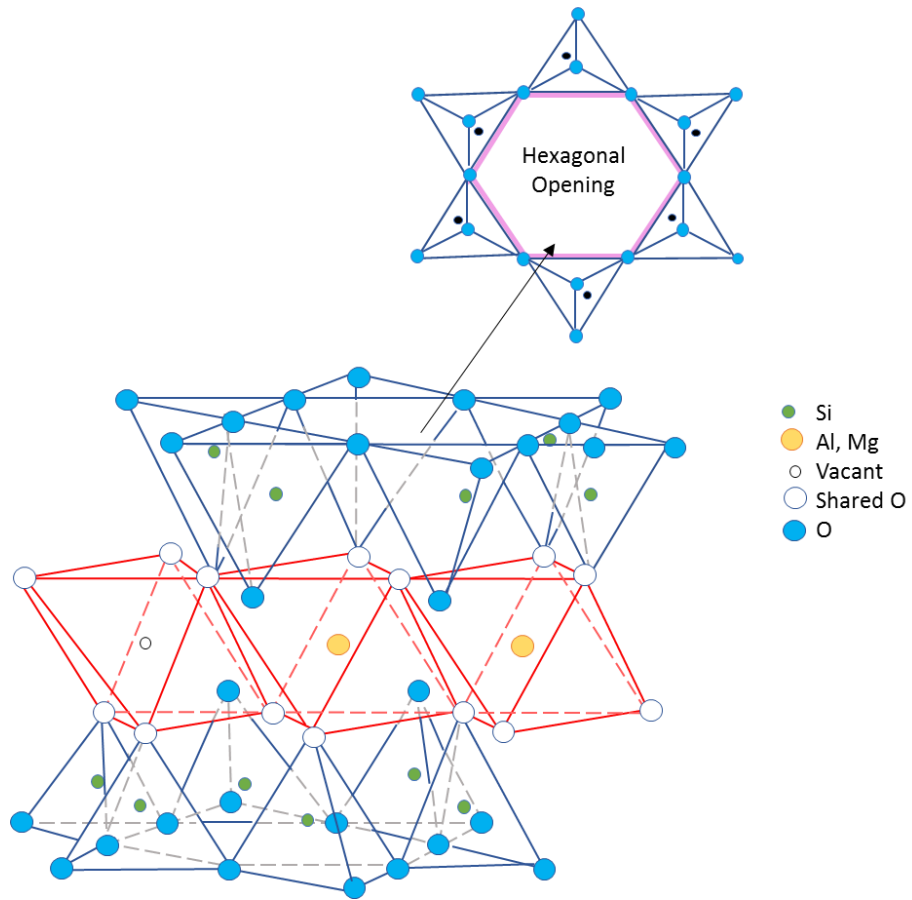


**Fig 1.5.** Alumina or magnesia sheet composed of octahedron structures joined together and sandwiched between two silica sheets composed of silica tetrahedron structures joined together: adapted from (Vanderbilt Minerals, 2014b)

Only two of every three octahedral positions are occupied to maintain the charge balance within the clay lattice when  $\text{Al}^{3+}$  is the predominant cation, as in montmorillonite (Fig 1.4. a). In contrast, all octahedral positions are filled when the central cation is  $\text{Mg}^{2+}$ , as in saponite ( trioctahedral clay) (Fig 1.4. b).

A single MAS platelet is 0.96 nm thick and up to several hundred nm across (Vanderbilt Minerals, 2014b).

In water, clay particles are delaminated into individual clay platelets and form a viscous colloidal structure. The strength of the colloidal structure, as well as the degree of viscosity

depends on the degree of hydration. Modifications of parameters such as stirring intensity or water temperature does affect the degree or the time of hydration of MAS, and therefore conditions must be consistently controlled to achieve adequate hydration and reproducible results.

Clay hydration in polar liquids easily allows the delamination of smectite clays, which can be very difficult to achieve mechanically. This is due to the binding effect of counter ions and water found between platelets. When mixed together (Fig 1.6.), water easily forces the clay platelets further apart as it penetrates between them (osmosis) and hence cations diffuse away from platelet faces (diffusion) (Vanderbilt Minerals, 2014b).

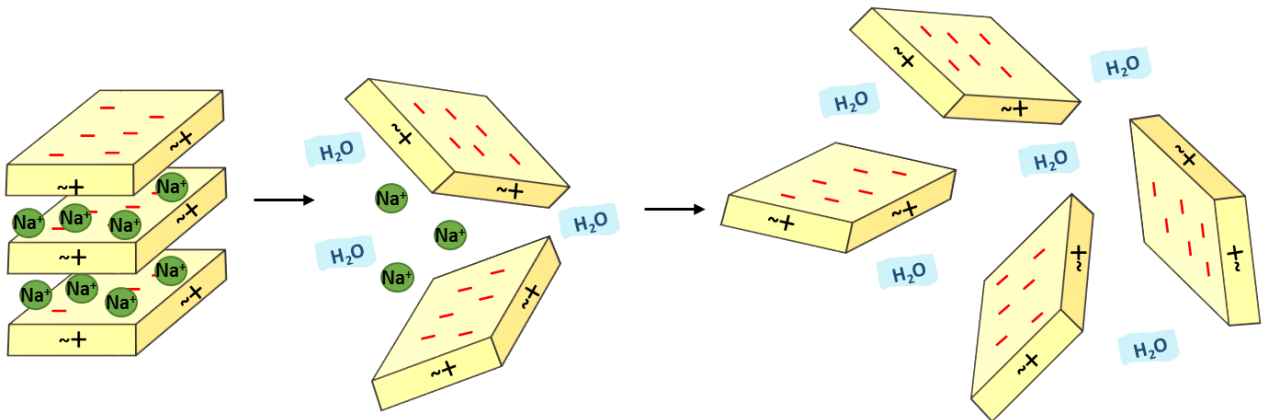


**Fig. 1.6.** Delamination of MAS in water achieved by the diffusion of counter ions from platelet faces towards water molecules by osmosis: adapted from(Vanderbilt Minerals, 2014b, 2014a)

The time required for complete hydration of magnesium aluminium silicate depends on the mechanical and thermal energy introduced during hydration. Following hydration and hence clay platelets separation, a three-dimensional colloidal structure forms as the weakly positive platelet edges are attracted by the platelet faces that are negatively charged. The colloidal structure formed accounts for the rheological characteristics of the clay as it can trap and aggregate solids (suspension), oils (emulsion) and gasses (foam) and is generally called the “house of cards” due to its shape (Fig 1.7.) (Vanderbilt Minerals, 2014b, 2014a). Clay dispersions are also thixotropic, increasing viscosity while undisturbed and decreasing

viscosity while under constant shear, and pseudoplastic, as their viscosity decreases with increasing the rate of shear.

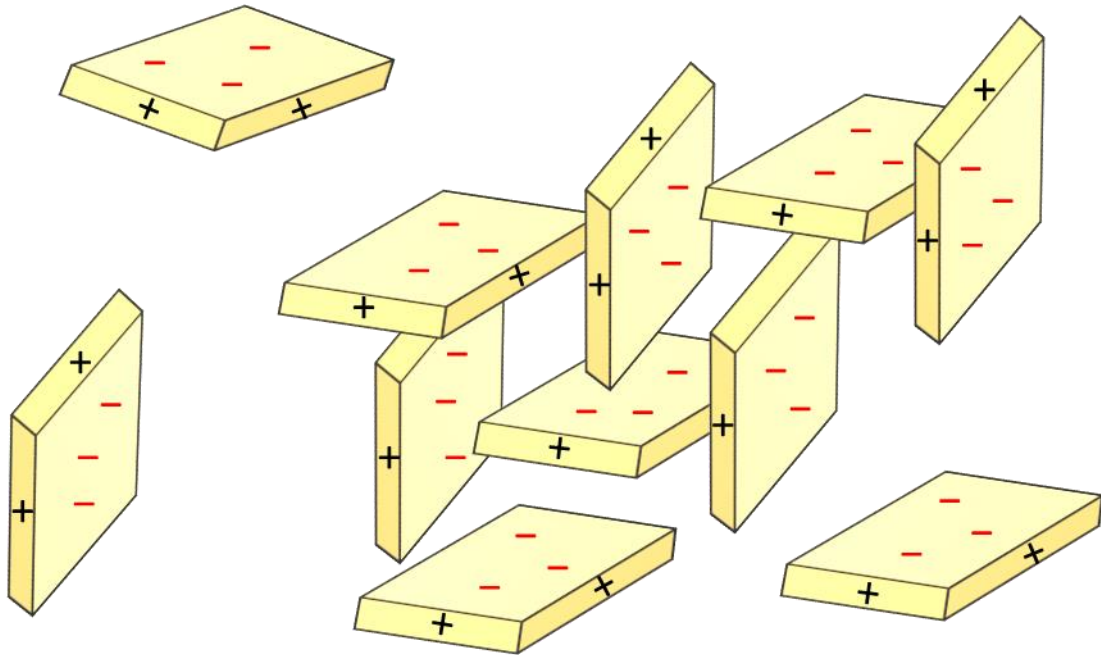


**Fig. 1.7.** MAS colloidal structure in water – “house of cards” following the attraction between the weakly positive platelet edges the platelet faces that are negatively charged:

adapted from (Vanderbilt Minerals, 2014b, 2014a)

However, the addition of excess water destabilizes the “house of cards”, leading to the formation of a diffuse negative double layer (Fig. 1.8.). Following the addition of water or water-soluble solvents, the exchangeable ions in the clay dispersion tend to accumulate near the negative faces of platelets due to electrostatic interactions, but at the same time, tend to diffuse toward the bulk of water. For these opposing effects to equilibrate, a diffuse atmosphere of counter ions forms, which diminishes as distancing from the platelet negative face occurs. The negative surface along with the diffuse counter ions therefore forms a “negative” double layer. The same happens for the weakly positive platelet edges, as a “positive” double layer is formed in association with electrolytes and water-miscible solvents (Vanderbilt Minerals, 2014a).

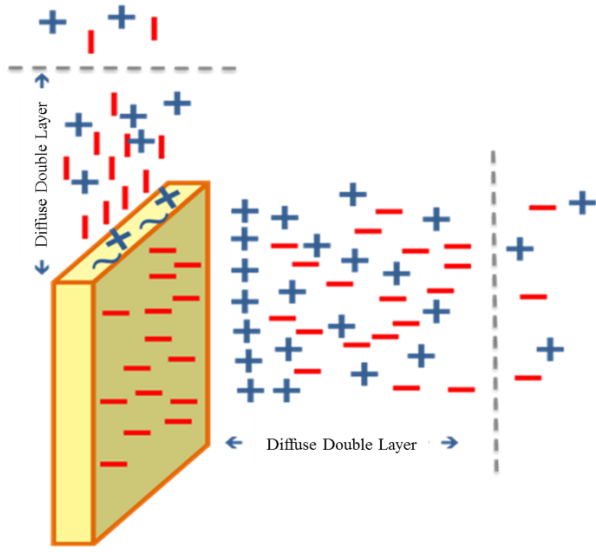


**Fig. 1.8.** Diffuse double layer formation following the addition of excess water and water miscible solvents which destabilizes the “house of cards” structure: adapted from (Vanderbilt Minerals, 2014b, 2014a)

#### 1.4.2. Chemical analysis

VEEGUM® F EP the grade of MAS used in present study was sent for analysis to Wienerberger, the largest manufacturer of bricks worldwide. Studies were performed at their laboratories using infrared spectroscopy and a calcimeter. The results showed that the VEEGUM® F EP clay is a mix of clay minerals and carbonates (Table 1.1.).

**Table 1.1.** Chemical analysis VEEGUM® F EP/ MAS showing the amount of oxides and carbonates present in the sample as weight (%). Results obtained using IR spectroscopy and a calcimeter.

	Weight (%)		Weight (%)
Silica	58.63	<i>Calcium carbonate</i>	1.13
Ferric oxide	2.50	<i>Magnesium carbonate</i>	2.55
Alumina	11.91	<i>Sodium carbonate</i>	0.71
Calcium oxide	2.43	<i>Potassium carbonate</i>	2.55
Magnesia	7.69	<i>TOTAL</i>	6.94
Sodium oxide	1.44		
Potassium oxide	3.26		
Titanium oxide	0.09		
Loss on ignition	11.90		
<b>TOTAL</b>	<b>99.85</b>		

The chemical analysis using IR spectrometry showed high amounts of silica (58.63 %), alumina (11.91 %) and magnesia (7.69 %) present in the analysed sample. The high percentage of magnesia and alumina confirm the presence of both montmorillonite and saponite clays within the material (Kanjanakawinkul *et al.*, 2013). Low quantities of ferric oxide, calcium oxide, potassium oxide and sodium oxide, as well as trace amounts of titanium oxide were observed, showing the presence of exchangeable cations adsorbed onto the clay structure via electrostatic interactions.

A loss on ignition of 11.90 % resulted from loss of water, organic matter and carbonates upon heating the sample between 120-150 °C (Weems, 1903). The clay was further analysed by heating it to 900-1100 °C. This process produced 3.06 % CO<sub>2</sub> which resulted from the thermal decomposition of the carbonates present.

The quantification of individual carbonates present in the sample was possible based on the IR results, as well as using a calcimeter. The calcimeter used works in accordance to the method of Scheibler which determines the carbonate content using a volumetric method. The method involves the addition of hydrochloric acid to the clay sample which leads to the conversion of the carbonates into CO<sub>2</sub>. The amount of CO<sub>2</sub> released produces a difference in pressure which is measured on a burette filled with water and deaerated. The difference in level on the burette is used to calculate the carbonate content as an equivalent calcium carbonate content (*Calcimeter Manual*, 2018).

VEEGUM® F EP grade is an ultrafine powder which complies with the European Pharmacopoeia monograph for Magnesium Aluminium Silicate and is indicated to be used as a dry material in pressed powders and in direct compression tablets (Vanderbilt Minerals, 2014a).

### **1.5. Applications and published studies**

The ability of smectite clays to adsorb or reversibly fixate polar compounds onto their structure and form complex dispersions and particles has been of considerable interest more recently and used to modulate drug release. Numerous studies carried out by Pongjanyakul *et al.* aimed to form intercalated complexes through the adsorption of different compounds (nicotine (NCT) and propranolol hydrochloride (PPN)) onto MAS as well as polymers such as chitosan (CS) (Pongjanyakul, Khunawattanakul and Puttipipatkhachorn, 2009; Khunawattanakul *et al.*, 2010; Rojtanatanya and Pongjanyakul, 2010; Pongjanyakul and Rojtanatanya, 2012; Kanjanakawinkul *et al.*, 2013; Rongthong *et al.*, 2013). The formed complexes and composites were essentially used to modulate drug release.

One of the studies published by the above authors in 2010 aimed to formulate and characterise PPN and MAS complex dispersions and particles (Rojtanatanya and Pongjanyakul, 2010). The authors described the step by step preparation technique for the single and double drug loaded complexes involving the incorporation of PPN solution in water into MAS dispersion in water at different pHs and their incubation at 37 °C with shaking to allow PPN adsorption. The authors observed the destabilisation of the MAS dispersion upon the addition of the PPN solution, leading to the formation of large

flocculates. The size, zeta potential and the amount of PPN present in the flocculates were all shown to be pH dependent. The authors described the filtration of the prepared complex particles and drying in the oven overnight at 50 °C, followed by grinding and sieving of the complexes to the desired particle size. Using FTIR and solid-state NMR the authors were able to demonstrate the intercalation of PPN into the silicate layers of MAS via mechanisms such as cation exchange, hydrogen bonding and water bridging. The drug was also shown to be molecularly dispersed and in amorphous form onto the surface of MAS using powder X-ray diffractometry (PXRD) and differential scanning calorimetry (DSC). The MAS-PPN complex dispersions and particles were then tested for their capability to mediate PPN release. Release studies were carried out using MAS-PPN complexes and showed that PPN release was controlled by diffusion and demonstrated that the MAS-PPN complexes represent strong candidates in mediating the drug release in oral dosage forms.

Following the above study published by Pongjanyakul and Rojtanatanya in 2010, the authors carried on research using MAS-PPN complexes as drug reservoirs in hydroxypropyl methylcellulose (HPMC) tablets (Pongjanyakul and Rojtanatanya, 2012). In this publication, tablets were prepared using the direct compression method and HPMC was added as a physical mixture. The PPN release from the tablets containing MAS-PPN complexes and HPMC showed a zero-order release, whereas the tablets containing MAS-PPN physical mixture and HPMC showed an anomalous PPN release.

Both studies published by Pongjanyakul and Rojtanatanya on MAS-PPN complex particles preparation and evaluation of their drug release are of high importance as they demonstrated the efficiency of the MAS to adsorb the highly soluble cationic PPN and modulate its release from a polymeric matrix.

Multiple other studies published using smectite clays showed their capacity to adsorb a wide variety of drugs and form complexes able to modulate drug release. Montmorillonite is an example of smectite clay often used due to its safety. Drugs such as chlorhexidine acetate, timolol maleate, donepezil, sertraline hydrochloride, theophylline, tetracycline, doxycycline, diclofenac sodium were shown to be adsorbed onto montmorillonite and form complexes (Nunes *et al.*, 2007; Park *et al.*, 2008; Parolo *et al.*, 2008; Joshi *et al.*, 2009; Meng *et al.*, 2009; Muśko and Sznitowska, 2013; Kaur and Datta, 2014; Trivedi *et al.*, 2018).

The adsorption of tetracycline onto montmorillonite detailed in a publication by Parolo *et al.* (2008) aimed to study the effects of pH and ionic strength on the adsorption process. The authors found that the adsorption of tetracycline onto montmorillonite was highest in the pH range 2 – 4 and concluded that the clay would be a good purifying agent to be used in waste waters containing tetracycline (Parolo *et al.*, 2008). A similar study was also published by Hamilton *et al* (2019). The authors aimed to adsorb tetracycline (TC) and doxycycline (DC) onto a variety of clays including montmorillonite and observe the effects of pH on the adsorption process and the antibacterial capacity of the formed complexes. The study concluded that the clay minerals tested successfully delivered TC and DC to exhibit antibacterial effects against bacterial strains that can occur in acute skin infections (*Staphylococcus epidermidis*, *Cutibacterium acnes*, and *Pseudomonas aeruginosa*) (Hamilton *et al.*, 2019). Both authors exploited the cation exchange capacity (CEC) of the minerals in producing the complexes for their study.

In a study published in 2019 by Boateng and Okeke, the authors studied the efficacy of composite wafers and films prepared using magnesium aluminium silicate (MAS) and two different polymers (hydroxypropyl methylcellulose (HPMC) and sodium alginate (SA)) compared to commercially available nicotine loaded strips. The authors found that the formulated wafers and films were safe and efficient (Boateng and Okeke, 2019).

The adsorption of theophylline (a drug used as a bronchodilator) onto VEEGUM® F was studied by Trivedi *et al.* (2018). The authors confirmed the intercalation of theophylline into the clay and moreover reported the potential use of the formed complexes as a potential platform to protect the drug against stomach acid and ensure its safe passage and release into the duodenum (Trivedi *et al.*, 2018).

Laity *et al.* 2015 aimed to investigate the compaction behaviour of MAS (Laity *et al.*, 2015). The authors measured the bulk compaction behaviour of MAS (force and displacement as functions of time) and found that this was dominated by non-reversible plastic effects during loading stage, followed by significant elastic recovery during unloading. The authors also used Small Angle X-ray Scattering (SAXS) to investigate the intragranular structure of MAS and its response to compaction, as well as the density variations in the compacted specimens when using different punches to prepare bi-convex specimens, specimens with a embossed

features and flat faced specimens. Results showed that MAS exhibited significant elastic recovery leading to tablet cracking. Furthermore, large stress variations were observed when punches with embossed features or a rounded surface were used also associated with the occurrence of cracks and tool wear. These findings are important because the elastic recovery of MAS may pose problems such as cracking during tablet compaction.

Currently MAS and other smectite clays are used as excipients in the formulation of some marketed drugs such as lamotrigine (Lamictal Chewable), pravastatin sodium, methenamine mandelate, as well as in the formulation of cosmetic products, due to their anticaking, abrasive, absorbent, lubricant, binding and bulking properties (Vanderbilt Minerals, 2014b).

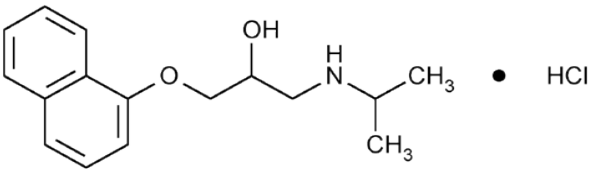
## **1.6. Active ingredients**

The present study aimed to characterise the adsorption of three model drugs onto the structure of MAS. The three drugs were propranolol hydrochloride (PPN), diltiazem hydrochloride (DIL) and metformin hydrochloride (MET). These cationic drugs are expected to interact with the negatively charged faces of MAS via hydrogen bonding, cation exchange and water bridging (Rojtanatanya and Pongjanyakul, 2010; Pongjanyakul and Rojtanatanya, 2012).

### **1.6.1. Propranolol hydrochloride (PPN)**

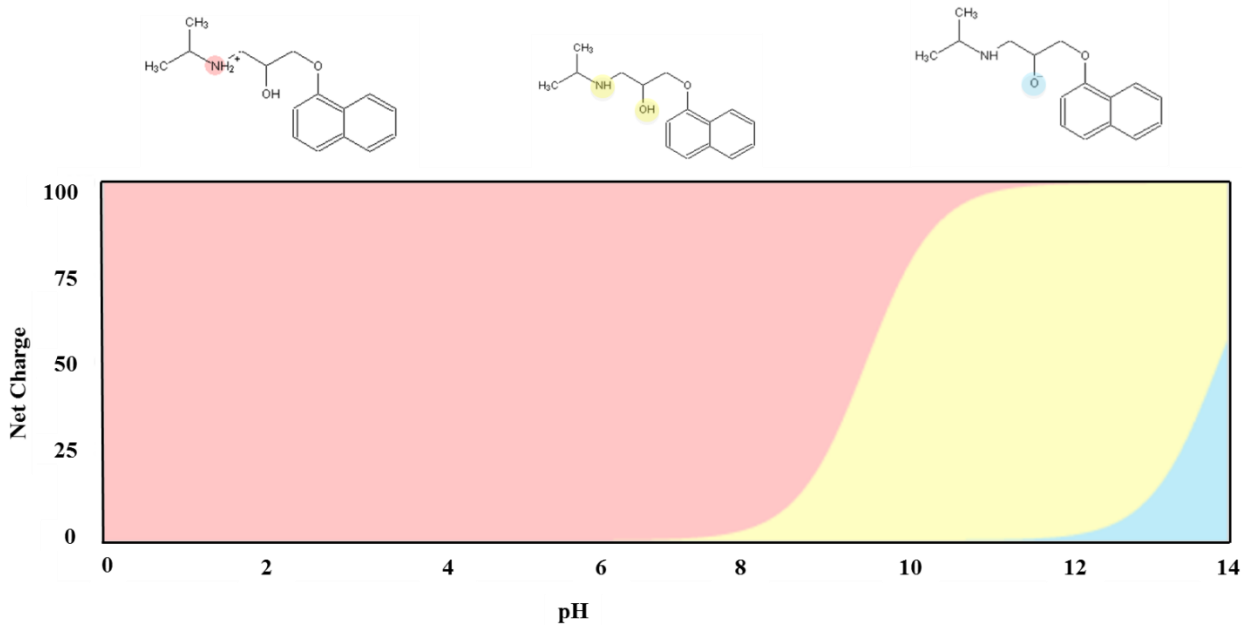
PPN represents the first of drugs acting as antagonists at  $\beta$ -adrenergic receptors of the heart ( $\beta$ -blockers), developed in the 1960s and introduced in 1964 (Patrick, 2001; Rojtanatanya and Pongjanyakul, 2010). Its therapeutic effect comes from antagonizing the adrenergic pathway that can lead to blocking receptors in heart, lungs, liver, pancreas, peripheral blood vessels and other parts of the body. It is used to treat angina pectoris, myocardial infarction and high blood pressure. It was also found to be effective against severe infantile haemangioma, gradually becoming the first-line therapy (Guan *et al.*, 2015).

**Table 1.2.** Chemical structure and physicochemical properties of PPN (Shalaeva *et al.*, 2007; Rojtanatanya and Pongjanyakul, 2010; Sugano, 2012)

CAS	Structure	MW (g/mol)	pKa
318-98-9		295.81	13.9 ± 0.4

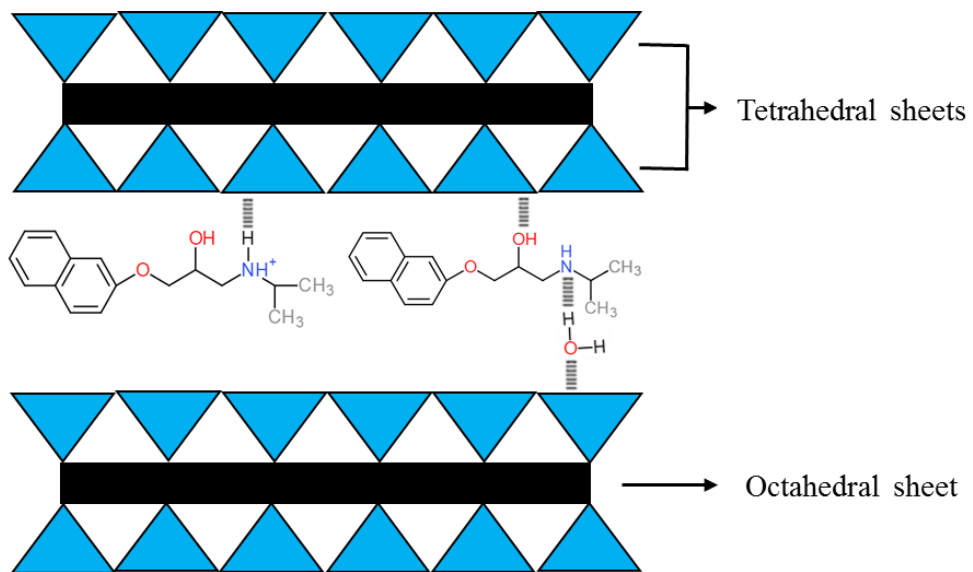
However, due to its high solubility in water, PPN has a short half-life of 3.9 hours and hence it needs to be administered frequently (2-3 times/day) in order to maintain adequate drug plasma levels (Datta, 2013). The development of sustained-release dosage forms would thus be beneficial, increasing patient compliance, safety and efficacy of the drug. Previous studies showed that MAS smectite clay particles may be used as carriers of PPN but further studies are required in order to investigate the physicochemical properties of the formed complexes at a molecular level, in the form of dispersions as well as solid particles, before establishing an innovative and efficient formulation technique (Rojtanatanya and Pongjanyakul, 2010; Kanjanakawinkul *et al.*, 2013).

PPN (Table 1.2) contains one amine basic group ( $\text{NH}_2-$ ), which gives its experimental pKa value of 9.5 (Shalaeva *et al.*, 2007; Sugano, 2012). The nitrogen atom has a hybrid  $\text{sp}^3$  orbital that is able to gain a proton, which determines the basic characteristic of amines (Alexandrescu and Danciulessu, 2009). In theory, PPN has a second pKa value of 13.9, given by the weakly acid hydroxyl ( $\text{OH}-$ ) group that can deprotonate in basic solution, at a pH over 9.8 (Fig 1.9.).



**Fig 1.9.** Behaviour of PPN with varying pH which can lead to protonation of the amine group, deprotonation of the hydroxyl group or make no change: adapted from (*ACD I-Lab, 2018*)

When combined, MAS and PPN can interact via electrostatic interaction by hydrogen bonding and water bridging, as well as cation exchange (Fig 1.10.) (Rojtanatanya and Pongjanyakul, 2010). The addition of the PPN solution to the MAS dispersion causes flocculation in the composite dispersion (Rojtanatanya and Pongjanyakul, 2010). The cationic nature of the drug leads to the compression of the diffuse double layers previously formed in water. Therefore, platelet edges and faces approach and form a more rigid structure. Effects depend upon the clay to drug ratio used in the preparation of samples.

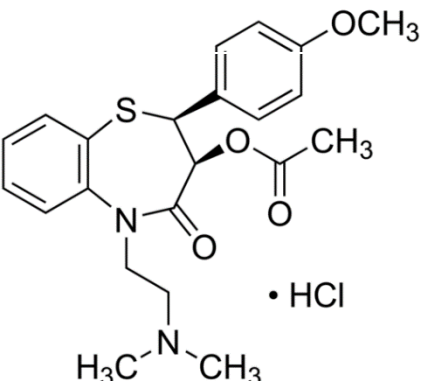


**Fig. 1.10.** Possible MAS – PPN chemical interaction by hydrogen bonding, water bridging and cation exchange: adapted from (Rojtanatanya and Pongjanyakul, 2010)

### 1.6.2. Diltiazem hydrochloride (DIL)

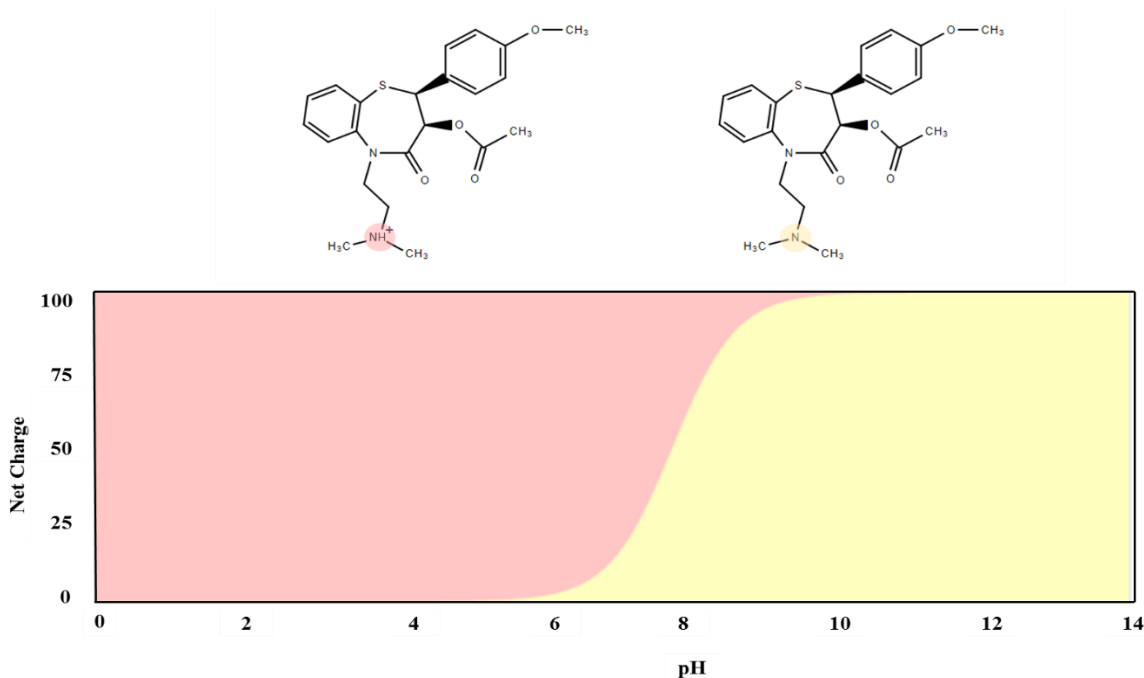
DIL (Table 1.3) is a non-dihydropyridine calcium channel blocker. It inhibits the calcium channels in the blood vessels which leads to vasodilatation and, hence, to a lower blood pressure. Furthermore, DIL inhibits the calcium channels in the heart which leads to a reduced cardiac contractility and a slower atrioventricular conduction velocity (Abernethy and Schwartz, 1999; Rodríguez Padial *et al.*, 2016). DIL therefore represents an efficient treatment for patients suffering from stable chronic angina due to its ability to reduce myocardial oxygen demand, as it lowers blood pressure, heart rate and cardiac contractility. The drug can also be efficiently used in treating arterial fibrillation due to its ability to control heart rate through its capability to reduce atrioventricular node conduction. In addition, DIL is also known to be effective antihypertensive agent.

**Table 1.3.** Chemical structure and physicochemical properties of DIL

CAS	Structure	MW	pKa (g/mol)
33286-22-5	 <chem>CN(C)C[N+](C)(C)CC(=O)N1Cc2ccccc2SC[C@H]1[C@@H](OCC(=O)c3ccc(O)cc3)[C@H](OCC(=O)c3ccc(O)cc3)[C@H]1OCC(=O)c3ccc(O)cc3</chem>	450.98	7.8 ± 0.4

DILs critical drawbacks are an elimination half-life of  $3.2 \pm 1.3$  h following oral administration, and a bioavailability of  $42 \pm 18$  % following first pass metabolism (Hermann *et al.*, 1983). Therefore, in order to acquire its therapeutic effects and to maintain adequate drug plasma levels, it needs to be administered frequently (3-4 times/day) (Shoaib, 2013; Li *et al.*, 2016). DIL therefore is a suitable target for extended drug release formulation. The potential benefits of DIL adsorption onto MAS prior its incorporation into a polymer matrix to achieve controlled drug release has not been reported in previous studies, although similar research has been carried out using polymers only (Levis and Deasy, 2003; Han *et al.*, 2013).

DIL molecule contains one secondary amine basic group (-NH-) which is able to gain a proton, hence giving the drug its pKa value of 7.8 (Fig. 1.11.) (ACD I-Lab, 2018).

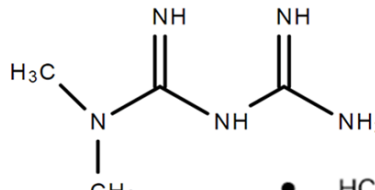


**Fig. 1.11.** Behaviour of DIL with varying pH which can lead to protonation of the amine group: adapted from(ACD I-Lab, 2018)

### 1.6.3. Metformin hydrochloride (MET)

MET (Table 1.4) is an orally administered biguanide that was firstly clinically used in 1958 (Wadher, Umekar and Kakde, 2011; Kinaan, Ding and Triggle, 2015). It represents the first choice of treatment for type 2 diabetes mellitus (non-insulin dependent diabetes mellitus), being highly prescribed worldwide (Li *et al.*, 2012). MET promotes glycaemic control by reducing the hepatic glucose production and the intestinal glucose absorption and by improving glucose uptake and utilisation (Li *et al.*, 2012). MET also has additional health benefits such as reduction of body weight, decrease of blood plasma lipid levels, as well as prevention of cardiovascular complications (DeFronzo and Goodman, 1995; Li *et al.*, 2012).

**Table 1.4.** Chemical structure and physicochemical properties of metformin hydrochloride

CAS	Structure	MW	pK <sub>a</sub>
1115-70-4		165.63	3.0 ± 1.0
			11.9 ± 0.4

Despite its therapeutic benefits, MET has a short plasma half-life of 1.5 – 4.5 h, requiring administration of 250 mg 2 – 3 times a day when larger doses are required, as well as a low absolute bioavailability of 50 – 60 %. Therefore, to maintain adequate drug plasma levels and hence prolong its therapeutic effects, sustained release formulations are required (Defang *et al.*, 2005; Li *et al.*, 2012). MET adsorption onto clay has been previously published. However, the incorporation of the formed complex into a polymer matrix to achieve controlled drug release has not been reported.

MET has two pK<sub>a</sub> values given by secondary amine groups present on the molecule (3.0 and 11.9), which can get protonated depending on the solution pH. METs behaviour with varying pH is described in Fig 1.12.

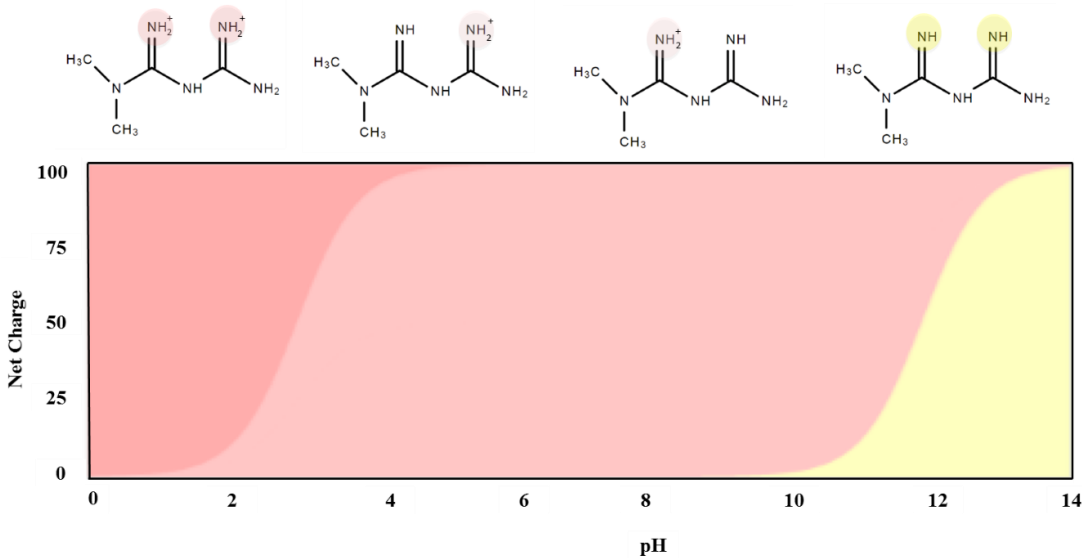


**Fig. 1.12.** Behaviour of MET with varying pH which can lead to protonation of the amine group: adapted from (*ACD I-Lab*, 2018)

### 1.7. Polymers used in controlling drug release

Polymers (Fig. 1.13.) are large molecules made up of many repeated smaller units, monomers, which interact with each other via polymerization (Sinko, 2010). Natural or synthetic, polymers are of high importance to the pharmaceutical industry as they offer a wide variety of physical and chemical characteristics which can be easily manipulated such as molecular weight, monomer structure and polymerisation that can alter for instance solubility or viscosity. Polymers can also be blended with other polymers which further offers advantages to the formulation of drug delivery systems (Jones, 2004). Polymers have found applications in both solid and liquid dosage forms (Jones, 2004; Sinko, 2010). These are widely used in the formulation tablets as binders, in film coating for taste masking and to protect the active ingredient, or to improve bioavailability and control drug release (Sinko, 2010). Being able to control drug release is extremely important, as an ideal drug delivery system should aim to deliver a drug at a specific site and at a certain release rate. The popularity of polymers has aided the rapid advances in the pharmaceutical industry since their introduction due to their efficacy in controlling drug release.

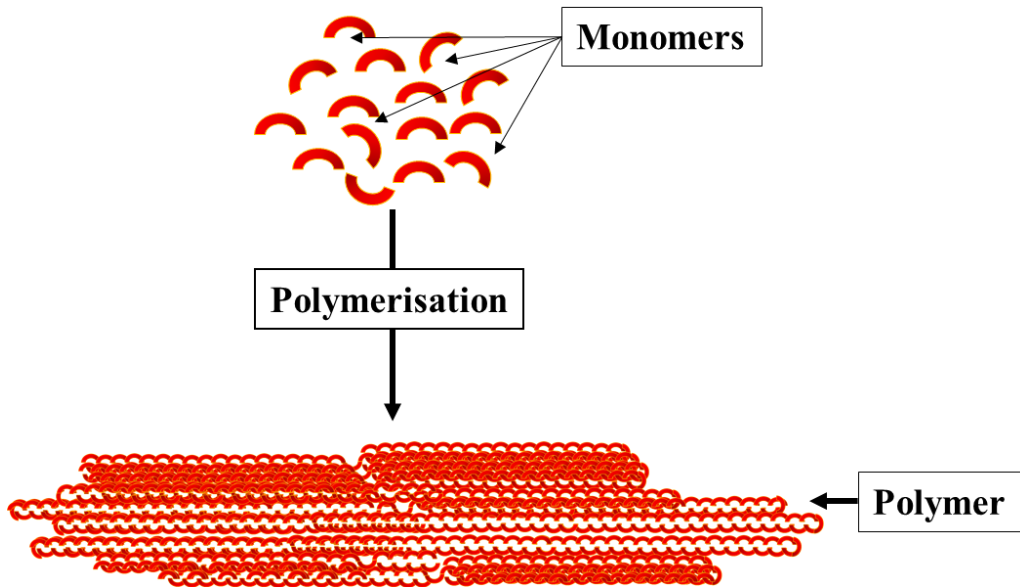


**Fig. 1.13.** Representation of polymer formation via polymerisation through the formation of covalent bonds between monomeric units

Drug release from a swelling controlled matrix system (drug homogenously dispersed in a polymer matrix) is governed by (1) diffusion, which involves aqueous medium infiltration into the polymeric matrix leading to hydration, gelation and swelling due to matrix relaxation, and (2) erosion due to polymer disentanglement (Varma *et al.*, 2004). These two processes lead to the occurrence of two fronts, a swelling front and an erosion front (Fig. 1.14.) and the distance between them depends on the relative rate of their movement towards each other. The distance between the diffusion and erosion fronts corresponds to the diffusion path length of the drug, hence determined by the thickness of the formed gel layer.

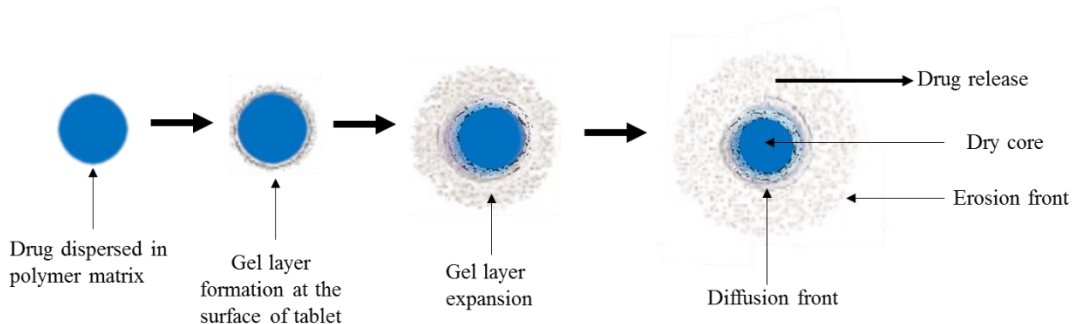


**Fig. 1.14.** Schematic demonstration of drug release from hydrophilic, swellable polymer matrix systems, determined by gel layer formation and its time dependent dynamics:  
adapted from (Varma *et al.*, 2004; Ghori and Conway, 2015)

Drug release rate from a controlled release drug delivery system depends three major variables: characteristics of the drug incorporated in the formulation (such as solubility, dose, molecular weight, size and shape), characteristics of the polymer (type, viscosity grade, amount, properties and combination with other polymers) and formulation (technique, excipients and geometry) (Varma *et al.*, 2004).

### 1.7.1. Xanthan gum (XG)

Xanthan gum (XG) is a polysaccharide having a repeating unit consisting of five sugar residues: one glucuronic acid, two glucose and two mannose. The polymeric chain is identical to cellulose, consisting of 1, 4-linked  $\beta$ -D-glucose. The distinguishable component from cellulose is the trisaccharide side backbone consisting of alpha-D-mannose typically containing a linked acetyl group, beta-D-glucuronic acid and a terminal beta-D-mannose usually linked to a pyruvate group (Fig. 1.15.) (CPKelco, 2008).

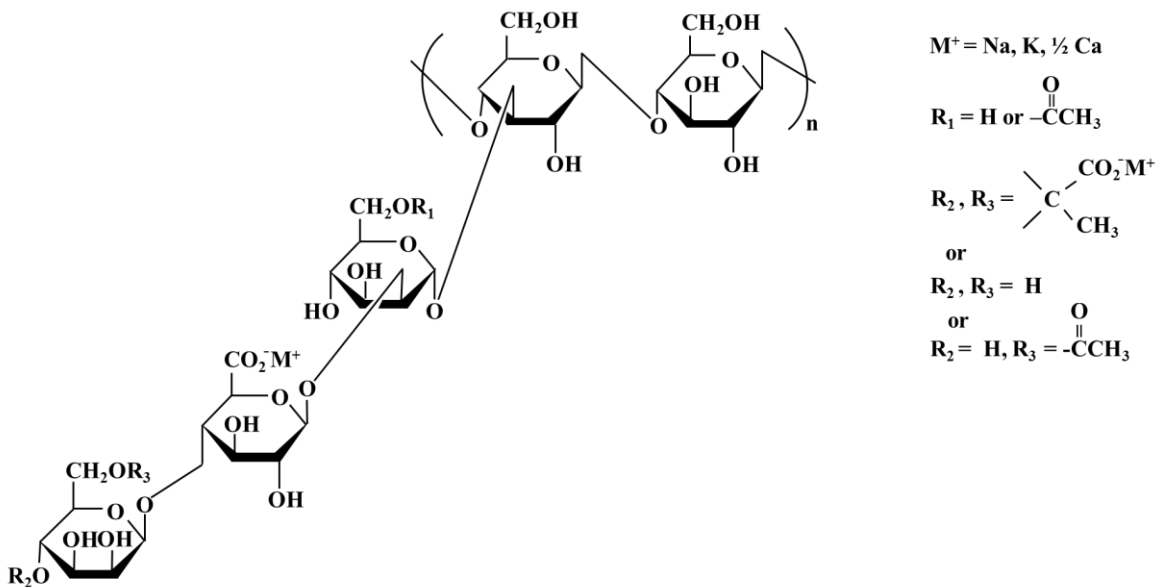


**Fig. 1.15.** Chemical structure of Xanthan Gum: adapted from (CPKelco, 2008)

In aqueous solution, the structure of XG changes from an ordered double helix at physiologically relevant salt concentrations and temperatures, to a random coil structure in low ionic strength solutions and at high temperatures (Andreopoulos and Tarantili, 2001; CPKelco, 2008). XG has thickening properties with pseudoplastic behaviour over a wide range of solution pH values and temperatures, which leads to its wide use in food industry and pharmaceutical industry (Talukdar and Kinget, 1995).

XG is also efficiently used as an excipient in the formulation of dosage forms for intended controlled drug delivery. XG is a hydrophilic matrix polymer normally used in small amounts in the formulation of tablets. When tablets get into the dissolution media (i.e. stomach, small intestine), the XG particles on its surface become hydrated and form a gel layer which is viscous and enables drug diffusion but is resistant to erosion. XG has been shown to provide time-independent release (Jian *et al.*, 2012). These therapeutic advantages led to the use of XG in numerous published studies as an excipient in tablets to control drug release (Talukdar and Kinget, 1995; Talukdar *et al.*, 1996; Andreopoulos and Tarantili, 2001; CPKelco, 2008; Jian *et al.*, 2012; Petri, 2015; Lazzari, Kleinebudde and Knop, 2018). In a publication by Talukdar and Kinget (1995) the authors described for the first time that the release rate of a drug from a XG matrix is influenced by drug solubility, and that the

swelling of XG was influenced by the buffer concentrations and ionic strength of the release medium (Talukdar and Kinget, 1995). Therefore, the authors concluded that a soluble drug follows a reciprocal relationship with the matrix swelling of XG, whereas the opposite is happening for insoluble drugs where a direct relationship between the drug release rate and the swelling of XG matrix is observed (Talukdar and Kinget, 1995).

Another study published by the same authors in 1996 aimed to compare the release behaviour from XG and HPMC matrices of caffeine and indomethacin (Talukdar *et al.*, 1996). The authors found that the behaviour of the two polymers was similar, however, the release from XG matrices showed absence of an initial burst release, was more reproducible and had the capacity of achieving zero-order release with the only disadvantage according to the authors found being the sensitivity of XG to the ionic strength of the release medium which has an impact on drug release. XG was also shown to have better flowability when compared to HPMC (Talukdar *et al.*, 1996).

In a study published .in 2019, XG was successfully used to formulate alcohol resistant matrix tablets to control the release of theophylline and avoid alcohol-induced dose dumping (Lazzari, Kleinebudde and Knop, 2018).

XG is often used in tablets as an excipient in combination with other polymers or other materials (Petri, 2015). In a study published by Jian *et al.* in 2012, the authors aimed to combine XG with another polysaccharide, Galactomannan (G) (from *Gleditsia sinensis* Lam.), to control the delivery of theophylline for colon targeted delivery (Jian *et al.*, 2012). The authors found that the synergistic interactions between XG and G led to a greater performance in controlling drug release when compared to the tablets formulated using a single polysaccharide component (either XG or G).

Although numerous studies have demonstrated the efficacy of XG in controlling drug release on its own or in combination with other polymers, XG has never been used in combination with MAS, which therefore adds novelty to the present study.

### **1.7.2. Polyethylene oxide (PEO)**

PEO is a synthetic polymer obtained commercially upon catalytic polymerisation of ethylene oxide (Fig. 1.16.). It has the same chemical structure as polyethylene glycol (PEG), but a

higher molecular weight, usually over 100,000. PEO is soluble in a wide variety of solvents (ethanol, acetone, toluene, chloroform etc.) and in water. When dissolved in water, PEO tablets hydrate, swell and form a gel layer outside the dry core. When the swelling process is finished, the tablets begin to dissolve (erode) as the polymeric chains unfold and disentangle in the dissolution medium (Ma, Deng and Chen, 2014).

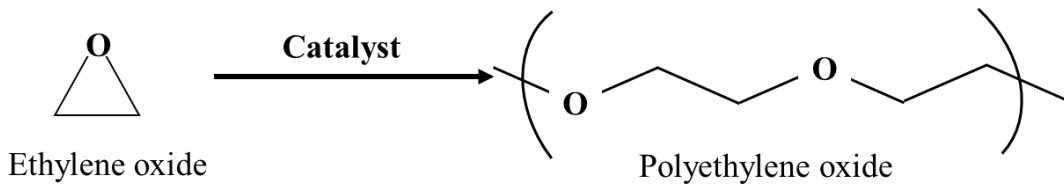


**Fig. 1.16.** Polyethylene oxide (PEO) synthesis

Due to its physicochemical properties such as rapid hydration and high water solubility, non-toxicity, pH insensitivity to physiological fluids and easy manufacturing, PEO is widely used in the formulation of controlled drug release systems. Numerous studies published over the past years reported the application of PEO on its own or in combination with other excipients to modulate drug release (Ma, Deng and Chen, 2014).

Kim *et al.* suggested PEO as an alternative to HPMC (Kim, 1995, 1998). However, a study published in 2000 by Maggi *et al.* found that matrices containing plain HPMC led to a slower release rate and was more efficient when compared to matrices containing plain PEO, following the use of the two polymers in three layered Geomatrix® systems.

In a study published in 2013 by Palmer *et al.* the authors used PEO in combination with another matrix-forming polymer, sodium carboxymethylcellulose (NaCMC), to control the release of chlorpheniramine maleate, venlafaxine hydrochloride, propranolol hydrochloride and verapamil hydrochloride (Palmer *et al.*, 2013). The authors found that using a synergistic interaction between PEO and NaCMC in the tablets significantly slowed drug release (beyond 12 h) when compared to the tablets containing a single polymer component (PEO or NaCMC).

Shojaee *et al.* reported in 2015 the use of PEO as an excipient in modulating the release of theophylline and pointed out the importance of particle size on drug release (Shojaee *et al.*, 2015).

Previous studies reported the combination of PEO with clay. In 2018, Pappa *et al.* reported the intercalation of PEO between nanolayers of Sodium Montmorillonite to formulate nanostructured composites, intended for the dissolution modulation of aprepitant. Authors found that the PEO and clay nanocomposites were highly effective as drug carriers for sustained release (Pappa *et al.*, 2018).

Although multiple studies have reported the efficient use of PEO as an excipient in the formulation of controlled release systems on its own or in combination with other polymers or materials such as clay, the effect of the polymer on the clay adsorption capacity has not been previously explored at a molecular level. Hence, the information reported in this study will allow a formulator to draw conclusions on parameters that need to be manipulated in order to improve drug release modulation.

### **1.8. Isothermal titration calorimetry (ITC)**

Isothermal titration calorimetry (ITC) is a powerful well-established biophysical technique used to measure the formation and dissociation of molecular complexes in many branches of science from cell biology to food chemistry. To perform an experiment, the instrument periodically injects a ligand (guest solution) into the calorimetric cell containing a macromolecule (host solution) under isothermal conditions (Duff, Jr., Grubbs and Howell, 2011). The heat absorbed or released as chemical bonds form or break is then measured as the power that must be supplied to maintain both sample and reference cells at a constant temperature (Moore *et al.*, 2016; Di Trani, Moitessier and Mittermaier, 2017). Exothermic reactions result in gradual power decreases, relative to the baseline, whereas endothermic reaction result in gradual power increases (Di Trani, Moitessier and Mittermaier, 2017). The spikes in power signals are then integrated to determine the total amount of heat absorbed or released and the resulting data is fit to a variety of equations to yield binding site size, affinity ( $K$ ), stoichiometry ( $N$ ), enthalpy ( $\Delta H$ ) and therefore, entropy ( $-T\Delta S$ ) and free energy ( $\Delta G$ ) of the binding events (Moore *et al.*, 2016).

For a simple one binding site model (Fig. 1.17.) the non-linear least squares fit of the data can be used to determine  $K_a$  and  $\Delta H$ , followed by the calculation of  $\Delta G$  and  $-T\Delta S$  using from the link between Van't Hoff equation and Gibbs free energy:

$$\Delta G = \Delta H - T\Delta S \quad \text{Eq. 1.1. (a)}$$

$$= -RT \ln K_a \quad \text{Eq. 1.1. (b)}$$

where T is the absolute temperature in Kelvin and R is the gas constant.

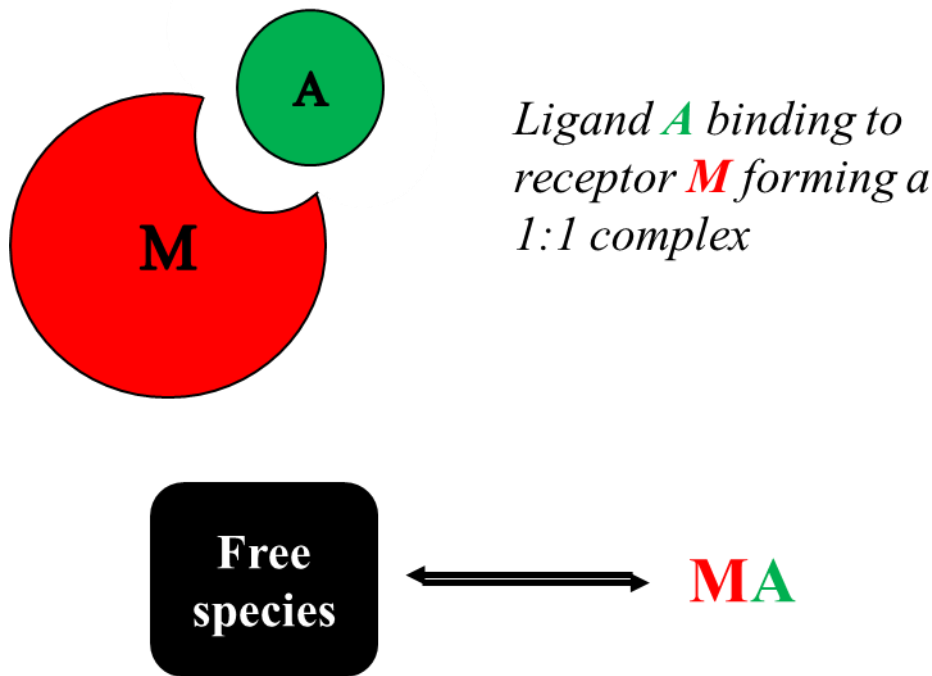


**Fig. 1.17.** Simple one binding site model where A is the ligand in the syringe and M is the macromolecule in the sample cell; upon binding these form a 1:1 complex

The change in heat capacity of the binding interaction at constant pressure ( $\Delta C_p$ ) may also be determined by running experiments at additional temperatures.  $\Delta C_p$  is determined from the temperature dependence of  $\Delta H$  using equation 1.2 (MicroCal, 1998; Le *et al.*, 2013).

$$\Delta C_p = \frac{(\Delta H_{T_2} - \Delta H_{T_1})}{T_2 - T_1} \quad \text{Eq. 1.2.}$$

For a competitive ligand binding involving the injection of a strong binding ligand A into a solution containing a competing ligand B and the macromolecule, two experiments are required for curve fitting. One experiment must be non-competitive between the ligand in the syringe A and ligand B, used to determine the binding parameters for competing ligand B (stoichiometry ( $N_B$ ), affinity ( $K_B$ ) and enthalpy ( $H_B$ )). The parameters determined are further used as an input allowing the determination of the binding parameters between ligand A and the macromolecule, which seem to interact more weakly in the presence of competing ligand B, from the competitive experiment (stoichiometry ( $N_A$ ), affinity ( $K_A$ ) and enthalpy ( $H_A$ )).

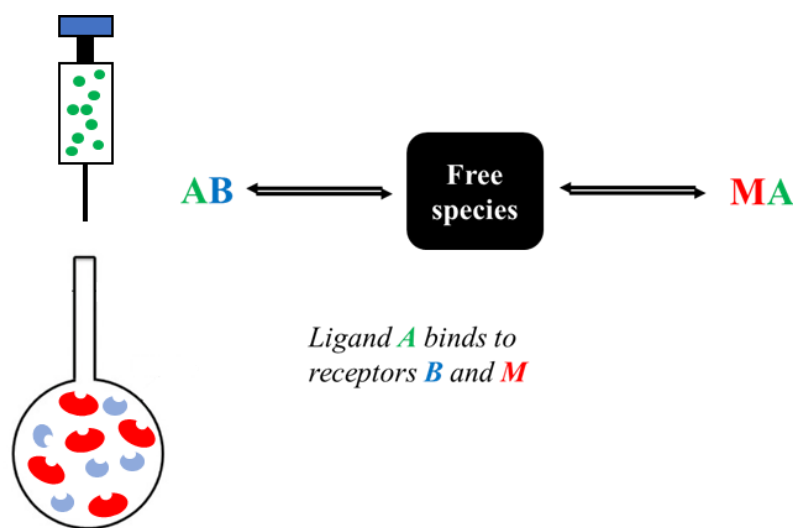


**Fig. 1.18.** Competitive ligand binding where A is the ligand in the syringe and M and B are the macromolecule and competitive ligand respectively, both present in the sample cell

More complicated models with equilibria involving multiple binding mechanisms need to be developed by the ITC user appropriately to predict the relationship between the forces and parameters leading to the binding event (Le *et al.*, 2013; Callies and Hernández Daranas, 2016).

Thermodynamically, a spontaneous interaction will have a negative  $\Delta G$  and, as the binding becomes tighter,  $\Delta G$  will also become increasingly negative.  $\Delta G$  for a binding isotherm has both an entropic and an enthalpic contribution. The entropic contribution comes from hydrophobic interactions and conformational changes, while the enthalpic contribution to

the binding isotherm occurs upon formation of hydrogen bonds, van der Waals interactions and electrostatic interactions between species. A binding interaction with a positive heat capacity change will become more entropic and less enthalpic with increasing temperature, while the opposite can be observed in binding interactions with a negative heat capacity (Callies and Hernández Daranas, 2016). The calculation of these thermodynamic parameters involved in the binding process allows the determination of fundamental information about the molecular interactions leading to the binding process. The information gained is essential in correlating thermodynamic and structural data to understand the process of drug adsorption onto clay and improve drug delivery (TA Instruments, 2000).

An adiabatic VP-ITC micro calorimeter operating between 2 °C and 80 °C fitted with two identical coin shaped cells was used in this research. The reference and sample cells have a total volume of 1.8 mL and a working volume of 1.4 mL, and the syringe has a total capacity of 290 µL. Both cells are placed in an isothermal jacket and allowed to equilibrate to a constant temperature at constant temperature prior to performing a titration.

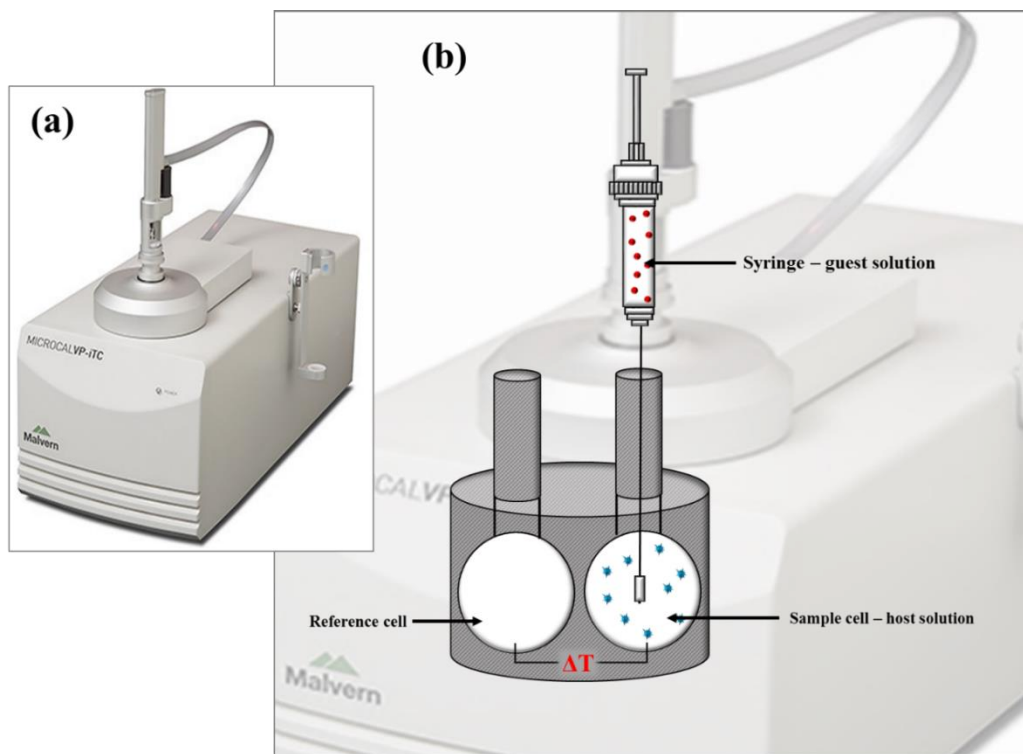


**Fig. 1.19.** VP-ITC micro calorimeter (a) (MicroCal, 1998); Schematic diagram of the VP-ITC micro calorimeter

### **1.9. Aims and objectives of current study**

The research presented in this thesis aims to rectify, the gap in fully understanding the capacity of magnesium aluminium silicates adsorption of cationic compounds onto its structure to form complexes often used to control drug release. The effects of two different polymers on the complexation process is also analysed due to the ability of polymers in modulating drug release. Three model cationic drugs namely propranolol hydrochloride, diltiazem hydrochloride and metformin hydrochloride are investigated. These drugs are selected due to the differences in their molecular weights as well as their pKa's. It is therefore proposed that these properties may affect their binding onto the MAS.

The study will therefore be approached according to the following aims:

- \* To formulate MAS-drug complex dispersions and particles and analyse their morphology using techniques such as scanning electron microscopy and small angle X-ray scattering.
- \* To comprehensively characterize the complexes made using techniques such as differential scanning calorimetry and X-ray powder diffraction.
- \* To use for the first time, isothermal titration calorimetry to understand the real time process of adsorption of cationic drugs onto MAS alone or in the presence of a polymer in aiding the understanding of the thermodynamics associated with the complexation process.
- \* To make tablet compacts using the direct compression method and evaluate drug release for the MAS-drug complexes in polymeric matrices in comparison to MAS-drug physical mixture in polymeric matrices, linking the behavior of release to the results obtained in calorimetric studies
- \* Propose a drug release model based on the calorimetric and drug release studies.

## 1.10. References

- Abernethy, D. and Schwartz, J. (1999) ‘Calcium-Antagonist Drugs’, *N Engl J Med*, 341, pp. 1447–1457.
- ACD I-Lab (2018). Available at: <https://ilab.acdlabs.com/iLab2/> (Accessed: 23 September 2018).
- Alexandrescu, E. and Danciulescu, D. (2009) *Organic chemistry*. Ploiesti: LVS Crepuscul.
- Andreopoulos, A. G. and Tarantili, P. A. (2001) ‘Xanthan gum as a carrier for controlled release of drugs’, *Journal of Biomaterials Applications*, 16(1), pp. 34–46.
- Aulton, M. E. (2007) *Aulton’s pharmaceutics*. 3rd edn. Edinburgh: Churchill Livingstone.
- Barton, C. D. and Karathanasis, A. D. (2002) ‘Clay Minerals’, *Clay Minerals*, pp. 187–192.
- Boateng, J. and Okeke, O. (2019) ‘Evaluation of clay-functionalized wafers and films for nicotine replacement therapy via Buccal Mucosa’, *Pharmaceutics*, 11(3).
- Calcimeter Manual (2018). Giesbeek, Netherlands: Eijkenkamp Soil & Water.
- Callies, O. and Hernández Daranas, A. (2016) ‘Application of isothermal titration calorimetry as a tool to study natural product interactions’, *Natural Product Reports*, 33(7), pp. 881–904.
- Carrado, K. A. and Bergaya, F. (eds) (2007) *Clay-based Polymer Nano-composites (CPN)*. Vol. 15. Chantilly, VA 20151-1125: THE CLAY MINERALS SOCIETY.
- Carretero, M. I. (2002) ‘Clay minerals and their beneficial effects upon human health. A review’, *Applied Clay Science*, 21(3–4), pp. 155–163.
- Carretero, M. I. and Pozo, M. (2009) ‘Clay and non-clay minerals in the pharmaceutical industry. Part I. Excipients and medical applications’, *Applied Clay Science*. Elsevier B.V., 46(1), pp. 73–80.
- CPKelco (2008) ‘KELTROL® / KELZAN® Xanthan Gum Book 8th edition’, pp. 1–28.
- Datta, S. M. (2013) ‘Clay-polymer nanocomposites as a novel drug carrier: Synthesis, characterization and controlled release study of Propranolol Hydrochloride’, *Applied Clay*

*Science*, 80–81, pp. 85–92.

Defang, O. *et al.* (2005) ‘In vitro and in vivo evaluation of two extended release preparations of combination metformin and glipizide’, *Drug Development and Industrial Pharmacy*, 31(7), pp. 677–685.

DeFronzo, R. A. and Goodman, A. M. (1995) ‘Efficacy of Metformin in Patients With Non-Insulin-Dependent Diabetes’, *Multicenter Metformin Study Group The New England Journal of Medicine*, 333(9), pp. 541–549.

Duff, Jr., M. R., Grubbs, J. and Howell, E. E. (2011) ‘Isothermal Titration Calorimetry for Measuring Macromolecule-Ligand Affinity’, *Journal of Visualized Experiments*, (55), pp. 5–8.

Ghori, M. and Conway, B. (2015) ‘Hydrophilic Matrices for Oral Control Drug Delivery’, *American Journal of Pharmacological Sciences*, pp. 103–109. doi: 10.12691/AJPS-3-5-1.

Gomes, C. de S. F. (2018) ‘Healing and edible clays: a review of basic concepts, benefits and risks’, *Environmental Geochemistry and Health*, 40(5), pp. 1739–1765.

Goyal, S. *et al.* (2017) ‘Oral Sustained Release Tablets: An Overview with a special emphasis on Matrix Tablet’, *American Journal of Advanced Drug Delivery*, 05(02).

Guan, Y. *et al.* (2015) ‘Propranolol hydrochloride-loaded liposomal gel for transdermal delivery: Characterization and in vivo evaluation’, *International Journal of Pharmaceutics*. Elsevier B.V., 487(1–2), pp. 135–141.

Hamilton, R. A. *et al.* (2019) ‘Formulation and antibacterial properties of clay mineral-tetracycline and -doxycycline composites’, *Applied Clay Science*, 179.

Han, X. *et al.* (2013) ‘Preparation and evaluation of sustained-release diltiazem hydrochloride pellets’, *Asian Journal of Pharmaceutical Sciences*, 8(4), pp. 244–251.

Hermann, P. *et al.* (1983) ‘Pharmacokinetics of diltiazem after intravenous and oral administration’, *European Journal of Clinical Pharmacology*, 24(3), pp. 349–352.

Jambhekar, S. and Breen, P. J. (2009) *Basic pharmacokinetics*. London: Pharmaceutical Press.

- Jian, H. *et al.* (2012) ‘Galactomannan (from Gleditsia sinensis Lam.) and xanthan gum matrix tablets for controlled delivery of theophylline: In vitro drug release and swelling behavior’, *Carbohydrate Polymers*, 87(3), pp. 2176–2182.
- Jones, D. (2004) *Pharmaceutical Applications of Polymers for Drug Delivery, Polysaccharides for Drug Delivery and Pharmaceutical Applications*.
- Joshi, G. V. *et al.* (2009) ‘Montmorillonite as a drug delivery system: Intercalation and in vitro release of timolol maleate’, *International Journal of Pharmaceutics*, 374(1–2), pp. 53–57.
- Kanjanakawinkul, W. *et al.* (2013) ‘Nicotine-magnesium aluminum silicate microparticle surface modified with chitosan for mucosal delivery’, *Materials Science and Engineering C*, 33(3), pp. 1727–1736.
- Kaur, M. and Datta, M. (2014) ‘Diclofenac Sodium Adsorption onto Montmorillonite: Adsorption Equilibrium Studies and Drug Release Kinetics’, *Adsorption Science & Technology*, 32(5), pp. 365–387.
- Khunawattanakul, W. *et al.* (2010) ‘Chitosan-magnesium aluminum silicate nanocomposite films: Physicochemical characterization and drug permeability’, *International Journal of Pharmaceutics*, 393(1–2), pp. 220–230.
- Khurana, S. *et al.* (2015) ‘Multifaceted role of clay minerals in pharmaceuticals’, *Future Science*, 1(3).
- Kim, J. (1995) ‘Drug release from compressed hydrophilic Polyox® WSR tablets’, *Journal of pharmaceutical sciences*, 84, pp. 303–306.
- Kim, J. (1998) ‘Effects of drug solubility, drug loading and polymer molecular weight on drug release from Polyox® tablets’, *Drug Dev. Ind. Pharm.*, 24, pp. 645–651.
- Kinaan, M., Ding, H. and Triggle, C. R. (2015) ‘Metformin: An Old Drug for the Treatment of Diabetes but a New Drug for the Protection of the Endothelium’, *Medical Principles and Practice*, 24(5), pp. 401–415.
- Laity, P. R. *et al.* (2015) ‘Using small-angle X-ray scattering to investigate the compaction

- behaviour of a granulated clay', *Applied Clay Science*, 108, pp. 149–164.
- Lazzari, A., Kleinebudde, P. and Knop, K. (2018) 'Xanthan gum as a rate-controlling polymer for the development of alcohol resistant matrix tablets and mini-tablets', *International Journal of Pharmaceutics*, 536(1), pp. 440–449.
- Le, V. H. *et al.* (2013) 'Modeling Complex Equilibria in ITC Experiments: Thermodynamic Parameters Estimation for a Three Binding Site Model', *Analytical Biochemistry*, 434(2), pp. 233–241.
- Levis, S. R. and Deasy, P. B. (2003) 'Use of coated microtubular halloysite for the sustained release of diltiazem hydrochloride and propranolol hydrochloride', *International Journal of Pharmaceutics*, 253(1–2), pp. 145–157.
- Li, G. *et al.* (2012) 'Metformin pathways: pharmacokinetics and pharmacodynamics', *Pharmacogenet Genomics*, 22(11), pp. 820–827.
- Li, J. *et al.* (2016) 'Formulation and development of ternary hybrid matrix tablets of diltiazem hydrochloride', *Powder Technology*, 294, pp. 66–70.
- Ma, L., Deng, L. and Chen, J. (2014) 'Applications of poly(ethylene oxide) in controlled release tablet systems: A review', *Drug Development and Industrial Pharmacy*, 40(7), pp. 845–851.
- Mahato, R. I. and Narang, A. S. (2012) *Dosage Forms and Drug Delivery*. 2nd edn. New York: CRC Press.
- Meng, N. *et al.* (2009) 'Controlled release and antibacterial activity chlorhexidine acetate (CA) intercalated in montmorillonite', *International Journal of Pharmaceutics*, 382(1–2), pp. 45–49.
- MicroCal (1998) *VP-ITC User's Manual*. Northampton.
- Moore, D. E. *et al.* (2016) 'Isothermal Titration Calorimetry Can Provide Critical Thinking Opportunities', *Journal of Chemical Education*, 93(2), pp. 304–310.
- Moynihan, H. and Crean, A. (2009) *The physicochemical basis of pharmaceuticals*. Oxford: Oxford University Press.

- Muśko, M. and Sznitowska, M. (2013) ‘Stability of extemporaneous pediatric oral liquids compounded from tablets and drug substance: Case of propranolol and theophylline’, *Acta Poloniae Pharmaceutica - Drug Research*, 70(1), pp. 137–145.
- Nunes, C. D. *et al.* (2007) ‘Loading and delivery of sertraline using inorganic micro and mesoporous materials’, *European Journal of Pharmaceutics and Biopharmaceutics*, 66(3), pp. 357–365.
- Palmer, D. *et al.* (2013) ‘Mechanism of synergistic interactions and its influence on drug release from extended release matrices manufactured using binary mixtures of polyethylene oxide and sodium carboxymethylcellulose’, *Colloids and Surfaces B: Biointerfaces*, 104, pp. 174–180.
- Pappa, C. *et al.* (2018) ‘Nanostructured Composites of Sodium Montmorillonite Clay and PEO Used in Dissolution Improvement of Aprepitant Drug by Melt Mixing’, *Applied Sciences*, 8(5), p. 786.
- Park, J. K. *et al.* (2008) ‘Controlled release of donepezil intercalated in smectite clays’, *International Journal of Pharmaceutics*, 359(1–2), pp. 198–204.
- Parolo, M. E. *et al.* (2008) ‘Tetracycline adsorption on montmorillonite: pH and ionic strength effects’, *Applied Clay Science*, 40(1–4), pp. 179–186.
- Patrick, G. (2001) *Medicinal Chemistry*. Oxford, UK: BIOS Scientific Publishers Limited.
- Petri, D. F. S. (2015) ‘Xanthan gum: A versatile biopolymer for biomedical and technological applications’, *Journal of Applied Polymer Science*, 132(23).
- Pongjanyakul, T., Khunawattanakul, W. and Puttipipatkhachorn, S. (2009) ‘Physicochemical characterizations and release studies of nicotine-magnesium aluminium silicate complexes’, *Applied Clay Science*, 44(3–4), pp. 242–250.
- Pongjanyakul, T. and Rojtanatanya, S. (2012) ‘Use of Propranolol-Magnesium Aluminium Silicate Intercalated Complexes as Drug Reservoirs in Polymeric Matrix Tablets’, *Indian Journal of Pharmaceutical Sciences*, 74(4), pp. 292–301.
- Rodrigues, L. A. de S. *et al.* (2013) ‘The systems containing clays and clay minerals from

modified drug release: A review', *Colloids and Surfaces B: Biointerfaces*, 103, pp. 642–651.

Rodríguez Padial, L. *et al.* (2016) 'Clinical Experience with Diltiazem in the Treatment of Cardiovascular Diseases', *Cardiology and Therapy*, 5(1), pp. 75–82.

Rojtanatanya, S. and Pongjanyakul, T. (2010) 'Propranolol-magnesium aluminum silicate complex dispersions and particles: Characterization and factors influencing drug release', *International Journal of Pharmaceutics*, 383(1–2), pp. 106–115.

Rongthong, T. *et al.* (2013) 'Quaternary polymethacrylate-magnesium aluminum silicate films: Molecular interactions, mechanical properties and tackiness', *International Journal of Pharmaceutics*, 458(1), pp. 57–64.

Shalaeva, M. *et al.* (2007) 'Measurement of Dissociation Constants (pKa Values) of Organic Compounds by Multiplexed Capillary Electrophoresis Using Aqueous and Cosolvent Buffers', *Journal of Pharmaceutical Sciences*, pp. 1–24.

Shoaib, M. H. (2013) 'Formulation development and evaluation of Diltiazem HCl sustained release matrix tablets using HPMC K4M and K100M Formulation development and evaluation of Diltiazem HCl sustained release matrix tablets using HPMC K4M and K100M', 1(September 2015), pp. 653–663.

Shojaee, S. *et al.* (2015) 'An Investigation on the Effect of Polyethylene Oxide Concentration and Particle Size in Modulating Theophylline Release from Tablet Matrices', *AAPS PharmSciTech*, 16(6), pp. 1281–1289.

Sinko, P. J. (2010) 'Pharmaceutical polymers', in *Martin's Physical Pharmacy and Pharmaceutical Sciences*, pp. 492–515.

Sugano, K. (2012) *Biopharmaceutics Modeling and Simulations : Theory, Practice, Methods, and Applications*. New Jersey: John Wiley and Sons.

TA Instruments (2000) 'Characterizing Binding Interactions by ITC', *Life Sciences*, pp. 1–5.

Talukdar, M. M. *et al.* (1996) 'Comparative study on xanthan gum and hydroxypropylmethyl cellulose as matrices for controlled-release drug delivery I. Compaction and in vitro drug

- release behaviour', *International Journal of Pharmaceutics*, 129(1–2), pp. 233–241.
- Talukdar, M. M. and Kinget, R. (1995) 'Swelling and drug release behaviour of xanthan gum matrix tablets', *International Journal of Pharmaceutics*, 120(1), pp. 63–72.
- Theng, B. K. G. (2012) *Formation and Properties of Clay-Polymer Complexes*. 2nd edn. Amsterdam: Elsevier Science.
- Di Trani, J. M., Moitessier, N. and Mittermaier, A. K. (2017) 'Measuring Rapid Time-Scale Reaction Kinetics Using Isothermal Titration Calorimetry', *Analytical Chemistry*, 89(13), pp. 7022–7030.
- Trivedi, V. *et al.* (2018) 'Intercalated theophylline-smectite hybrid for pH-mediated delivery', *Drug Delivery and Translational Research*. Drug Delivery and Translational Research, pp. 1–9.
- Vanderbilt Minerals (2014a) *VEEGUM / VAN GEL Magnesium Aluminum Silicate Magnesium Aluminum Silicate ® The Story*. Norwalk.
- Vanderbilt Minerals (2014b) 'VEEGUM ® Magnesium Aluminum Silicate VANATURAL ® Bentonite Clay For Personal Care and Pharmaceuticals What They Are', pp. 1–27.
- Varma, M. V. S. *et al.* (2004) 'Factors affecting mechanism and kinetics of drug release from matrix-based oral controlled drug delivery systems', *American Journal of Drug Delivery*, 2(1), pp. 43–57.
- Wadher, K., Umekar, M. and Kakde, R. (2011) 'Formulation and evaluation of a sustained-release tablets of metformin hydrochloride using hydrophilic synthetic and hydrophobic natural polymers', *Indian Journal of Pharmaceutical Sciences*, 73(2), p. 208.
- Weems, J. B. (1903) 'Chemistry of Clays', *Iowa Geological Survey Annual Report*, 14(15), pp. 319–346.

## *Chapter 2:*

### *Materials and methods*

## **Chapter 2: Materials and methods**

### **2.1. Materials**

VEEGUM F EP® (Magnesium Aluminium Silicate) was a gift from R.T. Vanderbilt Company, Norwalk, CT (USA). Its composition was confirmed by infrared (IR) spectroscopy (chapter 1, section 1.4.2.). This material complies with the European Pharmacopoeia monograph for Magnesium Aluminium Silicate and is indicated for use as a dry excipient in pressed powders and in direct compression tablets (Vanderbilt Minerals, 2014).

Propranolol hydrochloride (PPN), diltiazem hydrochloride (DIL) and metformin hydrochloride (MET) were supplied from TCI (Tokyo Chemical Industry, Tokyo).

POLYOX™ (MW 4,000,000) and XANTURAL® 75 were kind gifts from Colorcon, UK and CP Kelco, UK respectively.

Acetonitrile (HPLC grade), sodium phosphate dibasic dihydrate, 99+% (HPLC grade), 2 N sodium hydroxide and 2 N hydrochloric acid were purchased from Fisher Scientific (UK).

### **2.2. Methods**

#### **2.2.1. Formulation of single and double drug loaded MAS-drug complexes**

Drug solutions of either PPN, DIL or MET (2 % w/v) and three MAS dispersions (2 % w/v) were separately prepared under continuous stirring for 24 h, at 25 °C and 500 rpm. The pH of MAS dispersions and PPN, DIL or MET solutions prepared was further adjusted to pH 5 using 2 M hydrochloric acid or 2 M sodium hydroxide. For the single drug loading, MAS dispersion was combined with the drug solutions prepared (1:1 w/w), and the obtained flocculated mixture was incubated at 37 °C with shaking for 24 h. The MAS–drug complex dispersions obtained were then filtered using a Buchner filtration apparatus with vacuum and dried in the oven at 50 °C for 48 h.

For the second drug loading, 1:1 w/w MAS–drug complex dispersions were prepared as above. The collected complexes following filtration were redispersed into a fresh drug solution and incubated at 37 °C with shaking for 24 h. The MAS–drug flocculated complexes (Fig 2.1) obtained were filtered and dried in the oven at 50 °C for 48 hours.

The single and double drug loaded complex particles obtained were ground using a Retsch® PM 100 Ball Mill set at 350 rpm for 10 min, until fine powder was obtained and sieved to collect the particle size fraction between 123 – 65 µm.

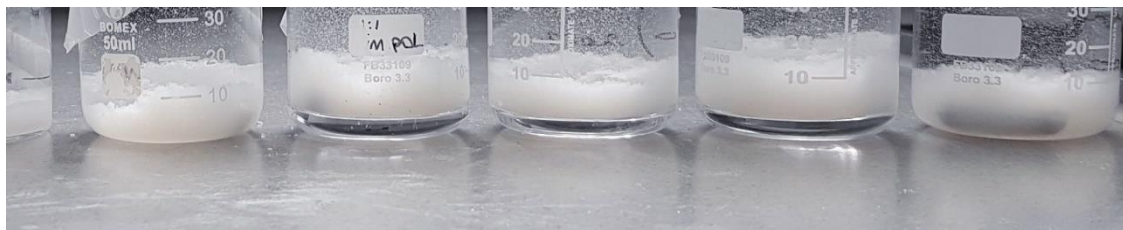


**Fig 2.1.** MAS-drug flocculated complex dispersions

### **2.2.2. Characterisation of MAS-drug complexes**

#### **2.2.2.1. Attenuated total reflectance Fourier transform infrared spectroscopy (ATR-FTIR)**

Infrared spectroscopy represents a powerful qualitative and quantitative analytical technique that can detect changes in the unique vibrational spectrum of a molecule. Hence, it can provide information about the chemistry of samples (Coates, 2000). The technique was used to elucidate the molecular interaction between MAS and PPN, DIL and MET. Experiments were performed on a Smart Orbit ATR-FTIR machine, using diamond as the ATR crystal. Both parent materials and dried complexes were scanned from 4000 to 400 cm<sup>-1</sup>. Samples were firmly pressed onto the crystal to ensure good sample contact and achieve consistent results (Perkin Elmer and Technical Note, 2012).

#### **2.2.2.2. Powder X-Ray diffractometry (PXRD)**

Experiments were performed on a D2 PHASER XRD from BRUKER and sample preparation involved the placement of sample powder (parent materials and samples from section 2.2.1) onto a transmitter holder. Analysis was performed at an angular range 2.5 - 70° (2θ) and a step angle of 0.02 ° (2θ) s<sup>-1</sup>. The X-ray source was generated as a Cu radiation at 30 kV and 10 mA.

Smectite clays are often called ‘expandable clays’, as they have the ability to absorb water. PXRD represents a useful tool, often used to identify clays. The diffractograms obtained

provided information about the physical form of the clay, drug and samples prepared, as well as of the changes in the basal spacing following complexation.

Bragg's Law (Eq. 2.1.) was used to calculate the basal spacing by the approximation of the 001 plane peak (basal distance) (Rojtanatanya and Pongjanyakul, 2010).

$$n\lambda = 2ds\sin\theta \quad \text{Eq. 2.1.}$$

$n = 1$  as the analysis of clay minerals is unidimensional.

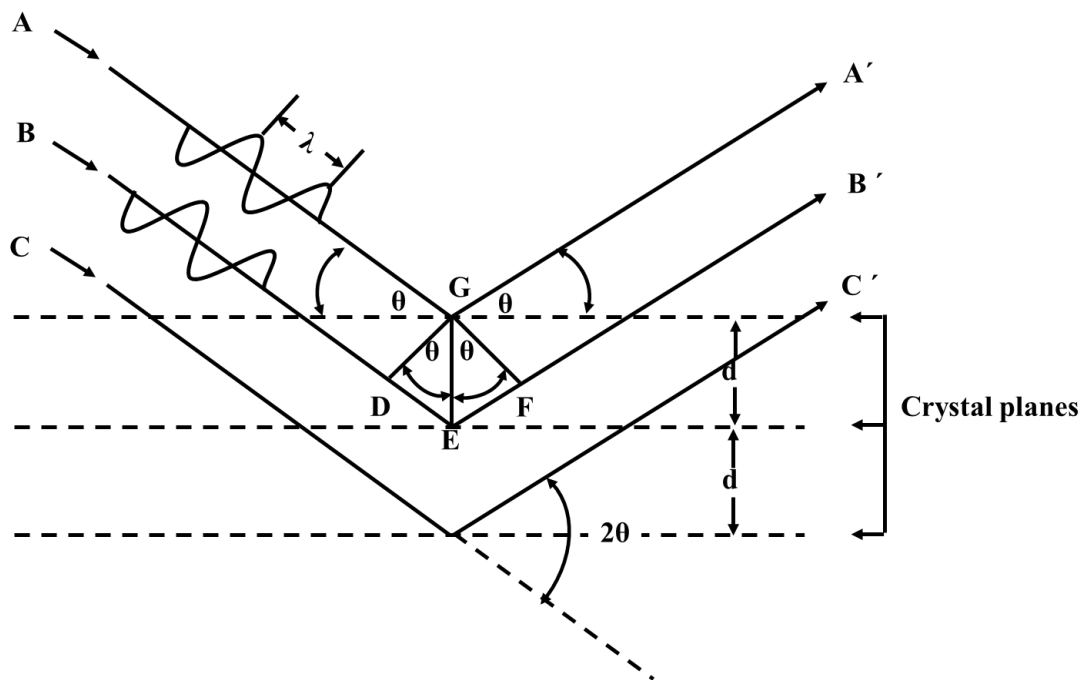


**Fig. 2.2.** Bragg's Law showing the scattering of x-rays from a crystal lattice

### 2.2.2.3. Differential scanning calorimetry (DSC)

DSC was used to study the thermal behaviour of raw materials (MAS, PPN, DIL and MET), as well as the double drug loaded complexes prepared. Sample preparation involved the placement of the sample powder (1-10 mg) onto a 40  $\mu\text{L}$  aluminium crucible with the lid hermetically sealed. The measurements were performed between 25 and 500  $^{\circ}\text{C}$ , at a rate of 10  $^{\circ}\text{C}/\text{min}$ .

#### **2.2.2.4. Scanning electron microscopy (SEM) with energy dispersive X-ray spectroscopy (EDX)**

The surface morphology in 3-D and the energy spectrum of samples were analysed using a QUANTA FEG 250 microscope equipped with EDX. The electronic beam voltage of the microscope was set at 20.0 kV and a working distance of 30 mm. Sample preparation involved placement of the material particles in powder form onto a sample holder, and then coating their surface in a thin layer of gold (1 – 5 nm), which made them electrically conductive.

#### **2.2.2.5. High Performance Liquid Chromatography (HPLC)**

High performance liquid chromatography was performed on a Shimadzu HPLC system (Fig. 2.3.), equipped with an auto sampler, using an XTerra<sup>®</sup> MS C18 150 mm × 4.6 mm × 3.5 µm column. The mobile phase was prepared using acetonitrile and 0.01 M disodium hydrogen orthophosphate (pH 3.5) at a ratio of 30:70 v/v respectively. The flow rate of the mobile phase was set at 1 mL/min and the analysis was performed at 230 nm, 236 nm or 233 nm based on the full wavelength spectrum of PPN, DIL and MET respectively. The preparation of 100, 75, 50, 40, 30, 20, 10, 5, 1 and 0.1 µg/mL standards with ultra-pure water using PPN, DIL and MET was used to generate the calibration graph.

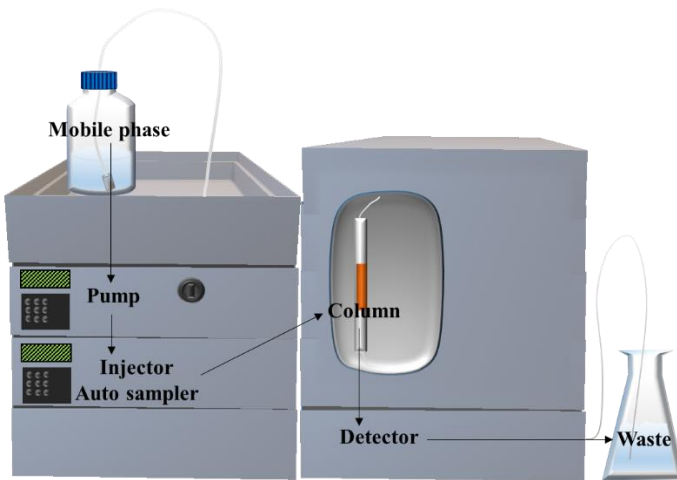


**Fig. 2.3.** HPLC system showing analysis steps involving mobile phase pumping, sample injection and sample passage through column, detector and finally into waste

#### **2.2.2.5.1. Method validation**

The HPLC method used was validated by the following parameters: linearity range, precision, limit of quantitation (LOQ) and limit of detection (LOD).

Linearity was evaluated over a series of drug stock solutions ranging from 100 to 0.1 µg/mL. A calibration graph was generated for each of the drugs by plotting the peak area versus the corresponding drug concentration. The slope, intercept and coefficient of determination ( $R^2$ ) generated from the calibration graph were used to evaluate the linearity of the technique. The results were recorded in triplicate on three different days.

For each of the drugs, the intra and inter day precision were determined from an assay of freshly prepared 1, 10, 50 and 100 µg/mL standard drug solutions, repeatedly run on the same day or on three different days. Results were evaluated statistically in terms of standard deviation (RSD %). LOD and LOQ were calculated over ten diluted drug solutions ranging from 100 to 0.1 µg/mL and used to estimate the sensitivity of the methods used for each of drugs. LOD and LOQ were calculated according to the International Conference on Harmonisation (ICH) guidelines, from the standard deviation of a y-intercept of a regression line (Ich, 2005).

#### **2.2.2.5.2. Determination of drug content in MAS – drug complex particles**

Drug content was determined by separately dispersing 50 mg of the prepared single and double drug loaded complex particles in 100 mL of 2 M HCl, ultra-pure water or pH 6.8 phosphate buffer under continuous stirring for 24 h, at 25 °C and 700 rpm. The dispersions obtained were filtered using 0.2 µm syringe filters and used to determine drug content in the MAS – drug complexes. The experiments were performed in triplicate to ensure reproducibility.

#### **2.2.2.6. Small angle X-ray scattering (SAXS)**

Small Angle X-Ray Scattering (SAXS) is a powerful non-destructive technique widely used to investigate the structural characteristics of materials, such as size, shape, size distribution and spatial fluctuation from electron density variations, associated with nano-scale morphological features within samples (Laity and Cameron, 2008; Odo *et al.*, 2015). Based on the spatial variation in electron density, SAXS has been extensively used for the analysis

of a wide variety of samples such as polymers, clays, nanoparticles, solvents and biological systems as both ‘static’ or dynamic systems (Laity and Cameron, 2008). SAXS is used to measure the scattering intensity at low angles and large distances, whereas XRD (X-Ray Diffraction) is used to study the structure of materials at small distances and wide angles (Li, Senesi and Lee, 2016).

In the present study SAXS was used to study the morphological changes of MAS upon the formation of flocculates following the adsorption of PPN, DIL or MET onto MAS, as well as to analyse the morphological characteristics of the MAS and the formed MAS-drug complexes in the solid-state form.

Following data analysis, the SAXS intensity is determined as a function of the scattering vector:

$$I(q) = N_p(1/q) \times n_e^2(1/q) \quad \text{Eq. 2.2.}$$

where  $N_p(1/q)$  is the number of scattering elements in the exposed volume, and  $n_e^2(1/q)$  is the square of the electron number in the exposed volume (Odo *et al.*, 2015).

The scattering vector is given by the following equation:

$$q = 4\pi\sin(\Theta/2)/\lambda \quad \text{Eq. 2.3.}$$

where  $\Theta$  is the scattering angle and  $\lambda$  is the X-ray beam wavelength.

Two-dimensional (2D-SAXS) measurements on MAS and the MAS-drug complex dispersions and particles prepared were performed on a Nanostar system (Bruker, Germany) (Fig.2.4.). Cu K $\alpha$  radiation ( $\lambda = 0.1542$  nm) was produced by a microfocus X-ray generator which generated a parallel X-ray beam, having an approximate 0.9 mm diameter spot size. The entire beam path was evacuated to minimise the scattering of air. The power setting used was 50.0 kV and 600  $\mu$ A and sample to detector distance was 1.0765 m. The sensitivity of the detector was calibrated using a silver behenate reference standard.



**Fig. 2.4.** Nanostar system from Bruker

*Solid-state analysis:* MAS and double drug loaded complexes (particle size 63-125 µm), as prepared and described in *Chapter 2, Section 2.4.*, were placed in disposable borosilicate glass capillary tubes (diameter 2.0 mm) and sealed at both ends (Fig.2.5.). 2D-SAXS patterns were collected for all the samples and for the background using an acquisition time of 1000 sec. Transmission was also calculated using a glassy carbon filter to correct for the probability of sample absorption using Eq. 2.4.

$$t = \frac{I_{X+GC} - t_{GC} \cdot I_X}{I_{GC} - t_{GC} \cdot I_0} \quad \text{Eq. 2.4.}$$

where  $t_{GC}$  is glassy carbon filter transmission,  $I_X$  is the number of counts collected from sample,  $I_{X+GC}$  is the number of counts from sample with glassy carbon filter,  $I_{GC}$  is the number of counts with glassy carbon filter and  $I_0$  is the number of counts from empty chamber.

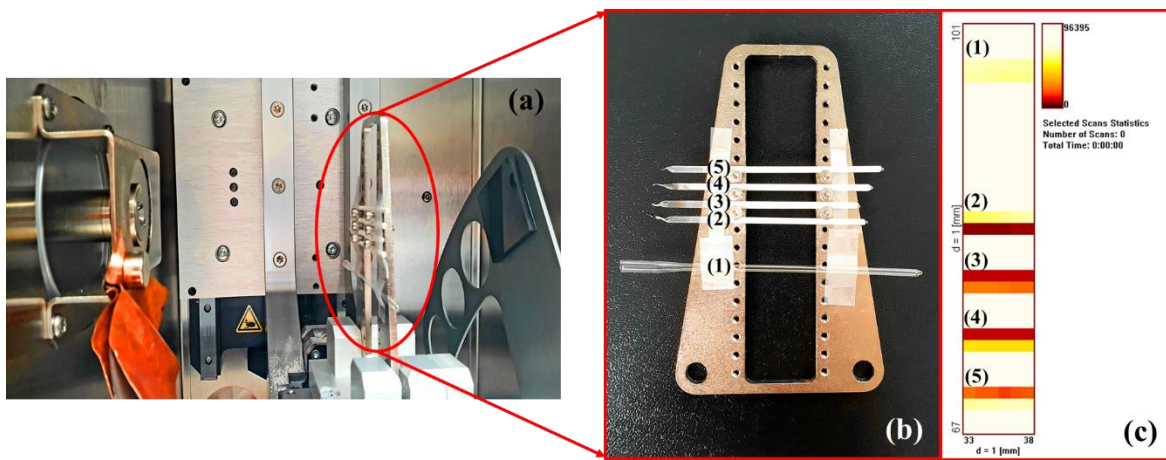


**Fig. 2.5.** SAXS analysis setup showing: (a) Nanostar chamber with the sample holder; (b) sample holder image showing empty borosilicate glass capillary tube (1) and filled capillary tubes with MAS (2), MAS-PPN (3), MAS-DIL (4) and MAS-MET (5) in powder form, particle size 63 – 125 µm; (c) nanography to detect sample coordinates for the analysis showing capillaries (1) to (5)

*Liquid-state analysis:* MAS and 1:1 v/v MAS-drug complex dispersions were prepared as described in Chapter 2, Section 2.4., using an MAS dispersion concentration of 0.25 % w/v. MAS dispersion and flocculated MAS-drug complexes were collected using a micropipette and placed in a metal cell fitted with a glass capillary (Fig 2.6.), having a 1 mm diameter. Nanography was used to determine the coordinates of the sample holder. Data acquisition time was 1000 s and the background scattering (i.e. ultra-pure water at pH 5) was subtracted from each sample prior to data analysis.



**Fig. 2.6.** SAXS analysis setup showing MAS-drug flocculated complex dispersion placed into a metal cell fitted with a glass capillary sealed at both ends (1 mm diameter)

#### 2.2.2.7. Microscopy

The morphology of the flocculated MAS-drug complex dispersions were analysed under a light microscope (Leica) at different magnifications. Sample preparation involved pipetting and spreading evenly a few drops of flocculated MAS-drug complex dispersions onto a glass slide.

Additional studies were performed on a VHX2000 Digital Microscope from KEYENCE using a blue daylight filter to enhance the contrast between the flocculated particles and the dispersion media.

#### 2.2.2.8. Calorimetric binding studies

Calorimetric binding studies were carried out at pH 5, 7 and 9 at a temperature range of 25–37°C on a VP-ITC micro calorimeter (Malvern Panalytical, UK). The instrument was used in high-gain mode, applying a reference power of 10-20  $\mu\text{cal s}^{-1}$  whilst stirring the sample cell contents at 307 rpm. The acidity of the working media in this study was chosen based on the  $\text{pK}_a$  value of the drugs used which are expected to be adsorbed onto the negatively charged MAS when ionised, and was adjusted using 2 M hydrochloric acid or 2 M sodium hydroxide (*ACD I-Lab*, 2018). Each interaction study required a separate experimental design. Experiments were repeated three times to ensure reproducibility.

#### **2.2.2.8.1. Calorimetric single injection mode (SIM) binding studies**

Calorimetric SIM binding studies were carried out at 25 °C and at three different pH values, 5, 7 and 9 to characterise the process of adsorption of PPN, DIL or MET onto MAS and identify the most favourable media for the reaction (screening).

MAS dispersions and solutions of PPN, DIL or MET were prepared separately using purified water under continuous stirring at 500 rpm at 25 °C for 24 h (MAS dispersion) and 30 min (PPN, DIL and MET solutions) respectively prior to the analysis. The pH of the prepared solutions and dispersions was further adjusted to 5, 7 and 9. Each of the drug solutions prepared was separately added in one 150 – 250 µL injection into the sample cell containing MAS. The single injection mode allowed for fast titration experiments compared to the conventional experiments and gave an indication of the binding isotherm in real time (MicroCal, 1998).

#### **2.2.2.8.2. Calorimetric multiple injection mode (MIM) binding studies**

Calorimetric MIM binding studies were carried out at pH 5 and two different temperatures 25 °C and 37 °C. The real-time binding isotherm was studied in 29-120 injections of 2-10 µL each into the sample cell every 260-550 s. MAS dispersions and drug solutions were prepared under continuous stirring. A mathematical model was then fitted to the data to get thermodynamic parameters which best reproduce the experimental data. Where necessary, data produced from the blank titrations was subtracted from the sample titration so that the dilution heat reflected only the interaction of interest.

#### **2.2.2.8.3. Effects of PEO and XG on the MAS-drug interactions**

Calorimetric MIM binding studies were carried out at pH 5 and two different temperatures 25 °C and 37 °C. The real-time binding isotherm was studied in 29-120 injections of 2-10 µL each into the sample cell every 260-550 s. PEO and XG dispersions (0.040 – 0.074 % w/v) were prepared separately using purified water under stirring at 500 rpm (25 °C) for 24 h. Each of the prepared dispersions was separately combined with one MAS dispersion (prepared as described in section 2.2.2.8.1.) and the resultant MAS-polymer mixture was used in the sample cell. Fresh drug solutions of either PPN, DIL or MET (prepared as

described in section 2.2.2.8.1.) were then separately added into the sample cell containing MAS-polymer complex.

### **2.2.3. Tablet formulation and characterisation**

#### **2.2.3.1. Tablet formulation and bulk compaction behaviour**

Tablets were prepared using direct compression method on a M500-50CT computer-controlled testing machine fitted with compression platens (Testometric Co. Ltd., UK) using flat-faced 10 mm stainless-steel dies and closely fitted punches (Fig 2.7.) (Specac, UK).

The powder mixture required to make the tablets containing MAS-drug complex was prepared by mixing the amount of MAS-PPN complex equivalent to a set amount of active ingredient (i.e. 30 mg PPN) with PEO or XG at a ratio of 1:1 w/w. The powder mixture required to make the tablets containing MAS-drug physical mixture and PEO or XG was prepared using the same amounts of powder as in the tablets containing MAS-drug complex particles (equivalent to a set amount of active ingredient). The powder combination was mixed in a 3-D shaker/mixer Turbula T2F (Stort Eskens Ltd., UK) for 10 min. Between 172 mg and 326 mg powder mixture (depending on polymer content (5 % w/w, 10 % w/w, 30 % w/w and 50 % w/w)) was poured into the die and tablets were formed by applying a set force of 10 kN. A pre-set maximum force was set at 16 kN. During the compression stage, the displacement was measured accurately through a short-travel extensometer by the movement of the cross head of the machine which was set at  $3 \text{ mm min}^{-1}$  while the lower punch remained fixed. After the set force was reached, the upper-punch was allowed to retract at a speed of  $1 \text{ mm min}^{-1}$ . Force and displacement as functions of time ( $F(t)$ , respectively  $x(t)$ ) were recorded automatically during the experiments. Once the experiment finished and the force applied returned to zero, the specimens were ejected from the die using the same instrument set at a speed of 10 mm/min. The weight, as well as diameter and height of the specimens were recorded immediately.

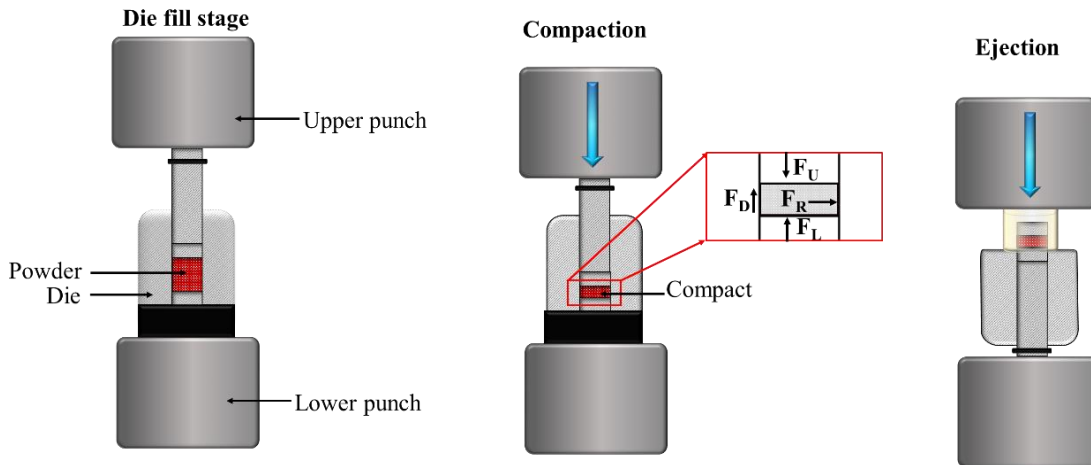


**Fig. 2.7.** Tablet press powder compaction described step by step: die fill stage, compaction and ejection

The effects of different compaction forces on the materials used were studied as the average pressure across the upper punch  $P(t)$  vs. the relative density of the compacted samples ( $\rho_{rel}$ ) (Eq. 2.5. and Eq. 2.6.) (Laity *et al.*, 2015).

$$P(t) = F(t)/\pi R^2 \quad \text{Eq. 2.5.}$$

$$\rho_{rel}(t) = \frac{m}{\rho \pi R^2 [h_0 - x(t)]} \quad \text{Eq. 2.6.}$$

where  $h_0$  is the filling depth of the powder bed and  $m$  is the mass of the tablet measured after ejection from die. Results were compared in each case between tablets containing MAS-drug complexes and tablets containing MAS-drug physical mixture.

### 2.2.3.2. True density and porosity determination

The true density of the powder mixtures used to make tablets was determined by helium pycnometry on an AccuPyc II 1340 (Micrometrics, UK). The technique uses inert gas displacement method to determine the sample volume and is non-destructive. The determination of the true density of the powder, along with the tablet weight, height and diameter allowed for the determination of tablet porosity (Eq. 2.7.).

$$\text{Tablet porosity} = \left[ 1 - \frac{\text{Tablet weight/Tablet volume}}{\text{True density of powder}} \right] \times 100 \quad \text{Eq. 2.7.}$$

### 2.2.3.3. Dissolution testing

The *in vitro* release characteristics of the tablets prepared as described in Section 2.2.3.1 were analysed using the USP dissolution apparatus (paddle method; PT-DT70 Pharma Test, Germany). Tablets were placed in sinker capsules (stainless steel wire helix) to prevent them from floating. Tablets were tested in two dissolution media according to USP 6: acid stage to simulate the gastric fluid using 900 ml of 0.1 M hydrochloric acid (pH 1.2) for 10 hours and buffer stage hours to simulate the intestinal fluid using 900 ml of 6.8 phosphate buffer (prepared by mixing 0.1M hydrochloric acid with 0.20 M tribasic sodium phosphate at a ratio 3 to 1 v/v) for 10 hours (United States Pharmacopeial Convention, 2011). The rotation speed of the paddles was 100 rpm. Samples were collected at suitable intervals and were analysed at 290 nm by the UV-Vis detector attached to the dissolution instrument. All experiments were performed in triplicate for reproducibility.

### 2.2.3.4. Kinetics of drug release

The dissolution profiles obtained were subjected to a methodology as described by Peppas model and also known as the power law which was used to determine the release mechanism that took place based on the value of the diffusional exponent (Dash *et al.*, 2010; Siahi-Shadbad *et al.*, 2011; Romero *et al.*, 2018). This model assumes that the drug is distributed uniformly through the polymeric matrix prior to the analysis (Siahi-Shadbad *et al.*, 2011). To determine the mechanism of drug release, the first 60 % of the drug release curve is fitted to a simple equation:

$$Q = ktn \quad \text{Eq. 2.8.}$$

where  $Q$  is the percentage of drug released at time  $t$ ,  $k$  is the release rate constant which describes the structure and geometry of the tablet, and  $n$  is the diffusional exponent which indicated the mechanism of drug release (Dash *et al.*, 2010; Siahi-Shadbad *et al.*, 2011; Romero *et al.*, 2018).

A value of  $n$  lower than 0.45 calculated from drug release of matrix cylindrical tablets indicates Fickian diffusion mechanism. A value of  $n$  higher than 0.89 shows however that

the dissolution process was controlled by erosion and that the rate of drug release was independent of time, ‘zero-order’ release. An anomalous transport or non-Fickian was considered when  $n$  was between 0.45 and 0.89 which suggested that drug release was governed by both diffusion and erosion (Ritger and Peppas, 1987; Costa, Manuel and Lobo, 2001; Siahi-Shadbad *et al.*, 2011).

The efficiency on retarding drug release of the different polymers used in the research, XG and PEO combined with both MAS-drug complexes and physical mixtures were compared using the following equations describing the mean dissolution time (MDT) and the dissolution efficiency (DE – area under the dissolution curve up to a certain time  $t$ ) (Costa, Manuel and Lobo, 2001; Siahi-Shadbad *et al.*, 2011).

$$MDT = \frac{\sum_{j=1}^n t \Delta M_j}{\sum_{j=1}^n \Delta M_j} \quad \text{Eq. 2.9.}$$

where  $j$  is the sample number,  $n$  is the number of dissolution sample times,  $t$  is the time at midpoint between  $t$  and  $t-1$  (that can be calculated with the formula  $(t + t - 1)/2$ ) and  $\Delta M_j$  is the additional amount of drug that dissolved between  $t$  and  $t-1$  (Costa, Manuel and Lobo, 2001; Siahi-Shadbad *et al.*, 2011).

$$DE = \frac{\int_0^T Y \times dt}{Y_{100} \times T} \times 100\% \quad \text{Eq. 2.10.}$$

where  $Y$  is the percent of drug release at time  $t$  and  $Y_{100}$  represents 100 % drug release (Costa, Manuel and Lobo, 2001; Siahi-Shadbad *et al.*, 2011).

### **2.3. References**

- ACD I-Lab (2018). Available at: <https://ilab.acdlabs.com/iLab2/> (Accessed: 23 September 2018).
- Coates, J. (2000) ‘Interpretation of Infrared Spectra, A Practical Approach’, *Encyclopedia of Analytical Chemistry*, pp. 10815–10837.
- Costa, P., Manuel, J. and Lobo, S. (2001) ‘Modeling and comparison of dissolution profiles’, *European Journal of Pharmaceutical Sciences*, 13, pp. 123–133.
- Dash, S. *et al.* (2010) ‘Kinetic Modeling On Drug Release From Controlled Drug Ddlivery Systems’, *Polish Pharmaceutical Society*, 67(3), pp. 217–223.
- ICH (2005) ‘ICH Topic Q2 (R1) Validation of Analytical Procedures : Text and Methodology’, *International Conference on Harmonization*, 1994(November 1996), p. 17.
- Laity, P. R. *et al.* (2015) ‘Using small-angle X-ray scattering to investigate the compaction behaviour of a granulated clay’, *Applied Clay Science*, 108, pp. 149–164.
- Laity, P. R. and Cameron, R. E. (2008) ‘A small-angle X-ray scattering study of powder compaction’, *Powder Technology*, pp. 119–127.
- Li, T., Senesi, A. J. and Lee, B. (2016) ‘Small Angle X - ray Scattering for Nanoparticle Research’, *Chemical Reviews*, 116, p. 11128–11180.
- MicroCal (1998) *VP-ITC User’s Manual*. Northampton.
- Odo, E. A. *et al.* (2015) ‘SAXS Study of Silicon Nanocomposites’, 5(3), pp. 65–70.
- Perkin Elmer and Technical Note (2012) ‘The Effects of Varying Force and Contact on ATR Spectra’, *Technical Note*, pp. 4–6.
- Ritger, P. L. and Peppas, N. A. (1987) ‘A simple equation for description of solute release I. Fickian and non-fickian release from non-swellable devices in the form of slabs, spheres, cylinders or discs’, *Journal of Controlled Release*, 5(4), pp. 23–36.
- Rojtanatanya, S. and Pongjanyakul, T. (2010) ‘Propranolol-magnesium aluminum silicate complex dispersions and particles: Characterization and factors influencing drug release’, *International Journal of Pharmaceutics*, 383(1–2), pp. 106–115.

Romero, A. I. *et al.* (2018) ‘Validation of kinetic modeling of progesterone release from polymeric membranes’, *Asian Journal of Pharmaceutical Sciences*, 13(1), pp. 54–62.

Siahi-Shabdar, M. R. *et al.* (2011) ‘Release Behaviour of Propranolol HCl from Hydrophilic Matrix Tablets Containing Psyllium Powder in Combination with Hydrophilic Polymers’, *AAPS PharmSciTech*, 12(4), pp. 1176–1182.

United States Pharmacopeial Convention (2011) ‘U.S. Pharmacopeial guidelines Dissolution’, *USP Dissolution*, 1, Stage 6, pp. 1–8.

Vanderbilt Minerals (2014) *VEEGUM / VAN GEL Magnesium Aluminum Silicate Magnesium Aluminum Silicate ® The Story*. Norwalk.

# *Chapter 3:*

## *Adsorption of propranolol hydrochloride onto magnesium aluminium silicate*

### Note to reader

Aspects of this chapter has been published in the International Journal of Pharmaceutics X under the title, “Real time calorimetric characterisation of clay – drug complex dispersions and particles”

(<https://doi.org/10.1016/j.ijpx.2018.100003>)

## **Chapter 3: Adsorption of propranolol hydrochloride onto magnesium aluminium silicate**

### **3.1. Methodology**

#### **3.1.1. Formulation of single and double drug loaded MAS-PPN complexes**

Please refer to chapter 2, section 2.2.1.

#### **3.1.2. Characterisation of MAS-PPN complexes**

##### **3.1.2.1. Attenuated total reflectance Fourier transform infrared spectroscopy (ATR-FTIR)**

Please refer to chapter 2, section 2.2.2.1.

##### **3.1.2.2. Powder X-Ray diffractometry (PXRD)**

Please refer to chapter 2, section 2.2.2.2.

##### **3.1.2.3. Differential scanning calorimetry (DSC)**

Please refer to chapter 2, section 2.2.2.3.

##### **3.1.2.4. Scanning electron microscopy (SEM) with energy dispersive X-ray spectroscopy (EDX)**

Please refer to chapter 2, section 2.2.2.4.

##### **3.1.2.5. High Performance Liquid Chromatography (HPLC)**

Please refer to chapter 2, section 2.2.2.5.

###### **3.1.2.5.1. Method validation**

Please refer to chapter 2, section 2.2.2.5.1.

###### **3.1.2.5.2. Determination of PPN content in MAS-PPN complex particles**

Please refer to chapter 2, section 2.2.2.5.2.

###### **3.1.2.6. Small angle X-ray scattering (SAXS)**

Please refer to chapter 2, section 2.2.2.6.

###### **3.1.2.7. Microscopy**

Please refer to chapter 2, section 2.2.2.6.

### **3.1.2.8. Calorimetric binding studies**

#### **3.1.2.8.1. Calorimetric single injection mode (SIM) binding studies**

Calorimetric SIM binding studies were performed as described in Chapter 2, section 2.2.2.8.1. PPN solution (0.150 % w/v) was added in one 150 µL injection into the sample cell containing MAS dispersion (0.037 % w/v) at each of the pH values studied (pH 5, 7 and 9). The binding isotherm was analysed by comparing the reaction rate for the adsorption of PPN onto MAS at the pH values studied. Furthermore, the evolved heat in the experiments was analysed through a set of sites curve fittings using a non-linear least squares model. This allowed the determination of the association constant  $K_a$  and thermodynamic parameters  $\Delta H$ ,  $\Delta G$  and  $-T\Delta S$ .

#### **3.1.2.8.2. Calorimetric multiple injection mode (MIM) binding studies**

Calorimetric MIM binding studies to characterise the adsorption of PPN onto MAS were performed as described in chapter 2, section 2.2.2.8.2. The real-time binding isotherm was studied in 120 injections of 2 µL each into the sample cell every 260 seconds. The reference power applied was 20 µcal/sec. The concentrations of the PPN solution (0.150 % w/v) and MAS dispersion (0.037 % w/v) were chosen as in section 3.1.2.8.1. One set of sites model was fitted to the data to get thermodynamic parameters which best reproduce the experimental data. Data produced from the blank titrations was subtracted from the sample titration where required.

#### **3.1.2.8.3. Effects of PEO and XG on the interaction between MAS and PPN**

MIM binding studies were performed to aid the study of the effects of PEO and XG on the adsorption of PPN onto MAS and were conducted as described in chapter 2, section 2.2.2.8.3. The binding isotherms between MAS (0.037 % w/v) and PEO (0.037 % w/v), and between PPN (0.150 % w/v) and PEO (0.037 % w/v) were studied in 30 injections of 10 µL each into the sample cell every 1500 seconds. The binding between PPN (0.150 % w/v) and MAS-PEO mixture (0.074 % w/v MAS mixed with 0.074 % w/v PEO at a ratio of 1:1) was studied in 120 injections of 2 µL each into the sample cell every 260 seconds. In all cases the reference power applied was 15 µcal/sec.

The binding isotherms between MAS (0.037 % w/v) and XG (0.020 % w/v) and between PPN (0.150 % w/v) and XG (0.020 % w/v) were studied in 29 injections of 4 µL each into the sample cell every 1200 seconds. The reference power applied was 15 µcal/sec.

The adsorption of PPN (0.150 % w/v) onto MAS in the presence of XG was studied using a mixture of MAS-XG (0.074 % w/v MAS dispersion mixed with 0.040 % w/w XG dispersion at a ratio of 1:1 v/v). The interaction was studied in 120 injections of 2 µL each into the sample cell every 260 seconds, applying a reference power of 10 µcal/sec.

A summary of the parameters used in the MIM and SIM ITC experiments can be found in Table 3.1.

**Table 3.1.** Compounds and parameters used in ITC SIM and MIM experiments

Cell		Syringe		Number of injections	Injection volume (µL)	Spacing (sec)	Reference power (µcal/sec)
Clay/polymer	Concentration (% w/v)	Drug/polymer	Concentration (% w/v)				
MAS	0.037	PPN	0.150	1	150	2500	20
MAS	0.037	PPN	0.150	120	2	260	20
MAS	0.037	PEO	0.037	30	10	1500	15
PEO	0.037	PPN	0.150	30	10	1500	15
MAS-PEO	0.037 MAS 0.037 PEO	PPN	0.150	120	2	260	15
MAS	0.037	XG	0.020	29	4	1200	10
XG	0.020	PPN	0.150	29	4	1200	10
MAS-XG	0.037 MAS 0.020 XG	PPN	0.150	120	2	260	10

### **3.2. Results and discussion**

#### **3.2.1. Attenuated total reflectance Fourier transform infrared spectroscopy (ATR-FTIR)**

ATR-FTIR was used to study the adsorption onto MAS of PPN based on the vibration of chemical bonds formed (Fig. 3.1.).

The spectrum of MAS indicated the presence of the hydroxyl group belonging to Si-OH at  $3625\text{ cm}^{-1}$  and the Si-O-Si stretching at  $980\text{ cm}^{-1}$  (Rojtanatanya and Pongjanyakul, 2010). A broad peak at  $3415\text{ cm}^{-1}$  belonging to the O-H stretching of water residues and a sharp peak at  $1640\text{ cm}^{-1}$  belonging to the hydroxyl group bending of water crystallization were observed (Rojtanatanya and Pongjanyakul, 2010).

The spectrum of PPN showed three distinctive peaks occurring between  $3380$  and  $3185\text{ cm}^{-1}$  which can be attributed to the secondary hydroxyl and amine groups within its structure. The peak observed at  $1268\text{ cm}^{-1}$  was attributed to aryl alkyl ether stretching, while the peak at  $970\text{ cm}^{-1}$  belonged to the naphthalene group belonging to PPN (Rojtanatanya and Pongjanyakul, 2010; Saeedi, Morteza-Semnani and Sagheb-Doust, 2013).

The analysis of single and double drug loaded MAS – PPN complexes showed spectrums very different to that of the spectrum of PPN or MAS. The presence of the Si-O-Si stretching at  $980\text{ cm}^{-1}$  belonging to the clay was still observed, whereas the peak showing the hydroxyl stretching belonging to Si-OH became smaller and shifted to a lower wavelength approx.  $3631\text{ cm}^{-1}$ . Also, the peaks attributed to the secondary hydroxyl and amine groups belonging to PPN completely disappeared. Hence, the change and disappearance of peaks belonging to both MAS and PPN confirms the PPN adsorption onto MAS, via hydrogen bonds formation between the silanol groups of MAS with the amine and/or hydroxyl groups of PPN (Rojtanatanya and Pongjanyakul, 2010).

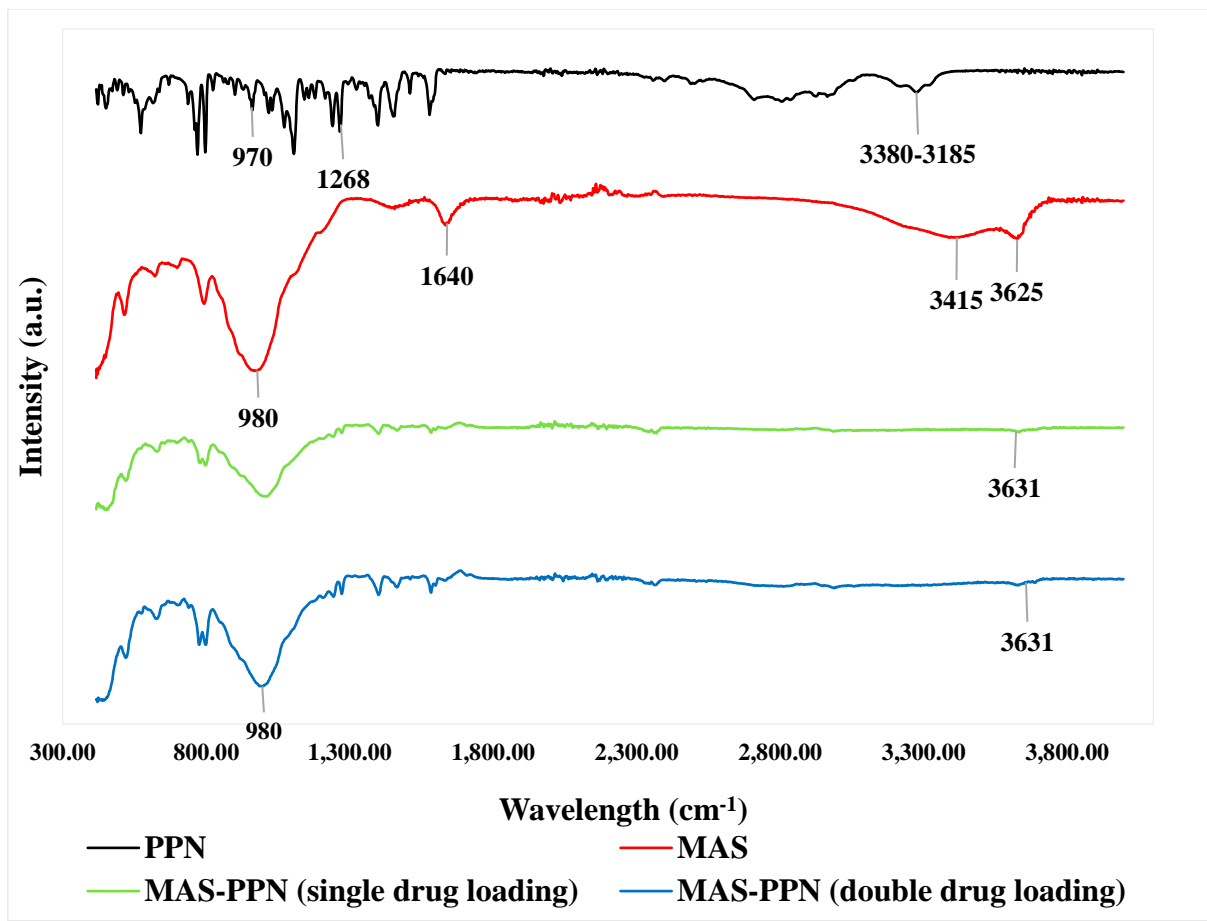


**Fig. 3.1.** ATR-FTIR spectra of PPN, MAS and single and double drug loaded MAS-PPN complex particles

### 3.2.2. Powder X-ray diffractometry (PXRD)

PXRD represents a useful tool, often used to identify clays. Smectite clays are often called ‘expandable clays’, as they have the ability to absorb water. Their typical basal spacing is 14 $\text{\AA}$  (1.4nm), but following water absorption this may vary between 9.6 $\text{\AA}$  (completely dried) to 21.4 $\text{\AA}$  (Tucker, 2001). Basal spacing also indicates the capacity of drug molecules to intercalate into the silicate layers of the clay (Ray *et al.*, 2002).

The diffractograms obtained provided information about the physical form of the clay, drug and samples prepared, as well as of the changes in the basal spacing following complexation. Bragg’s Law (Eq. 3.1) was used to calculate the basal spacing by the approximation of the 001 plane peak (basal distance) (Rojtanatanya and Pongjanyakul, 2010).

$$n\lambda = 2ds\sin\theta$$

**Eq. 3.1.**

$n = 1$  as the analysis of clay minerals is unidimensional.

The diffractogram acquired for MAS (Fig. 3.2.) showed a distinctive reflection at  $6.87^\circ$  ( $2\theta$ ) representing the thickness of the basal spacing and, using Bragg's Law, this was calculated as being 1.28nm, value similar to those suggested in literature (Pongjanyakul, Khunawattanakul and Puttipipatkhachorn, 2009; Rojtanatanya and Pongjanyakul, 2010).

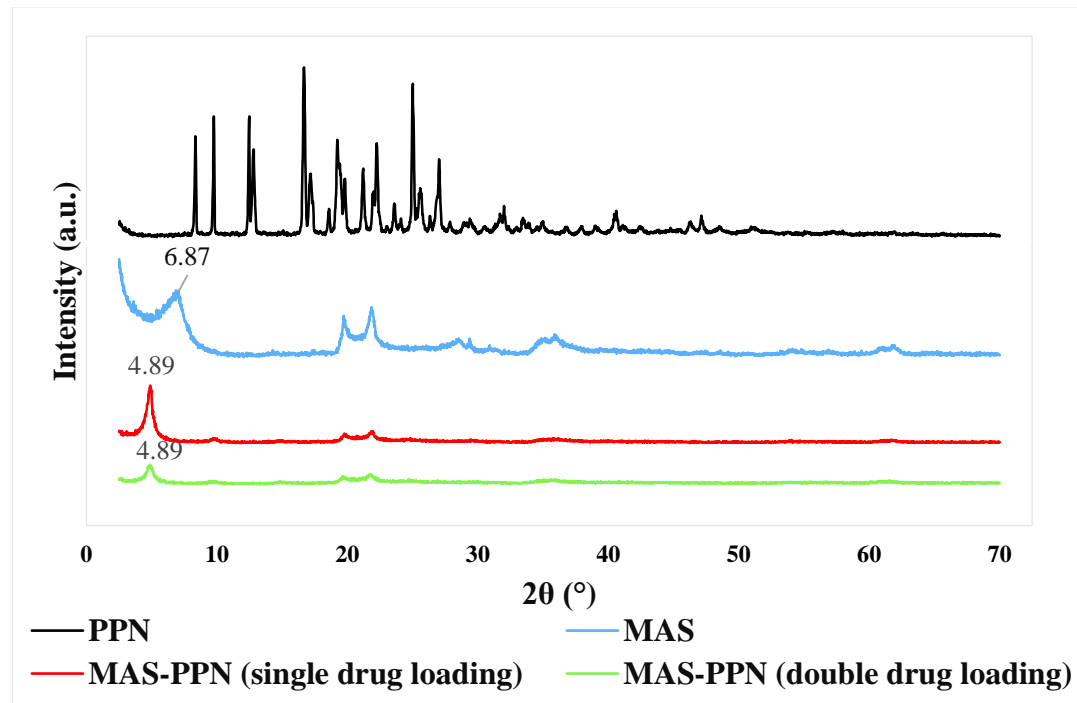


**Fig. 3.2.** PXRD patterns of MAS, PPN and MAS-PPN single and double drug loaded complexes

Figure 3.2 confirmed PPN to be crystalline in nature with strong distinctive intensities at 2-theta values at  $8.3^\circ$ ,  $9.7^\circ$ ,  $12.4^\circ$ ,  $12.7^\circ$ ,  $16.7^\circ$ ,  $16.6^\circ$ ,  $17.2^\circ$ ,  $22.0^\circ$  and  $25.0^\circ$  as reported by Shankland and Knight (1996) and by Fernandes *et al.* (2019) (Shankland and Knight, 1996; Fernandes *et al.*, 2019). The prepared MAS-PPN complexes showed PPN to be in the amorphous form as it did not present the PXRD pattern of the drug alone suggesting the molecular dispersivity of the drug in the prepared complexes. The reflection at  $6.87^\circ$  ( $2\theta$ ) representing the thickness of the silicate layer in the MAS sample was shifted to the left in

the diffractogram of the complexes prepared and had a different intensity, as the basal spacing increased following intercalation of drug particles into the clay platelets, which further increased stacking of the intercalated silicate layers (Ray *et al.*, 2002; Rojtanatanya and Pongjanyakul, 2010). The increase in basal spacing calculated using Bragg's Law was 1.81 nm for the single and double drug loaded MAS-PPN complexes (18.07 Å for the single drug loaded MAS-PPN complex particles and 18.08 Å for the double drug loaded MAS-PPN particles). Hence, the basal spacing increase suggests that PPN was intercalated into the clay platelets.

Upon the analysis of the single drug loaded MAS-PPN complexes at ambient temperature it was observed that the basal distance varied over time when the same sample was run repeatedly (the peak position and intensity changed) (Figure 3.3). This was linked to the sensitivity of the MAS to the room conditions that has humid air present (normal laboratory humidity between 25 – 45 % RH (Supuk *et al.*, 2013)), thereby causing rehydration and hence basal distance expansion within minutes (Milne and Warhaw, 1955).

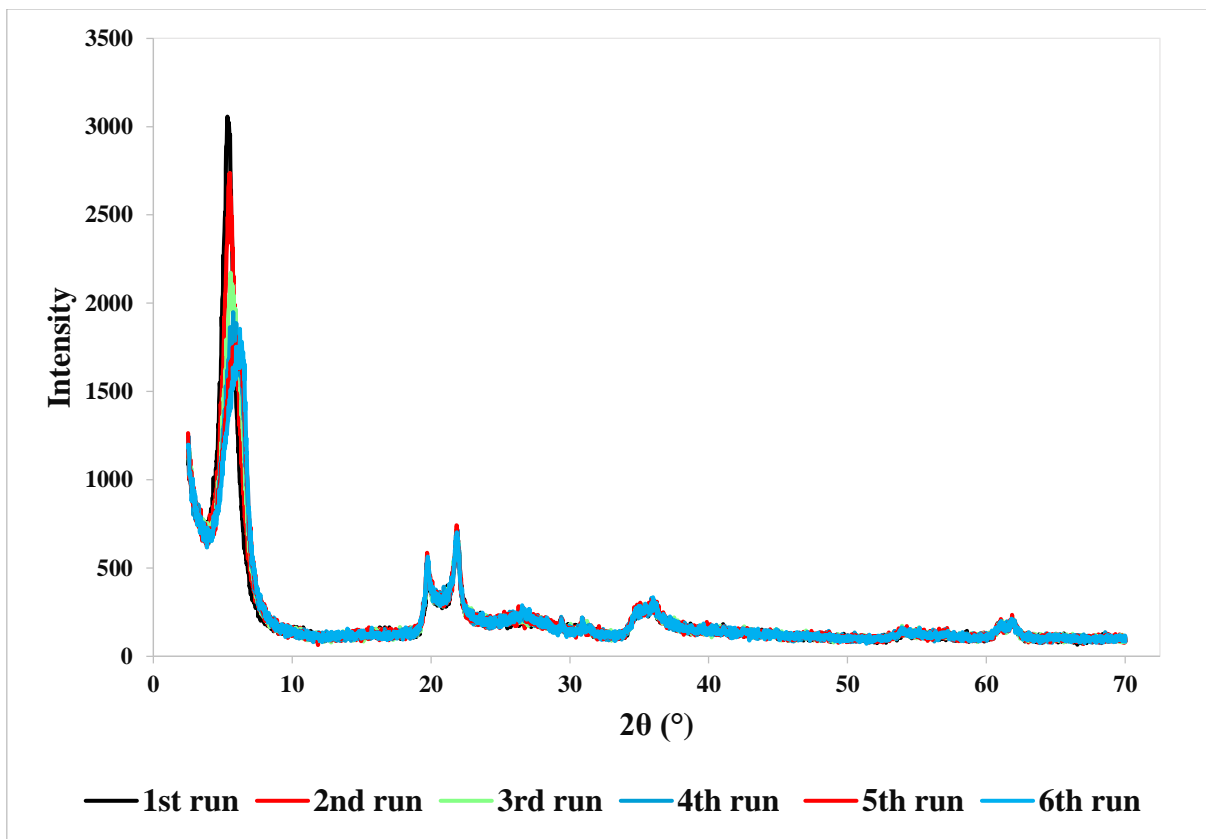


**Fig. 3.3.** PXRD successive runs testing variations in the basal distance of MAS-PPN single drug loaded complex following dehydration

Following the calculation of the basal distance after each consecutive run, it was observed that it gradually decreased (Fig. 3.3.), which was due to the water evaporation that occurred as the PXRD heated upon use. The basal distance dropped from 1.65 nm to 1.41 nm as the peak was shifted towards the position of the MAS peak shown in Fig 3.5. It was also observed that as the basal distance decreased, the peak also became broader, similar to the MAS basal distance peak.

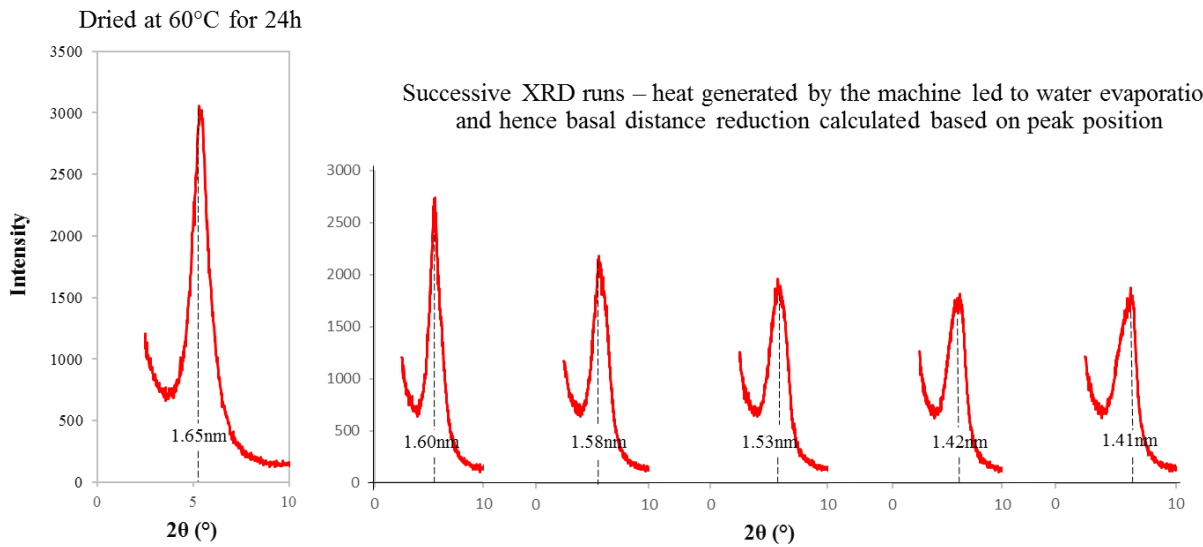


**Fig. 3.4.** PXRD successive runs testing variations in basal distance of MAS-PPN single drug loaded complex following dehydration and rehydration

When the peak position and intensity remained constant during two consecutive runs, the sample was placed in the oven to dry at 60 °C for 48 h, in order to check for further changes caused by dehydration and rehydration. However, after the drying process was completed, the basal distance did not change. It was interesting to note that only the peak intensity did, showing that a relatively small dehydration to still occur (Fig. 3.4.). When the sample was run again after 30 minutes at room temperature, the basal distance increased back to 1.58 nm due to sample rehydration, hence confirming its sensitivity to humidity (Fig. 3.5.).

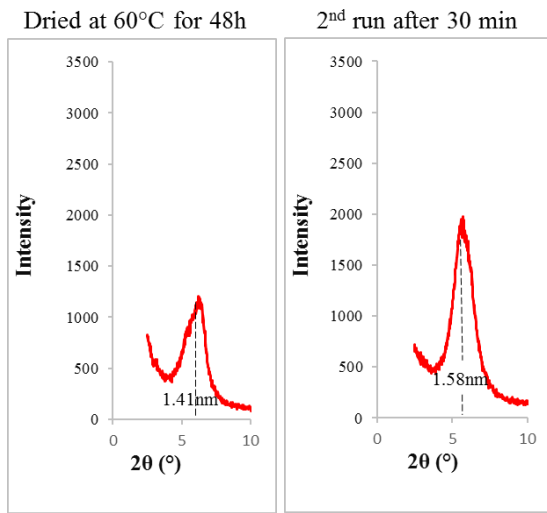


**Fig. 3.5.** PXRD successive runs testing variations in basal distance of MAS-PPN single drug loaded complex following dehydration and rehydration

Successive PXRD runs on MAS alone were performed to ensure that the clay dehydration and rehydration were responsible for sample sensitivity to humidity. Results showed a decrease in the distance between platelets from 1.30 to 1.22 nm following dehydration caused by the PXRD heating upon use (Fig. 3.6.).

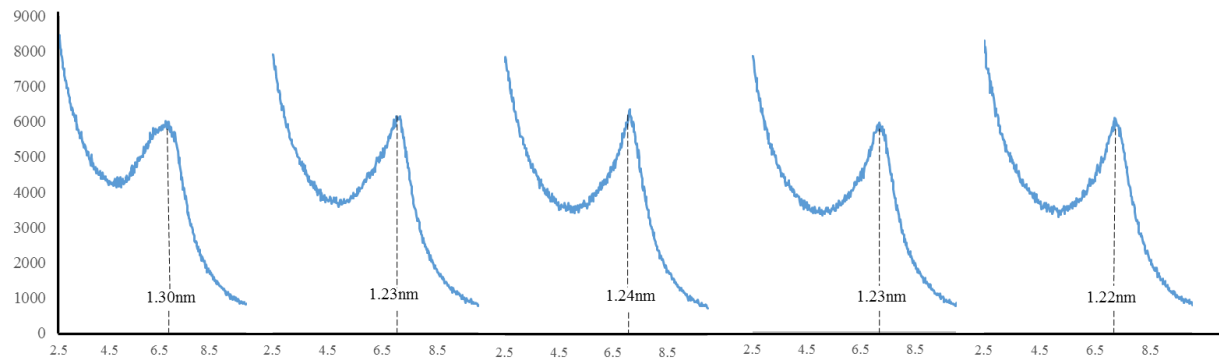


**Fig. 3.6.** PXRD successive runs testing variations in basal distance of MAS following dehydration

The rehydration and dehydration process can possibly impact on drug release from these complexes.

### 3.2.3. Differential scanning calorimetry (DSC)

Thermograms were obtained for MAS, PPN, as well as single drug loaded, and double drug loaded MAS-PPN complexes.

The thermogram of MAS showed the presence of a broad endothermic peak at 115°C that occurred following dehydration.

The thermogram of PPN revealed a sharp endothermic peak at  $167 \pm 1^\circ\text{C}$  indicating its melting point (Pongjanyakul and Rongthong, 2010; Rojtanatanya and Pongjanyakul, 2010). This was followed by another broad endothermic peak at  $336 \pm 1^\circ\text{C}$  representing the decomposition of PPN.

The single and double drug loaded MAS-PPN complex particles prepared were shown to be amorphous and the absence of the melting point of PPN on their thermograms confirmed the molecular dispersion the drugs in amorphous form in the complexes (Rojtanatanya and Pongjanyakul, 2010).

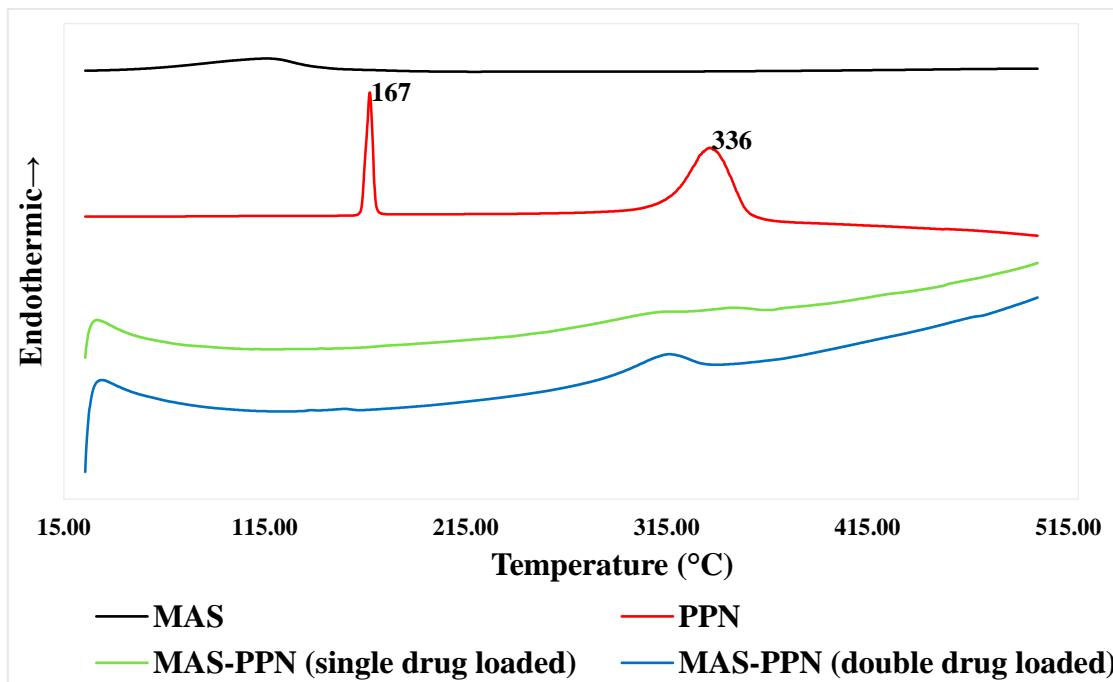


**Fig. 3.7.** Thermograms obtained for MAS, PPN and MAS-PPN single and double drug loaded complex particles (n=3)

### **3.2.4. Scanning electron microscopy with energy dispersive X-ray spectroscopy (SEM/EDX)**

MAS, PPN, as well as the single and double drug loaded MAS-PPN complex particles prepared were studied using SEM to understand and compare their surface morphology. EDX was used to confirm the chemical elements existing in the samples. The atomic distribution of elements slightly varied (Bandyopadhyay and Bose, 2013).

MAS particles were shown to be aggregated together in big clusters (Fig. 3.8.) (Mita, Rupa and Achowicz, 2010; Pongjanyakul and Rojtanatanya, 2012). However, individual flakes were observed on its surface upon increasing magnification representing the tetrahedral and octahedral sheets which are characteristic to phyllosilicates (Carrado and Bergaya, 2007).

The analysis of the atomic distribution onto MAS surface revealed the presence of high amounts of silicon, aluminium and magnesium, as well as traces amounts of iron, calcium, sodium, titanium and potassium. The high percentage of silicon, magnesium and aluminium confirm the presence of both montmorillonite and saponite clays within the material, whereas the other elements may indicate its provenience (Kanjanakawinkul *et al.*, 2013). Results are in agreement with the chemical analysis of MAS presented in Chapter 1, Section 1.4.2.

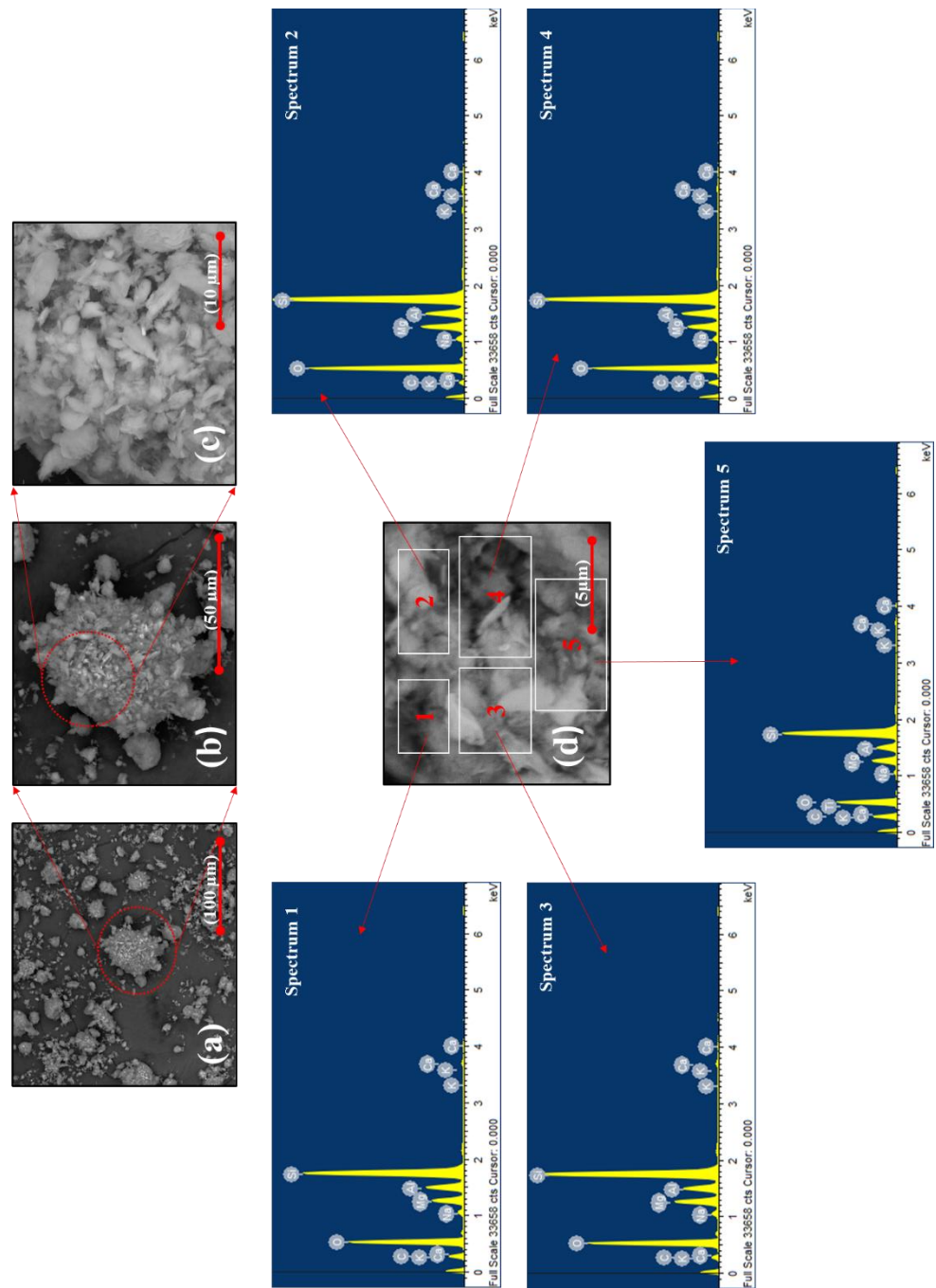


**Fig. 3.8.** Surface characterisation of MAS using SEM/EDX. SEM images at different magnifications  $\times 500$  (a),  $\times 1500$  (b),  $\times 5000$  (c) and  $\times 10\,000$  (d); atomic distribution profile at five different sample locations (Spectrum 1-5)

PPN was shown to be formed of large crystalline particles having a smooth surface (Fig. 3.9.). EDX analysis of PPN confirmed the presence of distinctive elements such as chlorine and nitrogen in the tested specimen.

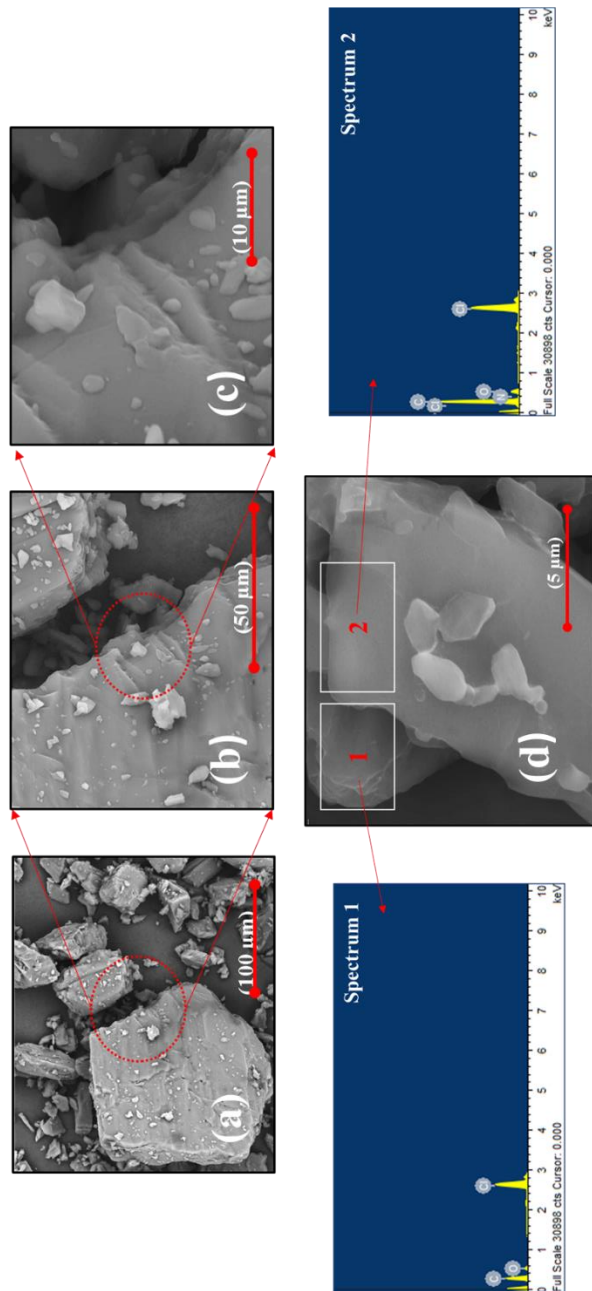


**Fig. 3.9.** Characterisation of PPN surface using SEM/EDX. SEM images at different magnifications  $\times 500$  (a),  $\times 1500$  (b),  $\times 5000$  (c) and  $\times 10\,000$  (d); atomic distribution profile at two different sample locations (Spectrum 1 and 2)

The analysis of the single and double drug loaded MAS-PPN complex particles (Fig. 3.10. and Fig. 3.11.) using SEM/EDX showed that both samples were similar, but highly different when compared to the MAS and pure PPN. Images showed that changes in the microstructural properties of the clay powder occurred following the complexation process which may explain why the formed MAS-PPN complexes can be used to offer controlled drug release (Mita, Rupa and Achowicz, 2010). The analysis of atomic distribution in the single and double drug loaded MAS-PPN complex particles revealed the presence of elements belonging to both PPN and MAS which was expected.

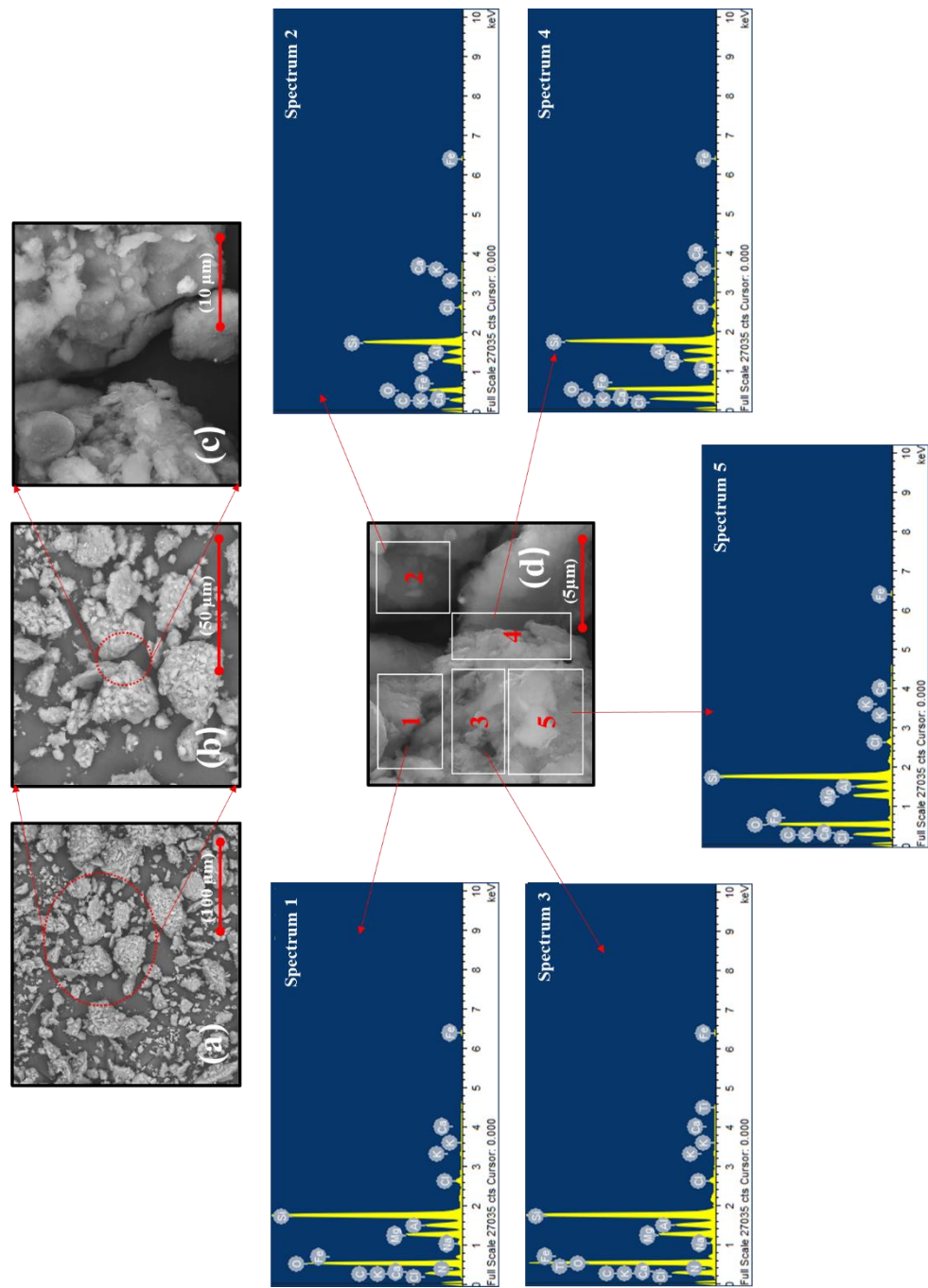


**Fig. 3.10.** Surface characterisation of MAS-PPN single drug loaded complex using SEM/EDX. SEM images at different magnifications  $\times 500$  (a),  $\times 1500$  (b),  $\times 5000$  (c) and  $\times 10\,000$  (d); atomic distribution profile at five different sample locations (Spectrum 1-5)

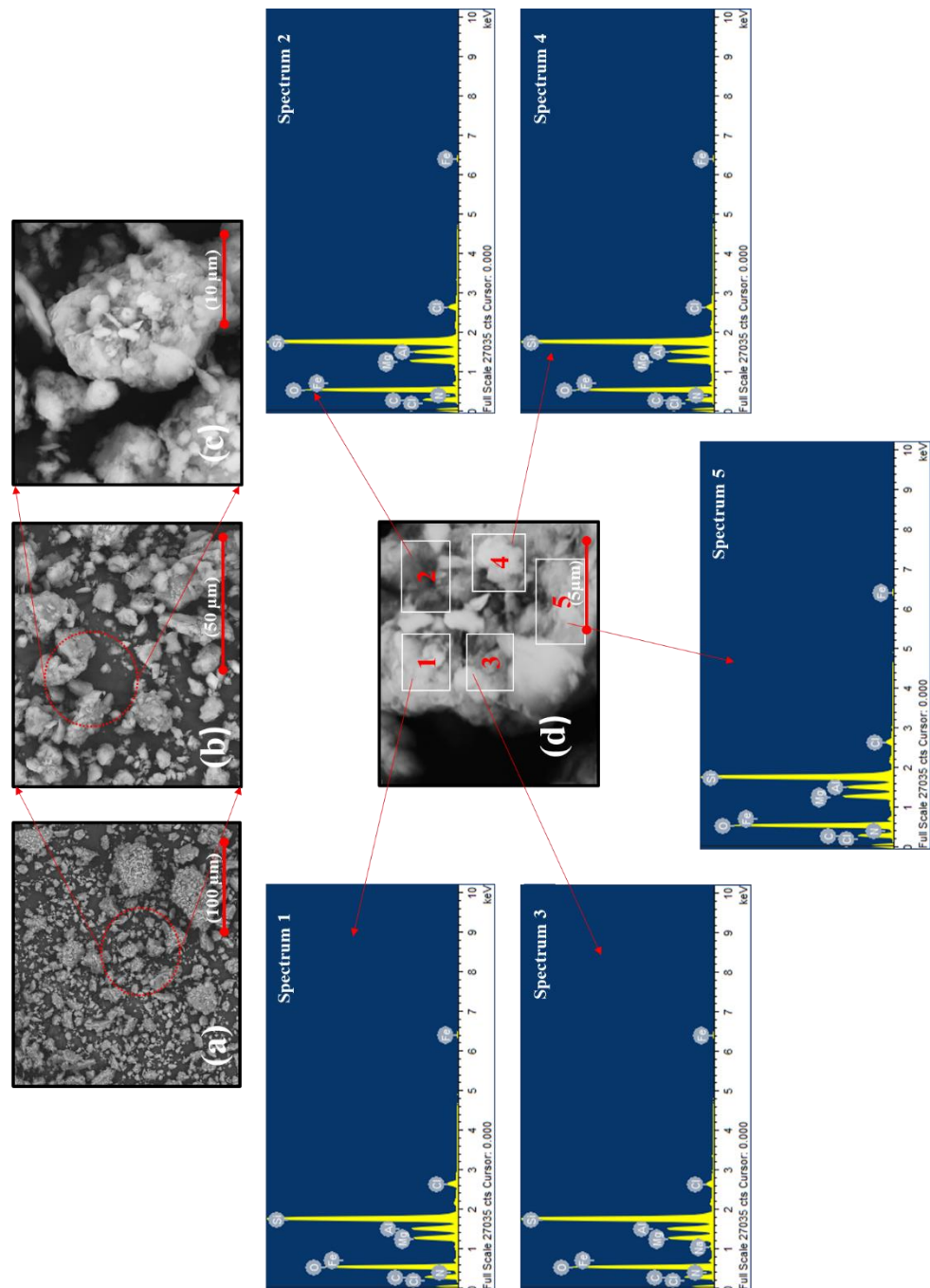


**Fig. 3.11.** Surface characterisation of MAS-PPN double drug loaded complex using SEM/EDX. SEM images at different magnifications  $\times 500$  (a),  $\times 1500$  (b),  $\times 5000$  (c) and  $\times 10000$  (d); atomic distribution profile at five different sample locations (Spectrum 1-5)

It should be noted that the use of this characterisation technique may introduce a selective bias in the overall results for the MAS-PPN complexes, due to the analysis of only small

particulates selected from the overall sample prepared, which is appropriate for this type of analysis (Bohor and Hughes, 1971). However, the analysis was only used for qualitative purposes, to explore the surface morphology of the samples.

### 3.2.5. High performance liquid chromatography (HPLC)

#### 3.2.5.1. Method validation

The calibration curve generated using the pure drug solution (PPN) was found to be linear over the concentration range studied ( $R^2 \geq 0.999$ ). The linearity was defined by an equation ( $y = 129827x + 68927$ ) which was further used in the recovery studies (Fig. 3.12.).

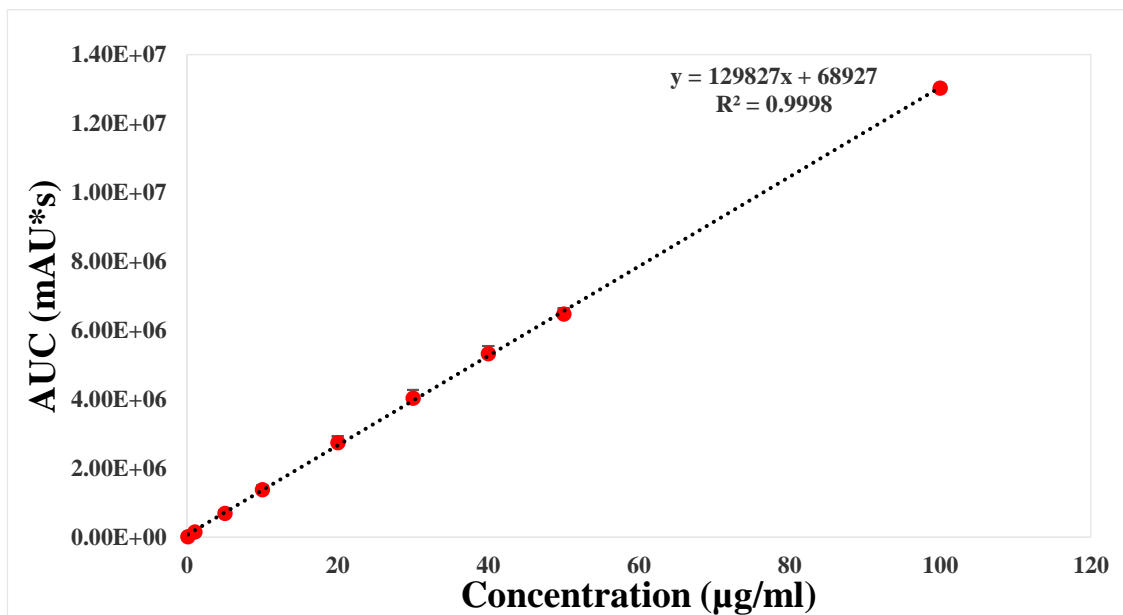


**Fig 3.12.** Calibration curve for PPN (100 to 0.1 μg/ml) showing linearity ( $R^2=0.9998$ )

The method was proved to be precise for the detection of PPN. The intermediate and intra assay precision at three different concentration levels of 10, 50 and 100 μg/mL ranging from 0.09 % to 0.61 % and from 0.25 % to 1.04 % respectively, hence lower than 2 % RSD which complies with the acceptable criteria for quality control of pharmaceutical preparations (Ermer and Ploss, 2005; Chatpalliwar, Porwal and Upmanyu, 2012).

Due to the basic nature of PPN, its analysis using HPLC was prone to peak tailing and poor peak shape due to column overloading (McCalley, 2010; Sadeghi *et al.*, 2013). Therefore,

the sensitivity of the method was important in ensuring a good peak resolution and efficiency because it limits sample overloading (Sadeghi *et al.*, 2013). The LOQ showing the lowest drug concentration that can be recovered within acceptable limits of precision and accuracy was found to be 2.30 µg/mL, indicating the high sensitivity of the proposed method and its suitability for the detection of PPN in solution at low concentrations. Also, LOD showing the lowest detectable amount of drug distinguishable from the blank was 0.76 µg/mL which also highlights the sensitivity of the method. Hence, the method proposed for the detection of PPN was shown to be suitable for the quantification of low sample concentrations due to its high sensitivity. Summary of the method validation can be found in Table 3.2.

**Table 3.2.** HPLC method validation for PPN showing linearity range, intermediate and intra assay precision, LOD and LOQ

Range (µg/mL)	Linearity (R <sup>2</sup> )	Intermediate precision (RSD) (%)	Intra assay precision (RSD) (%)	LOD (µg/mL)	LOQ (µg/mL)
100 – 0.1	≥ 0.9998	1 µg/mL: 5.60 10 µg/mL: 1.04 50 µg/mL: 0.25 100 µg/mL: 0.33	1 µg/mL: 1.62 10 µg/mL: 0.55 50 µg/mL: 0.09 100 µg/mL: 0.61	0.76	2.30

### 3.2.5.2. Determination of PPN content in MAS-PPN complex particles

Drug recovery from the single and double drug loaded MAS-PPN complex particles was influenced by the dissolution media used (Table 3.3.). Results showed that a higher amount of PPN was recovered by dispersing the MAS-PPN particles in 2M HCl and pH 6.8 buffer compared to ultra-pure water suggesting that the polydispersity of MAS particles was influenced by the increased ions present in the dissolution media (Rojtanatanya and Pongjanyakul, 2010). An increase in the PPN content was also observed in the MAS-PPN double drug loaded complexes suggesting that there were still available binding sites onto MAS after adsorption equilibrium was reached following the single drug loading which allowed further adsorption of PPN particles (Rojtanatanya and Pongjanyakul, 2010). During the analysis there were no impurities or degradants observed on the chromatograms. The

information is of high importance as it can affect the accurate quantification of PPN from MAS–PPN complexes which, in turn, can impact on the formulation of a tablet dosage form.

**Table 3.3.** PPN content in single drug loaded and double drug loaded MAS–PPN complex particles using three different dissolution media: 2M HCl, ultra-pure water (pH 5) and phosphate buffer (pH 6.8)

	Recovered PPN (% w/w)	
	MAS-PPN single drug loaded	MAS-PPN double drug loaded
2M HCl	19.53 ± 0.01*	25.94 ± 0.42*
pH 5.0 Ultra-pure water	9.54 ± 0.14*	16.09 ± 0.57*
pH 6.8 Phosphate Buffer	12.61 ± 0.18*	20.65 ± 0.55*

Note: \*values are reported as the mean ± SD of at least three determinations

### 3.2.6. Small angle X-Ray scattering (SAXS)

#### 3.2.6.1. Solid-state nanometre scale morphology

The samples (MAS and double drug loaded MAS-PPN complexes in powder form (particle size 63 – 125 µm)), were placed in borosilicate glass capillary tubes and the acquisition time and conditions for the analysis were kept the same, hence allowing for comparisons between them (chapter 2, section 2.2.2.6).

2D-SAXS data patterns for MAS and double drug loaded MAS-PPN complexes as recorded by the instrument (Fig 3.13.) were shown to be symmetric and circular, which was due to the analysis of the compounds in powder form (randomly orientated particles). The particles therefore showed no preferred orientation at the nanometre scale. The intensity plots of both MAS and MAS-PPN showing Log {I(a.u.)} vs. q [nm<sup>-1</sup>] had a smooth curve, showing the intensity decreasing from q ≈ 0.099 nm<sup>-1</sup> (at 2θ = 0.14°) at the edge of the beam stop, to q = 2.275 nm<sup>-1</sup> (at 2θ = 3.20°) at the peripheral limit of the detector (Fig. 3.13.). No peaks or other specific features were observed. The scattering intensity of the background was found to be minimal in comparison to the sample scattering intensity (Fig. 3.13.). The background subtraction was therefore considered unnecessary. However, data was corrected for transmission through the calculation on the transmission factor using glassy carbon.

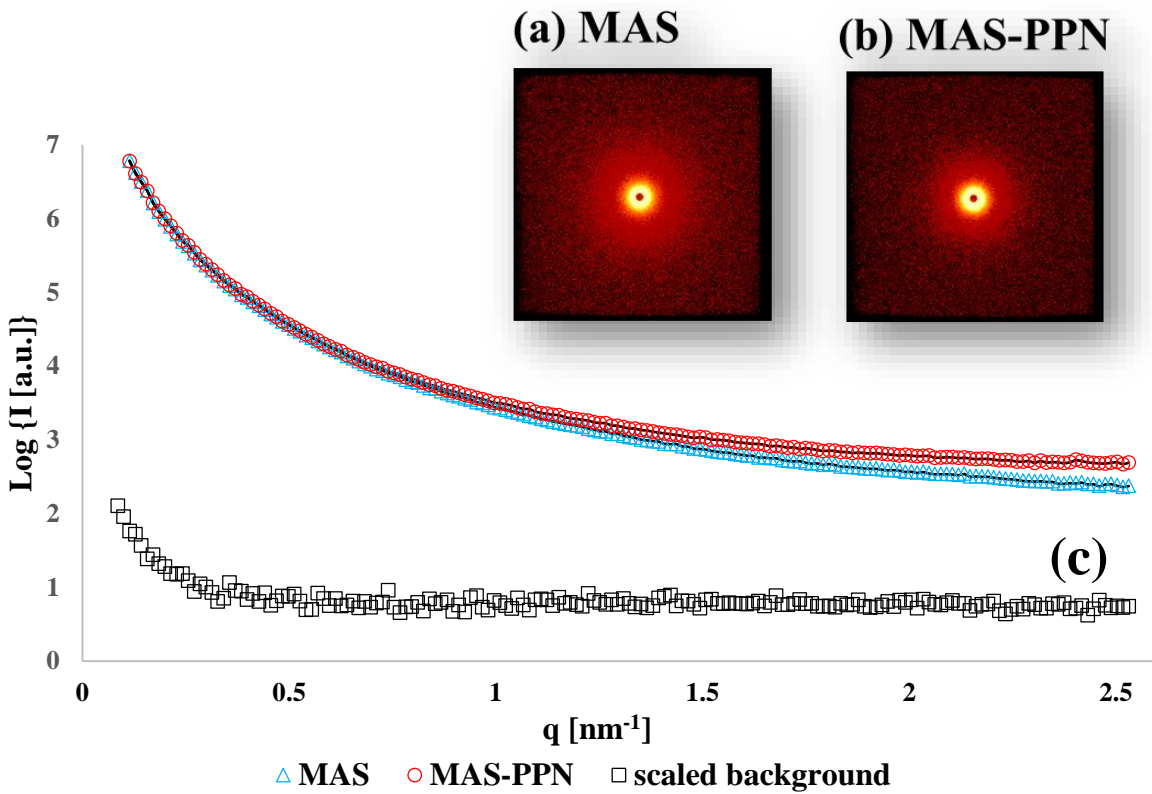


**Fig. 3.13.** Typical SAXS data for specimens in powder form: (a and b) 2D-SAXS patterns for MAS and MAS-PPN complexes showing the centre of the beam stop; (c) 1D-SAXS intensity curves for MAS and MAS-PPN complexes (open symbols showing uncorrected data and line showing data after scaled background subtraction), and scaled background (open black square symbols)

The analysis of the data in the form of a double logarithmic plot of intensity ( $\log I$  [a.u.]) vs. the scattering vector ( $\log \{q\}$  [ $\text{nm}^{-1}$ ])) for both MAS and MAS-PPN complexes followed straight lines with no peaks or other specific features (Fig. 3.14.). The straight lines indicate power-law scattering behaviour, which can be described using Eq. 3.2.

$$I(q) = I_0 q^{-\alpha} \quad \text{Eq. 3.2.}$$

where  $I_0$  and  $\alpha$  are constants.  $I_0$  depends on multiple factors such as collection time, incident X-ray intensity, strength of scattering etc. and  $\alpha$  is the power-law constant that can be calculated from the slope of the linear part of the double-logarithmic plot of intensity vs. the

scattering vector. A slope of  $-3.63$  was obtained for MAS, and a slightly different slope of  $-3.57$  was obtained for the MAS-PPN complex particles.

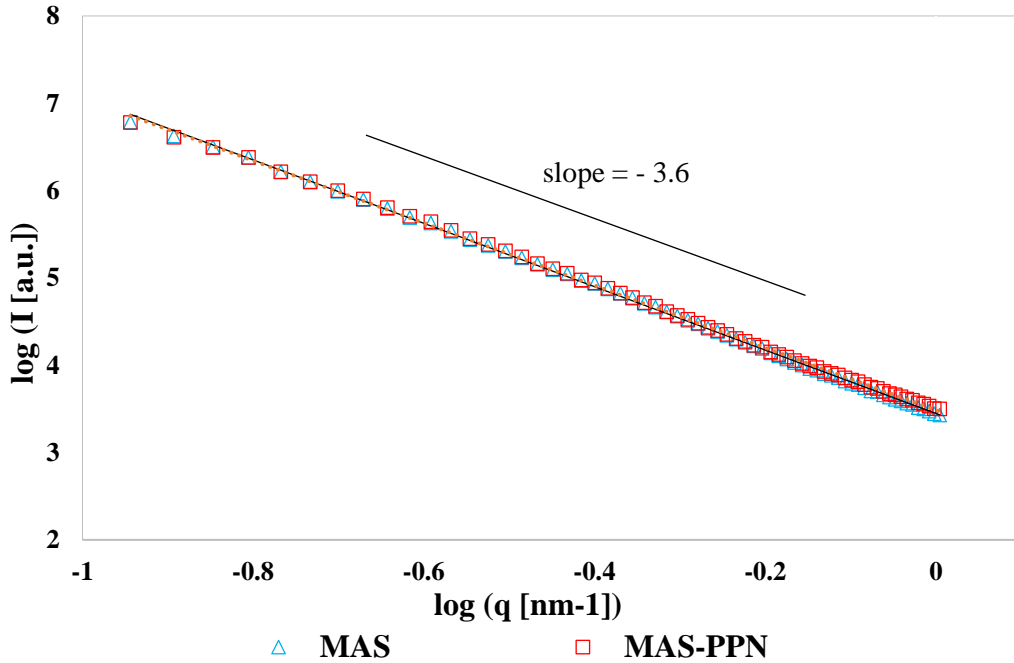


**Fig. 3.14.** Double-logarithmic plot of intensity vs. the scattering vector for MAS and MAS-PPN complexes in powder form (particle size  $63 - 125 \mu\text{m}$ ), showing the slope of the linear part for the data which allows the calculation of the power-law constant  $a$  as  $-3.63$  for MAS and  $-3.57$  for MAS-PPN complexes

The value of  $a$  depends on sample morphology and allows the determination of mass and surface fractal dimensions ( $D_m$  and  $D_s$  respectively). Fractal geometry is applied to simplify the interpretation of the scattering effects from complex and disordered structures.

For mass and surface fractals the following conditions must be obeyed by  $\alpha$ :

$$\alpha = D_m \text{ and } 0 < D_m < 3 \quad \text{Eq. 3.3.}$$

or

$$\alpha = 6 - D_s \text{ and } 2 < D_m < 3 \quad \text{Eq. 3.4.}$$

Hence, upon calculation, a surface fractal dimension value ( $D_s$ ) of 2.37 and 2.43 was obtained for MAS and MAS-PPN complexes respectively, indicating that both samples tested had surface fractals over a length scale of 0.1 nm to 1.0 nm. The values obtained indicate an irregular, rough and space filling surface with the surface of MAS ( $D_m = 2.37$ ) being relatively smoother compared to the surface of MAS-PPN complexes ( $D_m = 2.43$ ). This may be an indication of PPN being intercalated, although this assumption however would be hard to demonstrate as other factors may contribute to slight differences between samples (such as hydration).

The  $\alpha$  value obtained for MAS in this study is higher than that reported in a similar study published by Laity et. al. in 2014, showing  $\alpha \approx 3$ . The difference in results shows a difference in structure, most probably due to the different type of MAS used (clay granules vs. fine powder used in present study) (Laity *et al.*, 2015). However, a surface fractal dimension  $D_s$  value close the one obtained in this study was obtained for montmorillonite in a study published in 2007 by De Stefanis *et al.* (De Stefanis *et al.*, 2007). The authors used small angle neutron scattering (SANS) to determine the fractal dimension and found that montmorillonite had a surface fractal of 2.60, which implies a rough and irregular surface. Similar results were also obtained in a study published in by Pernyeszi and Dékány in 2003, where the authors reported a surface fractal dimension of 2.78 for montmorillonite using SAXS (Pernyeszi and Dékány, 2003).

The results presented in these studies hence implies the fact that MAS, which is a mixture of montmorillonite and saponite clays, has a rough and irregular morphology at nanometre scale. Furthermore, the MAS-PPN complex was also shown to have a rough and irregular nanometre scale morphology, being only slightly different from that of MAS.

### 3.2.6.2. Liquid-state nanometre scale morphology

Data acquired for the MAS dispersion and the flocculated complexes formed between MAS and PPN, was represented using a Guinier plot ( $\log(I)$  vs.  $q^2$ ). For both the MAS and the flocculated MAS-PPN complexes, the shape of the curves did not follow a linear dependence over the whole range of  $q$ . Furthermore, a careful observation of the graphs shows two linear

regions separated by a transition region (Fig. 3.15.). This behaviour suggests a polydisperse system in which cluster size is variable.  $q$  indicates structural characteristics, hence, the larger slope values in the higher  $q$  range compared to the lower  $q$  range indicated more scattering at higher  $q$  values (Odo *et al.*, 2015). This suggests the presence of large cluster aggregates in the samples. No peaks or other specific features were observed.

Similar SAXS profiles to those obtained in this study were also reported in a publication by Rice and Lin (Shang, James A. and Jar-shyong, 2001). The authors focused on analysing the basal distance for colloidal montmorillonite at various concentrations and for illite using an indirect Fourier transform.

Due to the large size of clay particles which may exceed 80 nm (near the limit of the SAXS instrument), the basal distance of clays can be calculated instead of the true dimension of the particles (Shang, James A. and Jar-shyong, 2001). Using the Guinier plot, the slope of the best linear fit to the regions of lower  $q$  values allows the calculation of the radius of gyration for thickness  $R_g$ . The radius of gyration can be calculated only in the low  $q$  region because Guinier plot is valid in the range where  $qR_g$  is lower than unity (Li, Senesi and Lee, 2016). Due to the polydispersity of the MAS and MAS-PPN dispersions, the thickness  $R_g$  could not be determined accurately. The results of the thickness  $R_g$  calculated from the Guinier plot may contain high errors due to the resolution of the technique which involves the selection of a linear region (Shang, James A. and Jar-shyong, 2001).

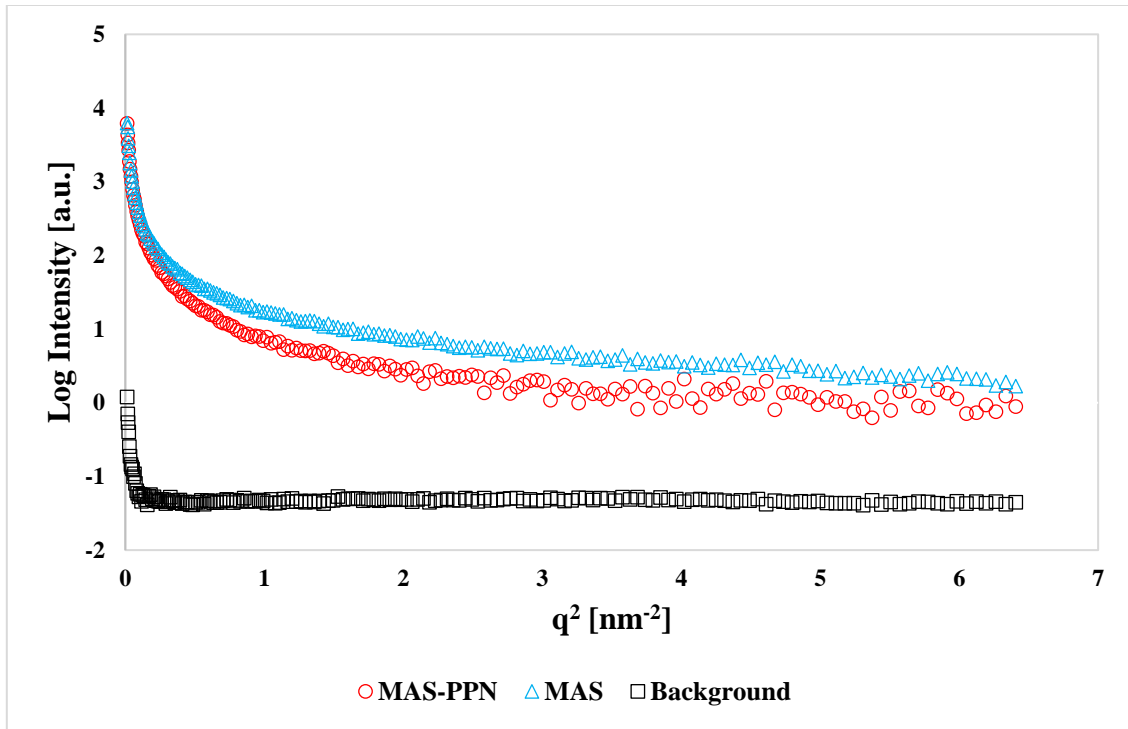


**Fig. 3.15.** Guinier plot of MAS dispersion and MAS – PPN complex dispersion showing two linear regions in the high and low  $q$  values

The analysis of the data in the form of double logarithmic plot of intensity ( $\log I$  [a.u.]) vs. the scattering vector ( $\log \{q\} [\text{nm}^{-1}]$ ) for both MAS dispersion and MAS-PPN flocculates followed straight lines with no peaks or other specific features, indicating power-law scattering behaviour (Fig. 3.16.).

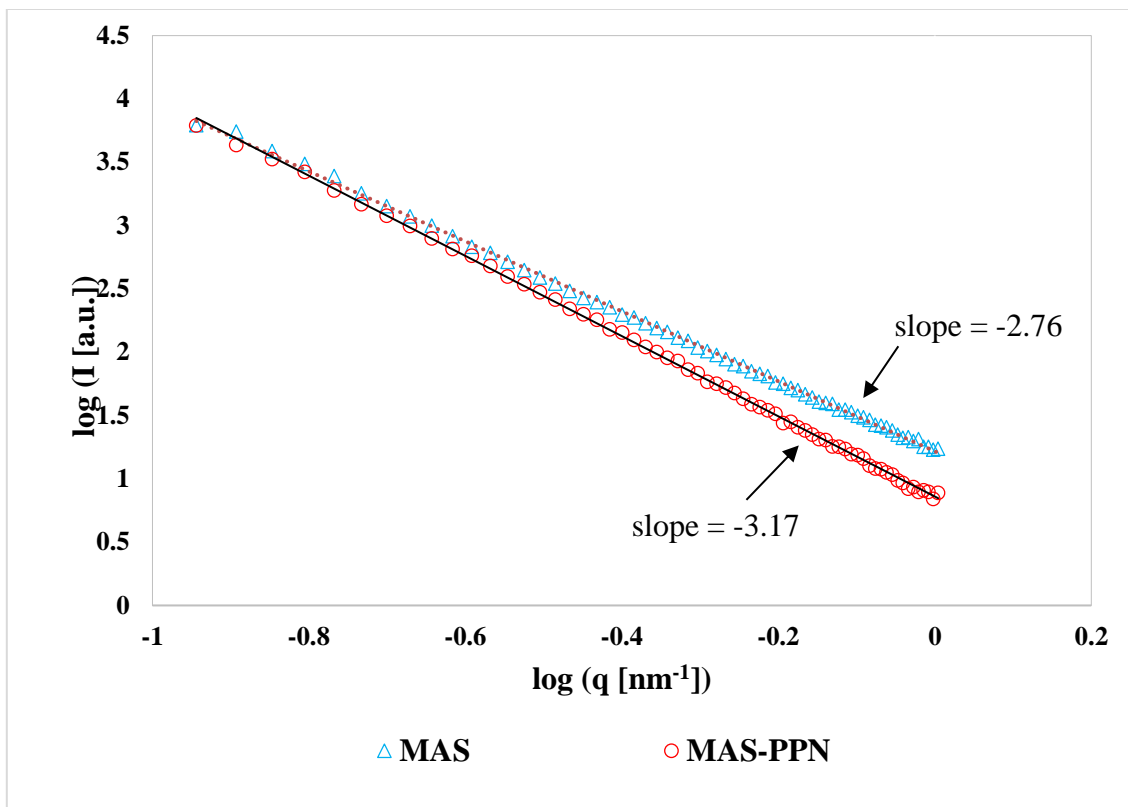


**Fig. 3.16.** Double-logarithmic plot of intensity vs. the scattering vector for MAS and MAS-PPN complexes in liquid form, showing power law behaviour

A slope of  $-2.76$  was obtained for MAS dispersion, while a considerably different slope of  $-3.17$  was obtained for the MAS-PPN complex dispersion. The difference in results shows a difference in structure, with the MAS-PPN complex dispersion having a more complex structure. This behaviour was expected since the MAS flocculated upon the addition of the PPN solution.

### 3.2.7. Microscopy

The observation of the MAS dispersion and MAS-PPN flocculates prepared as described in chapter 2, section 2.2.1 under a light microscope showed that upon the addition of the PPN solution to the MAS dispersion, precipitates formed. The MAS dispersion was formed of dispersed particles (Fig. 3.17.) compared to the flocculates which were shown to be aggregated in large clusters (Fig. 3.18.).

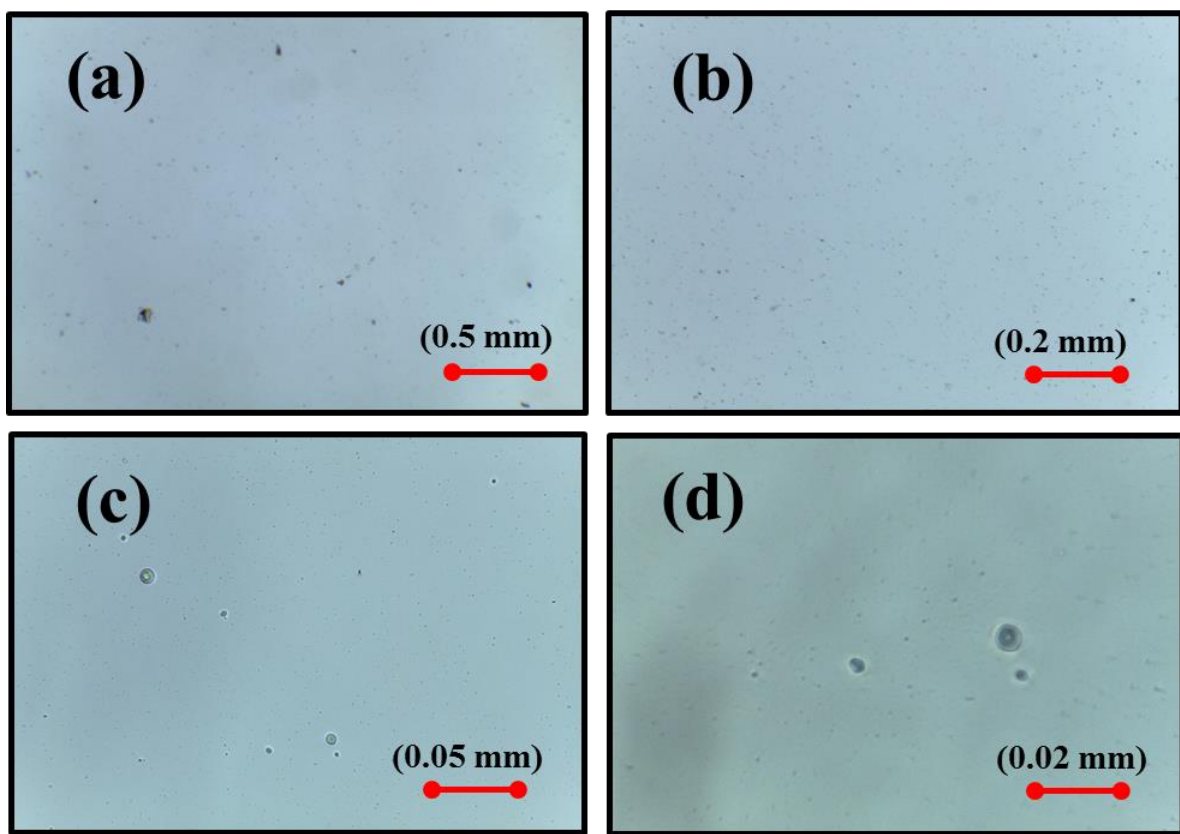


**Fig. 3.17.** Microscopy images of dilute MAS dispersion (0.037 % w/v) in purified water (pH 5) at different magnifications ( $\times 4$ ,  $\times 10$ ,  $\times 40$  and  $\times 100$ )

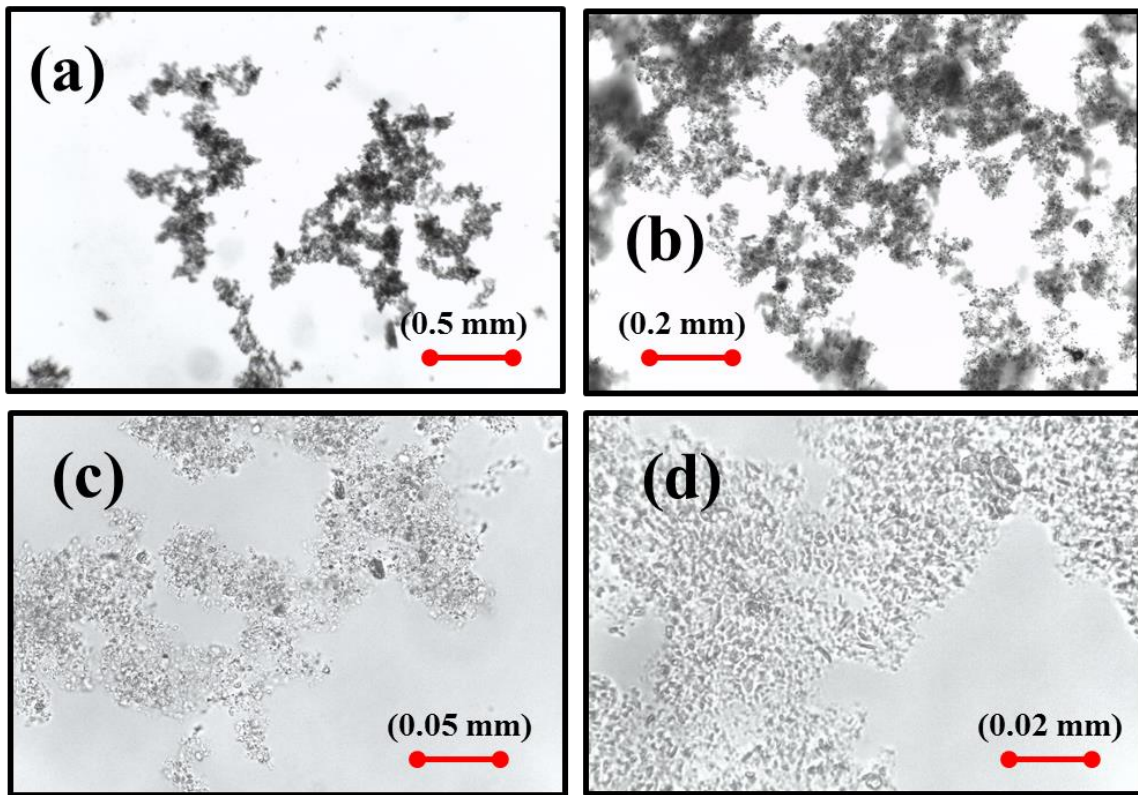


**Fig. 3.18.** Microscopy images of single drug loaded MAS-PPN complex dispersion prepared using purified water (pH 5) at different magnifications ( $\times 4$ ,  $\times 10$ ,  $\times 40$  and  $\times 100$ )

### 3.2.8. Calorimetric binding studies

#### 3.2.8.1. Calorimetric single injection mode (SIM) binding studies between MAS and PPN

SIM ITC experiments performed on the VP-ITC allowed for fast titration experiments that confirmed the adsorption of PPN onto MAS. SIM experiments showed that the adsorption process was highly exothermic and more energetic as pH became more acidic, shown by the peak returning more rapidly to the baseline (Fig. 3.19.). This can be related to the ionisation of the drug (pka 9.5) (Shalaeva *et al.*, 2007; Rojtanatanya and Pongjanyakul, 2010; *ACD I-Lab*, 2018). PPN is considered to be present in solution in its ionised form at pH 5, but its ionisation reduces gradually at pH 7 and considerably as the pH is further increased (*ACD I-Lab*, 2018). This implies different physicochemical reactions taking place between MAS

and PPN depending on the drug ionisation in aqueous solution. Furthermore, MAS polydispersity may be affected by the ions in the solution which, in turn, can affect the rate of adsorption of PPN onto MAS (Rojtanatanya and Pongjanyakul, 2010).

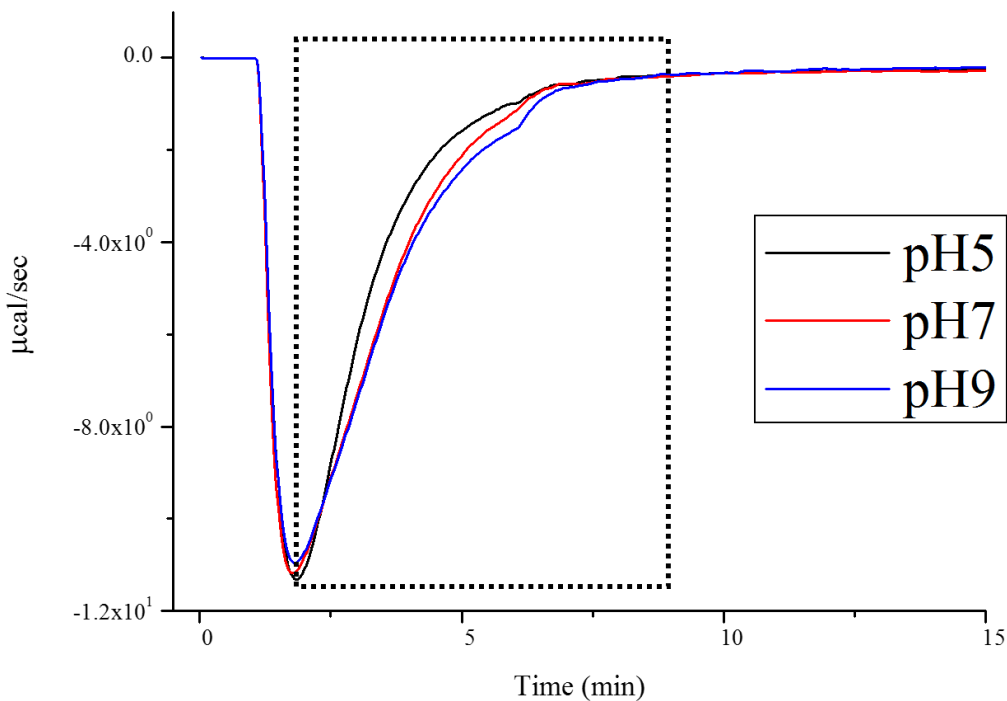


**Fig. 3.19.** SIM titration of PPN solution into MAS dispersion at pH 5 (black), pH 7 (red) and pH 9 (blue) (25 °C). The return to the baseline highlighted in black is used determine the most rapid interaction. Results are based on three independent repeats done under similar conditions.

The analysis of the return to the baseline in the SIM experiments through one set of sites curve fitting using a non-linear least squares model allowed the observation of behaviour of adsorption of PPN onto MAS with varying pH (Fig. 3.20. and Table 3.4.).

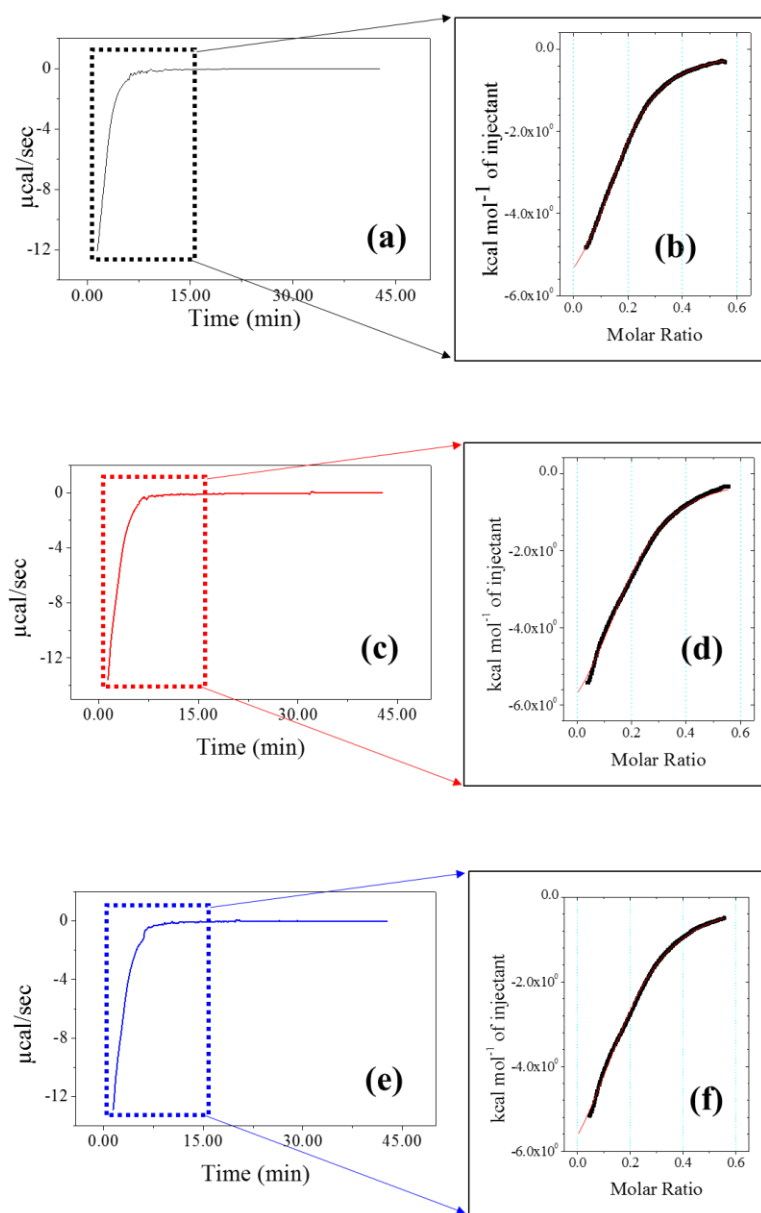


**Fig. 3.20.** SIM calorimetric binding studies evaluating the adsorption of PPN onto MAS at pH 5 (a), pH 7 (c) and pH 9 (e) ( $25^\circ\text{C}$ ). Data analysed through one set of sites curve fitting showing the enthalpy change ( $\text{kcal mol}^{-1}$  of injectant) obtained from injecting PPN (0.150 % w/v) into MAS (0.037 % w/v). Results are based on three independent repeats done under similar conditions.

In all cases, the overall change in enthalpy was found to be exothermic with a comparatively small entropic contribution to the total change in Gibbs free energy. These findings firstly imply that the binding phenomenon was predominantly enthalpically driven as high energy

resulted from broken and created hydrogen bonds and electrostatic interactions. Secondly the similarity in values implies that pH did not affect the thermodynamics of the binding process. The binding affinity ( $K_a$ ) gradually decreased with varying pH (Table 3.4.) suggesting that at pH 5 the adsorption process was more energetic and the conditions for the reaction were at optimum.

**Table 3.4.** SIM calorimetric binding studies evaluating the adsorption of PPN onto MAS at pH 5, 7 and pH 9 (25 °C). Data analysed through one set of sites curve fitting using a non-linear least squares model to calculate affinity (K), changes in enthalpy ( $\Delta H$ ), entropy( $\Delta S$ ) or Gibbs free energy ( $\Delta G$ ). Results are based on three independent repeats done under similar conditions.

	pH 5	pH 7	pH 9
<b>K<sub>a</sub></b> (M)	2.22E+04 ± 0.00	1.67E+04 ± 1.91E+03	1.07E+04 ± 2.52E+03
<b>ΔG</b> (kcal/ mol)	-5.46 ± 0.19	-5.48 ± 0.05	-5.87 ± 0.12
<b>ΔH</b> (kcal/ mol)	-7.62 ± 0.96	-7.33 ± 0.38	-8.20 ± 0.56
<b>-TΔS</b> (kcal/ mol)	2.16 ± 0.71	1.85 ± 0.96	2.33 ± 1.76

The ITC data is thus in agreement with previously published results showing that the adsorption of PPN onto MAS is enthalpically driven and entropically unfavourable suggesting hydrogen bonding and electrostatic interactions to dominate the interactions (Rojtanatanya and Pongjanyakul, 2010; Pongjanyakul and Rojtanatanya, 2012).

### 3.2.8.2. Calorimetric multiple injection mode (MIM) binding studies between MAS and PPN

Multiple injection experiments at pH 5 and at two different temperatures (25 and 37 °C) further confirmed the highly exothermic interaction between PPN and MAS (Fig. 3.21.), as observed in the SIM ITC experiments. The MIM stepwise experiments however gave

detailed and more accurate information about the driving forces involved in the adsorption process compared with the SIM experiments. In agreement with previous SIM experiments, binding was characterised by a negative enthalpy change, and a comparatively small entropy change, i.e. implying that it was an enthalpically driven process (Fig. 3.21.). The adsorption process of PPN onto MAS was shown to be similar at both 25 and 37 °C.

Control binding studies between water at pH 5 and either MAS dispersion (pH 5) or PPN solution (pH 5) showed very little evidence of binding/self-association through small heats of dilution (Fig. 3.21. a and b).

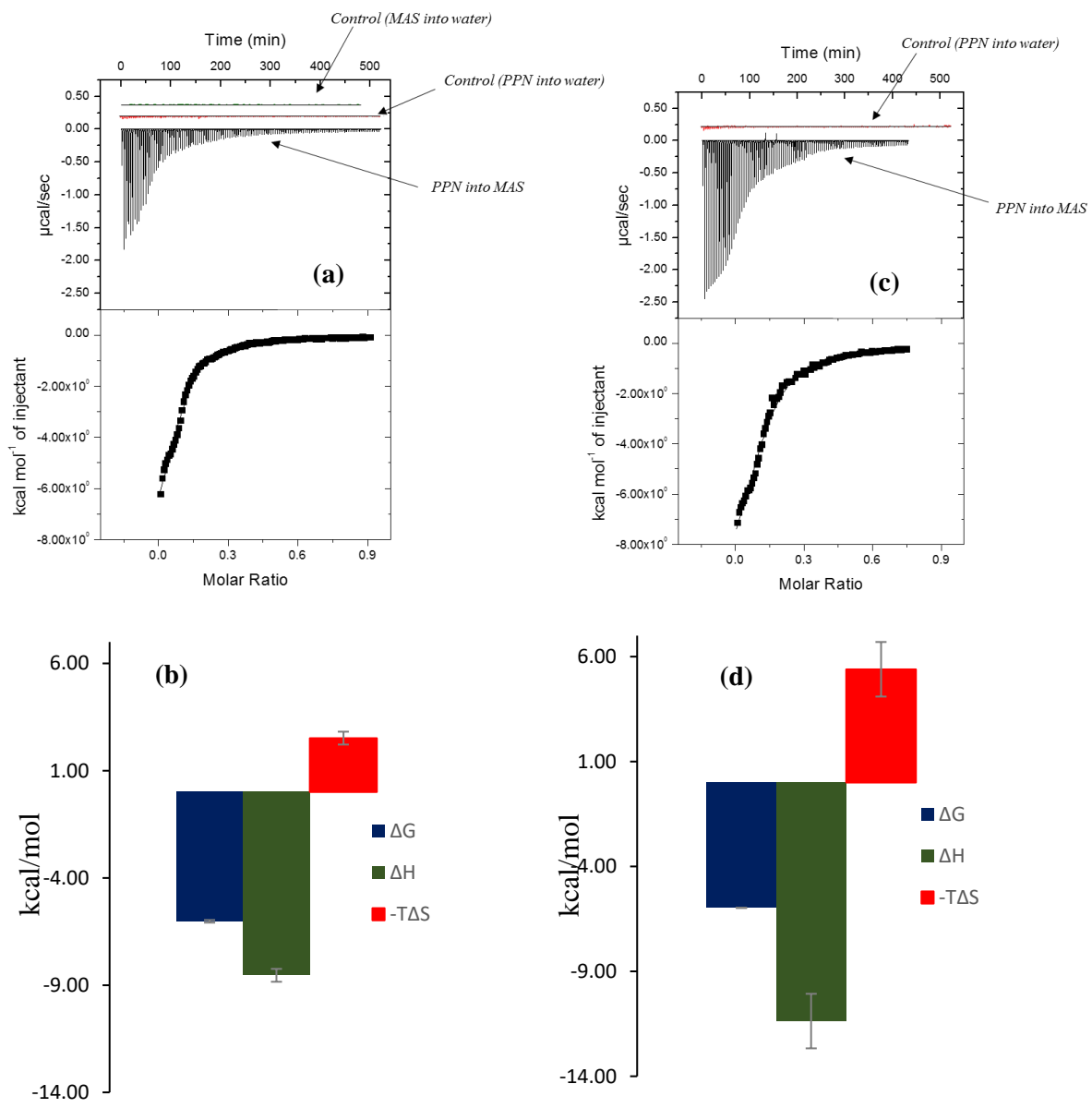


**Fig. 3.21.** Multiple injection mode calorimetric titration of 0.150 % w/v PPN solution (pH 5) into 0.037 % w/v MAS dispersion (pH 5) at 25 °C (a) and 37 °C (c). Raw data (top) and integrated heats (bottom) as a function of molar ratio. Control runs suggesting limited interaction between water and PPN or MAS; Thermodynamic profile for binding of PPN onto MAS at 25 °C (b) and 37 °C (d) showing enthalpy ( $\Delta H$ ), entropy( $\Delta S$ ) or Gibbs free energy ( $\Delta G$ ). Results are based on three independent repeats done under similar conditions.

The increase in temperature slightly decreased the affinity of PPN with MAS as observed from the reduction of the association constant  $K_a$  ( $2.61E+04 \pm 2.71E+03$  M at  $25^\circ\text{C}$  and  $1.48E+04 \pm 1.48E+03$  M at  $37^\circ\text{C}$ ). The overall change in Gibbs free energy ( $\Delta G$ ) was comparatively similar at both temperatures ( $-6.03 \pm 0.06$  kcal/mol at  $25^\circ\text{C}$  compared with  $-5.97 \pm 1.37$  kcal/mol at  $37^\circ\text{C}$ ), confirming both reactions occurred spontaneously. The enthalpic contribution calculated from the change in heat associated with binding was greater at  $37^\circ\text{C}$  ( $-11.37 \pm 1.36$  kcal/mol compared with  $-8.54 \pm 0.32$  kcal/mol at  $25^\circ\text{C}$ ), while the entropic contribution was comparatively small in both cases confirming the interaction to be enthalpically driven at both temperatures.

**Table 3.5.** Multiple injection mode calorimetric binding studies evaluating the adsorption of PPN onto MAS at  $25$  and  $37^\circ\text{C}$  (pH 5). Data analysed through one set of sites curve fitting using a non-linear least squares model to calculate affinity (K), changes in enthalpy ( $\Delta H$ ), entropy( $\Delta S$ ) or Gibbs free energy ( $\Delta G$ ). Results are based on three independent repeats done under similar conditions.

	<b>25 °C</b>	<b>37 °C</b>
<b><math>K_a</math></b> (M)	$2.61E+04 \pm 2.71E+03$	$1.48E+04 \pm 1.48E+03$
<b><math>\Delta G</math></b> (kcal/ mol)	$-6.03 \pm 0.06$	$-5.97 \pm 1.37$
<b><math>\Delta H</math></b> (kcal/ mol)	$-8.54 \pm 0.32$	$-11.37 \pm 1.36$
<b><math>-T\Delta S</math></b> (kcal/ mol)	$2.52 \pm 0.35$	$5.40 \pm 0.01$

The binding interaction had a negative heat capacity  $\Delta C_p$  ( $-0.24$  kcal mol  $K^{-1}$ ) indicating that upon increasing temperature the binding became more exothermic and enthalpically driven, thus in agreement with the binding parameters calculated.

### 3.2.8.3. Effects of PEO on the adsorption of PPN onto MAS

#### 3.2.8.3.1. Binding between MAS and PEO

The interaction between MAS and PEO at 25 and 37 °C showed different heat patterns. The exothermic non-constant heats and non-sigmoidal curve suggest that PEO can weakly bind to MAS (Gao, 2004).

The binding isotherm at 25 °C (Fig. 3.22. a) showed non-constant heats at the end of titration in the presence of excess PEO. This could be due to the aggregation of PEO-MAS complexes or a contribution of the PEO or MAS self-aggregation in water at pH 5. Aggregation is a random process that can contribute to the experimental heat measured by the calorimeter and compete with the binding process (Velazquez-Campoy and Freire, 2006). The increase in temperature was shown to reduce aggregation. This was suggested by the constant ITC heat signals at the end of MAS titration with excess PEO at 37 °C (Fig. 3.22. b).

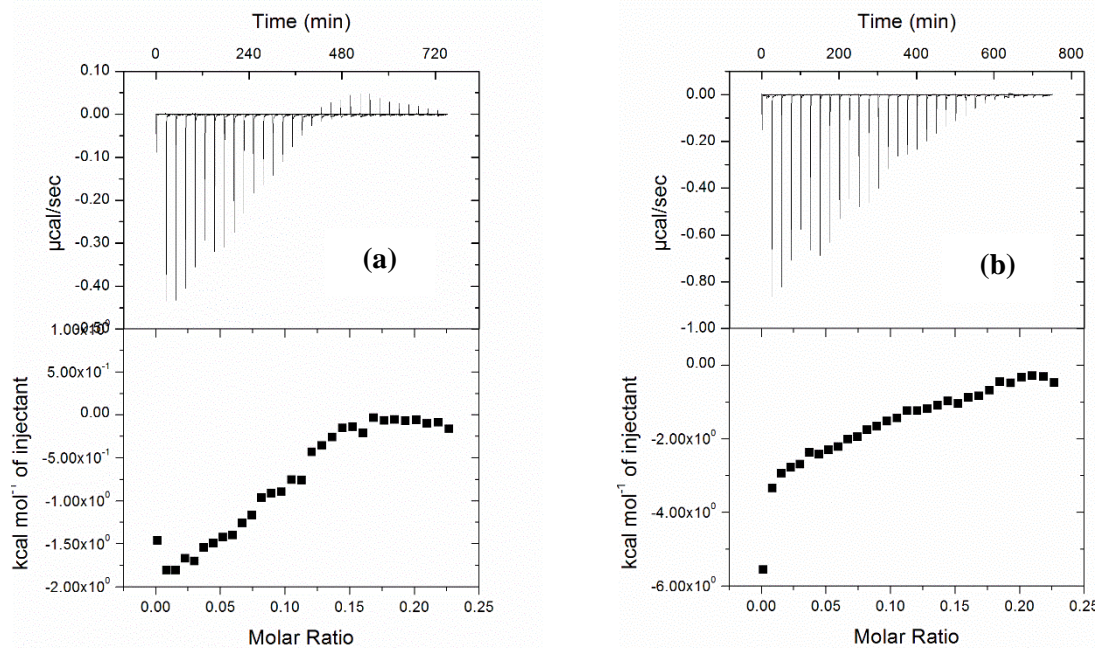


**Fig. 3.22.** Titration of 0.037 % w/v PEO dispersion (pH 5) into 0.037 % w/v MAS dispersion (pH 5) at 25 °C (a) and 37 °C (b). Raw data (top) and integrated heats (bottom) as a function of molar ratio.

A further investigation of PEO dilution into water at pH 5 (25 °C) (Fig. 3.23. a) showed a monotonous decrease of ITC heat signals without a sigmoidal behaviour, suggesting that PEO self-associates weakly in aqueous solution. PEO aggregates coexist with PEO unimers in aqueous solution (Dai and Tam, 2005). Due to its amphiphilic structure (hydrophobic backbone and hydrophilic side groups), PEO may show a tendency to self-aggregate in aqueous solution, even at a low concentration. Constant dilution heats were however observed for MAS dilution into water, showing no aggregation behaviour for MAS in water at pH 5 (25 °C) (Fig. 3.23. b).

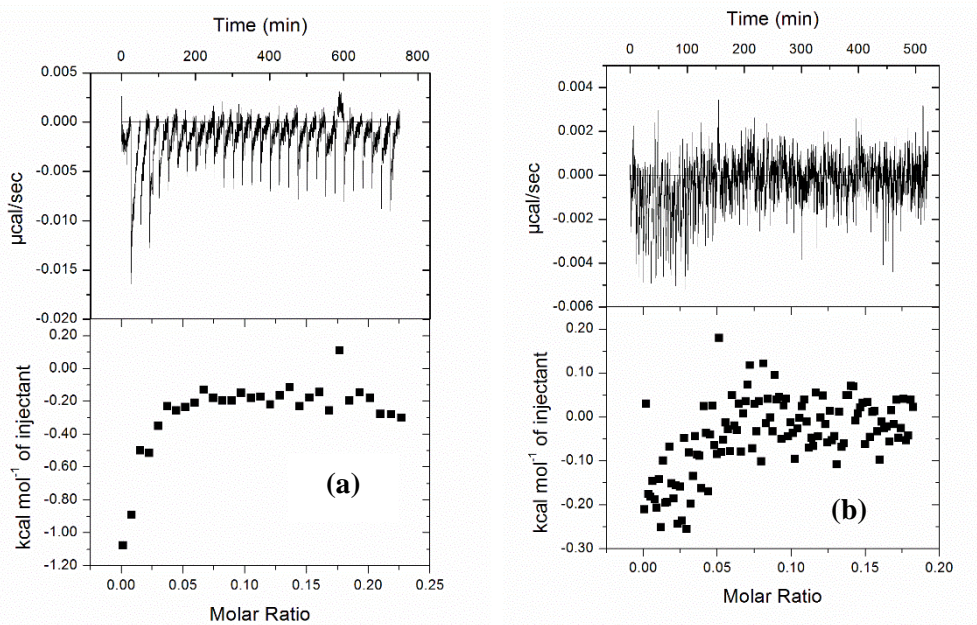


**Fig. 3.23.** (a) Titration of 0.037 % w/v PEO dispersion (pH 5) into water (pH 5) at 25 °C; (b) Titration of water (pH 5) into 0.037 % w/v MAS dispersion (pH 5) at 25 °C. Raw data (top) and integrated heats (bottom) as a function of molar ratio

The data above therefore suggests that PEO can intercalate between the MAS particles, and hence, a model may be proposed (Fig. 3.24.).

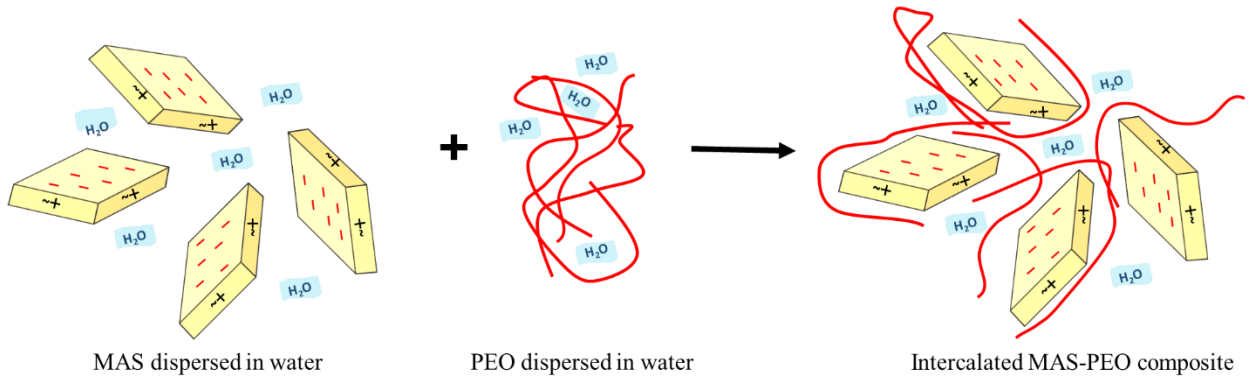


**Fig. 3.24.** Scheme of MAS-PEO intercalated composite formation using MAS dispersed in water and PEO dispersed in water: adapted from (Gao, 2004). Note: Red lines are PEO polymer

### 3.2.8.3.2. Binding between PPN and PEO

Experiments conducted at pH 5 and 25 °C, showed constant dilution heats, and hence no interaction occurring between PPN and PEO (Fig. 3.25.). The same behaviour was reported by Palmer et. al in 2013 in analysing controlled drug release through synergistic interactions between two PEO and NaCMC (Palmer *et al.*, 2013).

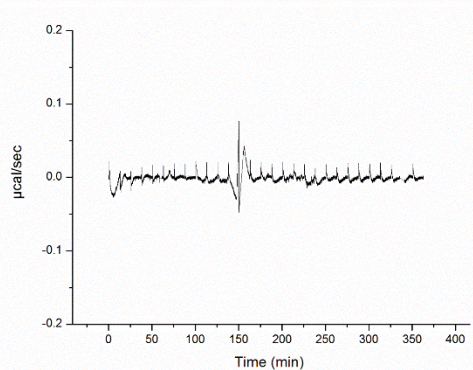


**Fig. 3.25.** Titration of PPN solution (pH 5) into PEO dispersion (pH 5) at 25 °C

### **3.2.8.3.3. PPN adsorption onto MAS-PEO complex**

Multiple injection stepwise experiments at pH 5 allowed the observation of the binding between PPN (0.150 % w/v) and MAS-PEO mixture (0.037 % w/v MAS; 0.037 % w/v PEO). The binding was highly exothermic at the two different temperatures studied (25 and 37 °C) and was characterised by a negative enthalpy change ( $\Delta H$ ) (-12.44 ± 0.10 kcal/mol at 25 °C and -10.68 ± 0.19 kcal/mol at 37 °C) and a positive entropy change (-T $\Delta S$ ) (5.99 ± 0.47 kcal/mol at 25 °C and 3.59 ± 0.23 kcal/mol at 37 °C), suggesting that the process was enthalpy driven and entropically unfavourable, as high energy resulted from broken and created hydrogen bonds as well as electrostatic van der Waals interactions.

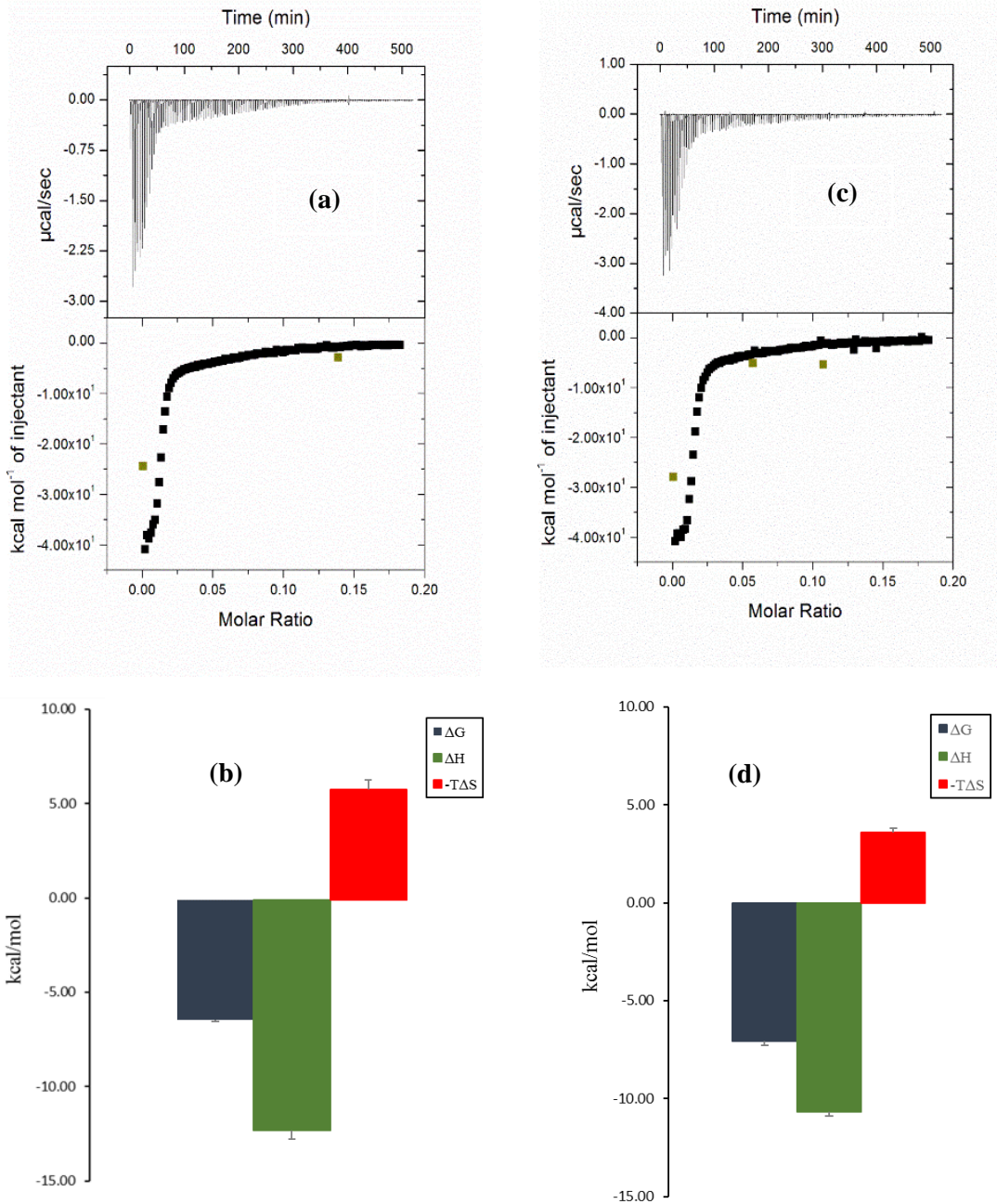


**Fig. 3.26.** Titration of 0.150 % w/v PPN solution (pH 5) into MAS-PEO mixture (0.037 % w/v MAS; 0.037 % w/v PEO; pH 5) at 25 °C (a) and 37 °C (c). Raw data (top) and integrated heats (bottom) as a function of molar ratio; Thermodynamic profile for adsorption of PPN onto MAS-PEO complex at 25 °C (b) and 37 °C (d) showing enthalpy ( $\Delta H$ ), entropy( $\Delta S$ ) or Gibbs free energy ( $\Delta G$ ). Results are based on three independent repeats done under similar conditions.

The change in temperature did not have a great impact on PPN adsorption onto MAS-PEO mixture. Gibbs free energy ( $\Delta G$ ) was approximately identical for PPN titration into MAS-PEO mixture at both temperatures ( $-6.46 \pm 0.52$  kcal/mol at 25 °C and  $-7.09 \pm 0.18$  kcal/mol at 37 °C), suggesting that both reactions occurred spontaneously (Table 3.25.). The enthalpic contribution ( $\Delta H$ ) was however greater at 25 °C ( $-12.44 \pm 0.10$  kcal/mol compared to  $-10.68 \pm 0.19$  kcal/mol at 37 °C), while the entropic contribution was slightly lower at 37 °C ( $3.59 \pm 0.23$  kcal/mol compared to  $5.99 \pm 0.47$  kcal/mol at 37 °C), indicating that the interaction was less enthalpy driven at 37 °C. The increase in temperature led to a gradual increase in the binding affinity ( $K_a$ ) between PPN and MAS-PEO mixture at 37 °C ( $5.37E+04 \pm 7.54E+03$  M at 25 °C compared to  $8.63E+04 \pm 6.11E+03$  M at 37 °C).

**Table 3.6.** The binding parameters (affinity, free energy, binding enthalpy and entropy factor) for PPN solution (0.150 % w/v) titration into a MAS and PEO mixture (0.037 % w/v MAS; 0.037 % w/v PEO) at 25 and 37 °C (pH 5).

	25 °C	37 °C
<b><math>K_a</math></b> (M)	$5.37E+04 \pm 7.54E+03$	$8.63E+04 \pm 6.11E+03$
<b><math>\Delta G</math></b> (kcal/ mol)	$-6.46 \pm 0.52$	$-7.09 \pm 0.18$
<b><math>\Delta H</math></b> (kcal/ mol)	$-12.44 \pm 0.10$	$-10.68 \pm 0.19$
<b><math>-T\Delta S</math></b> (kcal/ mol)	$5.99 \pm 0.47$	$3.59 \pm 0.23$

Differences between PPN adsorption onto MAS, compared to PPN adsorption onto MAS-PEO mixture were observed (Table 3.4. compared to Table 3.6.), which are most likely due to the addition of the PEO polymer to the reaction. At both temperatures studied the binding affinity ( $K_a$ ) was greater for the titration of PPN into the MAS-PEO mixture ( $5.37E+04 \pm 7.54E+03$  M at 25 °C and  $8.63E+04 \pm 6.11E+03$  M at 37 °C), compared to the affinity obtained upon binding between PPN and MAS ( $2.61E+04 \pm 2.71E+03$  M at 25 °C and  $1.48E+04 \pm 1.48E+03$  M at 37 °C), suggesting a stronger binding. Studies showed no interaction between PEO and PPN. However, MAS and PEO binding was confirmed, which may imply that some of the sites available onto the clay for PPN adsorption would have been saturated with PEO during the preparation of the MAS-PEO mixture prior to the injection

of PPN. Hence, PEO binding onto the clay may interfere with the amount of PPN adsorbed onto MAS and with the strength of the binding. This may potentially impact on PPN release from tablets made of MAS-PPN complex particles and PEO (added as physical mixture) as the polymer may saturate available sites onto the clay preventing the drug to be readsorbed once released.

Based on the findings concerning the binding reactions taking place between MAS, PPN and PEO, a reaction scheme may be proposed, allowing a formulator to understand factors that may influence dissolution from PEO matrices containing MAS and PEO (Fig. 3.27).

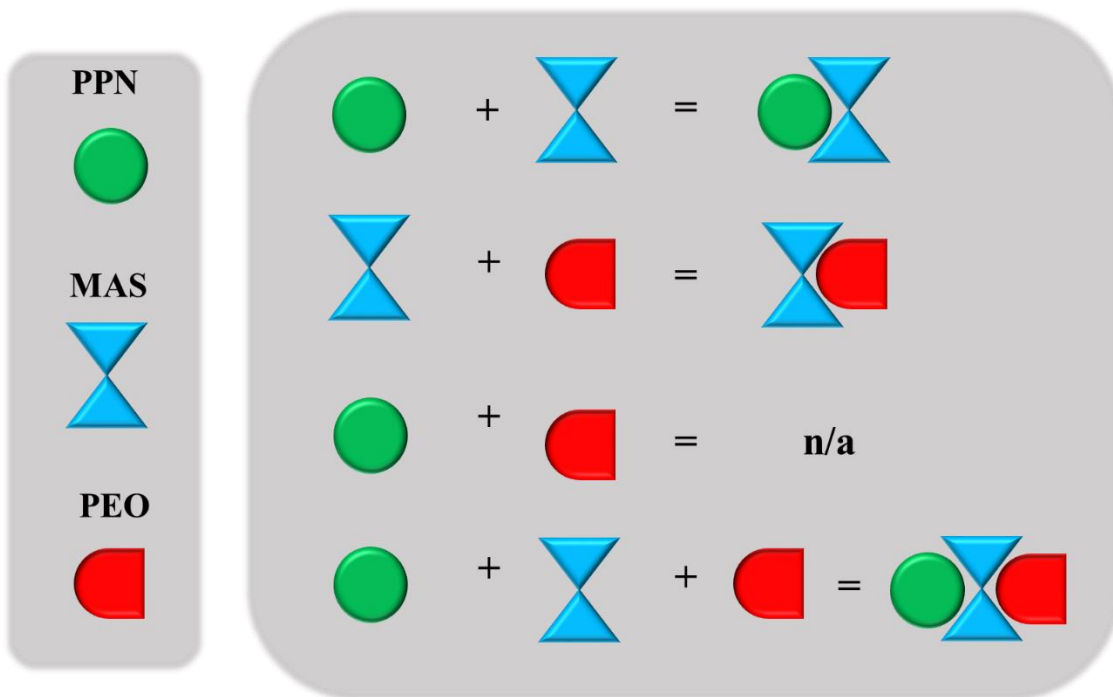


**Fig. 3.27.** Schematic representation using shapes of possible chemical interactions between PPN, MAS and PEO based on isothermal titration calorimetry results

### 3.2.8.4. Effects of XG on the adsorption of PPN onto MAS

#### 3.2.8.4.1. Binding between MAS and XG

Following the titration of XG dispersion into the MAS dispersion, no interactions were observed between the anionic polysaccharide and the negatively charged MAS. The mixture

between MAS and XG was shown to be homogenous with no precipitation being observed in the calorimetric cell at the end of the experiment (Vanderbilt Minerals, 2009).

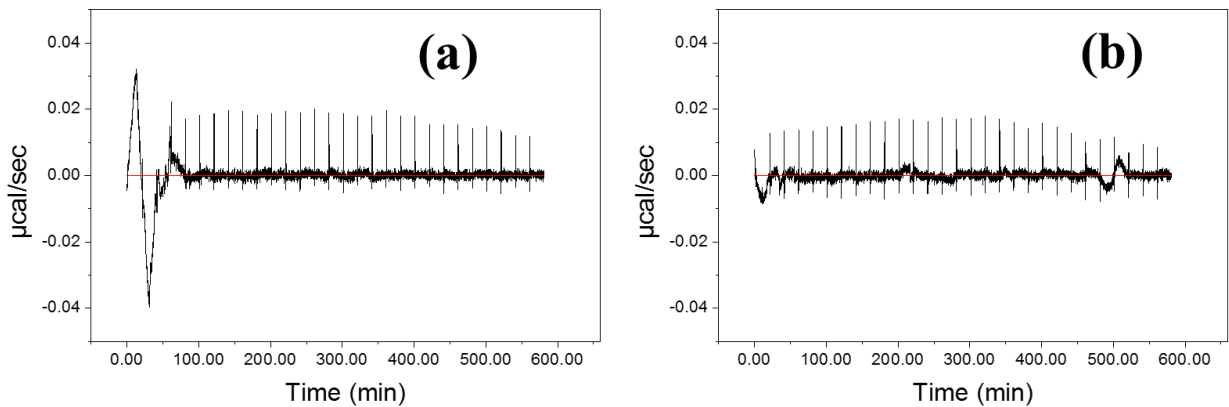


**Fig. 3.28.** Raw data for titration of 0.020 % w/v XG dispersion (pH 5) into 0.037 % w/v MAS dispersion (pH 5) at 25 °C (a) and 37 °C (b). Results are based on three independent repeats done under similar conditions.

The lack of interaction between XG and MAS may lead to very few polymer segments being adsorbed possibly at the platelet edges, with very long polymer tails suspended in solution (Fig. 3.29.) (Vanderbilt Minerals, 2014).

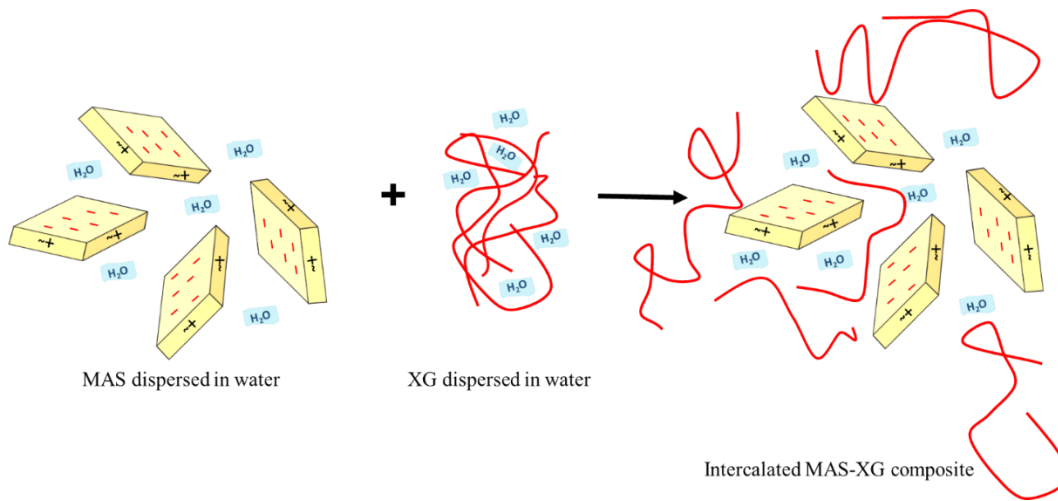


**Fig. 3.29.** Scheme of MAS-XG composite formation using MAS dispersed in water and PEO dispersed in water: adapted from (Gao, 2004). Note: Red lines are XG polymer

### 3.2.8.4.2. Binding between PPN and XG

Binding was observed between PPN (0.150 % w/v) and XG (0.020 % w/v), which was expected considering nature of the compounds, cationic PPN and anionic XG which makes them compatible for intermolecular interactions. Control binding studies between water at pH 5 and XG dispersion at pH 5 showed very little evidence of binding/self-association through small heats of dilution (Fig. 3.30.).

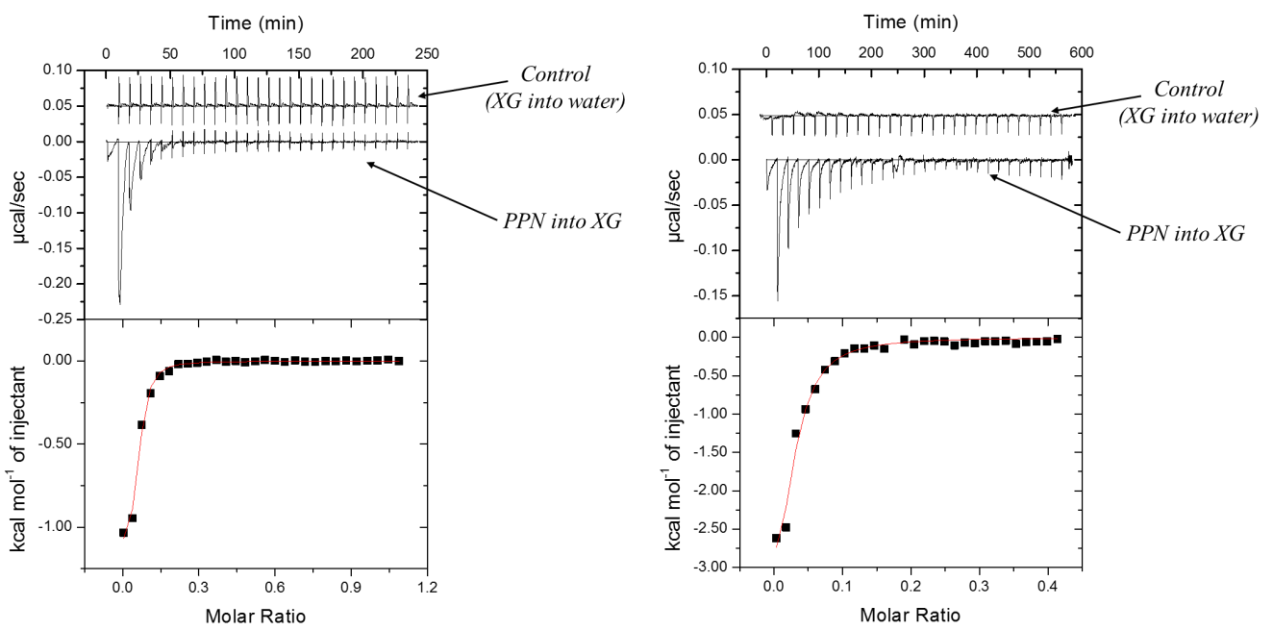


**Fig. 3.30.** Calorimetric titration of 0.150 % w/v PPN solution (pH 5) into 0.020 % w/v XG dispersion (pH 5) at 25 °C (a) and 37 °C (c). Raw data (top) and integrated heats (bottom) as a function of molar ratio. Control runs suggesting limited interaction between water and XG

The analysis of the thermodynamic profile through a set of sites curve fitting revealed that the binding between PPN and XG was enthalpy and entropy driven, shown by the negative  $\Delta H$  and  $-T\Delta S$  at both temperatures studied (Table 3.7.). The increase in experimental temperature from 25 °C to 37 °C led to the binding becoming gradually more enthalpy driven ( $-1.40 \pm 0.26$  kcal/mol at 25 °C compared to  $-6.16 \pm 2.11$  kcal/mol at 37 °C) and entropically unfavourable ( $-5.40 \pm 1.90$  kcal/mol at 25 °C compared  $-1.52 \pm 1.07$  kcal/mol at 37 °C). The

reaction had the same binding energy ( $\Delta G$ ) at both temperatures ( $-6.80 \pm 0.17$  kcal/mol at 25 °C and  $-6.75 \pm 0.11$  kcal/mol at 37 °C). A slightly higher affinity ( $K_a$ ) of PPN for XG was observed at 25 °C ( $9.79E+01 \pm 2.04E+01$  M), compared to 37 °C ( $5.91E+01 \pm 9.67$  M) suggesting a more energetic process and more optimal reaction conditions.

**Table. 3.7.** Multiple injection mode calorimetric binding studies evaluating the binding between PPN (0.150 % w/v) and XG (0.20 % w/v) at 25 and 37 °C (pH 5). Data analysed through one set of sites curve fitting using a non-linear least squares model to calculate affinity (K), changes in enthalpy ( $\Delta H$ ), entropy(- $T\Delta S$ ) or Gibbs free energy ( $\Delta G$ ). Results are based on three independent repeats done under similar conditions.

	25 °C	37 °C
<b>K<sub>a</sub></b> (M)	$9.79E+04 \pm 2.04E+04$	$5.91E+04 \pm 9.67E+03$
<b>ΔG</b> (kcal/ mol)	$-6.80 \pm 0.17$	$-6.75 \pm 0.11$
<b>ΔH</b> (kcal/ mol)	$-1.40 \pm 0.26$	$-6.16 \pm 2.11$
<b>-TΔS</b> (kcal/ mol)	$-5.40 \pm 1.90$	$-1.52 \pm 1.07$

### 3.2.8.4.3. PPN adsorption onto MAS-XG complex

Binding between PPN (0.150 % w/v (pH 5)) and MAS-XG mixture (0.037 % w/v MAS; 0.020 % w/w XG; pH 5) led to a different titration profile when compared to the binding between MAS (0.037 % w/v) and PPN (0.150 % w/v) or the binding between MAS (0.037 % w/v) and XG (0.020 % w/v) (Fig. 3.31.). This can be related to the competition between MAS and XG for the binding with PPN, as these were both shown to interact with PPN separately in previous experiments (chapter 3, sections 2.2.8.2. and 2.2.8.4.2). A competitive binding model was fitted to the data using the affinity ( $K_a$ ) and enthalpy ( $\Delta H$ ) obtained in non-competitive binding experiments between PPN and XG at both 25 and 37 °C (Table. 3.8).

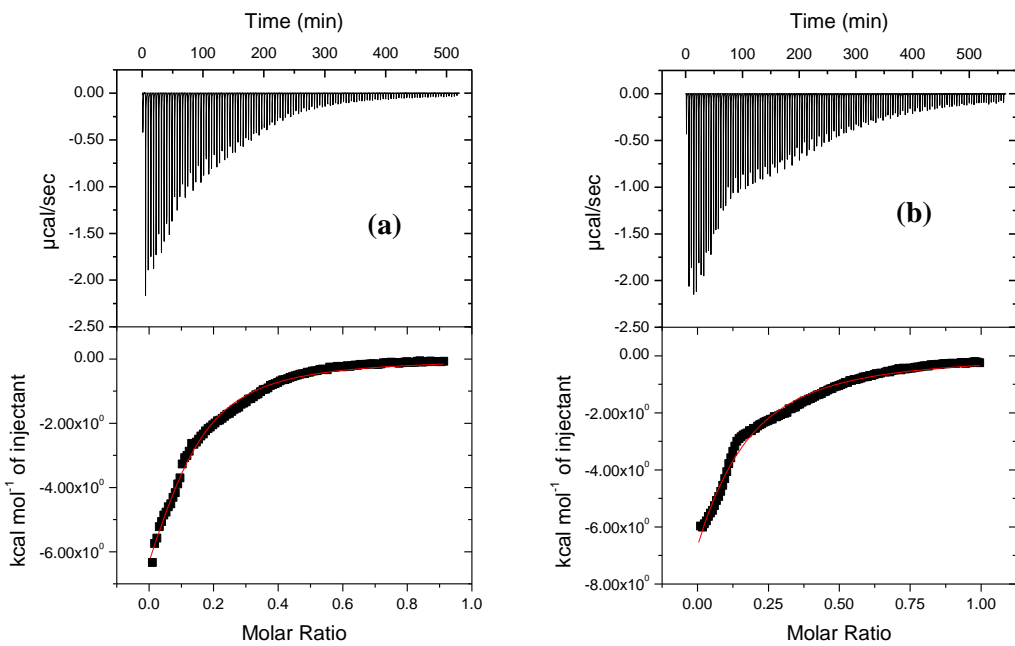


**Fig. 3.31.** Titration of 0.150 % w/v PPN solution (pH 5) into a mixture of MAS and XG (0.037 % w/v MAS; 0.020 % w/w XG; pH 5), at 25 °C (a) and 37 °C (c). Raw data (top) and integrated heats (bottom) as a function of molar ratio; Thermodynamic profile for adsorption of PPN onto MAS-XG mixture at 25 °C (b) and 37 °C (d) showing enthalpy ( $\Delta H$ ), entropy( $\Delta S$ ) or Gibbs free energy ( $\Delta G$ ). Results are based on three independent repeats done under similar conditions.

Results showed that the binding phenomenon between PPN and MAS in the presence of XG was enthalpy and entropically driven as shown by the negative enthalpy ( $\Delta H$ ) and entropy ( $-T\Delta S$ ) at both temperatures. The binding affinity ( $K_a$ ) gradually decreased upon increasing temperature, suggesting that at 25° C the binding was more energetic ( $3.85E+06 \pm 6.06E+05$  M at 25 °C and  $1.37E+06 \pm 2.19E+05$  M at 37 °C). The same behaviour was observed between MAS and PPN in the simple MAS-PPN titration experiments (section 3.2.8.2.). However it was observed that an increase in affinity between MAS and PPN occurred when XG is added to the reaction ( $2.61E+04 \pm 2.71E+03$  M 25 °C and  $1.48E+04 \pm 1.48E+03$  M at 37 °C obtained in the simple MAS-PPN binding studies). Another difference to be noted is that the binding between MAS and PPN is more enthalpy driven in the presence of XG which may be due to the competition for the PPN which affects the binding ( $(-1.45E+01 \pm$

0.85 kcal/mol at 25 °C and -3.03E+01 ± 1.26 kcal/mol at 37 °C) obtained in the MAS-PPN binding experiments in the presence of XG, compared to the enthalpy obtained in the simple MAS-PPN binding experiments (-6.03 ± 0.06 kcal/mol at 25 °C and -5.97 ± 1.37kcal/mol at 37 °C)).

**Table. 3.8.** Results showing data analysed through competitor binding model to calculate affinity (K) and changes in enthalpy ( $\Delta H$ ) and entropy ( $-T\Delta S$ ) for the PPN-MAS binding in the presence of XG following multiple injection calorimetric binding studies between PPN (0.150 % w/v) and XG-MAS mixture (0.037 % w/v MAS; 0.020 % w/w XG) at 25 and 37 °C (pH 5). Results are based on three independent repeats done under similar conditions.

	25 °C	37 °C
<b>K<sub>a</sub></b> (M)	3.85E+06 ± 6.06E+05	1.37E+06 ± 2.19E+05
<b>ΔH</b> (kcal/ mol)	-1.45E+01 ± 0.85	-3.03E+01 ± 1.26
<b>-TΔS</b> (kcal/ mol)	-8.84E+03	-8.55E+03

Based on the findings concerning the binding reactions taking place between MAS, PPN and XG, a reaction scheme may be proposed (Fig. 3.32.). This will be of further use in dissolution experiments to explain the drug release process from XG matrix tablets containing MAS and PPN.

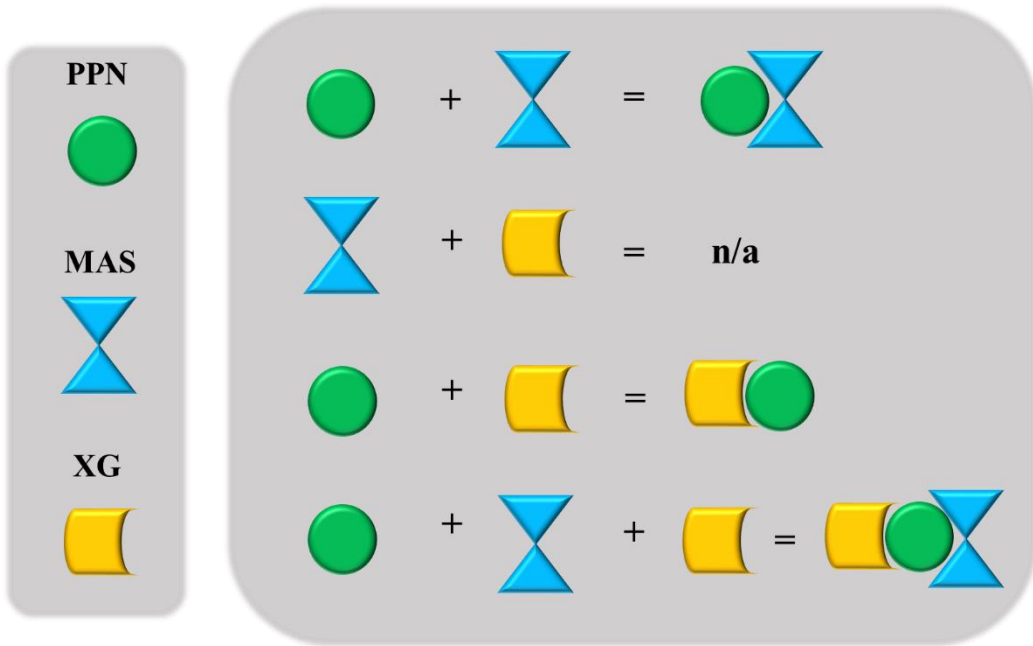


**Fig. 3.32.** Schematic representation using shapes of possible chemical interactions between PPN, MAS and XG based on isothermal titration calorimetry results.

### **3.3. Conclusions**

Results confirmed the ability of the MAS to adsorb PPN onto its surface and form flocculates in the MAS dispersion.

The flocculates were dried and characterised using a wide variety of techniques such as ATR-FTIR, PXRD, DSC, SEM/EDX, HPLC, SAXS which all confirmed changes as a result of the binding process which may have benefits for drug release. Binding was evaluated using SIM and MIM ITC experiments. These revealed that the binding phenomenon between MAS and PPN was predominantly enthalpically driven as high energy resulted from broken and created hydrogen bonds and electrostatic interactions. pH was shown to have no effects on the binding process (at pH 5, 7 and 9), while upon increasing temperature from 25 to 37 °C the binding became more exothermic and enthalpically driven. The binding between XG or PEO and PPN and MAS was also assessed. No binding was observed between PPN and PEO, while the PEO was shown to be adsorbed onto the MAS. Influence of the PEO on the PPN adsorption onto MAS was also observed when PPN was adsorbed onto MAS-PEO mixture, which is most probably due to a reduction in the available sites onto the MAS for PPN binding. No binding was observed between XG and MAS, while PPN was shown to interact with XG. PPN adsorption onto MAS-XG mixture was shown to be influenced by the competition of both MAS and XG for the PPN.

### **3.4. References**

- ACD I-Lab (2018). Available at: <https://ilab.acdlabs.com/iLab2/> (Accessed: 23 September 2018).
- Bandyopadhyay, A. and Bose, S. (eds) (2013) *Characterization of Biomaterials Chapter 4*. Oxford, UK: Elsevier.
- Bohor, B. F. and Hughes, R. E. (1971) ‘Scanning Electron Microscopy of Clays and Clay Minerals’, *Clays and Clay Minerals*, 19(1969), pp. 49–54.
- Carrado, K. A. and Bergaya, F. (eds) (2007) *Clay-based Polymer Nano-composites (CPN)*. Vol. 15. Chantilly, VA 20151-1125: THE CLAY MINERALS SOCIETY.
- Chatpalliwar, V. A., Porwal, P. K. and Upmanyu, N. (2012) ‘Validated gradient stability indicating HPLC method for determining Diltiazem Hydrochloride and related substances in bulk drug and novel tablet formulation’, *Journal of Pharmaceutical Analysis*, 2(3), pp. 226–237.
- Dai, S. and Tam, K. C. (2005) ‘Laser light scattering and isothermal titration calorimetric studies of poly(ethylene oxide) aqueous solution in presence of sodium dodecyl sulfate’, *Journal of Colloid and Interface Science*, 292(1), pp. 79–85.
- Ermer, J. and Ploss, H. J. (2005) ‘Validation in pharmaceutical analysis: Part II: Central importance of precision to establish acceptance criteria and for verifying and improving the quality of analytical data’, *Journal of Pharmaceutical and Biomedical Analysis*, 37(5), pp. 859–870.
- Fernandes, J. B. M. et al. (2019) ‘The development and characterization of propranolol tablets using tapioca starch as excipient’, *Anais da Academia Brasileira de Ciencias*, 91(1).
- Gao, F. (2004) ‘Clay/polymer composites: The story’, *Materials Today*, 7(11), pp. 50–55.
- Kanjanakawinkul, W. et al. (2013) ‘Nicotine-magnesium aluminum silicate microparticle surface modified with chitosan for mucosal delivery’, *Materials Science and Engineering C*, 33(3), pp. 1727–1736.
- Laity, P. R. et al. (2015) ‘Using small-angle X-ray scattering to investigate the compaction

behaviour of a granulated clay', *Applied Clay Science*, 108, pp. 149–164.

Li, T., Senesi, A. J. and Lee, B. (2016) 'Small Angle X - ray Scattering for Nanoparticle Research', *Chemical Reviews*, 116, p. 11128–11180.

McCalley, D. V. (2010) 'The challenges of the analysis of basic compounds by high performance liquid chromatography: Some possible approaches for improved separations', *Journal of Chromatography A*, 1217(6), pp. 858–880.

Milne, I. H. and Warhaw, C. M. (1955) 'Methods of Preparation and Control of Clay Mineral Specimens in X-Ray Diffraction Analysis', *Clays and Clay Minerals*, 4, pp. 22–30.

Mita, A. R. A., Rupa, A. K. and Achowicz, R. J. (2010) 'Preliminary Approach to Application of Modified Smectite Clay to Form Tablets in Direct Compression Process', pp. 366–368.

Odo, E. A. *et al.* (2015) 'SAXS Study of Silicon Nanocomposites', 5(3), pp. 65–70.

Palmer, D. *et al.* (2013) 'Mechanism of synergistic interactions and its influence on drug release from extended release matrices manufactured using binary mixtures of polyethylene oxide and sodium carboxymethylcellulose', *Colloids and Surfaces B: Biointerfaces*, 104, pp. 174–180.

Pernyeszi, T. and Dékány, I. (2003) 'Surface fractal and structural properties of layered clay minerals monitored by small-angle X-ray scattering and low-temperature nitrogen adsorption experiments', *Colloid and Polymer Science*, 281(1), pp. 73–78.

Pongjanyakul, T., Khunawattanakul, W. and Puttipipatkhachorn, S. (2009) 'Physicochemical characterizations and release studies of nicotine-magnesium aluminum silicate complexes', *Applied Clay Science*, 44(3–4), pp. 242–250.

Pongjanyakul, T. and Rojtanatanya, S. (2012) 'Use of Propranolol-Magnesium Aluminium Silicate Intercalated Complexes as Drug Reservoirs in Polymeric Matrix Tablets', *Indian Journal of Pharmaceutical Sciences*, 74(4), pp. 292–301.

Pongjanyakul, T. and Rongthong, T. (2010) 'Enhanced entrapment efficiency and modulated drug release of alginate beads loaded with drug-clay intercalated complexes as

microreservoirs', *Carbohydrate Polymers*, 81(2), pp. 409–419.

Ray, S. S. *et al.* (2002) 'New Polylactide / Layered Silicate Nanocomposites . 1 . Preparation , Characterization , and Properties', *Direct*, 25, pp. 3104–3110.

Rojtanatanya, S. and Pongjanyakul, T. (2010) 'Propranolol-magnesium aluminum silicate complex dispersions and particles: Characterization and factors influencing drug release', *International Journal of Pharmaceutics*, 383(1–2), pp. 106–115.

Sadeghi, F. *et al.* (2013) 'Validation and Uncertainty Estimation of an Ecofriendly and Stability-Indicating HPLC Method for Determination of Diltiazem in Pharmaceutical Preparations', *Journal of Analytical Methods in Chemistry*.

Saeedi, M., Morteza-Semnani, K. and Sagheb-Doust, M. (2013) 'Evaluation of Plantago major L. seed mucilage as a rate controlling matrix for sustained release of propranolol hydrochloride', *Acta Pharmaceutica*, 63(1), pp. 99–114.

Shalaeva, M. *et al.* (2007) 'Measurement of Dissociation Constants (pKa Values) of Organic Compounds by Multiplexed Capillary Electrophoresis Using Aqueous and Cosolvent Buffers', *Journal of Pharmaceutical Sciences*, pp. 1–24.

Shang, C., James A., R. and Jar-shyong, L. (2001) 'Thickness and Surface Characteristics of Colloidal 2:1 Aluminosilicates Using an Indirect Fourier Transformorm of Small- angle X-ray Scattering Data', *Clays and Clay Minerals*, 49(4), pp. 277–285.

Shankland, K. and Knight, K. S. (1996) 'Some observations on the crystal structure of (R,S)-propranolol hydrochloride', *International Journal of Pharmaceutics*, 137(2), pp. 255–259.

De Stefanis, A. *et al.* (2007) 'Study of structural irregularities of smectite clay systems by small-angle neutron scattering and adsorption', *Applied Surface Science*, 253(13 SPEC. ISS.), pp. 5633–5639.

Supuk, E. *et al.* (2013) 'The influence of salt formation on electrostatic and compression properties of flurbiprofen salts', *International Journal of Pharmaceutics*, 458, pp. 118–127.

Tucker, M. E. (2001) *Sedimentary Petrology: An Introduction to the Origin of Sedimentary Rocks*. 3rd edn. United Kingdom: Blackwell Publishing.

Vanderbilt Minerals (2009) ‘VANZAN® Xanthan Gum’, pp. 1–12.

Vanderbilt Minerals (2014) ‘VEEGUM ® Magnesium Aluminum Silicate VANATURAL ® Bentonite Clay For Personal Care and Pharmaceuticals What They Are’, pp. 1–27.

Velazquez-Campoy, A. and Freire, E. (2006) ‘Isothermal titration calorimetry to determine association constants for high-affinity ligands’, *Nature Protocols*, 1(1), pp. 186–191.

# *Chapter 4:*

## *Adsorption of diltiazem hydrochloride onto magnesium aluminium silicate*

### Note to reader

Aspects of this chapter has been published in the Journal of Pharmaceutical Analysis under the title, “Thermodynamics of clay – Drug complex dispersions: Isothermal titration calorimetry and high-performance liquid chromatography”

(<https://doi.org/10.1016/j.ipha.2019.12.001>)

## **Chapter 4: Adsorption of diltiazem hydrochloride onto magnesium aluminium silicate**

### **4.1. Methodology**

#### **4.1.1. Formulation of single and double drug loaded MAS-PPN complexes**

Please refer to chapter 2, section 2.2.1.

#### **4.1.2. Characterisation of MAS-PPN complexes**

##### **4.1.2.1. Attenuated total reflectance Fourier transform infrared spectroscopy (ATR-FTIR)**

Please refer to chapter 2, section 2.2.2.1.

##### **4.1.2.2. Powder X-Ray diffractometry (PXRD)**

Please refer to chapter 2, section 2.2.2.2.

##### **4.1.2.3. Differential scanning calorimetry (DSC)**

Please refer to chapter 2, section 2.2.2.3.

##### **4.1.2.4. Scanning electron microscopy (SEM) with energy dispersive X-ray spectroscopy (EDX)**

Please refer to chapter 2, section 2.2.2.4.

##### **4.1.2.5. High Performance Liquid Chromatography (HPLC)**

Please refer to chapter 2, section 2.2.2.5.

###### **4.1.2.5.1. Method validation**

DC-DIL (desacetyl diltiazem) was formed from DIL via hydrolysis (Fig. 4.1.): DIL stock solution (100 µg/mL) was prepared in dilute acid (2M HCl) and DIL standard solutions in the range of 75 to 0.1 µg/mL were prepared from the stock solution using purified water. Samples were left for 72 h at room temperature until complete hydrolysis has occurred. This was demonstrated by the lack of DIL retention peak on the chromatograms as it became replaced entirely by the DC-DIL peak. The concentration of DC-DIL present in the standards was determined from the equilibrated hydrolysis reaction (Fig. 4.1.).

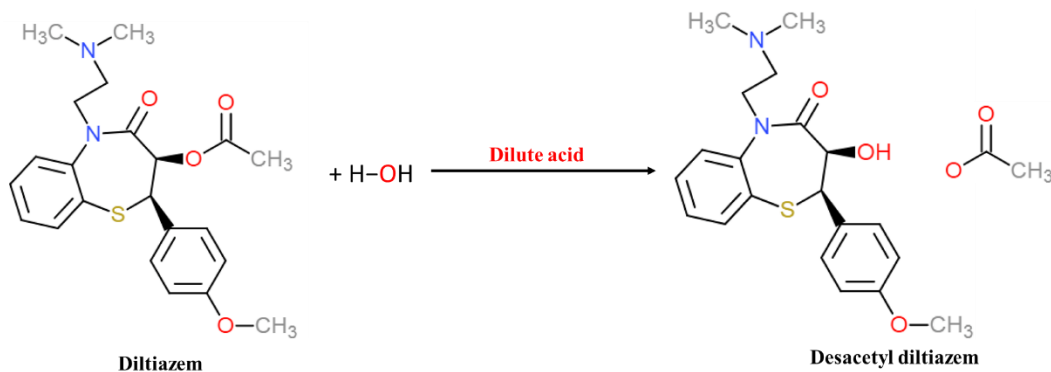


**Fig. 4.1.** DIL undergoing dilute acid hydrolysis and product DC-DIL

Linearity range, precision, limit of quantitation (LOQ) and limit of detection (LOD) were separately determined to validate the method used as described in chapter 2, section 2.2.2.5.1.

#### 4.1.2.5.2. Determination of DIL content in MAS-DIL complex particles

The HPLC method as described in chapter 2, section 2.2.2.5.2. was used for the detection and recovery of DIL and DC-DIL, the main degradant of DIL, which was observed in samples during analysis.

#### 4.1.2.6. Small angle X-ray scattering (SAXS)

Please refer to chapter 2, section 2.2.2.6.

#### 4.1.2.7. Microscopy

Digital microscopy was used to observe the formation of flocs upon the addition of DIL solution (0.050 % w/v) to MAS dispersion (0.100 % w/v) prepared as described in chapter 2, section 2.2.1. Studies were performed using a VHX2000 Digital Microscope as described in chapter 2, section 2.2.2.7. Images were recorded at different mixing times (2 min, 30 min, 60 min, 120 min, 180 min and 24 h) and were compared. Images of the MAS dispersion prior to the addition of DIL were also acquired.

#### 4.1.2.8. Calorimetric binding studies

##### 4.1.2.8.1. Calorimetric single injection mode (SIM) binding studies

SIM experiments were performed as described in chapter 2, section 2.2.2.8.1. DIL solution (0.045 % w/v (1 mM)) was added in 1 injection of 250 µL into the sample cell containing MAS dispersion (0.010 % w/v). The pH of the prepared solutions and dispersions were adjusted using 2 M hydrochloric acid and 2 M sodium hydroxide to 5, 7 and 9. Experiments were conducted in triplicate to ensure reproducibility.

##### 4.1.2.8.2. Calorimetric multiple injection mode (MIM) binding studies

MIM ITC studies were carried out at 25 °C and pH 5 as described in chapter 2, section 2.2.2.8.2. The binding isotherm was studied in 120-140 injections of 2 µl each into the sample cell every 260 seconds. MAS dispersion (0.036 and 0.010 % w/v) and DIL solution (0.144 % w/v (3.2 mM) and 0.020 % w/v 0.45 mM) were prepared as described in chapter 2, section 2.2.2.8.1.

A competitor binding model (Fig. 4.2.) was fitted to the data to get thermodynamic parameters which best follow the experimental data, which was developed using AFFINImeter (AFFINImeter, Spain).

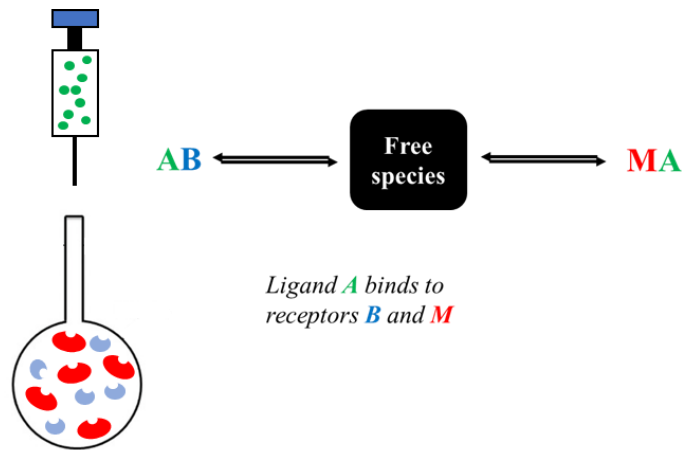


**Fig 4.2.** Competitive ligand binding where A is the ligand in the syringe (DIL) and M and B are the macromolecule and competitive ligand respectively (montmorillonite and saponite making up the MAS), both present in the sample cell

The total molar concentration of MAS was estimated and the relative molar fractions of each kind of clay ( $r_b$ ,  $r_m$ ) were considered unknown and set as fitted parameters in the analysis:  $r_b \cdot [B] + r_m \cdot [M] = [\text{MAS}]$ .

#### 4.1.2.8.3. Effects of PEO on the adsorption of DIL onto MAS

Calorimetric studies were carried out at 25 °C and pH 5, to study the effects of PEO on MAS-DIL binding. Experiments were undertaken between PEO and MAS, PEO and DIL, as well as DIL and MAS-PEO mixture. Control binding studies were also performed. The binding isotherm was studied in 30 – 35 injections of 8 – 10 µL each into the sample cell every 550 – 1500 seconds. MAS dispersion (0.037 % w/v) and DIL solution (0.090 % w/v (2 mM)) were prepared as described in chapter 2, section 2.2.2.8.1. PEO dispersion (0.020 – 0.037 % w/v) was prepared as described in chapter 2, section 2.2.2.8.3. The MAS-PEO mixture was prepared using a 1:1 v/v mixture of separately prepared MAS dispersion (0.074 % w/v) and PEO dispersion (0.040 % w/v). A competitor binding model (Fig. 4.3.) was fitted to the data to determine thermodynamic parameters which was developed using AFFINImeter (AFFINImeter, Spain).

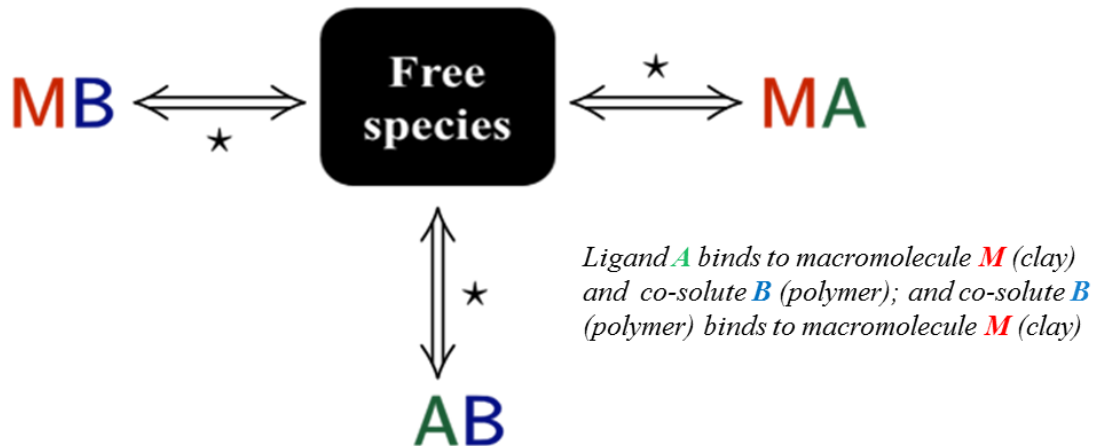


**Fig 4.3.** Competitive ligand binding where A is the ligand in the syringe (DIL) and M and B are the macromolecule and co-solute respectively (MAS and PEO respectively), both present in the sample cell

#### 4.1.2.8.3. Effects of XG on the adsorption of DIL onto MAS

Binding studies to determine the effects of XG on MAS-DIL binding were carried out at 25 °C and pH 5. Experiments were also conducted between XG and MAS, XG and DIL, as well as DIL and MAS-XG mixture. Control binding studies were also performed. The binding isotherms were studied in 29 – 35 injections of 4 – 8 µL each into the sample cell every 550 – 1200 seconds. MAS dispersion (0.037 % w/v) and DIL solution (0.090 % w/v (2 mM)) were prepared as described in chapter 2, section 2.2.2.8.1. XG dispersion (0.020 % w/v) was prepared as described in chapter 2, section 2.2.2.8.3. The MAS-XG mixture was prepared using a 1:1 v/v mixture of separately prepared MAS dispersion (0.074 % w/v) and XG dispersion (0.040 % w/v). A competitor binding model (Fig. 4.2.) was fitted to the data to determine thermodynamic parameters using AFFINImeter (AFFINImeter, Spain).

A summary of the parameters used in the MIM and SIM ITC experiments can be found in Table 4.1.

**Table 4.1.** Compounds and parameters used in ITC SIM and MIM experiments

	Cell		Syringe		Number of injections	Injection volume (µL)	Spacing (sec)	Reference power (µcal/sec)
Clay/polymer	Concentration (% w/v)	Drug/polymer	Concentration (% w/v)					
<b>MAS</b>	0.010	<b>DIL</b>	0.045	1	50	2500	20	
<b>MAS</b>	0.036	<b>DIL</b>	0.144	120	2	260	20	
<b>MAS</b>	0.010	<b>DIL</b>	0.020	140	2	260	20	
<b>MAS</b>	0.037	<b>PEO</b>	0.037	30	10	1500	15	
<b>PEO</b>	0.020	<b>DIL</b>	0.090	35	8	550	10	
<b>MAS-PEO</b>		0.037 MAS 0.020 PEO (ratio of 1:1 v/v)		<b>DIL</b>	0.090	35	8	550
<b>MAS</b>	0.037	<b>XG</b>	0.020		29	4	1200	10
<b>XG</b>	0.020	<b>DIL</b>	0.090		35	8	550	10
<b>MAS-XG</b>		0.037 MAS 0.020 XG (ratio of 1:1 v/v)		<b>DIL</b>	0.090	35	8	550

## **4.2. Results and discussion**

### **4.2.1. Attenuated total reflectance Fourier transform infrared spectroscopy (ATR-FTIR)**

ATR-FTIR was used to study the adsorption of DIL onto MAS based on the vibration of chemical bonds formed (Fig. 4.4.).

Characteristic peaks were observed on the spectrum of MAS such as the hydroxyl group belonging to Si-OH at  $3625\text{ cm}^{-1}$  and the Si-O-Si stretching at  $980\text{ cm}^{-1}$ , as well as peaks related to water residues (O-H stretching  $3415\text{ cm}^{-1}$ ) and water of crystallisation (O-H group bending at  $1640\text{ cm}^{-1}$ ) (Rojtanatanya and Pongjanyakul, 2010; Totea *et al.*, 2019).

The spectrum of MAS-DIL double drug loaded complexes was very different from the spectrum of DIL alone, but similar to the spectrum of MAS. The presence of the Si-O-Si stretching belonging to the clay was still observed as a broad peak at  $980\text{ cm}^{-1}$ . Peaks attributed to the hydroxyl stretching of the Si-OH group was observed at  $3631\text{ cm}^{-1}$ . The C=O carbonyl groups belonging to DIL at  $1680\text{ cm}^{-1}$  and  $1740\text{ cm}^{-1}$  and to C=C aromatic ring stretching belonging to DIL at  $1511\text{ cm}^{-1}$  were still observed but less intense. The peak belonging to the amine group on the DIL structure observed at  $1217\text{ cm}^{-1}$  was still present but became broader. The peaks attributed to R–O–R stretching at  $1026\text{ cm}^{-1}$  and C–O ester stretching at  $1059\text{ cm}^{-1}$  on DIL structure were not observed on the spectrum of MAS – DIL complex particles. The change and disappearance of some of the peaks characteristic to both DIL and MAS demonstrated the potential interaction between them by the formation of hydrogen bonds between the silanol groups of MAS with the amine and hydroxyl groups of DIL (Rojtanatanya and Pongjanyakul, 2010; Totea *et al.*, 2019).

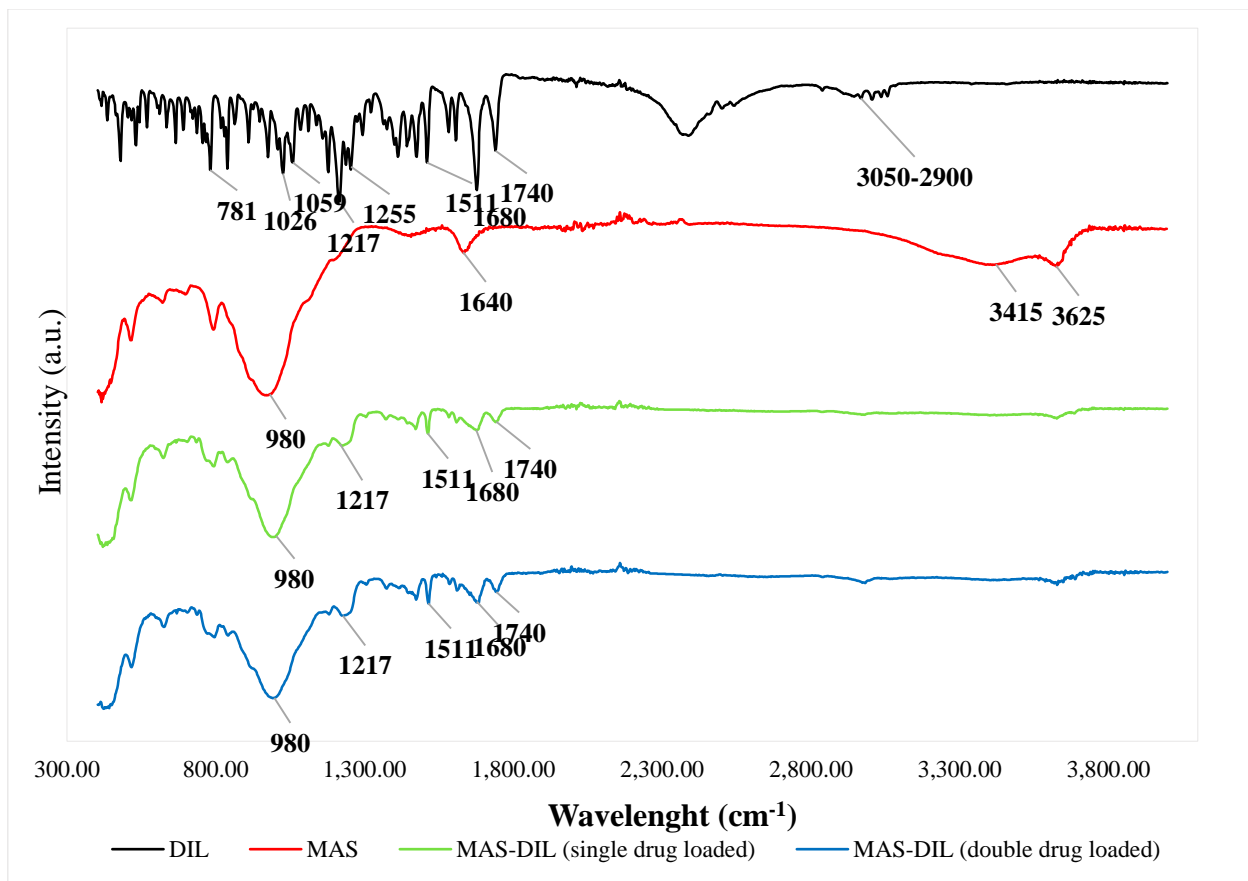


**Fig. 4.4.** ATR-FTIR scans on MAS, DIL and MAS – DIL single and double drug loaded complex particles

#### 4.2.2. Powder X-ray diffractometry (PXRD)

The prepared MAS-DIL complexes were shown to be amorphous in nature and very different to the PXRD pattern of DIL or MAS alone (Fig. 4.5.). The amorphous characteristic of the MAS-DIL samples suggests the molecular dispersivity of the drug in the prepared complexes. The reflection at  $6.87^\circ$  ( $2\theta$ ) representing the thickness of the silicate layer in the MAS sample was shifted to the left in the diffractogram of the complexes prepared and had a different intensity. The increase in basal spacing calculated using Bragg's Law (first order of reflection,  $n=1$ ) was 21.34 nm for the single drug loaded MAS-DIL complexes and 20.16 nm for the double drug loaded MAS-DIL complexes, suggesting an increase in basal spacing of MAS from 1.28 nm up to  $\approx 2.10$  nm upon intercalation of DIL into the clay platelets (Ray *et al.*, 2002; Rojtanatanya and Pongjanyakul, 2010).

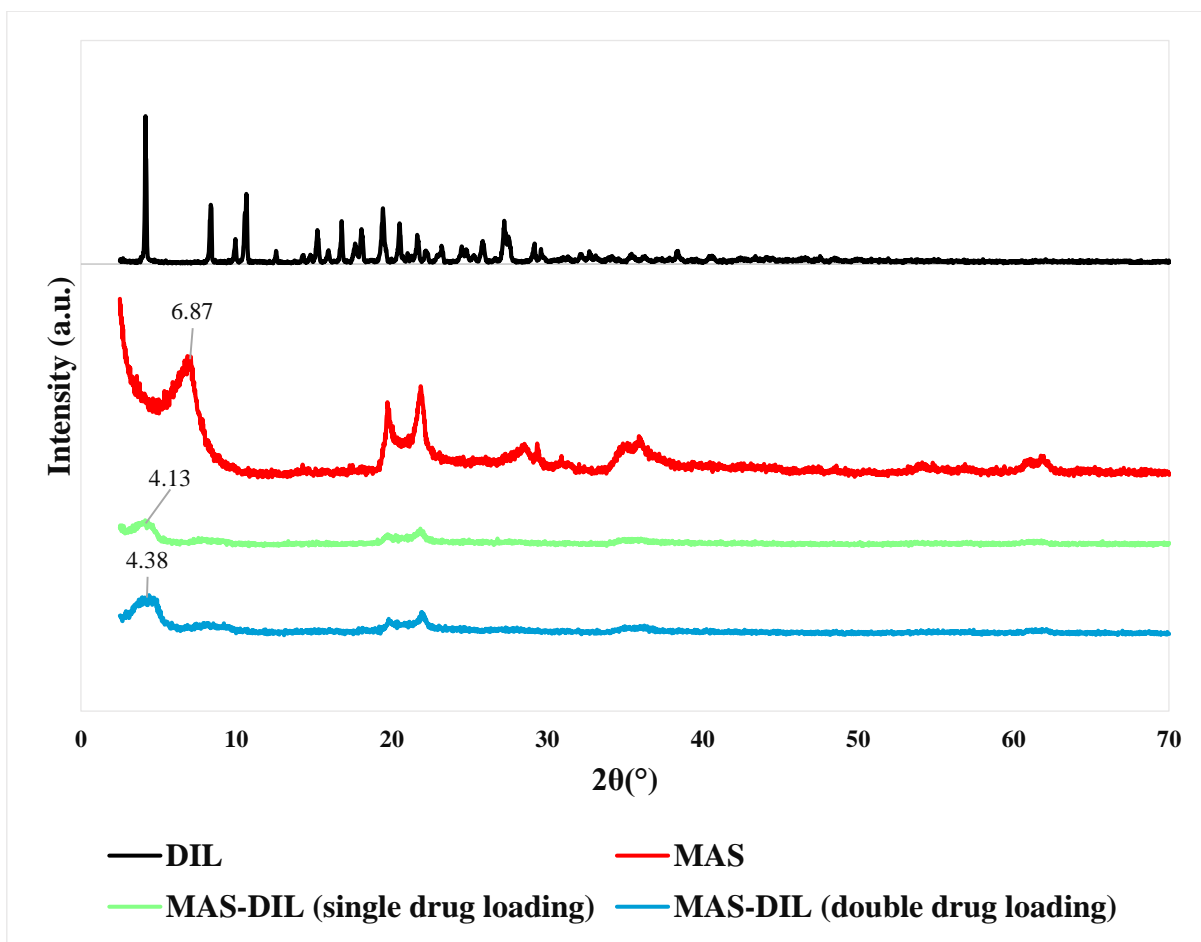


**Fig. 4.5.** PXRD patterns of MAS, DIL and MAS-DIL single and double drug loaded complexes

#### 4.2.3. Differential scanning calorimetry (DSC)

Thermograms were obtained for MAS, DIL, as well as single drug loaded, and double drug loaded MAS-DIL complexes to study their crystallinity.

The melting point of DIL was indicated by a sharp endothermic peak at  $215 \pm 1$  °C (Fig. 4.6.) (Prasad *et al.*, 2013). The single and double drug loaded MAS-DIL particles were shown to be amorphous (Fig. 4.6.). The absence of DIL melting point on their thermograms confirmed its molecular dispersion in amorphous form in the complexes.

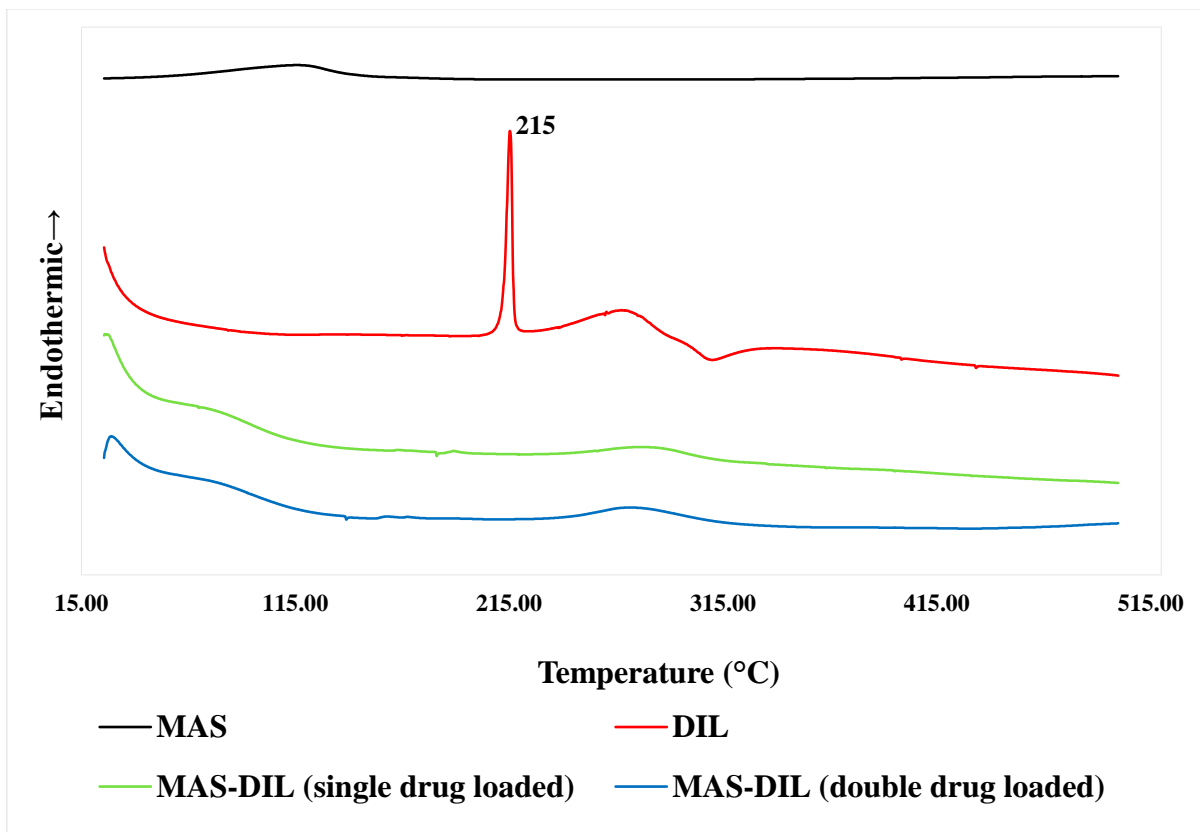


**Fig. 4.6.** Thermograms obtained for MAS, DIL and MAS-DIL single and double drug loaded complex particles (n=3)

#### 4.2.4. Scanning electron microscopy with energy dispersive X-ray spectroscopy (SEM/EDX)

DIL, as well as the single and double drug loaded MAS-DIL complex particles prepared were studied using SEM and EDX to understand and compare their surfaces and study the chemical elements existing in the samples. Due to the low sensitivity of the technique, the atomic distribution of elements slightly varied and hence, chemical elements found in samples were not compared quantitatively (Bandyopadhyay and Bose, 2013).

DIL was shown to be formed of small crystals having a smooth surface, clumped together in larger particles (Fig. 4.7.). Distinctive elements such as chlorine, nitrogen and sulphur belonging to DIL were confirmed using EDX.

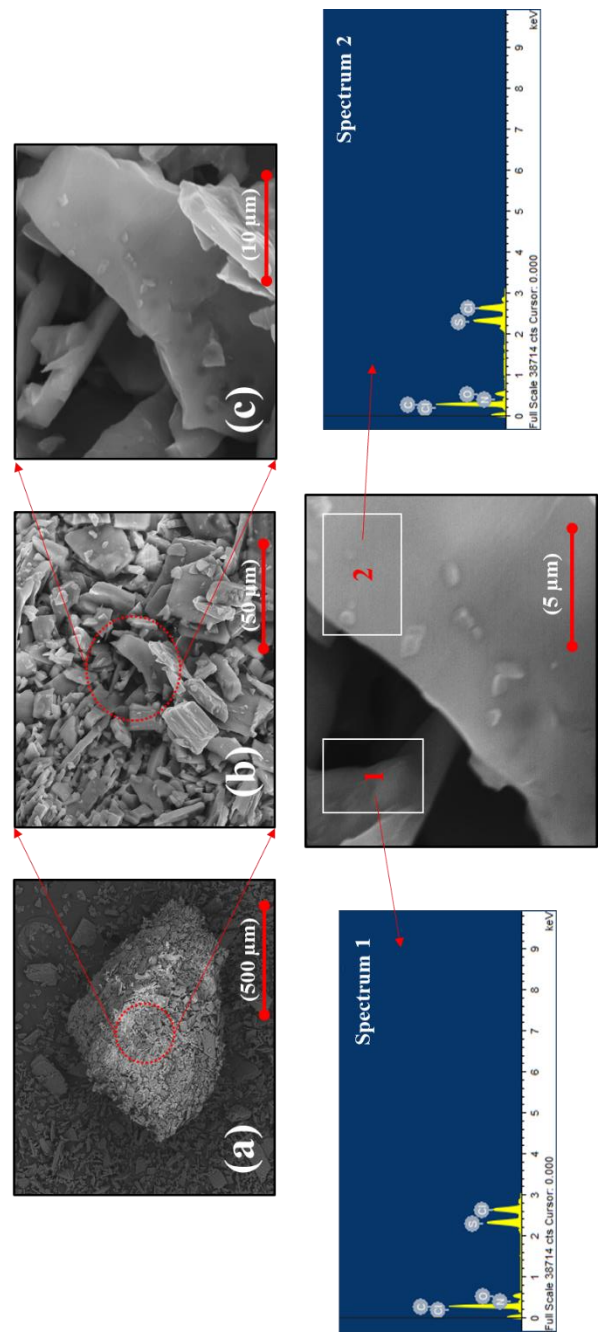


**Fig. 4.7.** Characterisation of DIL surface using SEM/EDX. SEM images at different magnifications  $\times 100$  (a),  $\times 1500$  (b),  $\times 5000$  (c) and  $\times 10\,000$  (d); atomic distribution profile at two different sample locations (Spectrum 1 and 2)

The single and double drug loaded MAS-DIL complexes were shown to have a similar structure (Fig. 4.8 and Fig. 4.9.). Their irregular layered surface was however very different

from that of MAS (described in chapter 3, section 3.2.4.) and DIL, demonstrating changes in the microstructural properties of the MAS powder that occur following DIL adsorption (Mita, Rupa and Achowicz, 2010). These changes may provide an insight into their successful use to control drug release (Rojtanatanya and Pongjanyakul, 2010).

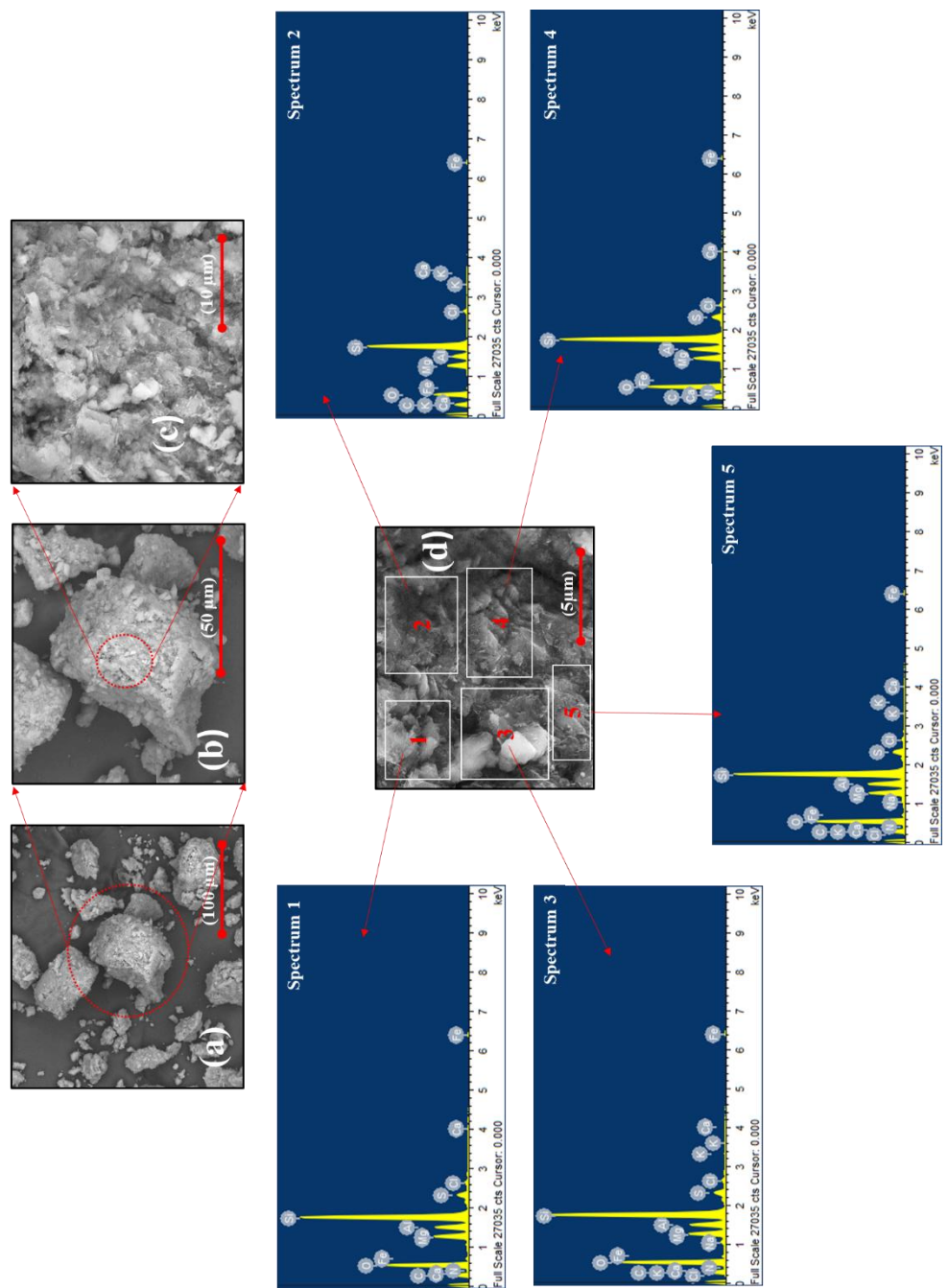


**Fig. 4.8.** Surface characterisation of MAS-DIL single drug loaded complex using SEM/EDX. SEM images at different magnifications  $\times 500$  (a),  $\times 1500$  (b),  $\times 5000$  (c) and  $\times 10\,000$  (d); atomic distribution profile at five different sample locations (Spectrum 1-5)

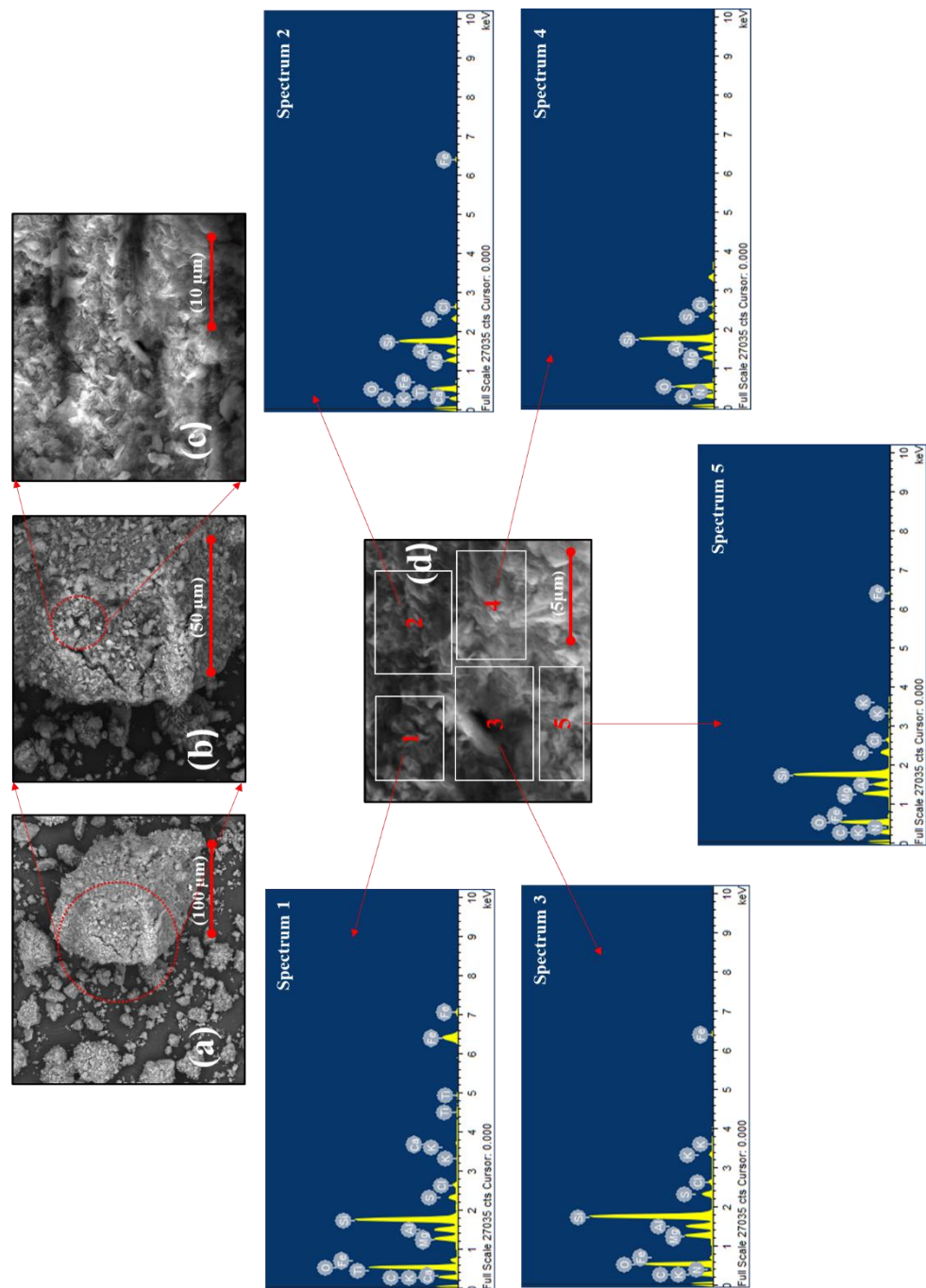


**Fig. 4.9.** Surface characterisation of MAS-DIL double drug loaded complex using SEM/EDX. SEM images at different magnifications  $\times 500$  (a),  $\times 1500$  (b),  $\times 5000$  (c) and  $\times 10000$  (d); atomic distribution profile at five different sample locations (Spectrum 1-5)

As in chapter 3, the use of this characterisation technique may introduce a selective bias in the overall results due to the analysis of only small particulates selected from the overall

sample prepared, which is appropriate for this type of analysis (Bohor and Hughes, 1971). However, the analysis was only used for qualitative purposes, to explore the surface morphology of the samples.

#### 4.2.5. High performance liquid chromatography (HPLC)

##### 4.2.5.1. Method validation

An assay of freshly prepared standard DIL and DC-DIL solutions at four different concentrations (1.00, 10.00, 50.00 and 100.00 µg/mL and 0.83, 8.25, 41.26, 82.52 µg/mL respectively) were repeatedly run on the same day and on three different days was used to evaluate the intra and inter day precision in terms of standard deviation RSD %.

The calibration graphs generated for DIL and DC-DIL were found to be linear over the concentration range studied ( $R^2 \geq 0.999$ ). Linearity was defined by an equation ( $y = 31421x - 8569$  and  $y = 38079x - 7042.4$  for the DIL and DC-DIL respectively) that was further used in the recovery studies (Fig. 4.10.).

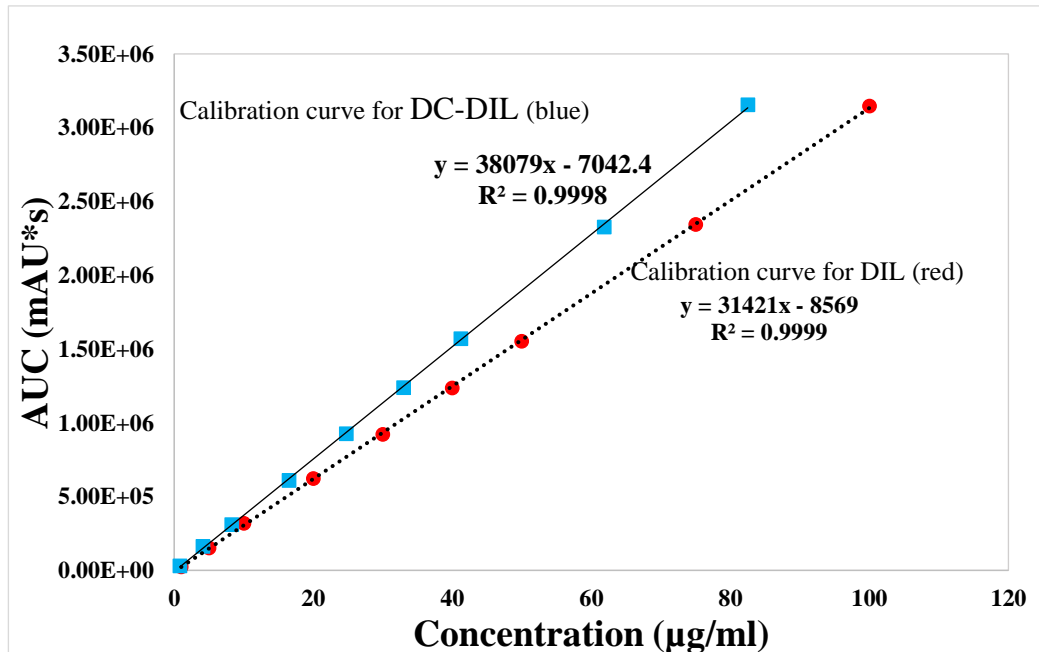


**Fig 4.10.** Calibration curve for DIL (red) (100 to 0.1 µg/ml) showing linearity ( $R^2=0.9999$ ) and for DC-DIL (blue) (82.52 – 0.83 µg/ml)

The method was shown to be precise for the detection of both DIL and DC-DIL, the intermediate and intra assay precision at four different concentrations on three different days being lower than 2 % RSD (Table. 4.2.) which complies with the acceptable criteria for quality control of pharmaceutical preparations (Ermer and Ploss, 2005; Chatpalliwar, Porwal and Upmanyu, 2012). The sensitivity of the method is important in limiting possible peak tailing and poor peak shape due to column overloading (McCalley, 2010; Sadeghi *et al.*, 2013). LOQ (the lowest drug concentration that can be recovered within acceptable limits of precision and accuracy) was found to be 1.72 µg/mL for DIL and 1.65 µg/mL for DC-DIL indicating the high sensitivity of the proposed method at low concentrations of DIL and DC-DIL. LOD (the lowest detectable amount of drug distinguishable from the blank) was 0.57 µg/mL for DIL and 0.55 µg/mL for DC-DIL confirming the sensitivity of the method proposed.

**Table. 4.2.** HPLC method validation for DIL and DC-DIL

	Range (µg/mL)	Linearit y ( $R^2$ )	Intermediate precision (RSD)(%)	Intra assay precision (RSD) (%)	LOD (µg/mL)	LOQ (µg/mL)
<b>DIL</b>	100 – 0.1	$\geq 0.9999$	1 µg/mL: 5.32	1 µg/mL: 1.67	0.57	1.72
			10 µg/mL: 0.85	10 µg/mL: 0.48		
			50 µg/mL: 0.65	50 µg/mL: 0.17		
			100 µg/mL: 0.55	100 µg/mL: 0.16		
<b>DC-DIL</b>	82.52 – 0.83	$\geq 0.9998$	0.83 µg/mL: 1.26	0.83 µg/mL: 0.63	0.55	1.65
			8.25 µg/mL: 0.52	8.25 µg/mL: 0.91		
			41.26 µg/mL: 0.25	41.26 µg/mL: 0.39		
			82.52 µg/mL: 0.38	82.52 µg/mL: 0.63		

#### 4.2.5.2. Determination of DIL content in MAS-DIL complex particles

Determination of drug content in the MAS-DIL double drug loaded complex particles prepared as described in chapter 2, section 2.2.1 showed discrepancies between the different media used for the dispersion of the complex particles (Table 4.3.). The difference can be related to the behaviour of DIL and MAS in the dissolution media, as well as to the mechanism of adsorption of DIL onto MAS.

**Table 4.3.** DIL and DC-DIL content in double drug loaded MAS-DIL complex particles

	<b>Recovered DIL (% w/w)</b>	<b>Recovered DC-DIL (% w/w)</b>
<b>2M HCl</b>	n/a <sup>\$</sup>	25.78 ± 0.32*
<b>Ultra-pure water</b>	16.48 ± 0.42*	1.31 ± 0.03*
<b>pH 6.8 Phosphate Buffer</b>	17.61 ± 0.22*	1.55 ± 0.02*

Note: \*values are reported as mg of drug per g MAS

<sup>\$</sup>DIL completely degraded, hence only degradant DC-DIL recovered

Results showed that only DC-DIL was recovered by dispersing the MAS-DIL particles in 2M HCl. The degradant was identified following a shift in the retention time on the chromatograms from approx. 7 min (DIL standard solution), to approx. 3.8 min (recovered DIL) (Fig. 4.11.). This behaviour was attributed to the hydrolysis of DIL under acidic conditions and the peak was identified as being DC-DIL , the main degradant of DIL (Pharmaceutical, Europe and Collection, 2008; Chatpalliwar, Porwal and Upmanyu, 2012; Sadeghi *et al.*, 2013). A reduction in the exposure time of the MAS-DIL complex to the acid solution from 24 h to 30 min allowed the observation of the two peaks belonging to DIL and DC-DIL on the same chromatogram (Fig. 4.10. b and c).

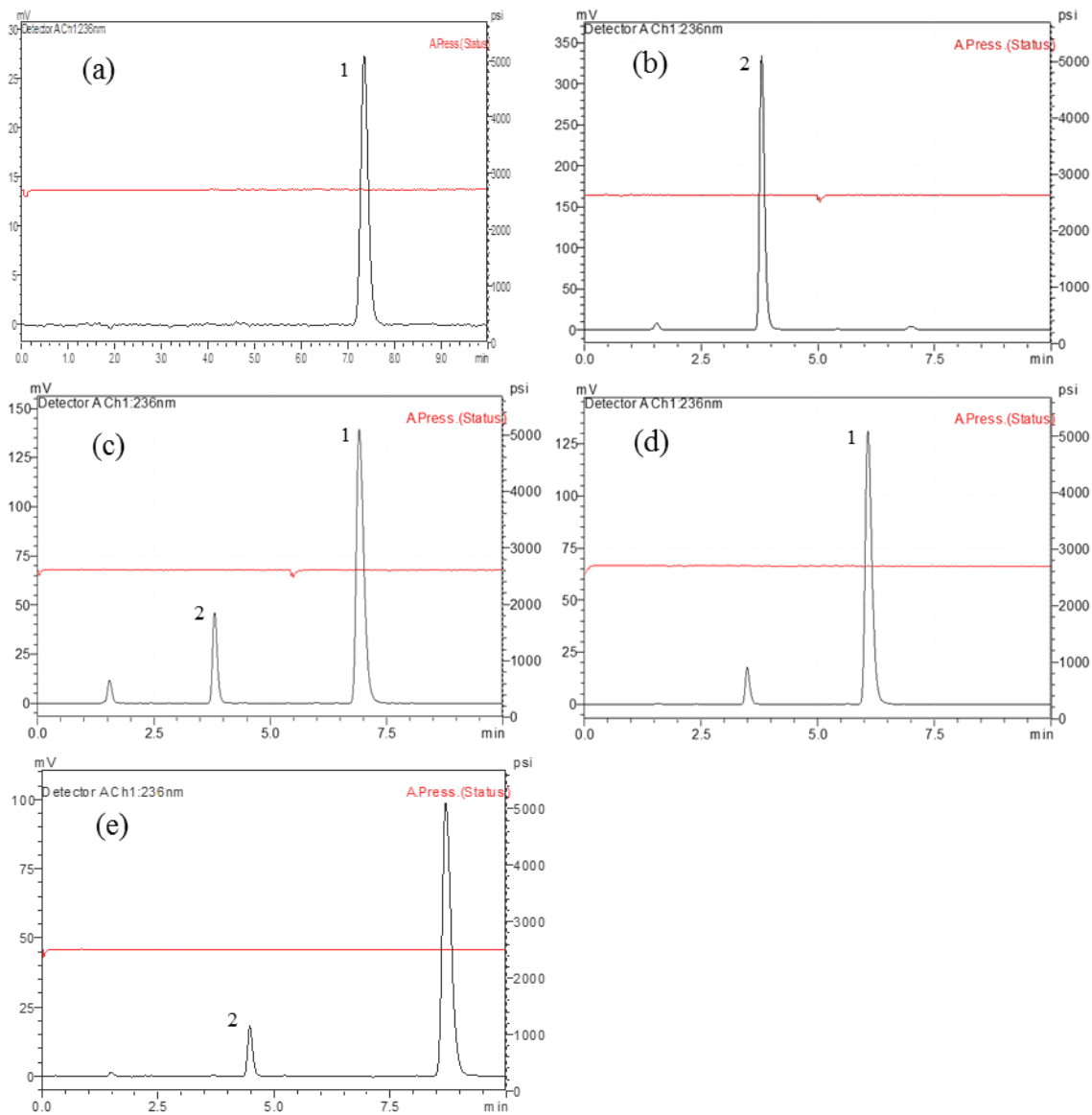


**Fig. 4.11.** Typical HPLC chromatograms of: DIL standard solution at 25 °C (a) and DIL recovered from MAS-DIL complex using 2 M HCl (24 h exposure) (b), 2 M HCl (30 min exposure) (c), ultra – pure water (d) and pH 6.8 phosphate buffer (e) showing the presence of DIL (1) and degradant DC-DIL (2)

Further studies evaluating DIL content in MAS-DIL double drug loaded complex particles by dispersing the particles in ultra-pure water (pH 5) and phosphate buffer (pH 6.8) showed a considerable reduction of DIL degradation. The results showed less than 10 % of DIL

recovered from the complexes hydrolysed over 24 h in water and phosphate buffer, hence confirming the effect of 2 M HCl on DIL leading to degradant DC-DIL.

#### **4.2.6. Small Angle X-ray Scattering**

##### **4.2.6.1. Solid-state nanometre scale morphology**

For the analysis of MAS-DIL complexes in powder form (particle size 63 – 125 µm), similar conditions to previous studies on MAS powder (particle size 63 – 125 µm) were used, such as sample mounting in borosilicate glass capillary tubes and consistent acquisition time for the analysis, which allowed for comparisons (chapter 3, section 3.2.6.1.).

2D-SAXS data pattern for MAS-DIL complexes as recorded by the instrument was shown to be symmetric and circular, suggesting that at the nanometre scale, the particles showed no preferred orientation. The intensity plot showing Log {I(a.u.)} vs. q [nm<sup>-1</sup>] had a smooth curve, showing the intensity decreasing from  $q \approx 0.099 \text{ nm}^{-1}$  (at  $2\theta = 0.14^\circ$ ) at the edge of the beam stop, to  $q = 2.275 \text{ nm}^{-1}$  (at  $2\theta = 3.20^\circ$ ) at the peripheral limit of the detector. No peaks or other specific features were observed. Background subtraction was considered unnecessary due to the minimal background scattering in comparison to sample scattering intensity (Fig. 4.12.). Data was corrected for transmission through the calculation on the transmission factor using glassy carbon, to correct for sample absorption.

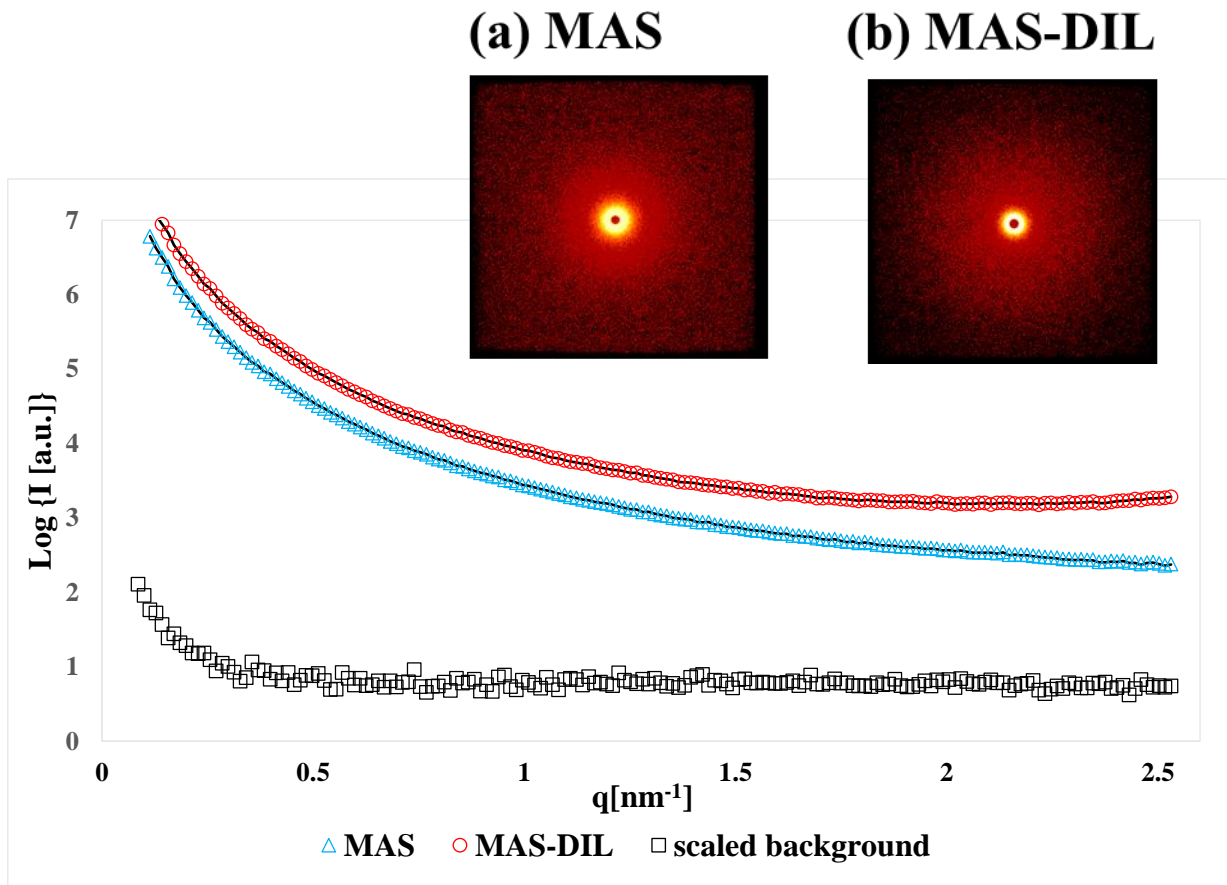


**Fig. 4.12.** Typical SAXS data for specimens in powder form: (a and b) 2D-SAXS patterns for MAS and MAS-DIL complexes showing the centre of the beam stop; (c) 1D-SAXS intensity curves for MAS and MAS-DIL complexes (open symbols showing uncorrected data and line showing data after scaled background subtraction), and scaled background (open black square symbols)

The analysis of the data in the form of double logarithmic plot of intensity ( $\log I$  [a.u.]) vs. the scattering vector ( $\log \{q\} [\text{nm}^{-1}]$ ) for MAS-DIL complexes followed a straight line with no peaks or other specific features, indicating power-law scattering behaviour (as described for the MAS powder in chapter 3, section 3.2.6.1).

A slope of  $-3.62$  was obtained for the MAS-DIL complexes in powder form, which was very similar to the slope obtained from the double logarithmic plot of intensity vs. the scattering vector for MAS ( $-3.63$ ) (Fig. 4.13.).

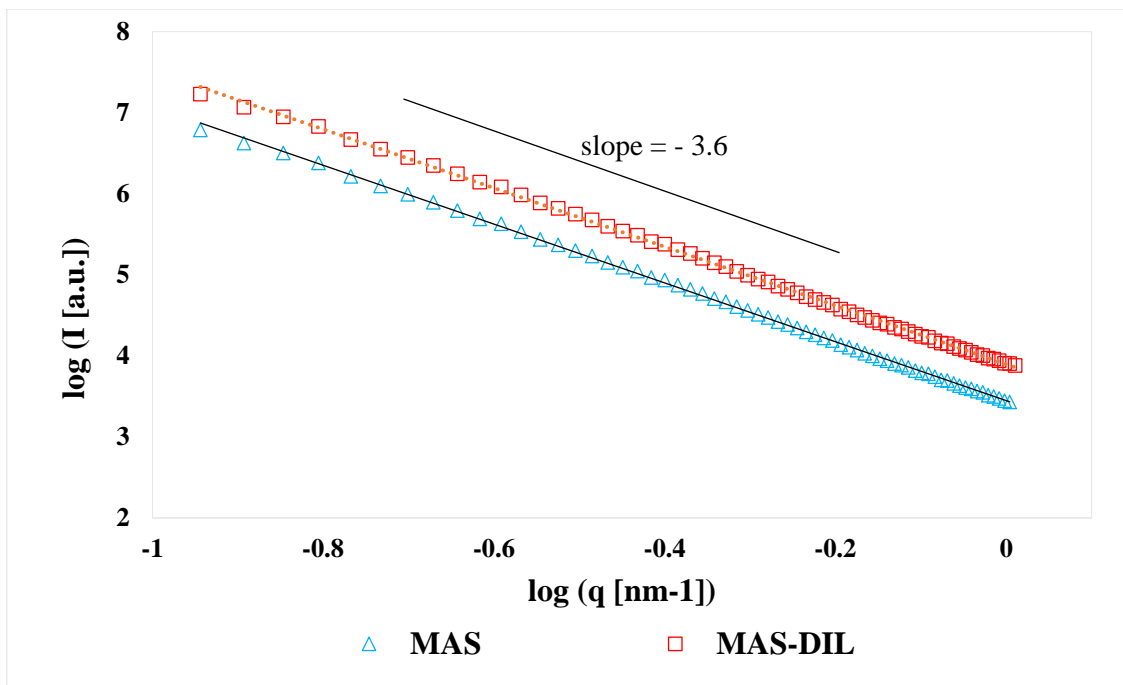


**Fig. 4.13.** Double-logarithmic plot of intensity vs. the scattering vector for MAS and MAS-DIL complexes in powder form (particle size  $63 - 125 \mu\text{m}$ ), showing the slope of the linear part for the data which allows the calculation of the power-law constant  $a$  as  $-3.63$  for MAS and  $-3.62$  for MAS-DIL complexes

Slope determination from the double logarithmic plot of intensity vs. the scattering vector allowed for the calculation of the surface fractal dimension  $D_s$  value for MAS-DIL complexes. Hence, upon calculation as described in chapter 3, section 3.2.6.1., a surface fractal dimension  $D_s$  of 2.38 was obtained for MAS-DIL complexes, suggesting that the sample tested was surface fractal over a length scale of 0.1 nm to 1.0 nm. The value also indicates an irregular, rough and space filling surface, and was very similar to the surface fractal dimension  $D_s$  value obtained for MAS ( $D_m = 2.37$ ). The similarity of surface fractal dimension values between the samples (MAS compared to MAS-DIL complexes) may create difficulties in differentiating between the two samples, hence not being an accurate indicator of DIL absorption onto clay.

#### 4.2.6.2. Liquid-state nanometre scale morphology

Data acquired from the MAS dispersion (0.050 % w/v) is presented and discussed in chapter 3, section 3.2.6.2.

Data acquired from the flocculated complexes formed between MAS and DIL (1:1 w/w), was represented using a Guinier plot ( $\log(I)$  vs.  $q^2$ ). The shape of the curve did not follow a linear dependence over the whole range of  $q$ , showing two linear regions separated by a transition region (Fig. 4.14.). This behaviour suggests poly-dispersive systems in which cluster size is variable, with large cluster aggregates in the samples (Odo *et al.*, 2015). No peaks or other specific features were observed.

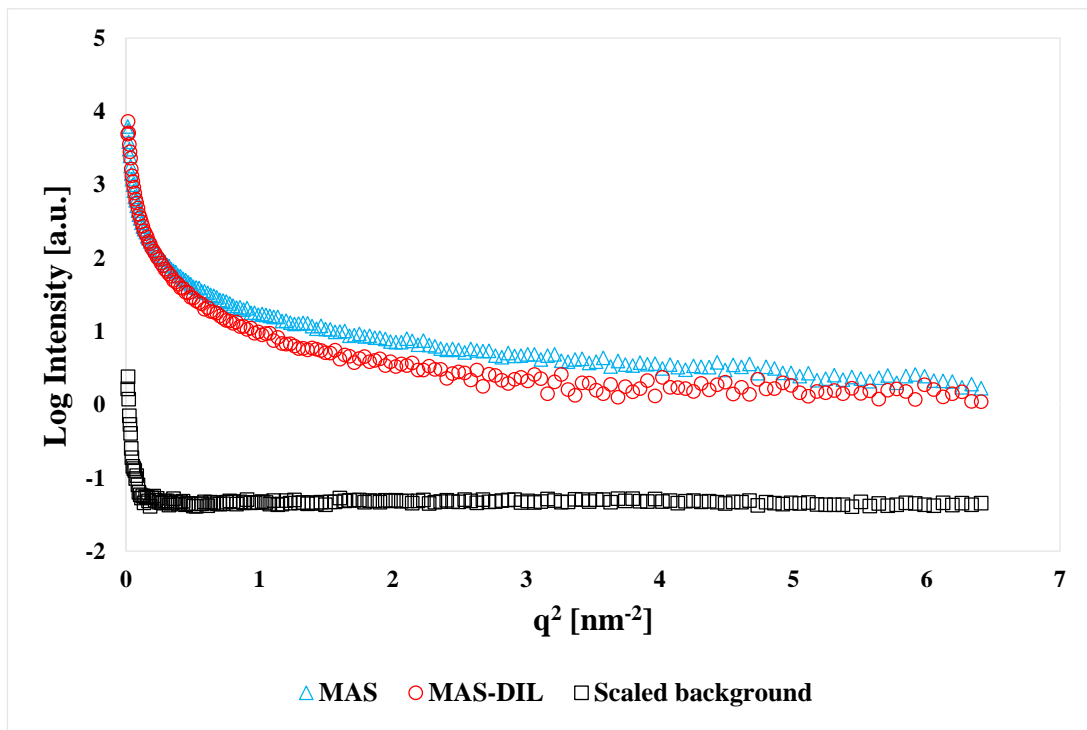


**Fig. 4.14.** Guinier plot of MAS dispersion (0.25 % w/v) and MAS-DIL complex dispersion (containing 0.25 % w/v MAS and 0.25 % w/v DIL) showing two linear regions in the high and low  $q$  values

The analysis of the data in the form of double logarithmic plot of intensity ( $\log I$  [a.u.]) vs. the scattering vector ( $\log \{q\} [\text{nm}^{-1}]$ ) for the MAS-DIL flocculates followed straight lines with no peaks or other specific features, indicating power-law scattering behaviour (Fig. 4.15.). This behaviour was also observed following the analysis of the MAS dispersion (Fig. 4.15.).

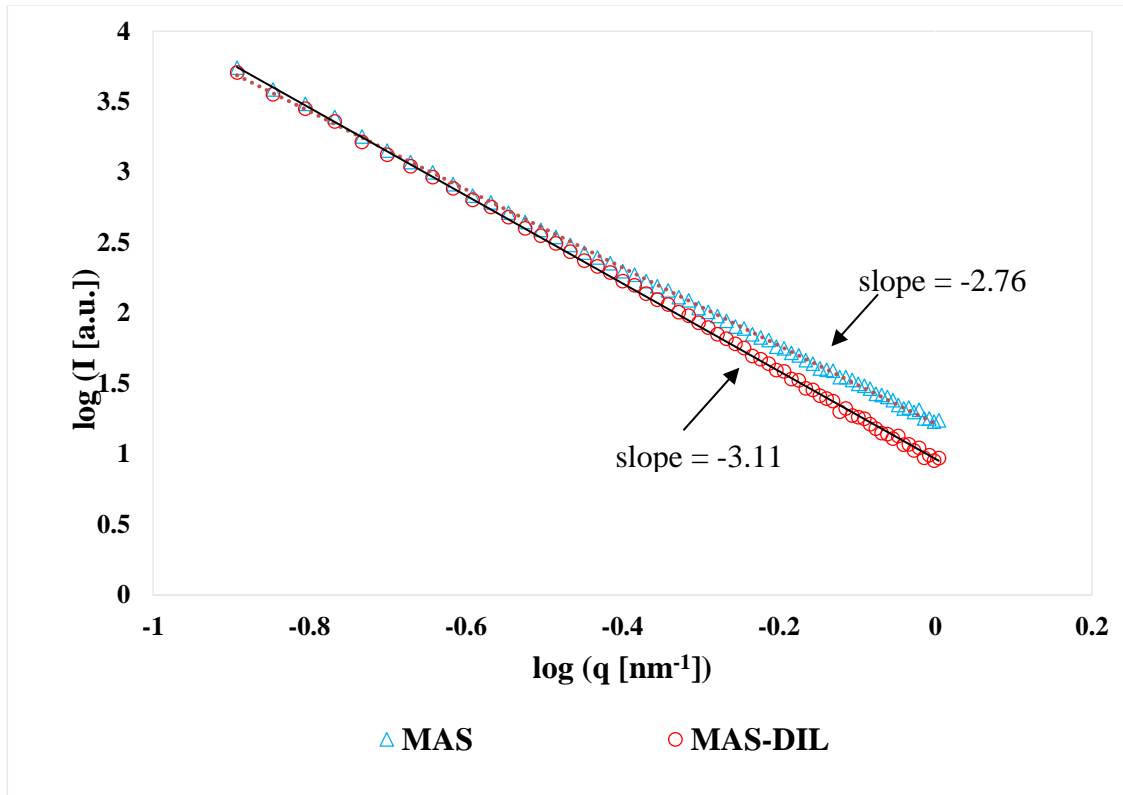


**Fig. 4.15.** Double-logarithmic plot of intensity vs. the scattering vector for MAS and MAS-DIL complexes (containing 0.25 % w/v MAS and 0.25 % w/v DIL) in liquid form, showing power law behaviour

A slope of  $-3.11$  was obtained for the MAS-DIL complex dispersion, which was considerably different from the one obtained for MAS ( $-2.76$ ). The difference in results shows a difference in structure, with the MAS-DIL complex dispersion having a more complex structure. This behaviour was expected since the MAS flocculated upon the addition of the DIL solution.

#### 4.2.7. Microscopy

The initial analysis of the MAS dispersion using digital microscopy (Fig. 4.17. b) allowed the observation of clay particles dispersed in water forming a colloidal structure, described in literature as the ‘house of cards’ through the attraction between the negatively charged faces and the partially positive edges of the clay platelets (Fig. 4.17. a) (Vanderbilt Minerals, 2014). Following DIL addition, the initially monodispersed particles start aggregating as flocs start forming after only 2 min (Fig. 4.16. d), due to the destabilisation of the ‘house of

cards' structure formed in water upon clay hydration (Rojtanatanya and Pongjanyakul, 2010). With time, flocs were observed to get larger, more porous and spread out as the particles clustered together (Fig. 4.16. e-g). After 24 h, a decrease in the size of the flocculated clustered particles was observed as loosely bound aggregates that "break off" and reattach to other aggregates in a more stable form (Fig. 4.17. h-j) (Chakraborti, 2005).

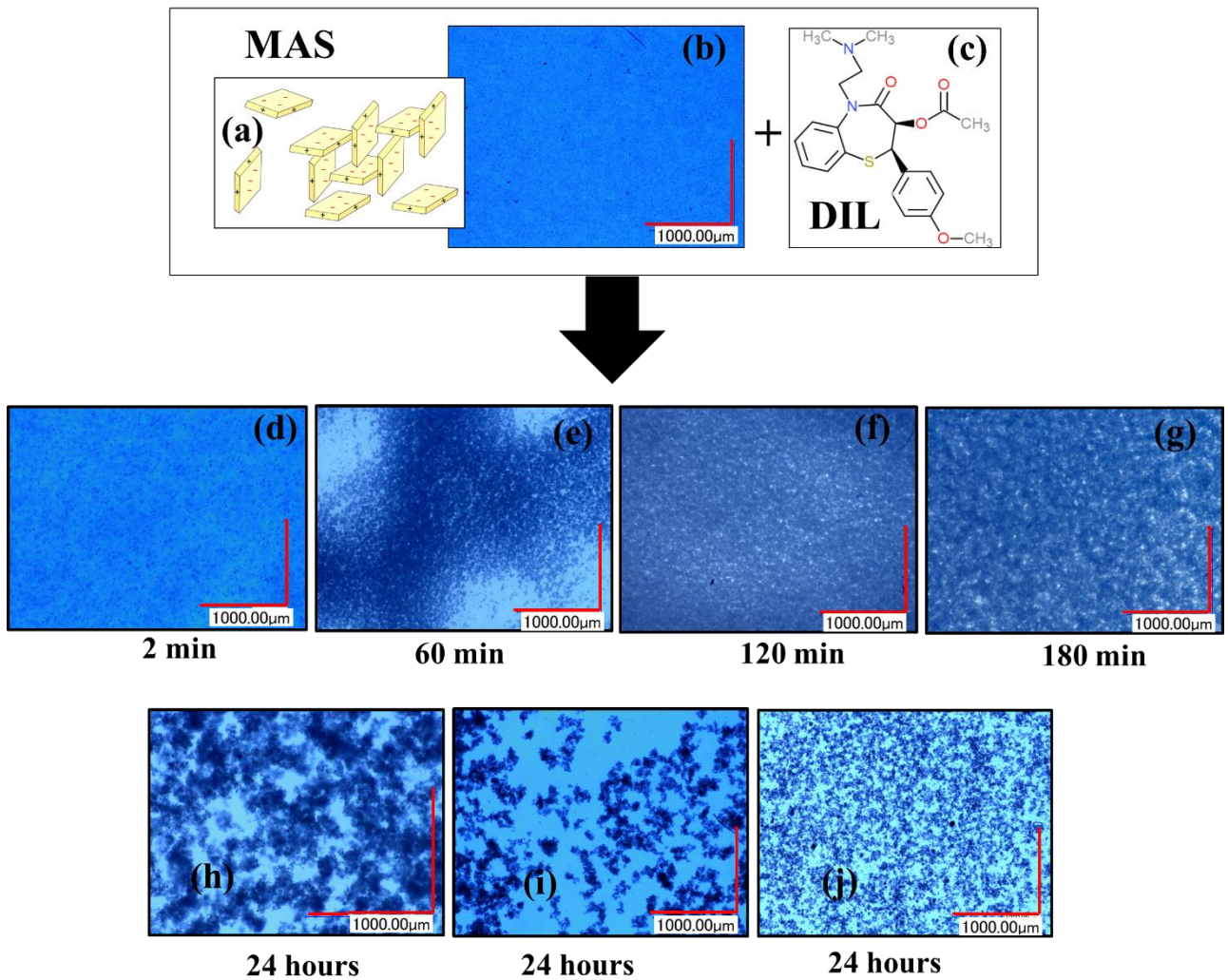


**Fig. 4.16.** Scheme of the 'house of cards' formed upon MAS dispersion in water: adapted from (Vanderbilt Minerals, 2014) (a); Chemical representation of DIL structure (c); Digital microscopy images of MAS (b) and complexes formed between MAS and DIL at different times of aggregation (d – j)

#### 4.2.8. Calorimetric binding studies

##### 4.2.8.1. Calorimetric single injection mode (SIM) binding studies between MAS and DIL

SIM experiments confirmed that binding occurred between MAS and DIL (Fig. 4.17.). The binding isotherm between MAS and DIL was shown to be highly exothermic at the pH values studied. The power signal returned to baseline faster at pH 9 compared with pH 5 and 7, indicating a more rapid interaction. Considering the ionisation of DIL, a more favourable interaction at pH 9 implies that DIL is more readily adsorbed onto MAS via hydrogen bonding and water bridging with the drug being mainly present in solution in its unionised form at this pH. This may be explained by the increased length of the alkyl ammonium chain and large molecular weight (MW) of DIL, which was shown to result in a greater contribution to adsorption onto the clay via Van der Waals forces in previous studies (Theng, 1972; Yariv and Harold, 2001).

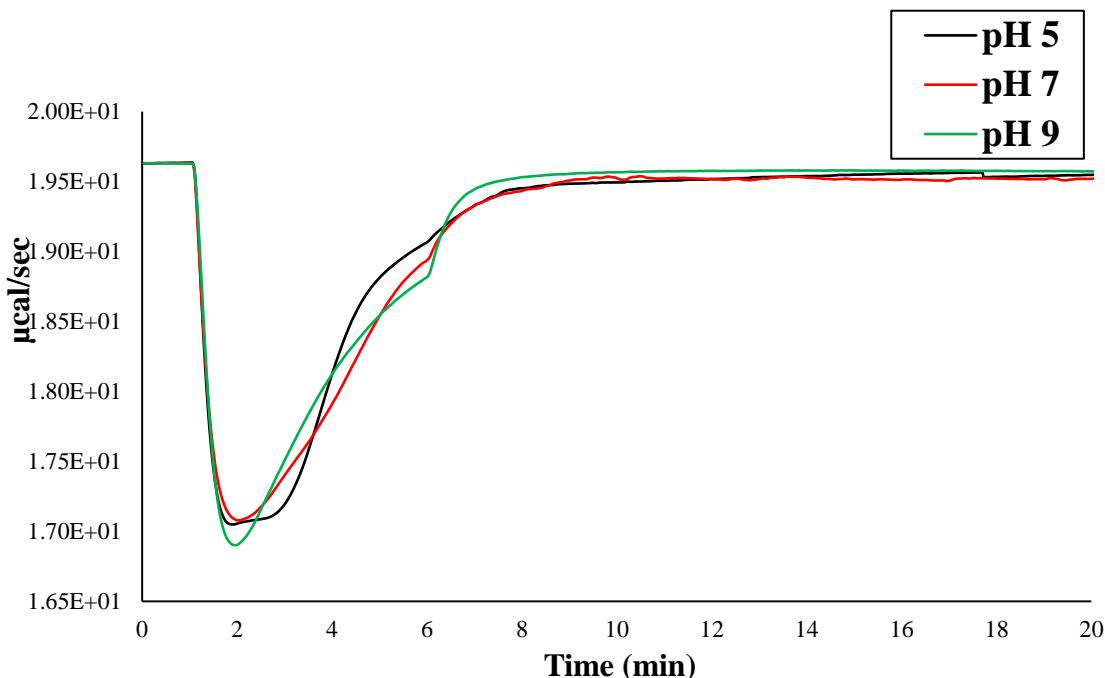


**Fig. 4.17.** Titration of 0.045 % w/v (1 mM) DIL solution (pH 5) into 0.010 % w/v MAS dispersion pH 5 (black), pH 7 (red) and pH 9 (green) at 25 °C

#### 4.2.8.2. Calorimetric multiple injection mode (MIM) binding studies

The binding between MAS and DIL was further explored in detail using MIM stepwise experiments at pH 5 and at 25 °C. The working pH was chosen based on drug ionisation, DIL being mostly ionised in solution at pH 5 ( $pK_a$  7.8) and hence, expected to interact with the negatively charged faces of MAS platelets (Vanderbilt Minerals, 2014; ACD I-Lab, 2018). Experiments confirmed the binding and showed the presence of more than one binding event at both a higher and lower concentration (Fig. 4.18. a and 4.19. b). The experiment at low concentration (Fig. 4.18. b) allowed the highly detailed observation of the binding events, confirming that there were no other additional processes taking place. Control binding experiments showed no interaction between MAS dispersion and water, and between DIL solution and water at pH 5 and 25 °C.

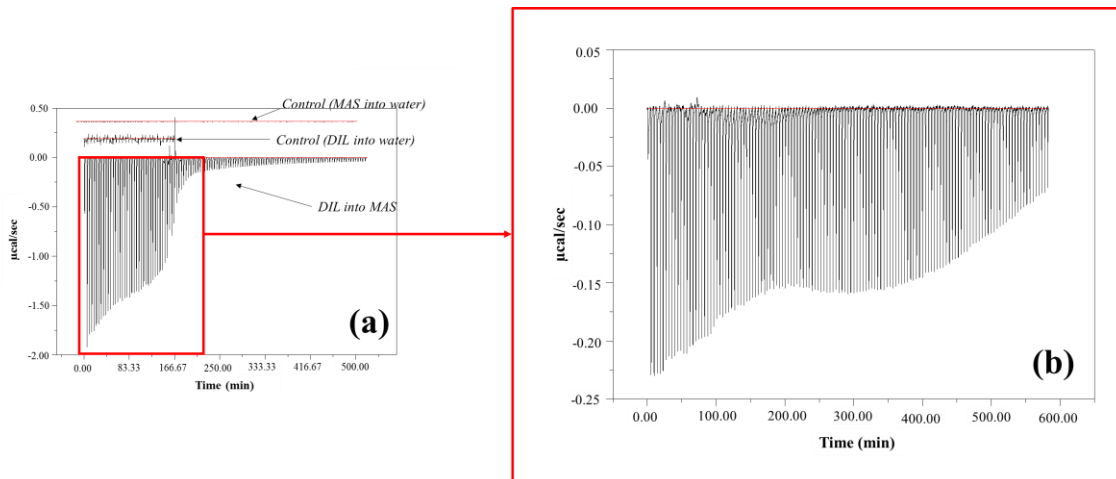


**Fig. 4.18.** ITC raw data showing: titration of 0.144 % w/v (3.2 mM) DIL into 0.036 % MAS and blank titrations (water into MAS 0.036 % w/v and DIL 0.144 % w/v (3.2 mM) into water) (a); titration of 0.020 % w/v (0.45 mM) DIL into 0.010 % w/v MAS (b). All experiments were undertaken at pH 5 and 25 °C.

The presence of multiple binding events following MAS-DIL binding was not observed in the ITC SIM experiments (section 4.2.8.1.), hence emphasising the importance of MIM stepwise experiments in describing chemical interactions in detail.

A competitor binding model (Fig. 4.2.) was fitted to the data to determine the thermodynamic parameters of the reaction. For this analysis it was assumed that the two different types of clay within MAS (montmorillonite and saponite) placed into the sample cell may potentially

interact differently upon the addition of DIL. This assumption was made based on the isomorphic substitution of a limited number of octahedral  $\text{Al}^{3+}$  with  $\text{Mg}^{2+}$  in montmorillonite and the substitution of a limited number of tetrahedral  $\text{Si}^{4+}$  by  $\text{Al}^{3+}$  in saponite, naturally balanced by exchangeable  $\text{Na}^+$  ions that can be easily displaced and replaced, giving the clay the ability to act like a reservoir.

Initially the concentrations of both clays were considered equal to total MAS, that is,  $[\text{B}]=[\text{M}]=[\text{MAS}]$  and AFFINImeter was used to fit the data with the competitive model using  $\text{rb}$  and  $\text{rm}$  (the correction of the nominal concentration of the compounds in the cell) as fitted parameter with the following constraint  $\text{rb} + \text{rm} = 1$  (Fig. 4.19). The fitting of  $\text{rb}$  and  $\text{rm}$  allows the calculation of the real concentration of both kinds of clay.

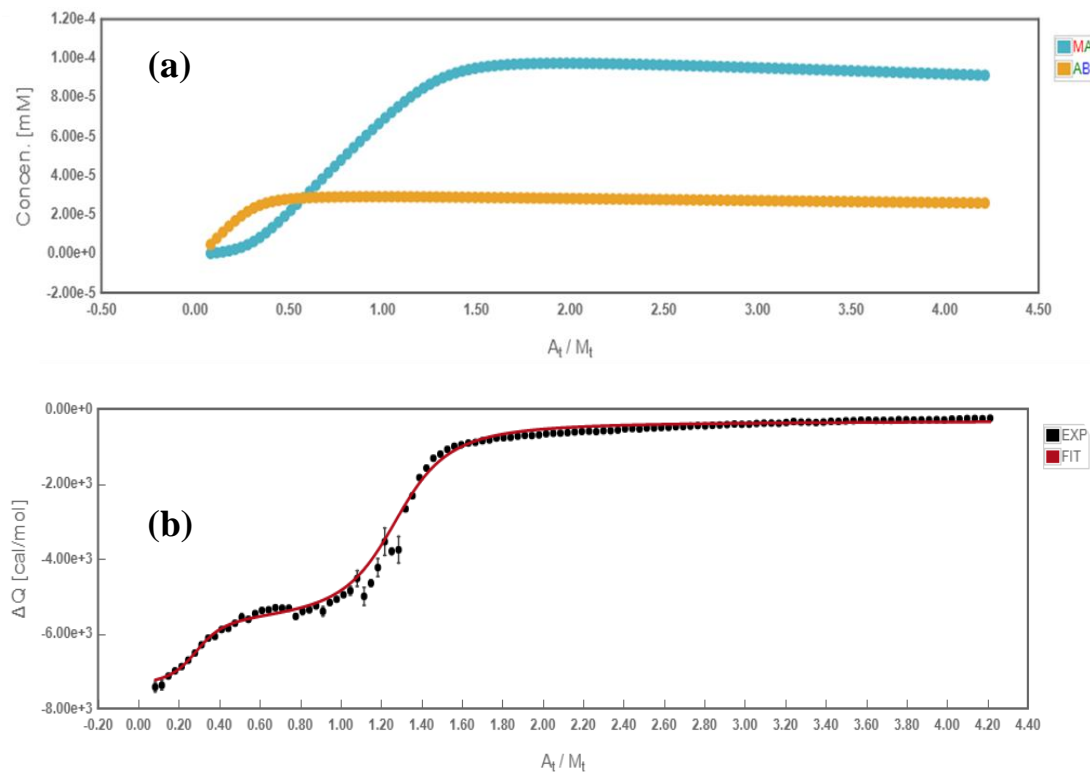


**Fig. 4.19.** Species distribution plot showing the binding between ligand A (DIL) and macromolecules M and B (MAS mixture of montmorillonite and saponite) reaching saturation point (a); Thermodynamic profile through a competitive curve fitting model for adsorption of DIL solution (0.144 % w/v (3.2 mM)) pH 5 onto MAS dispersion (0.036 % w/v) pH 5 at 25 °C (b)

The analysis revealed that approx. 24 % of the MAS interacts stronger with DIL ( $K_a=2.5E+7 \pm 1.1 E+6$  M) and 76% of MAS interacts weaker with DIL ( $K_a=4.7E+5 \pm 7.59 E+3$  M) (Table 4.4.). The binding events had similar negative enthalpies ( $-6.71 E+3 \pm 1.29 E+1$  kcal/mol and  $-8.94 E+3 \pm 2.18 E+1$  kcal/mol) and negative entropies ( $-9.28E2$  kcal/mol and  $-1.02E3$  kcal/mol), suggesting that in both cases the binding was enthalpy driven, as high energy resulting from broken and created hydrogen bonds and electrostatic Van der Waals interactions and had a slight entropic contribution (Table 4.4.). This implies that montmorillonite and saponite are able adsorb DIL through a similar mechanism which may be due to their similar structure. The presence of two binding events upon the adsorption of a cationic compound onto MAS has not been reported in literature before.

Another explanation for the presence of two binding events in the ITC experiments upon DIL interaction with MAS may be due to the hydrolysis of DIL in solution, hence the interaction of both DIL and DC-DIL with the MAS. However, this is very unlikely as in recovery studies (section 4.2.5.2) no degradation of DIL was observed in standard solutions prepared in ultra-pure water at pH 5 (all solutions used for the ITC studies were freshly prepared in a similar manner 30 min before each experiment as described in chapter 2, section 2.2.2.8.1). Furthermore, the stability of diltiazem at pH 5 has also reported in literature (Suleiman *et al.*, 1990). The details of the kinetics associated with the degradation of DIL is reported elsewhere and is out of the scope of this study (Suleiman *et al.*, 1990)

**Table 4.4.** Multiple injection mode calorimetric binding studies studying the adsorption of DIL (0.144 % w/v (3.2 mM)) onto MAS (0.036% w/v) at 25°C (pH 5). Data analysed through a competitive curve fitting model to calculate affinity (K) and changes in enthalpy ( $\Delta H$ ) and entropy ( $-T\Delta S$ ).

Reaction	r	$K_a$		
			[M <sup>n</sup> ]	[cal/mol]
<b>M +A ↔ MA</b>	0.76	$4.80 E+5 \pm 7.59 E+3$	$-6.71 E+3 \pm 1.29 E+1$	$-9.28E+2$
<b>A+ B ↔ AB</b>	0.24	$2.54 E+7 \pm 1.10 E+6$	$-8.94 E+3 \pm 2.18 E+1$	$-1.02E+3$

The change in the experimental temperature from 25 °C to 37 °C had no major effects on the binding between MAS and DIL, as very similar values were obtained upon the calculation of affinity ( $K$ ), changes in enthalpy ( $\Delta H$ ) and entropy ( $-T\Delta S$ ) through the fitting a competitive model to the data (Fig. 4.20. and Table 4.5.)

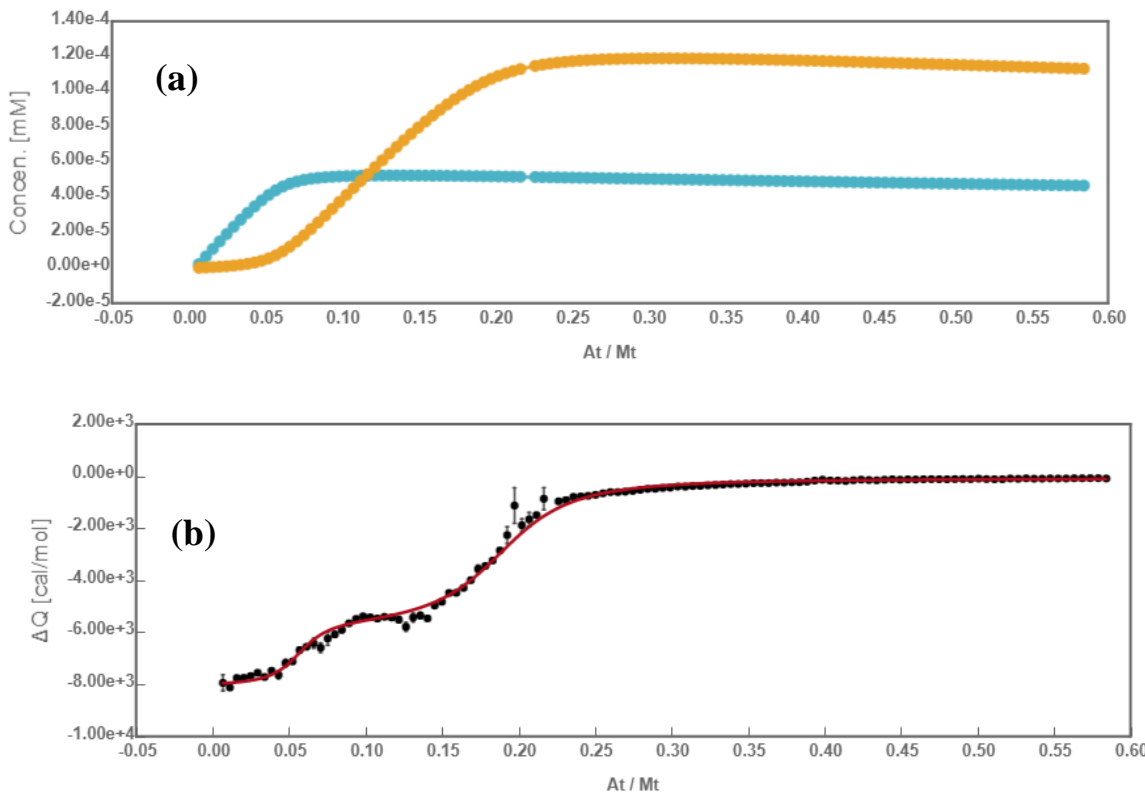


**Fig. 4.20.** Species distribution plot showing the binding between ligand A (DIL) and macromolecules M and B (MAS mixture of montmorillonite and saponite) reaching saturation point (a); Thermodynamic profile through a competitive curve fitting model for adsorption of DIL solution (0.144 % w/v (3.2 mM)) pH 5 onto MAS dispersion (0.036 % w/v) pH 5 at 37 °C (b)

**Table 4.5.** Multiple injection mode calorimetric binding studies studying the adsorption of DIL (0.144 % w/v (3.2 mM)) onto MAS (0.036% w/v) at 25°C (pH 5). Data analysed through a competitive curve fitting model to calculate affinity (K) and changes in enthalpy ( $\Delta H$ ) and entropy (-T $\Delta S$ ).

Reaction	r	K <sub>a</sub>	H	-T $\Delta S$
		[M <sup>n</sup> ]	[cal/mol]	[cal/mol]
M + A ↔ MA	0.37	2.35 E+5 ± 1.95 E+3	-5.68 E+3 ± 1.37 E+1	-2.19E+3
A + B ↔ AB	0.63	1.77 E+7 ± 2.32 E+6	-7.94 E+3 ± 2.56 E+1	-1.83E+3

Based on the results, it can be concluded that DIL is expected to be adsorbed onto MAS via cation exchange due to the presence of one amine group, as well as via hydrogen bonding and water bridging, and an interaction model may be proposed (Fig. 4.21.) (Rojtanatanya and Pongjanyakul, 2010).

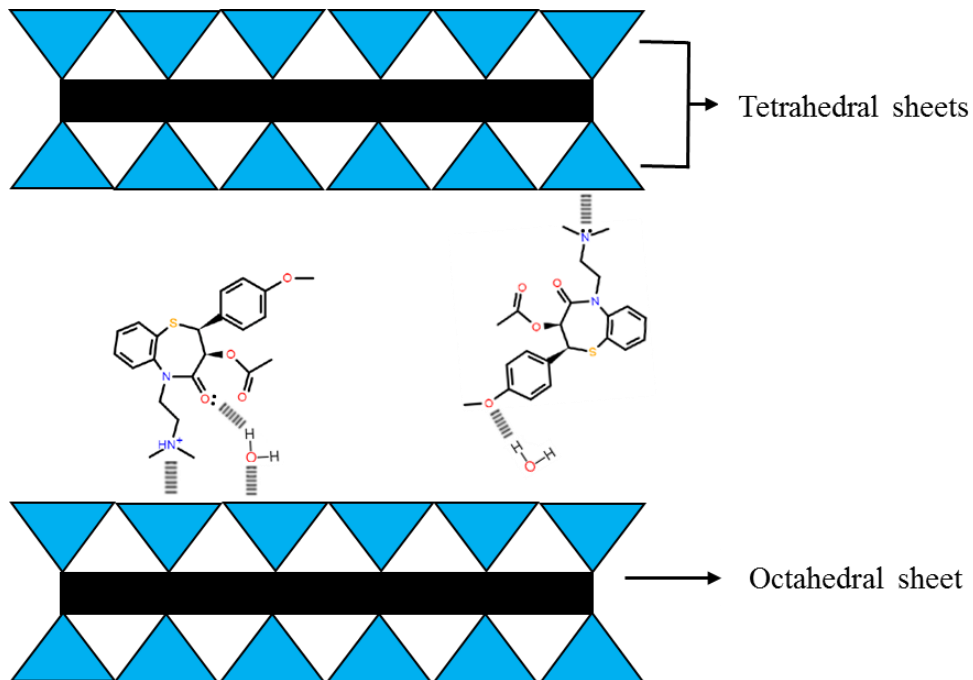


**Fig. 4.21.** Possible DIL-MAS chemical interaction: cation exchange, hydrogen bonding and water bridging

#### **4.2.8.3. Effects of PEO on the adsorption of DIL onto MAS**

\*\*Binding between MAS and PEO, MAS and water, and PEO and water:

*Results are presented in chapter 3, section 2.2.1.*

The interaction between MAS and PEO at 25 °C was shown to be exothermic. Non-constant heats and non-sigmoidal curve suggested that PEO can weakly bind to MAS and form a complex by intercalation of PEO particles between the MAS platelets (Fig. 4.22.) (Gao, 2004). The binding isotherm showed non-constant heats at the end of titration in the presence of excess PEO. This could be due to the aggregation of the PEO-MAS mixture or a contribution of the PEO self-aggregation in water at pH 5.

PEO dilution into water at pH 5 (25 °C) (Fig. 4.22.) showed a monotonous decrease of ITC heat signals without a sigmoidal behaviour, suggesting that PEO self-associates weakly in aqueous solution. Due to its amphiphilic structure (hydrophobic backbone and hydrophilic side groups), PEO may show a tendency to self-aggregate in aqueous solution, even at a very low concentration.

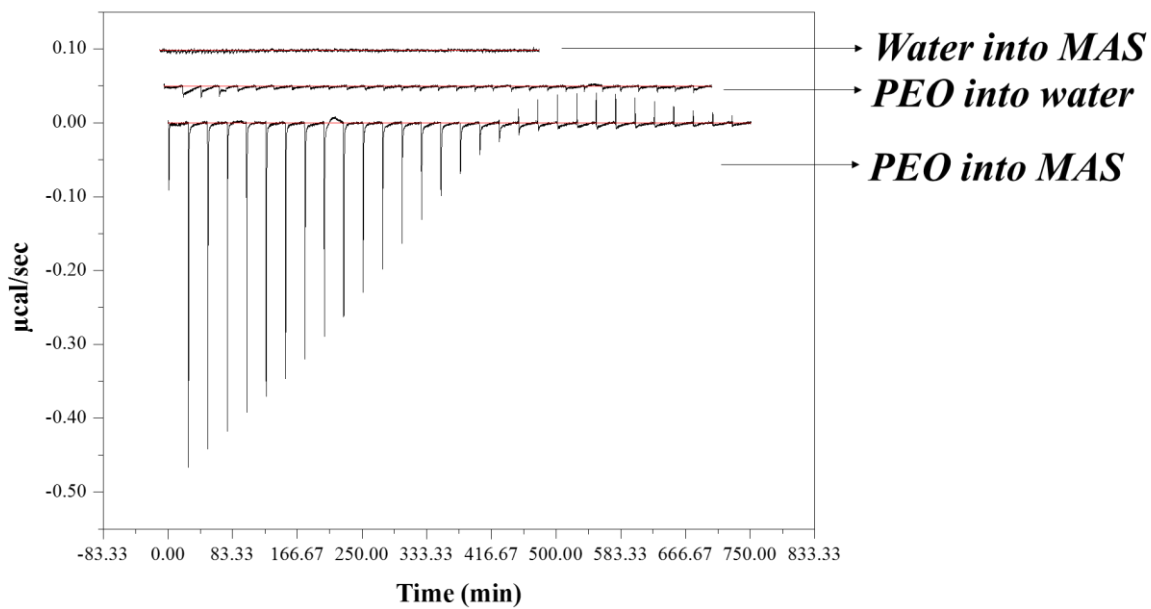


**Fig. 4.22.** Raw data for titration of 0.037 % w/v PEO dispersion (pH 5) into 0.037 % w/v MAS dispersion (pH 5) at 25 °C; Control run between 0.037 % w/v PEO dispersion solution (pH 5) and water (pH5) at 25 °C and between 0.037 % w/v MAS dispersion solution (pH 5) and water (pH5) at 25 °C.

The simple binding experiment between DIL and PEO (Fig. 4.23.) was linked the data showing the effects of PEO on DIL adsorption onto MAS (Fig. 4.24. Hence, a competitive binding model was fitted to the data showing the binding between MAS, DIL and PEO, using the parameters obtained following the fitting of a one set of sites model to the data showing DIL and PEO binding. Results showed that the binding between DIL and PEO was enthalpy and entropy driven (Table 4.6.). Furthermore, the binding between MAS and DIL in the presence of PEO was shown to be enthalpy driven and entropically unfavourable, which was also the case for the binding between MAS and PEO (Table 4.6.). This behaviour suggests that the entropic effects observed in the simple MAS-DIL binding experiment (negative  $-T\Delta S$ ) are reduced upon the addition of the polymer to the mixture. It should however be noted that further experimental design to reduce the concentrations of compounds in the cell and syringe (MAS-PEO and DIL respectively) would allow for a

better observation of the expected binding events between MAS and DIL, MAS and PEO and DIL and PEO.

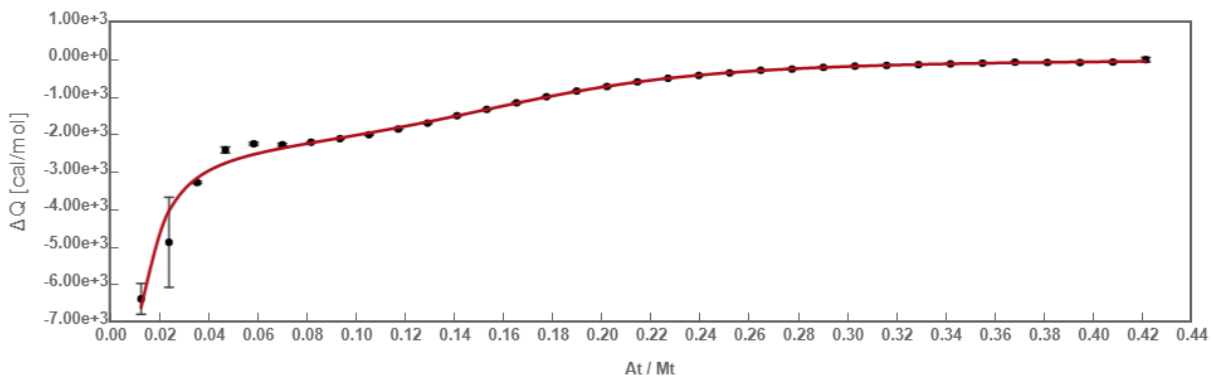


**Fig. 4.23.** Thermodynamic profile through a competitive curve fitting model for adsorption of DIL solution (0.090 % w/v (2 mM)) pH 5 onto MAS-PEO mixture (0.037 % w/v MAS and 0.020 % w/v PEO mixed together at a ratio of 1:1 v/v) pH 5 at 25 °C

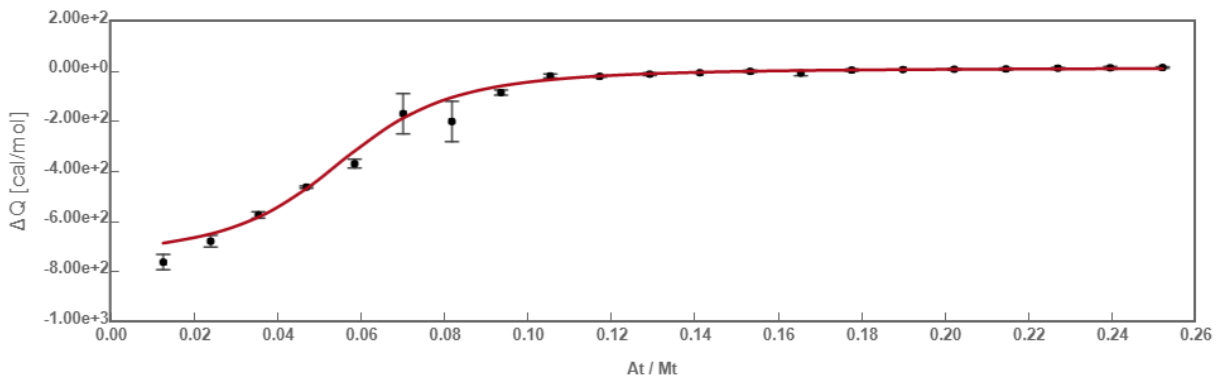


**Fig. 4.24.** Thermodynamic profile through a one set of sites curve fitting model for adsorption of DIL solution (0.090 % w/v (2 mM)) pH 5 onto PEO dispersion (0.020 % w/v) pH 5 at 25 °C

**Table 4.6.** Calorimetric binding studies evaluating the adsorption of DIL (0.090 % w/v (2 mM)) onto MAS (0.036 % w/v) at 25°C (pH 5). Data analysed through a competitive curve fitting model to calculate affinity (K) and changes in enthalpy ( $\Delta H$ ) and entropy (-T $\Delta S$ ).

Reaction	r	$K_a$	H		-T $\Delta S$
			[M <sup>n</sup> ]	[cal/mol]	
<b>M + A ↔ MA</b>	0.06	5.2897E+5 ± 4.7516E+4	-6.9949E+4 ± 7.8197E+3	6.23E+04	
<b>*A + B ↔ AB</b>	0.05	1.7682E+5 ± 1.9010E+3	-8.6260E+2 ± 5.4944E+0	-6.19E+03	
<b>M + B ↔ MB</b>	0.06	8.7715E+5 ± 1.1242 E+5	-6.8785E+4 ± 7.8152E+3	6.08E+04	

\*binding parameters for DIL binding to PEO

#### 4.2.8.4. Effects of XG on the adsorption of DIL onto MAS

Previous experiments presented in Chapter 3 showed no interactions taking place between XG and MAS (chapter 3, section 3.2.8.4.1., Fig. 3.28.).

Following titration of XG dispersion (0.20 % w/v) into MAS dispersion (0.37 % w/v) at pH 5 and 25 ° C no interaction was observed between the anionic polysaccharide and the negatively charged MAS (Fig. 4.25.). The mixture between MAS and XG was shown to be visually homogenous with no precipitation being observed in the calorimetric cell at the end of the experiment (Vanderbilt Minerals, 2009).

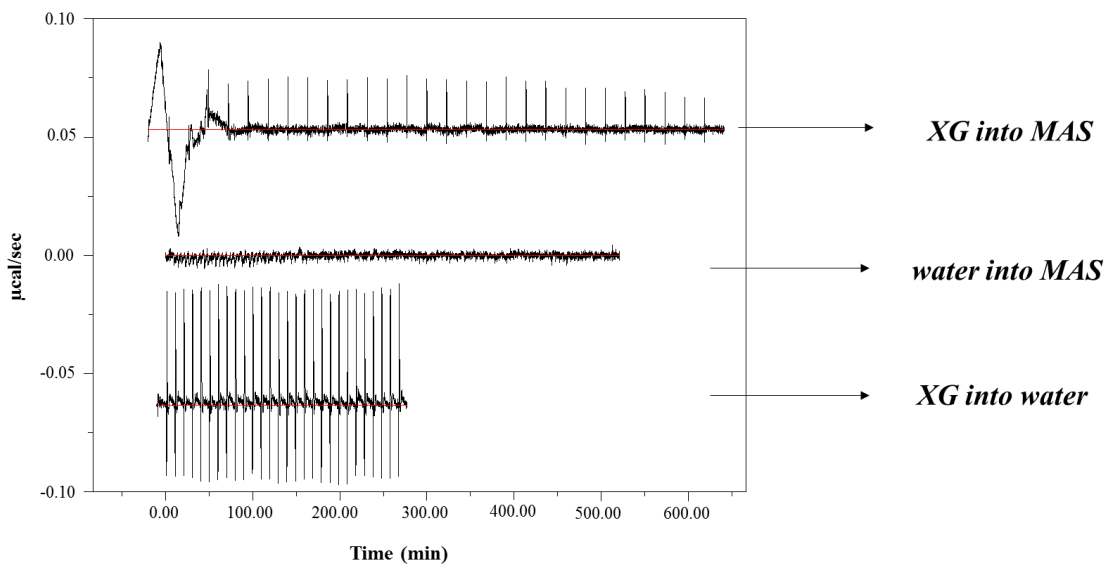


**Fig. 4.25.** Raw data for titration of 0.020 % w/v XG dispersion (pH 5) into 0.037 % w/v MAS dispersion (pH 5) at 25 °C, control run between 0.020 % w/v XG dispersion (pH 5) and water (pH 5) at 25 °C and control run between 0.037 % w/v MAS dispersion (pH 5) and water (pH5) at 25 °C

Constant dilution heats were observed for MAS (0.037 % w/v) dilution into water, showing no aggregation behaviour for MAS in water at pH 5 (25 °C) (Fig. 4.25). Furthermore, control binding studies at pH 5 and 25 °C between water at pH 5 and XG dispersion (0.20 % w/v) showed very little evidence of binding/self-association through small heats of dilution (Fig. 4.26.).

Titration of DIL solution (0.090 % w/v (2 mM)) into XG dispersion (0.020 % w/v) at 25 °C and pH 5 showed the presence of small heats of dilution, which implies very little evidence of binding/self-association (Fig. 4.26.). No binding was further observed between DIL (0.144 % w/v (3.2 mM) and water at 25° C and pH 5 (Fig. 4.26.).

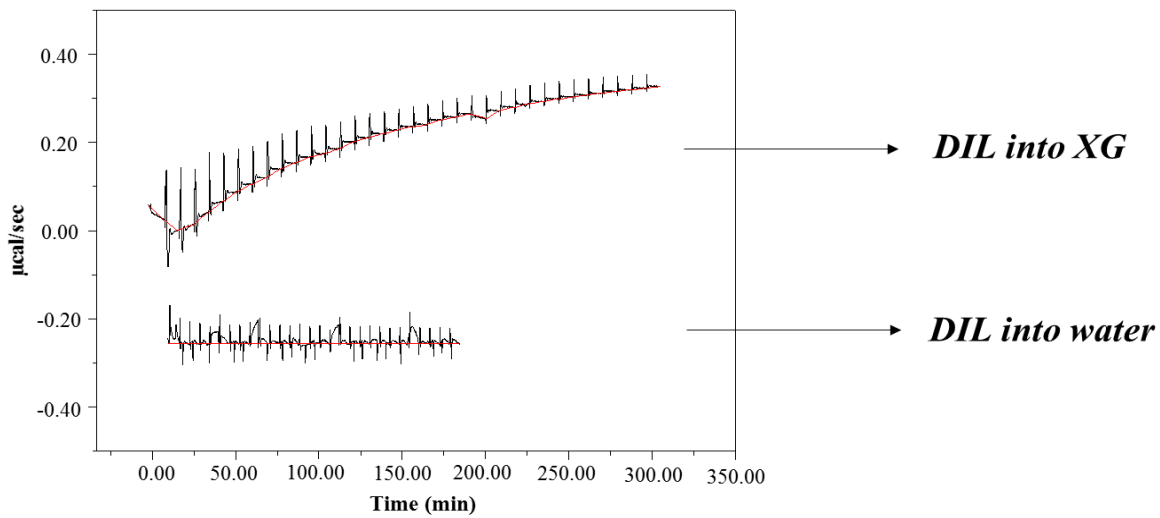


**Fig. 4.26.** Raw data for titration of 0.090 % w/v (2 mM) DIL solution (pH 5) into 0.020 % w/v XG dispersion (pH 5) at 25 °C and control run between (0.144 % w/v (3.2 mM) (pH 5)) DIL solution and water (pH5) at 25 °C

The adsorption of DIL onto MAS in the presence of XG was shown to be highly exothermic. Two binding events were observed similar to the simple MAS-DIL binding experiment. A competitor binding model (Fig. 4.2.) was fitted to the data to determine the thermodynamic parameters of the reaction, considering that the two different types of clay within MAS (montmorillonite and saponite) placed into the sample cell may potentially interact differently upon the addition of DIL ( Fig. 4.27.).

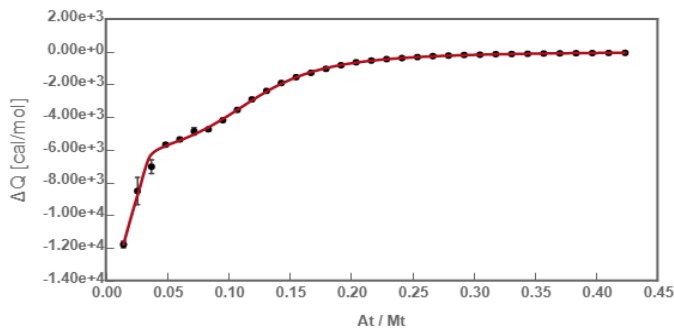


**Fig. 4.27.** Thermodynamic profile through a one set of sites curve fitting model for adsorption of DIL solution (0.090 % w/v (2 mM)) pH 5 onto MAS-XG mixture (0.037 % w/v MAS and 0.020 % w/v XG mixed together at a ratio of 1:1 v/v) pH 5 at 25 °C

The binding was shown to be enthalpy driven and entropically unfavourable (Table 4.7.), which implies that the hydrophobic effects observed in the simple MAS-DIL experiments (negative  $-T\Delta S$ ) are reduced upon the addition of the XG to the reaction (mixed with MAS prior to DIL addition).

**Table 4.7.** Multiple injection mode calorimetric binding studies studying the adsorption of DIL (0.090 % w/v (2 mM)) onto MAS-XG mixture (0.037 % w/v MAS and 0.020 % w/v XG mixed together at a ratio of 1:1 v/v) at 25°C (pH 5). Data analysed through a competitive curve fitting model to calculate affinity ( $K$ ) and changes in enthalpy ( $\Delta H$ ) and entropy ( $-T\Delta S$ ).

Reaction	r	$K_a$		
			$[M^{-n}]$	$[cal/mol]$
$M + A \leftrightarrow MA$	0.10	$8.34 E+4 \pm 1.85 E+3$	$-6.80 E+3 \pm 3.53 E+1$	$1.83 E+2$
$A + B \leftrightarrow AB$	0.02	$1.74 E+7 \pm 2.4 E+7$	$-1.24 E+4 \pm 6.76 E+2$	$2.66 E+3$

### **4.3. Conclusions**

Results confirmed the ability of the MAS to adsorb DIL onto its surface and form flocculates in the MAS dispersion.

The flocculates were dried and characterised using a wide variety of techniques such as ATR-FTIR, PXRD, DSC, SEM/EDX, HPLC, SAXS which all confirmed changes as a result of the binding process which may have benefits for drug release.

The SIM and MIM ITC experiments revealed that the binding phenomenon between DIL and MAS was predominantly enthalpically driven as high energy resulted from broken and created hydrogen bonds and electrostatic interactions, with a slight entropic contribution. Two binding events upon MAS and DIL binding were observed in the ITC MIM experiments, which could not be seen in the ITC SIM experiments and may be caused by DIL adsorption onto the two different types of clays found in the MAS, montmorillonite and saponite.

The ITC experiments also showed binding occurring between PEO and DIL. DIL adsorption onto MAS was shown to be influenced by presence of PEO in the binding experiments between DIL and MAS-PEO mixture. No binding was observed between DIL and XG. Furthermore, the binding between DIL and MAS was shown to be influenced by the presence of the XG in the binding experiments between DIL and MAS-XG, leading to the binding getting more enthalpy driven.

#### 4.4. References

- ACD I-Lab (2018). Available at: <https://ilab.acdlabs.com/iLab2/> (Accessed: 23 September 2018).
- Bandyopadhyay, A. and Bose, S. (eds) (2013) *Characterization of Biomaterials Chapter 4*. Oxford, UK: Elsevier.
- Bohor, B. F. and Hughes, R. E. (1971) ‘Scanning Electron Microscopy of Clays and Clay Minerals’, *Clays and Clay Minerals*, 19(1969), pp. 49–54.
- Chakraborti, R. (2005) ‘Effects of Floc Size and Shape in Particle Aggregation’, in Droppo, G. et al. (eds) *Flocculation in Natural and Engineered Environmental Systems*. Boca Raton, Florida: CRC Press, pp. 95–120.
- Chatpalliwar, V. A., Porwal, P. K. and Upmanyu, N. (2012) ‘Validated gradient stability indicating HPLC method for determining Diltiazem Hydrochloride and related substances in bulk drug and novel tablet formulation’, *Journal of Pharmaceutical Analysis*, 2(3), pp. 226–237.
- Ermer, J. and Ploss, H. J. (2005) ‘Validation in pharmaceutical analysis: Part II: Central importance of precision to establish acceptance criteria and for verifying and improving the quality of analytical data’, *Journal of Pharmaceutical and Biomedical Analysis*, 37(5), pp. 859–870.
- Gao, F. (2004) ‘Clay/polymer composites: The story’, *Materials Today*, 7(11), pp. 50–55.
- McCalley, D. V. (2010) ‘The challenges of the analysis of basic compounds by high performance liquid chromatography: Some possible approaches for improved separations’, *Journal of Chromatography A*, 1217(6), pp. 858–880.
- Mita, A. R. A., Rupa, A. K. and Achowicz, R. J. (2010) ‘Preliminary Approach to Application of Modified Smectite Clay to Form Tablets in Direct Compression Process’, pp. 366–368.
- Odo, E. A. et al. (2015) ‘SAXS Study of Silicon Nanocomposites’, 5(3), pp. 65–70.
- Pharmaceutical, S., Europe, T. and Collection, I. (2008) ‘A stability-indicating HPLC

procedure for determination of diltiazem ...’, *Pharmaceutical Technology Europe*, 20(3), pp. 38–40, 42–45.

Prasad, M. B. *et al.* (2013) ‘Development and evaluation of diltiazem hydrochloride controlled-release pellets by fluid bed coating process.’, *Journal of advanced pharmaceutical technology & research*, 4(2), pp. 101–7.

Ray, S. S. *et al.* (2002) ‘New Polylactide / Layered Silicate Nanocomposites . 1 . Preparation , Characterization , and Properties’, *Direct*, 25, pp. 3104–3110.

Rojtanatanya, S. and Pongjanyakul, T. (2010) ‘Propranolol-magnesium aluminum silicate complex dispersions and particles: Characterization and factors influencing drug release’, *International Journal of Pharmaceutics*, 383(1–2), pp. 106–115.

Sadeghi, F. *et al.* (2013) ‘Validation and Uncertainty Estimation of an Ecofriendly and Stability-Indicating HPLC Method for Determination of Diltiazem in Pharmaceutical Preparations’, *Journal of Analytical Methods in Chemistry*.

Suleiman, M. S. *et al.* (1990) ‘Degradation Kinetics of Diltiazem’, *Drug Development and Industrial Pharmacy*, 16(4), pp. 685–694.

Theng, B. K. G. (1972) ‘Formation, properties, and practical applications of clay—organic complexes’, *Journal of the Royal Society of New Zealand*, 2(4), pp. 437–457.

Totea, A. M. *et al.* (2019) ‘Real time calorimetric characterisation of clay – drug complex dispersions and particles’, *International Journal of Pharmaceutics: X*, 1(December 2018), p. 100003. Available at: <https://linkinghub.elsevier.com/retrieve/pii/S2590156718300033>.

Vanderbilt Minerals (2009) ‘VANZAN® Xanthan Gum’, pp. 1–12.

Vanderbilt Minerals (2014) ‘VEEGUM ® Magnesium Aluminum Silicate VANATURAL ® Bentonite Clay For Personal Care and Pharmaceuticals What They Are’, pp. 1–27.

Yariv, S. and Harold, C. (2001) *Organoclay Complexes and Interactions*. CRC Press.

## ***Chapter 5:***

***Adsorption of metformin hydrochloride onto  
magnesium aluminium silicate***

## **Chapter 5: Adsorption of metformin hydrochloride onto magnesium aluminium silicate**

### **5.1. Methodology**

#### **5.1.1. Formulation of single and double drug loaded MAS-MET complexes**

Please refer to chapter 2, section 2.2.1.

#### **5.1.2. Characterisation of MAS-MET complexes**

##### **5.1.2.1. Attenuated total reflectance Fourier transform infrared spectroscopy (ATR-FTIR)**

Please refer to chapter 2, section 2.2.2.1.

##### **5.1.2.2. Powder X-Ray diffractometry (PXRD)**

Please refer to chapter 2, section 2.2.2.2.

##### **5.1.2.3. Differential scanning calorimetry (DSC)**

Please refer to chapter 2, section 2.2.2.3.

##### **5.1.2.4. Scanning electron microscopy (SEM) with energy dispersive X-ray spectroscopy (EDX)**

Please refer to chapter 2, section 2.2.2.4.

##### **5.1.2.5. High Performance Liquid Chromatography (HPLC)**

Please refer to chapter 2, section 2.2.2.5.

###### **5.1.2.5.1. Method validation**

Please refer to chapter 2, section 2.2.2.5.1.

###### **5.1.2.5.2. Determination of drug content in MAS-MET complex particles**

Please refer to chapter 2, section 2.2.2.5.2.

###### **5.1.2.6. Small angle X-ray scattering (SAXS)**

Please refer to chapter 2, section 2.2.2.6.

###### **5.1.2.7. Microscopy**

Please refer to chapter 2, section 2.2.2.6.

### **5.1.2.8. Calorimetric binding studies**

#### **5.1.2.8.1. Calorimetric single injection mode (SIM) binding studies**

Calorimetric SIM binding studies were performed as described in Chapter 2, section 2.2.2.8.1. MET solution (0.016 % w/v) was added in one 250 µL injection into the sample cell containing MAS dispersion (0.10 % w/v) at each of the pH values studied (pH 5, 7 and 9). The binding isotherm was analysed by comparing the reaction rate for the adsorption of MET onto MAS at the pH values studied.

#### **5.1.2.8.2. Calorimetric multiple injection mode (MIM) binding studies**

Calorimetric MIM binding studies to characterise the adsorption of MET (0.033 % w/v) onto MAS were performed as described in chapter 2, section 2.2.2.8.2. The real-time binding isotherm was studied in 29 injections of 10 µL each into the sample cell every 500 seconds. The reference power applied was 20 µcal/sec. MET solution (0.033 % w/v) was used in the syringe, and the MAS dispersion (0.037 % w/v) was used in the sample cell. One set of sites model was fitted to the data to get thermodynamic parameters which best reproduce the experimental data. Data produced from the blank titrations (dilution of MET (0.033 % w/v) into water was subtracted from the sample titration prior to fitting the data to a one set of sites binding model.

#### **5.1.2.8.3. Effects of PEO and XG on the interaction between MAS and MET**

MIM binding studies were performed to aid the study of the effects of PEO and XG on the adsorption of MET onto MAS and were conducted as described in chapter 2, section 2.2.2.8.3. The binding isotherms between MAS (0.037 % w/v) and PEO (0.037 % w/v) was previously studied in chapter 3, section 3.2.8.3.1. The MET (0.300 % w/v) and PEO (0.020 % w/v) interaction was studied in 30 injections of 10 µL each into the sample cell every 500 seconds. The binding between MET (0.300 % w/v) and MAS-PEO mixture (0.040 % w/v MAS mixed with 0.040 % w/v PEO at a ratio of 1:1 v/v) was studied in 30 injections of 10 µL each into the sample cell every 500 seconds. In all cases the reference power applied was 10 µcal/sec.

The binding isotherms between MAS (0.037 % w/v) and XG (0.020 % w/v) was previously studied in chapter 3, section 3.2.8.4.1. Binding between MET (0.033 % w/v) and XG (0.020

% w/v) was studied in 30 injections of 10 µL each into the sample cell every 500 seconds. The reference power applied was 10 µcal/sec.

The adsorption of MET (0.080 % w/v) onto MAS in the presence of XG was studied using a mixture of MAS-XG (0.040 % w/v MAS dispersion mixed with 0.040 % w/w XG dispersion at a ratio of 1:1 v/v). The interaction was studied in 25 injections of 2 µl each into the sample cell every 500 sec, applying a reference power of 10 µcal/sec. This is all summarised in Table 5.1.

**Table 5.1.** Compounds and parameters used in ITC SIM and MIM experiments

Cell	Syringe		Number of injections	Injection volume (µL)	Spacing (sec)	Reference power (µcal/sec)
Clay/polymer	Concentration (% w/v)	Drug				
MAS	0.016	MET	0.010	1	250	20
MAS	0.037	MET	0.033	29	10	500
PEO	0.020	MET	0.300	30	10	1500
MAS-PEO	0.020 MAS 0.020 PEO	MET	0.150	30	10	500
XG	0.020	MET	0.033	30	10	500
MAS-XG	0.020 MAS 0.020 XG	MET	0.080	25	2	500

## **5.2. Results and discussion**

### **5.2.1. Attenuated Total Reflectance Fourier Transform Infrared Spectroscopy (ATR-FTIR)**

The analysis of the spectrum belonging MET (Fig. 5.1.) showed peaks in the region 1000–1200 cm<sup>-1</sup> representing stretching vibration of the C-N group (Sheela, Muthu and Krishnan, 2010). Peaks in the region 1565 – 1400 cm<sup>-1</sup> can be attributed to the asymmetric deformation of CH<sub>3</sub> groups and N-H in-plane deformation (Gunasekaran *et al.*, 2006). The adsorption bands observed at 1622 and 1580 have been linked to the fact that MET is a biguanide, corresponding to the C=N stretching vibration, whereas peaks observed at 3145, 3292 and 3370 cm<sup>-1</sup> can be assigned to the symmetric and asymmetric N-H stretching vibrations (Gunasekaran *et al.*, 2006; Sheela, Muthu and Krishnan, 2010).

The analysis of single and double drug loaded MAS-MET complex particles showed structural differences compared to MET and MAS spectrums. The presence of the Si-O-Si stretching at 980 cm<sup>-1</sup>, as well as the peak showing the hydroxyl stretching belonging to Si-OH stretching at approx. 3625 cm<sup>-1</sup>, both belonging to the MAS were still observed on the spectrums of MAS-MET complex particles (Fig. 5.1.). The sharp peak at 1640 cm<sup>-1</sup> belonging to the hydroxyl group bending of water crystallization onto the MAS was also observed (Pongjanyakul, Khunawattanakul and Puttipipatkhachorn, 2009; Rojtanatanya and Pongjanyakul, 2010; A.M. Totea *et al.*, 2019). The peaks observed at 1580 belonging to MET C=N stretching vibration were still observed on the spectrums of MAS-MET complex particles, while the peaks assigned to the N-H stretching vibrations changed as MET is expected to be adsorbed onto MAS via hydrogen bonds formation between the silanol groups of MAS with the amine groups of MET.

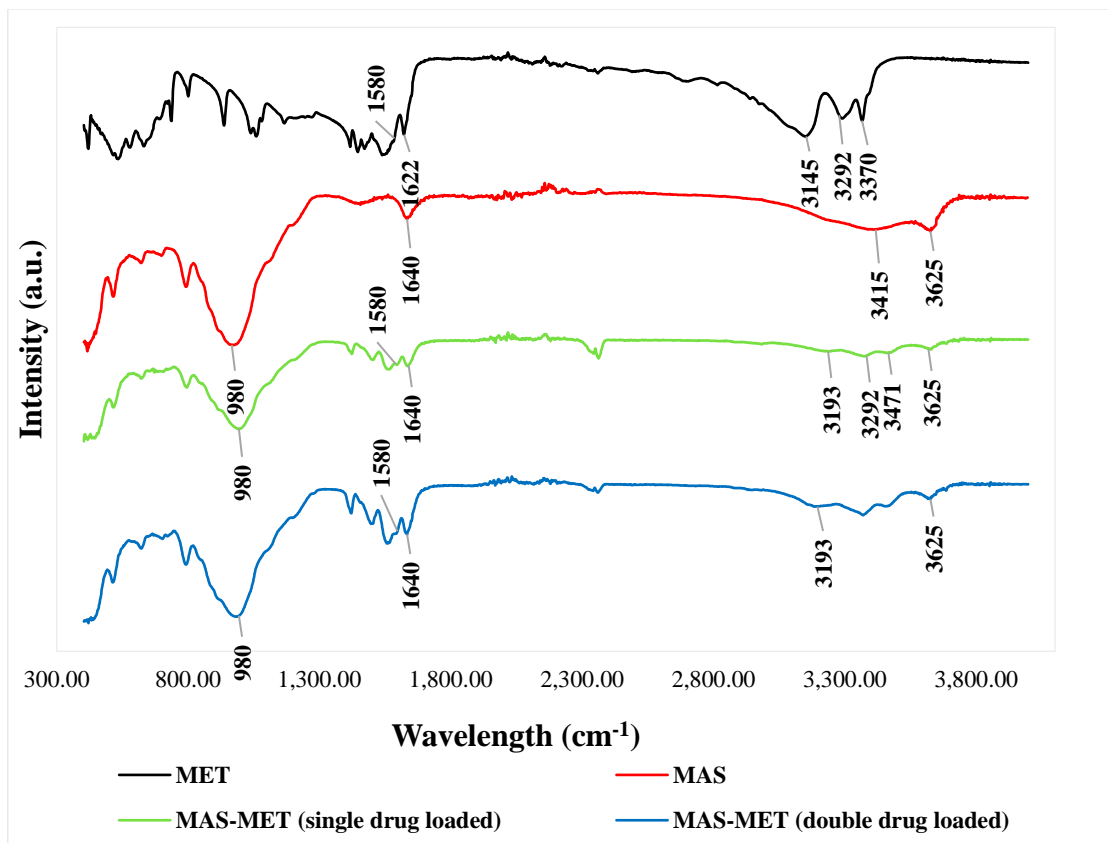


**Fig. 5.1.** ATR-FTIR repeated scans on MAS – MET single drug loaded complex

### 5.2.2. Powder X-Ray Diffractometry (PXRD)

Sharp, intense and representative diffraction peaks indicating the crystalline state of raw material MET were observed at  $2\theta$  angles  $12^\circ$ ,  $24^\circ$ ,  $23^\circ$ and  $37^\circ$  (Manoranjan, 2010; Jagdale *et al.*, 2011; Vaingankar and Amin, 2017).

The prepared single and double drug loaded MAS-MET complex particles were shown to be in amorphous form and did not follow the PXRD pattern of MET or MAS alone, suggesting the molecular dispersivity of the drug in the prepared complexes (Fig. 5.2.). The reflection at  $6.87^\circ$  ( $2\theta$ ) representing the thickness of the silicate layer in the MAS sample was observed in the diffractograms of the MAS-MET complexes prepared, although at a different intensity. The changes in basal spacing upon MET adsorption onto MAS was hence calculated using Bragg's Law (first order of reflection,  $n=1$ ) as 1.28 nm for the single drug loaded MAS-MET complexes and 1.30 nm for the double drug loaded MAS-MET

complexes, suggesting no increase in basal spacing of MAS (1.28 nm) most probably due to the samples tested being well dried. Previous analysis of MAS using PXRD presented in Chapter 3, Section 3.2.2 showed a reduction in the basal distance of MAS from 1.30 nm to 1.22 nm upon dehydration. The results hence suggest that an increase in basal distance may not accurately reflect the intercalation of a drug within clay platelets when humidity is not controlled to allow for comparisons due to the effects of humidity on the increase and decrease of basal distance (Milne and Warhaw, 1955; Rojtanatanya and Pongjanyakul, 2010).

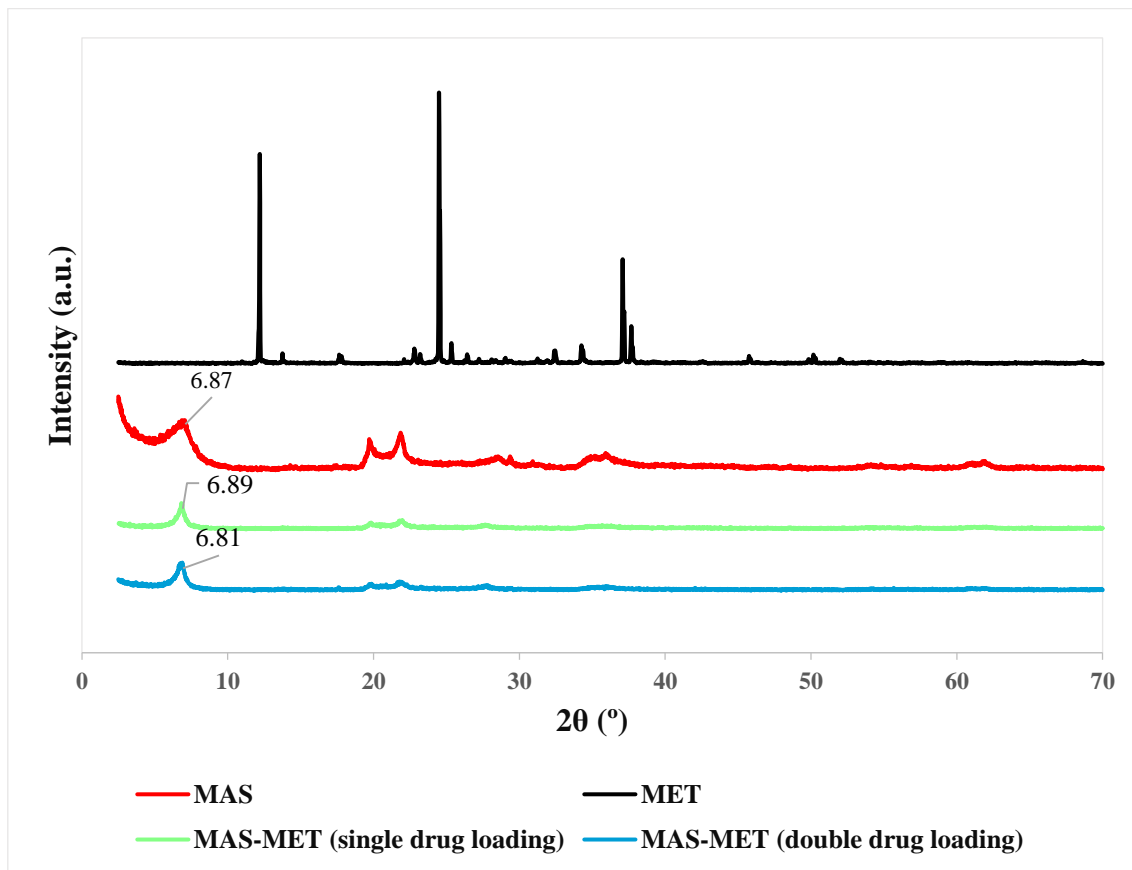


**Fig. 5.2.** PXRD patterns of MAS, MET and MAS-MET single and double drug loaded complexes

### 5.2.3. Differential Scanning Calorimetry (DSC)

The melting point of MET was indicated by a sharp endothermic peak at  $235 \pm 2$  °C (Fig. 5.2.) (Jagdale *et al.*, 2011). The single and double drug loaded MAS-MET complexes were

shown to be amorphous and the absence of MET melting point on their thermograms confirmed its molecular dispersion in amorphous form in the complexes (Fig. 5.3.) (Pongjanyakul and Rongthong, 2010; Rojtanatanya and Pongjanyakul, 2010; A. M. Totea *et al.*, 2019; A.M. Totea *et al.*, 2019).

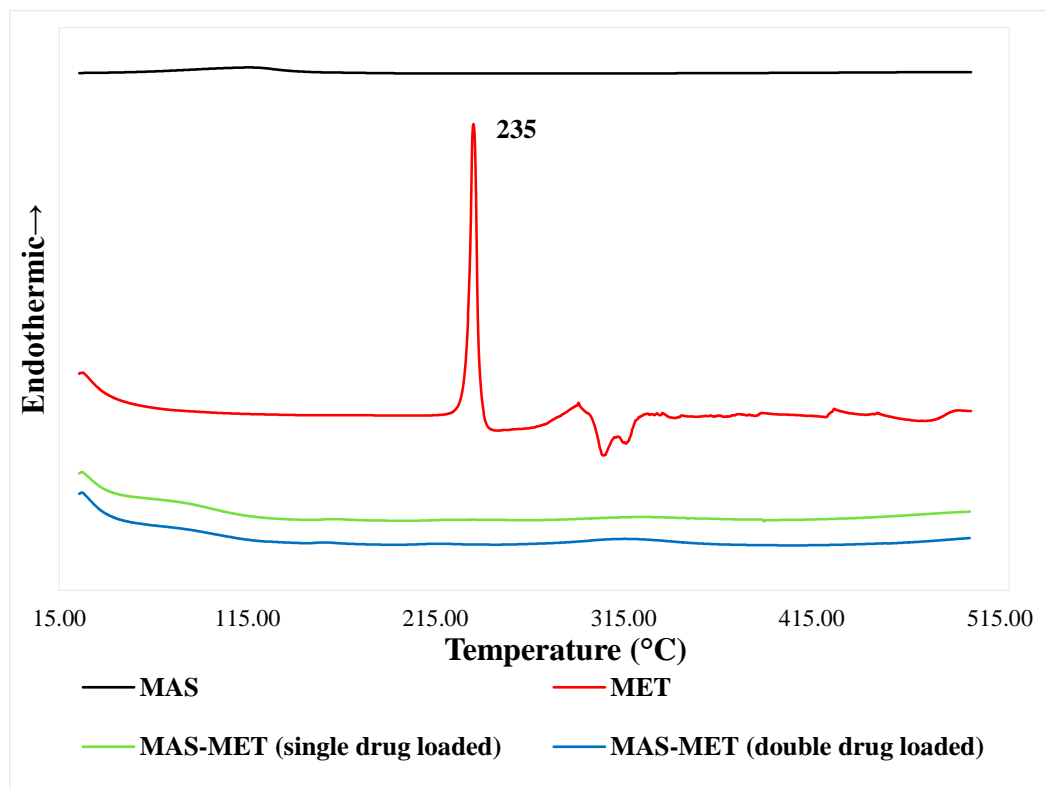


**Fig. 5.3.** DSC thermogram of MAS, MET and MAS – MET complexes (n=3)

#### 5.2.4. Scanning Electron Microscopy with Energy Dispersive X-Ray Spectroscopy (SEM/EDX)

MET, as well as the single and double drug loaded MAS-MET complex particles prepared were studied using SEM and EDX to understand and compare their surface study the chemical elements existing in the samples. Due to the low sensitivity of the technique, the atomic distribution of elements varied and hence, chemical elements found in samples were not compared quantitatively (Bandyopadhyay and Bose, 2013).

MET crystals were shown to be large and on their surface circular indents could be observed (Fig. 5.4.). EDX analysis of MET confirmed the presence of distinctive elements such as chlorine and nitrogen in the tested specimen (Fig. 5.4.).

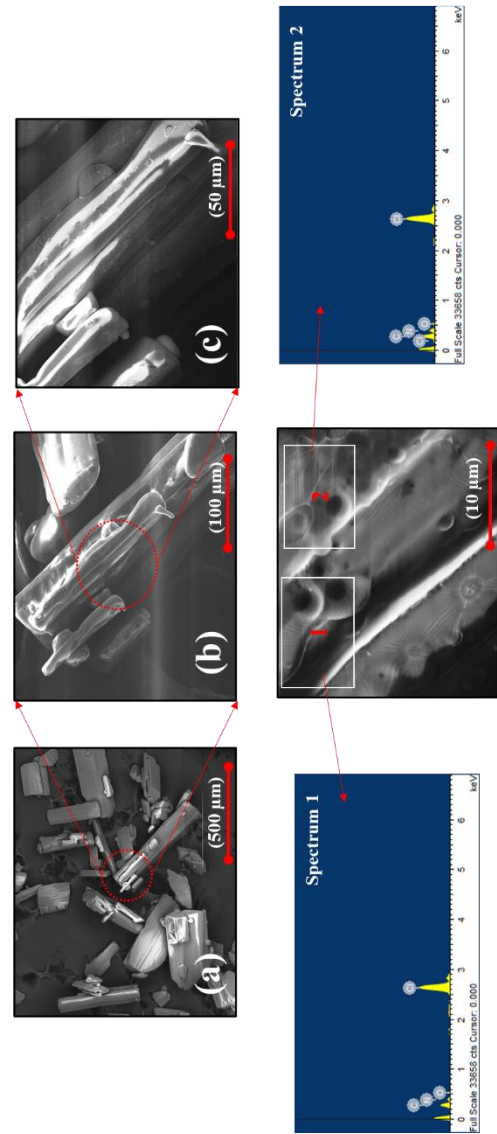


**Fig. 5.4.** Characterisation of MET surface using SEM/EDX. SEM images at different magnifications  $\times 100$  (a),  $\times 500$  (b),  $\times 1000$  (c) and  $\times 5\,000$  (d); atomic distribution profile at two different sample locations (Spectrum 1 and 2)

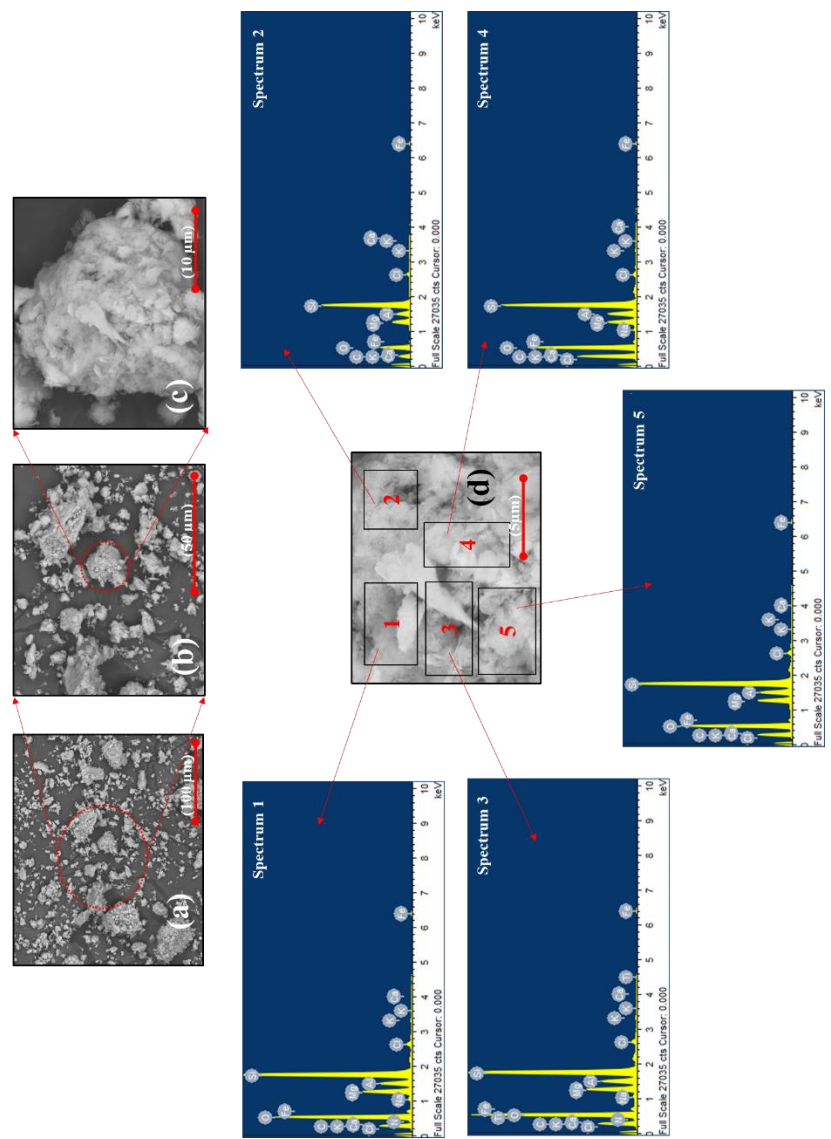


**Fig. 5.5.** Surface characterisation of MAS-MET single drug loaded complexes using SEM/EDX. SEM images at different magnifications  $\times 500$  (a),  $\times 1500$  (b),  $\times 5000$  (c) and  $\times 10\,000$  (d); atomic distribution profile at five different sample locations (Spectrum 1-5)

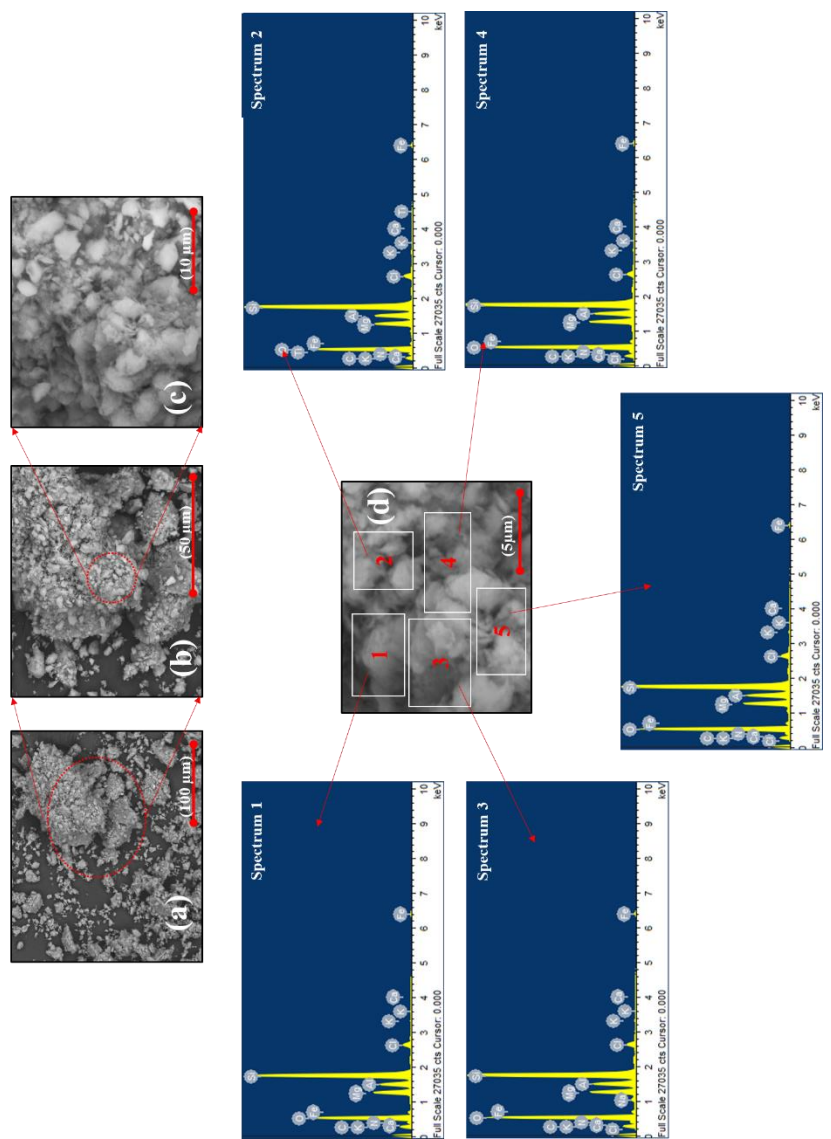


**Fig. 5.6.** Surface characterisation of MAS-MET double drug loaded complexes using SEM/EDX. SEM images at different magnifications  $\times 500$  (a),  $\times 1500$  (b),  $\times 5000$  (c) and  $\times 10\,000$  (d); atomic distribution profile at five different sample locations (Spectrum 1-5)

The single and double loaded complexes formed between MAS and MET looked very similar (Fig. 5.6. and 5.7.), having an irregular layered surface, very different to the MAS (as described in Chapter 3, Section 3.2.4.) or to the crystalline MET. This demonstrates changes in the microstructural properties of the clay powder following the complexation process and may explain why they can be used to offer controlled drug release (Mita, Rupa and Achowicz, 2010; Rojtanatanya and Pongjanyakul, 2010; Pongjanyakul and

Rojtanatanya, 2012; A.M. Totea *et al.*, 2019). As in chapters 3 and 4, the use of this characterisation technique may introduce a selective bias in the overall results due to the analysis of only small particulates selected from the overall sample prepared, which is appropriate for this type of analysis (Bohor and Hughes, 1971). However, the analysis was only used for qualitative purposes, to explore the surface morphology of the samples.

### 5.2.5. High Performance Liquid Chromatography (HPLC)

#### 5.2.5.1. Method validation

The calibration curve generated for the MET using pure drug solutions dissolved in water was found to be linear over the concentration range studied ( $R^2 \geq 0.999$ ) (Fig. 5.7.). The linearity was defined by an equation ( $y = 92162x + 17244$ ). This equation was further used in the MET recovery studies.

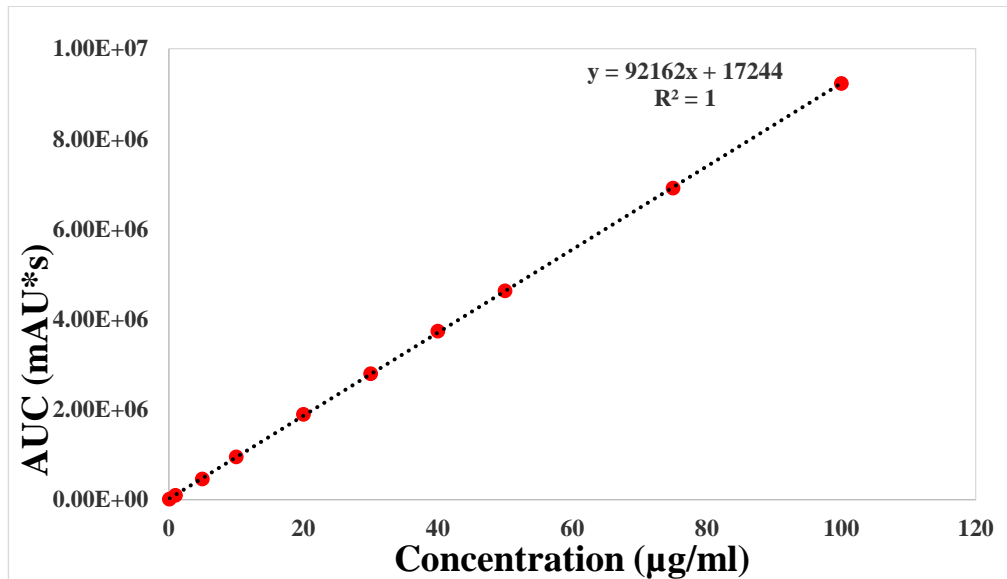


**Fig 5.7.** Calibration curve for MET (100 to 0.1  $\mu\text{g/ml}$ ) showing linearity ( $R^2=0.1$ )

The intermediate and intra assay precision at three different concentration levels of 10, 50 and 100  $\mu\text{g/mL}$  ranging from 0.09 % to 0.72 % and from 0.25 % to 1.72 % respectively proved the method to be precise for the detection of MET. This was evident in the lower than 2 % RSD which complies with the acceptable criteria for quality control of

pharmaceutical preparations (Ermer and Ploss, 2005; Chatpalliwar, Porwal and Upmanyu, 2012).

The LOQ showing the lowest drug concentration that can be recovered within acceptable limits of precision and accuracy was found to be 1.01 µg/mL indicating the high sensitivity of the proposed method and its suitability for the detection MET in solutions at low concentrations. LOD showing the lowest detectable amount of drug distinguishable from the blank was 0.33 µg/mL showing the sensitivity of the method. A summary of the method validation can be found in Table 5.2.

**Table. 5.2.** HPLC method validation for MET showing linearity range, intermediate and intra assay precision, LOD and LOQ

Range (µg/mL)	Linearity (R <sup>2</sup> )	Intermediate precision (%)	Intra assay (RSD) (%)	LOD (µg/mL)	LOQ (µg/mL)
100 – 0.1	≥ 0.9999	1 µg/mL: 2.68 10 µg/mL: 1.72 50 µg/mL: 0.97 100 µg/mL: 0.69	1 µg/mL: 1.85 10 µg/mL: 0.72 50 µg/mL: 0.71 100 µg/mL: 0.24	0.33	1.01

### 5.2.5.2. Recovery of MET content from MAS–MET complex particles

Determination of MET content in the MAS-MET complex particles prepared showed differences between the different media used for the dispersion of the complex particles (2 M HCl, pH 5 ultra-pure water, pH 6.8 buffer) (Table 5.3.), which was also observed in previous studies using PPN-MAS intercalated complexes (chapter 3, section 3.2.5.2.).

**Table 5.3.** MET content in double drug loaded MAS–MET complex particles using three different dissolution media: 2M HCl, ultra-pure water (pH 5) and phosphate buffer (pH 6.8)

Recovered MET (% w/w)	
MAS-MET double drug loaded	
2M HCl	8.75 ± 0.14*
pH 5.0 Ultra-pure water	1.31 ± 0.06*
pH 6.8 Phosphate Buffer	1.60 ± 0.08*

Note: \*values are reported as the mean ± SD of at least three determinations

MET is a highly stable drug with two pK<sub>a</sub> values, 2.8 and 11.5 and an aqueous solubility of 300 mg/mL in the pH range 1.2 – 6.8 (Desai *et al.*, 2014). Hence, the amount of MET recovered from the MAS – MET complex particles dispersed in 2 M HCl, ultra – pure water and pH 6.8 phosphate buffer should be pH independent. However, the amount of MET recovered was highly variable. No degradation products were observed on the chromatograms during the analysis in any of the dissolution media used.

### 5.2.6. Small Angle X-Ray Scattering

#### 5.2.6.1. Solid-state nanometre scale morphology

MAS-MET complexes in powder form (particle size 63 – 125 µm) were analysed using similar conditions to previous studies on MAS power (particle size 63 – 125 µm), such as sample mounting in borosilicate glass capillary tubes and consistent acquisition time for the analysis, which allowed for comparisons (chapter 2, section 2.2.2.6.).

2D-SAXS data pattern for MAS-MET complexes as recorded by the instrument was shown to be symmetric and circular, suggesting that at nanometre scale the particles showed no preferred orientation. This behaviour is due to the sample being analysed in its powder form, which implies randomly orientated particles. The intensity plot showing Log {I(a.u.)} vs. q [nm<sup>-1</sup>] had a smooth curve, showing the intensity decreasing from q ≈ 0.099 nm<sup>-1</sup> (at 2θ = 0.14°) at the edge of the beam stop, to q = 2.275 nm<sup>-1</sup> (at 2θ = 3.20°) at the peripheral limit of the detector. No peaks or other specific features were observed. Background subtraction was considered unnecessary due to the minimal background scattering in comparison to

sample scattering intensity (Fig. 5.8.) Data was corrected for transmission through the calculation on the transmission factor using glassy carbon, to correct for sample absorption.

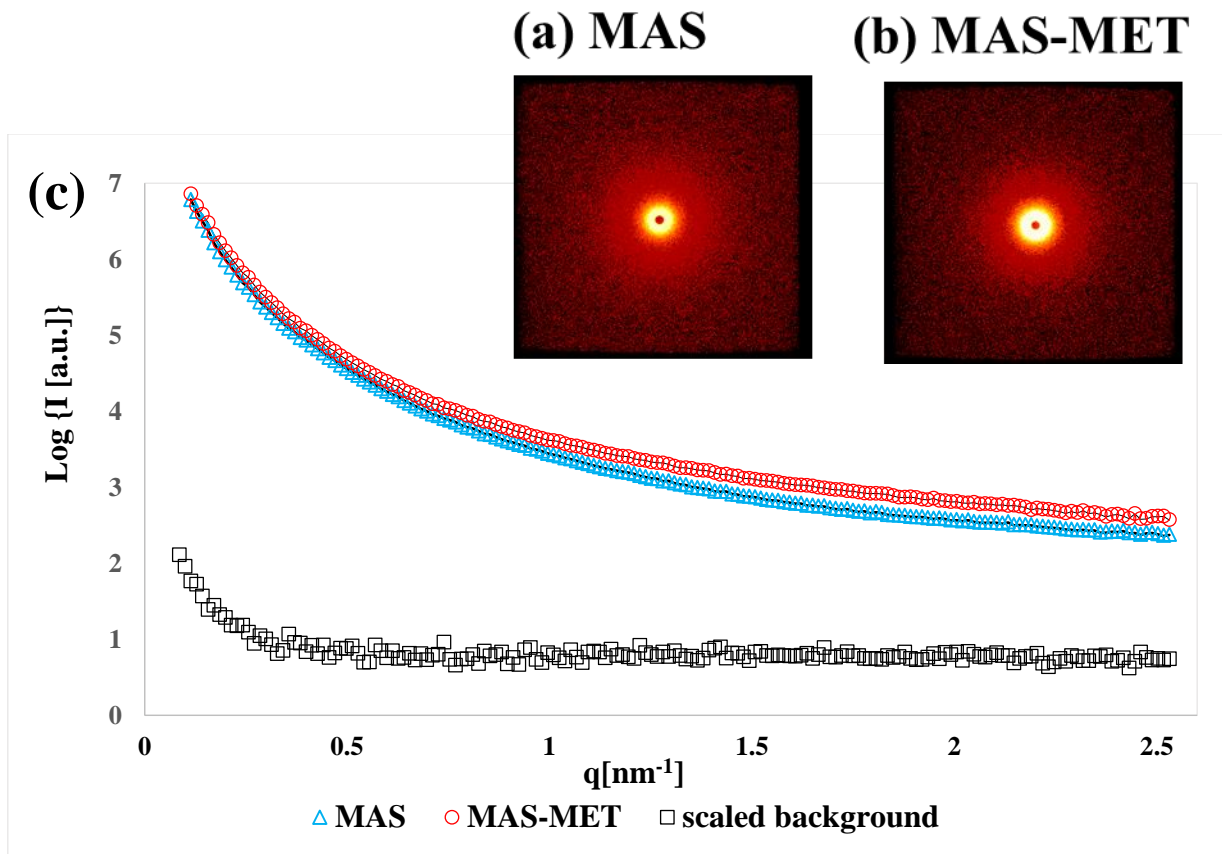


**Fig. 5.8.** Typical SAXS data for specimens in powder form: (a and b) 2D-SAXS patterns for MAS and MAS-MET complexes showing the centre of the beam stop; (c) 1D-SAXS intensity curves for MAS and MAS-MET complexes (open symbols showing uncorrected data and line showing data after scaled background subtraction), and scaled background (open black square symbols)

The analysis of the data in the form of double logarithmic plot of intensity ( $\log I [\text{a.u.}]$ ) vs. the scattering vector ( $\log \{q [\text{nm}^{-1}]\}$ ) followed a straight line with no peaks or other specific features, indicate power-law scattering behaviour (Fig. 5.9.), similarly to the MAS powder behaviour (as describes in Chapter 3, Section 3.2.6.1).

A slope of  $-3.55$  was obtained for the MAS-MET complexes, which was very similar to the slope obtained from the double logarithmic plot of intensity vs. the scattering vector for MAS ( $-3.63$ ) (Fig. 5.9.).

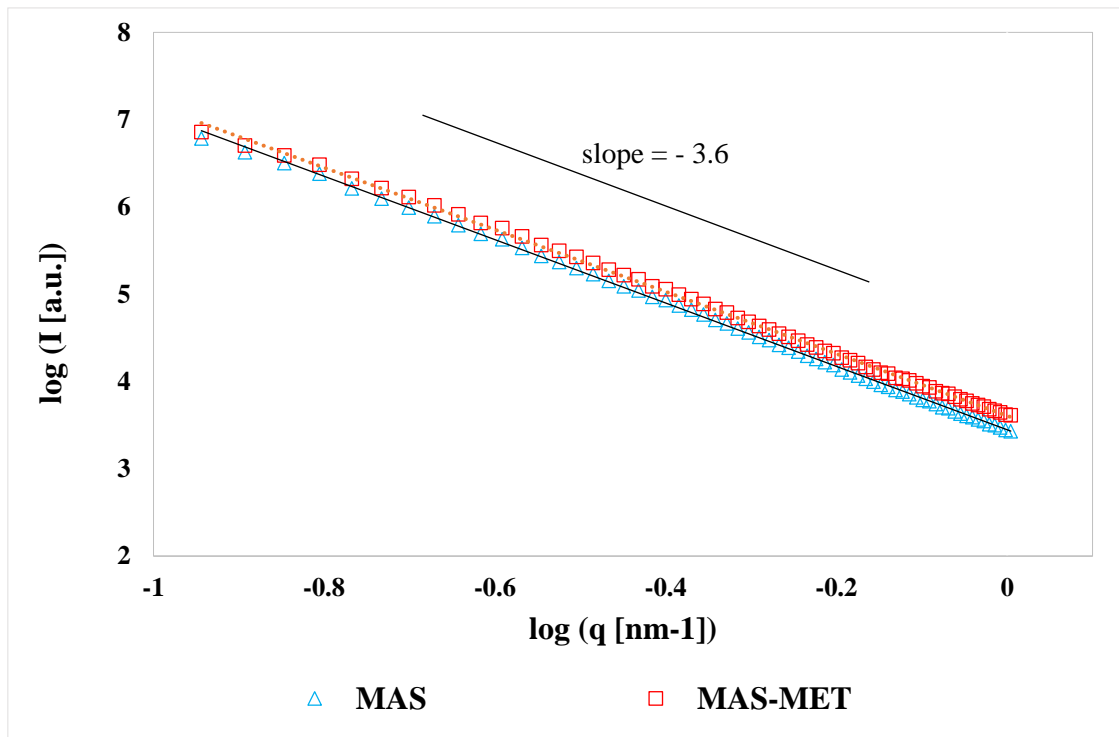


**Fig. 5.9.** Double-logarithmic plot of intensity vs. the scattering vector for MAS and MAS-MET complexes in powder form (particle size  $63 - 125 \mu\text{m}$ ), showing the slope of the linear part for the data which allows the calculation of the power-law constant  $a$  as  $-3.63$  for MAS and  $-3.57$  for MAS-MET complexes

Slope determination from the double logarithmic plot of intensity vs. the scattering vector allowed for the calculation of the surface fractal dimension  $D_s$  value for MAS-MET complexes (Fig. 5.9). Hence, upon calculation as described in Chapter 3, Section 3.2.6.1., a surface fractal dimension  $D_s$  of 2.43 was obtained for MAS-MET complexes, suggesting that the sample tested was surface fractal over a length scale of 0.1 nm to 1.0 nm. The value also indicates an irregular, rough and space filling surface, and was very similar to the surface fractal dimension  $D_s$  value obtained for MAS ( $D_m = 2.37$ ). The similarity of surface fractal dimension values between the samples (MAS compared to MAS-MET complexes)

may create difficulties in differentiating between them, hence not being an indicator of drug absorption onto clay.

### 5.2.6.2. Liquid-state nanometre scale morphology

Data acquired from the MAS dispersion (0.050 % w/v) is discussed in Chapter 3, section 3.2.6.2.

Data acquired from the flocculated complexes formed between MAS and MET (1 to 1 w/w) represented using a Guinier plot ( $\log(I)$  vs.  $q^2$ ) showed two linear regions separated by a transition region (Fig. 5.10.). This behaviour suggests poly-dispersive systems in which cluster size is variable, with large cluster aggregates in the samples (Odo *et al.*, 2015). No peaks or other specific features were observed.

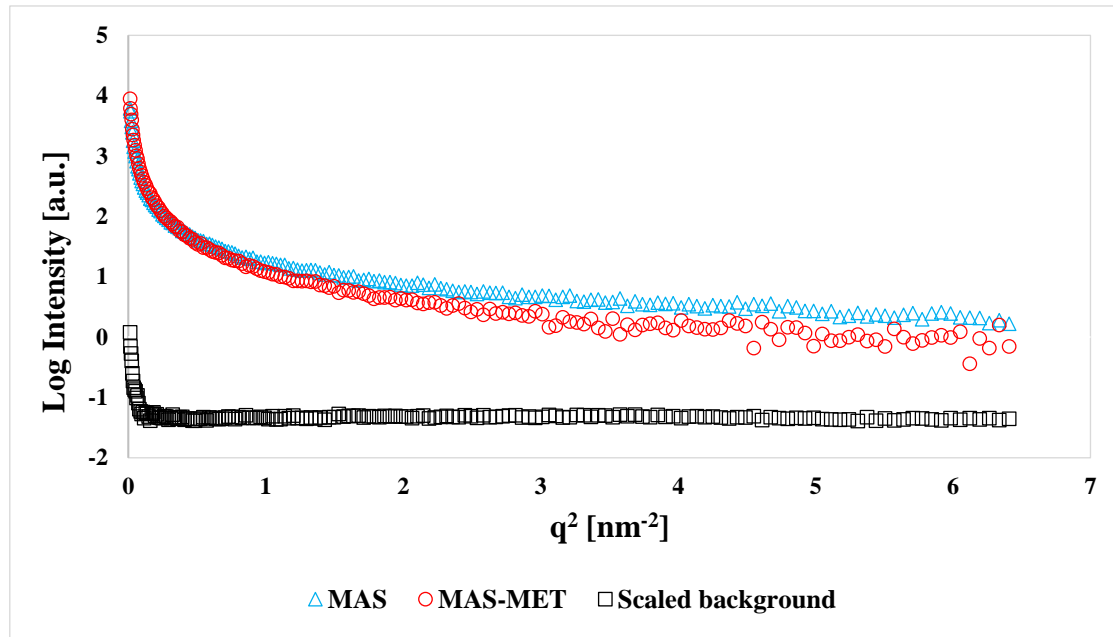


**Fig. 5.10.** Guinier plot of MAS dispersion and MAS-MET complex dispersion showing two linear regions in the high and low  $q$  values

The analysis of the data in the form of double logarithmic plot of intensity ( $\log I$  [a.u.]) vs. the scattering vector ( $\log \{q\} [\text{nm}^{-1}]$ ) for the MAS-MET flocculates followed straight lines with no peaks or other specific features, indicating power-law scattering behaviour (Fig. 5.11.). This behaviour was also observed following the analysis of the MAS dispersion (Fig. 5.11.).

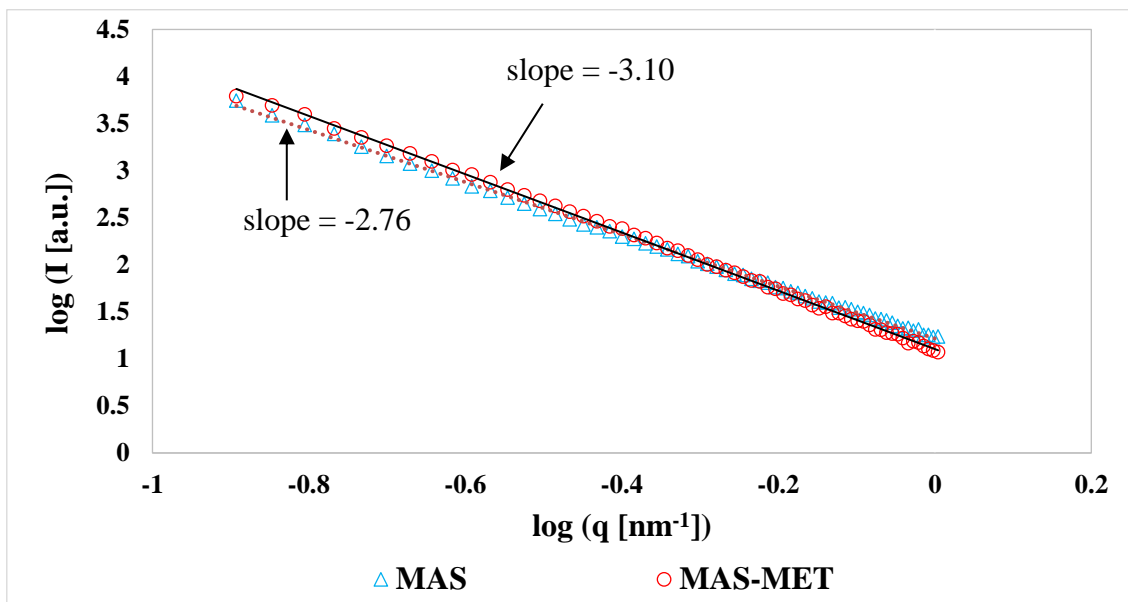


**Fig. 5.11.** Double-logarithmic plot of intensity vs. the scattering vector for MAS and MAS-MET complexes in liquid form, showing power law behaviour

A slope of  $-3.10$  was obtained for the MAS-MET complex dispersion, which was considerably different from the one obtained for MAS ( $-2.76$ ). The difference in results shows a difference in structure, with the MAS-MET complex dispersion having a more complex structure. This behaviour was expected since the MAS flocculated upon the addition of the MET solution.

### 5.2.7. Microscopy

The observation of the MAS-MET flocculates prepared as described in chapter 2, section 2.2.1 under a light microscope showed that upon the addition of the MET solution to the MAS dispersion precipitates formed. The MAS dispersion was formed of dispersed particles (chapter 3, section 3.2.7.) compared to the flocculates which were shown to be aggregated in large clusters (Fig. 5.12.).

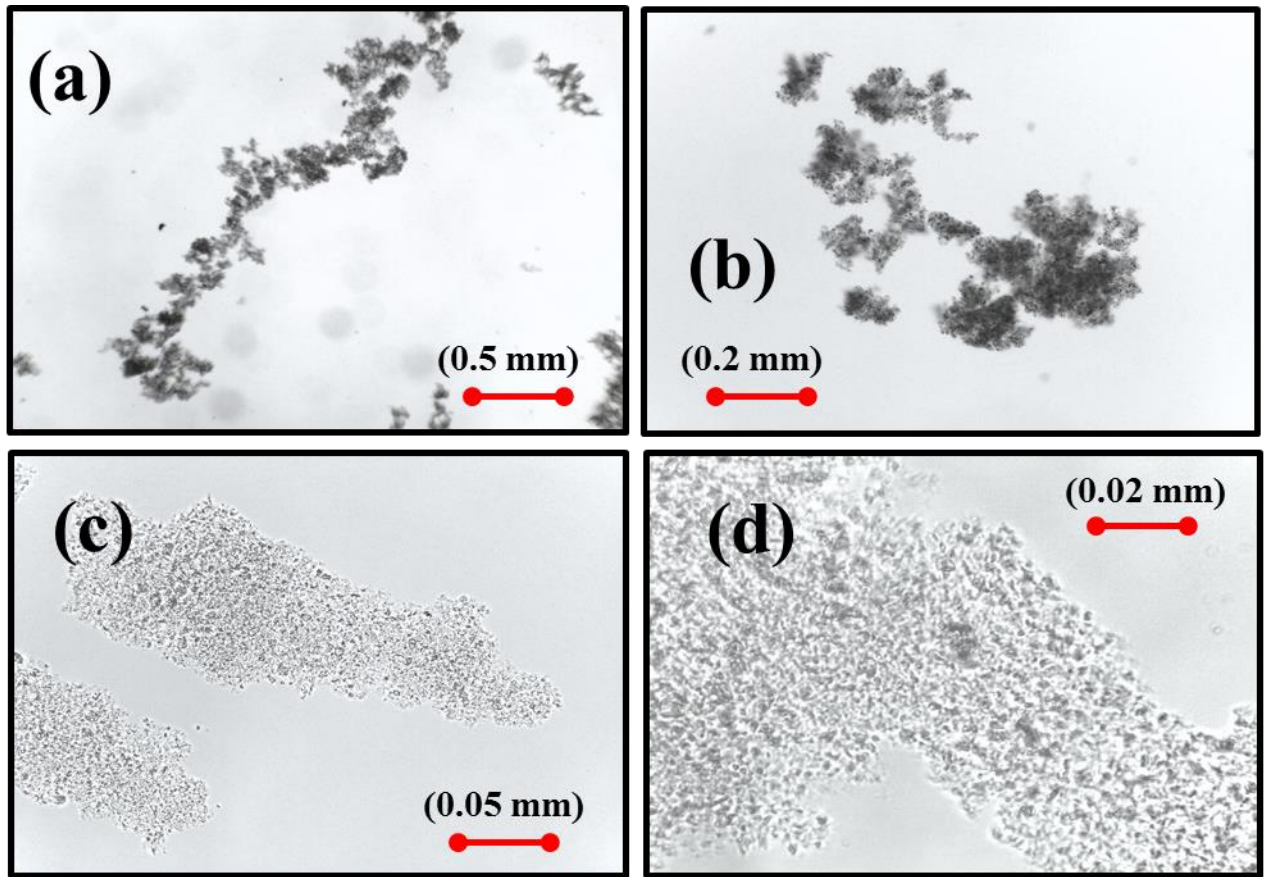


**Fig. 5.12.** Microscopy images of single drug loaded MAS-MET complex dispersion prepared using purified water (pH 5) at different magnifications:  $\times 4$  (a);  $\times 10$  (b);  $\times 40$  (c); and  $\times 100$  (d)

### 5.2.8. Calorimetric binding studies

#### 5.2.8.1. Calorimetric single injection model (SIM) binding studies

The interaction between MAS and MET was initially studied using ITC SIM experiments (Fig. 5.13.). The experiments confirmed the binding between MET and MAS, which was shown to be exothermic and varied with varying pH. The interaction was most favourable at pH 5 as shown by the sharper peak which returned slightly faster to the baseline compared to the peak observed in the ITC experiments at pH 7 and 9. This may be an effect of the slight ionisation of both nitrogen groups at pH 5, compared to pH 7 and 9 (chapter 1, section 1.6.3 (Fig. 1.13)).

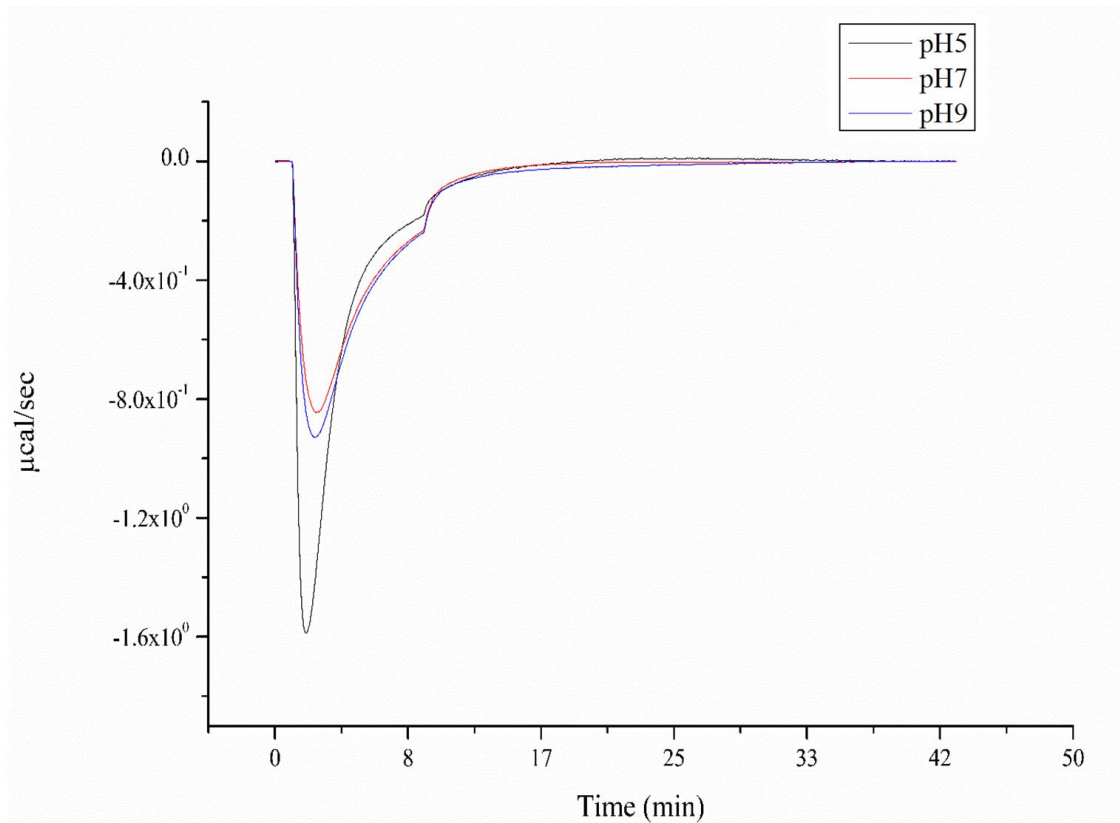


**Fig. 5.13.** Titration of 0.016 % w/v (1 mM) MET solution (pH 5) into 0.010 % w/v MAS dispersion pH 5 (black), pH 7 (red) and pH 9 (green) at 25 °C

#### 5.2.8.2. Calorimetric multiple injection mode (MIM) binding studies

Multiple injection experiments at pH 5 and at two different temperatures (25 and 37 °C) further confirmed the highly exothermic interaction between MET and MAS (Fig. 5.14.), observed in the SIM ITC experiments (Section 5.2.8.1). The MIM stepwise experiments however gave more detailed information about the driving forces involved in the process of adsorption of MET onto MAS.

In order to determine the heat of dilution for MAS and MET, the subtraction of the heat of dilution for MET (0.033 % w/v (pH 5)) and water (pH 5) was required for both experiments at 25 and 37 °C (Fig. 5.14.). A one set of sites model was fitted to the data and allowed the determination of thermodynamic parameters of the reaction: affinity ( $K_a$ ), changes in enthalpy ( $\Delta H$ ), entropy ( $\Delta S$ ) or Gibbs free energy ( $\Delta G$ ).

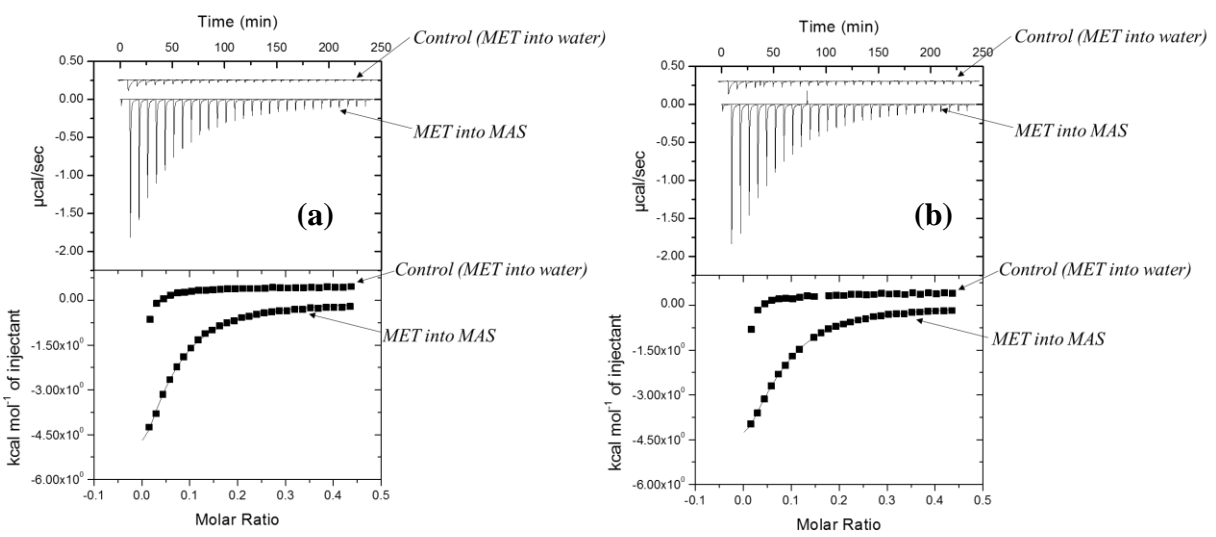


**Fig. 5.14.** Multiple injection mode calorimetric titration of 0.033 % w/v MET solution (pH 5) into 0.037 % w/v MAS dispersion (pH 5) at 25 °C (a) and 37 °C (b). Raw data (top) and integrated heats (bottom) as a function of molar ratio. Control runs suggesting interaction between water and MET

Binding was characterised by a negative enthalpy change, and a comparatively small entropy change at both 25 and 37 °C, implying that the binding was an enthalpically driven process (Fig. 5.15.).

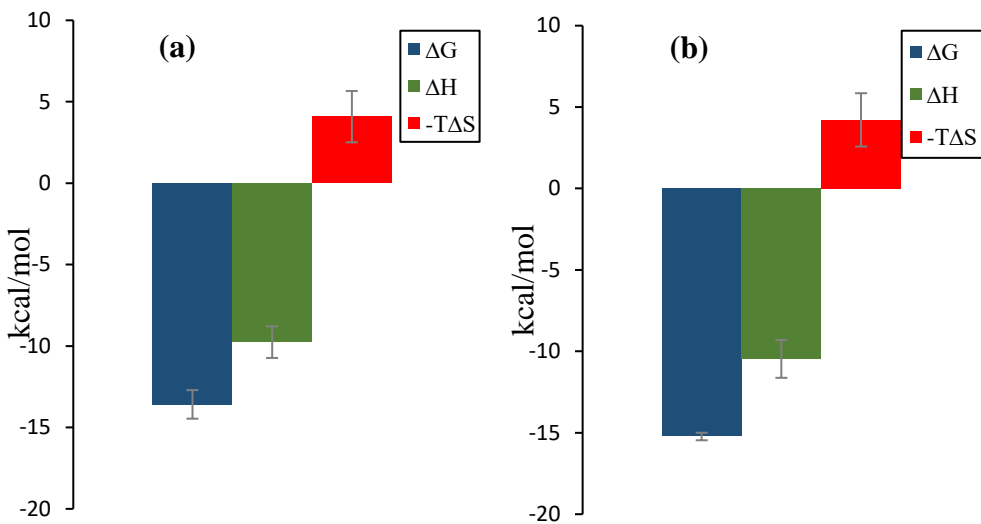


**Fig. 5.15.** Thermodynamic profile for binding of MET (0.033 % w/v) onto MAS (0.037 % w/v) at 25 °C (a) and 37 °C (b) showing enthalpy ( $\Delta H$ ), entropy ( $\Delta S$ ) or Gibbs free energy ( $\Delta G$ ). Results are based on three independent repeats done under similar conditions.

The increase in temperature caused a gradual increase in the affinity of MET with MAS as observed from the increase of the association constant  $K_a$  ( $1.47E+04 \pm 2.06E+03$  M at 25 °C and  $4.66E+04 \pm 1.2E+04$  at 37 °C) (Table 5.3.). The overall change in Gibbs free energy ( $\Delta G$ ) was comparatively similar at both temperatures ( $-12.11 \pm 4.04$  kcal/mol at 25 °C compared with  $-14.69 \pm 1.01$  kcal/mol at 37 °C), confirming that both reactions occurred spontaneously. The enthalpic contribution calculated from the change in heat associated with binding was slightly greater at 37 °C ( $10.47 \pm 1.61$  kcal/mol compared with  $-8.81 \pm 2.52$  kcal/mol at 25 °C), while the entropic contribution was comparatively small in both cases confirming the interaction to be enthalpically driven at both temperatures (Table 5.4.).

**Table 5.4.** Multiple injection mode calorimetric binding studies evaluating the adsorption of MET onto MAS at 25 and 37 °C (pH 5). Data analysed through one set of sites curve fitting using a non-linear least squares model to calculate affinity (K), changes in enthalpy ( $\Delta H$ ), entropy ( $\Delta S$ ) or Gibbs free energy ( $\Delta G$ ). Results are based on three independent repeats done under similar conditions. Heat of dilution for MET (0.033 % w/v) and water (pH 5) subtracted at both temperatures to correct data.

	<b>25 °C</b>	<b>37 °C</b>
<b>K<sub>a</sub></b> (M)	1.47E+04 ± 2.06E+03	4.66E+04 ± 1.2E+04
<b>ΔG</b> (kcal/ mol)	-12.11 ± 4.04	-14.69 ± 1.01
<b>ΔH</b> (kcal/ mol)	-8.81 ± 2.52	-10.47 ± 1.61
<b>-TΔS</b> (kcal/ mol)	3.13 ± 2.50	3.81 ± 1.08

The binding interaction had a negative heat capacity  $\Delta C_p$  (-0.14 kcal mol K<sup>-1</sup>) indicating that upon increasing temperature the binding became more exothermic and enthalpically driven, thus in agreement with the binding parameters calculated.

MET is therefore expected to be adsorbed onto MAS through the amine groups which allows cation exchange, as well as hydrogen bonding and water bridging depending on the ionisation state of the molecule (Fig. 5.16.).

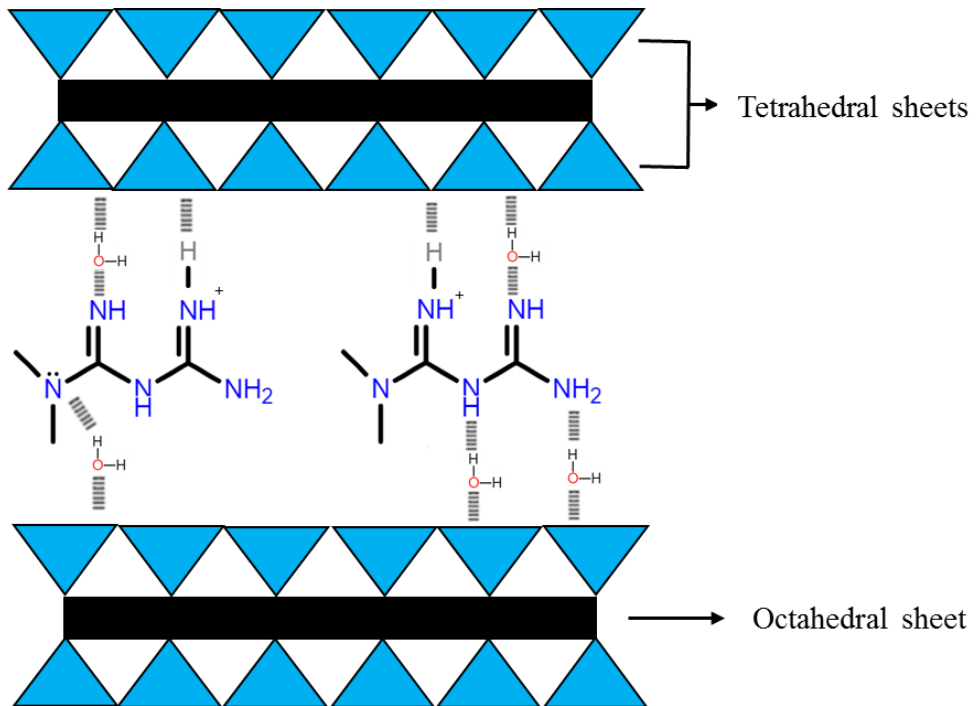


**Fig. 5.16.** Possible MAS-MET chemical interaction: cation exchange, hydrogen bonding and water bridging

### 5.2.8.3. Effects of PEO on the adsorption of MET onto MAS

#### 5.2.8.3.1. Binding between MET and PEO

Binding was observed between MET (0.300 % w/v) and PEO (0.020 % w/v PEO) at both 25 and 37 °C (Fig. 5.17.). However, the binding characteristics can only be confirmed after subtraction of suitable dilution of MET (0.300 % w/v) into water at 25 and 37 °C. Hence, further work is required for clarification of these results.

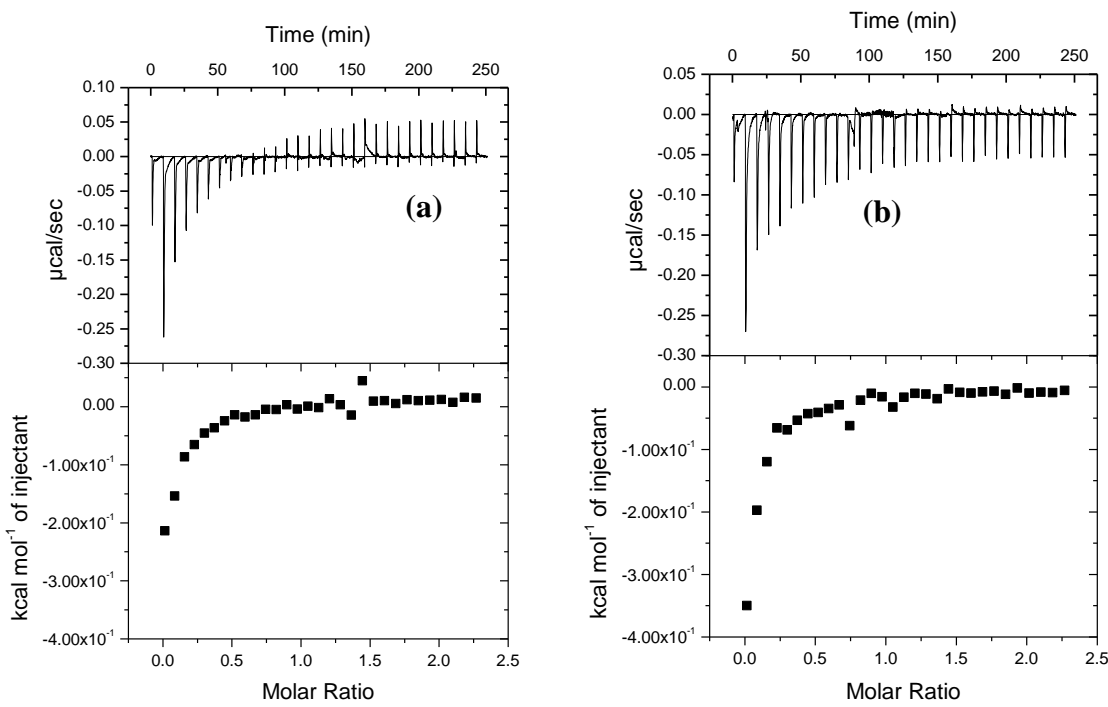


**Fig. 5.17.** Titration of 0.300 % w/v MET into 0.020 % w/v PEO dispersion at 25 °C (a) and 37 °C (b). Raw data (top) and integrated heats (bottom) as a function of molar ratio.

### 5.2.8.3.2. MET adsorption onto MAS-PEO complex

Results obtained following titration of 0.300 % w/v MET into MAS and PEO mixture (0.040 % w/v PEO dispersion mixed with 0.040 % w/v MAS dispersion at a 1 to 1 ratio v/v) at pH 5 and two different temperatures (25 and 37 °C) confirmed the adsorption of MET onto the MAS-PEO mixture (Fig. 5.18.). The interaction was shown to be exothermic, having multiple binding events, which are an effect of the polymer addition to the reaction as only one binding event was observed in the simple binding experiments between MET and MAS (section 5.2.8.2). Previous experiments showed no interaction occurring between MAS and water, and slight aggregation of PEO in aqueous solution (pH5) (chapter 3, sections 3.2.8.3.1. and 3.2.8.4.2.).

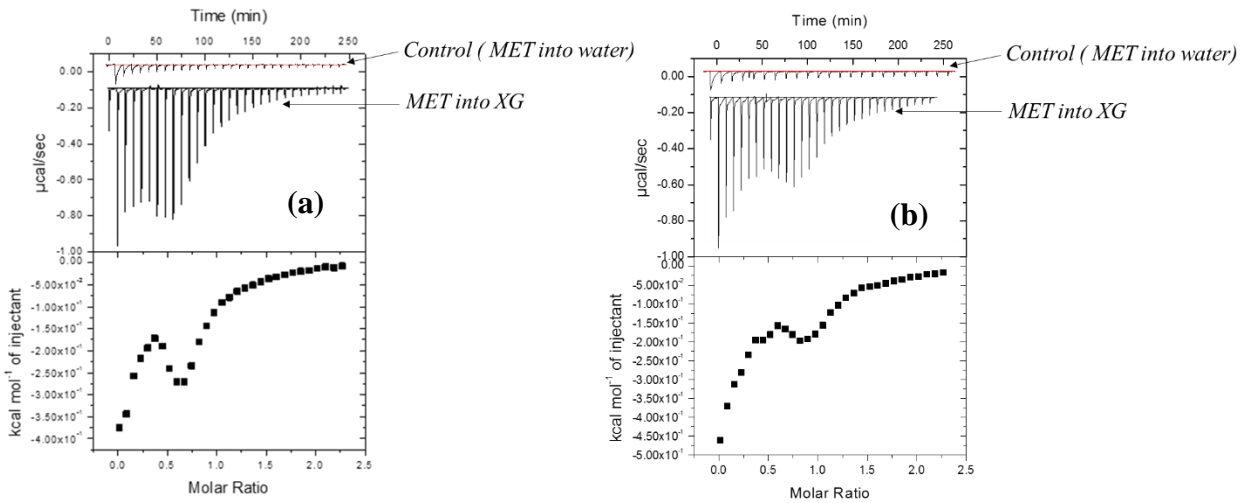


**Fig. 5.18.** Titration of 0.300 % w/v MET into MAS and PEO mixture (0.020 % w/v PEO; 0.020 % w/v MAS) at 25 °C (a) and 37 °C (b). Raw data (top) and integrated heats (bottom) as a function of molar ratio.

#### 5.2.8.4. Effects of XG on the adsorption of MET onto MAS

##### 5.2.8.4.1. Binding between MET and XG

Multiple injection experiments at pH 5 at 25 °C, showed no interaction occurring between MET (0.033 % w/v) and XG (0.020 % w/v XG) upon subtraction of MET (0.033 % w/v) dilution in water from the data (Fig. 5.19.) (Palmer *et al.*, 2013). Previous experiments presented in chapter 3, section 3.2.8.4.2 demonstrated that there was no interaction occurring upon dilution of XG dispersion into water (pH5).

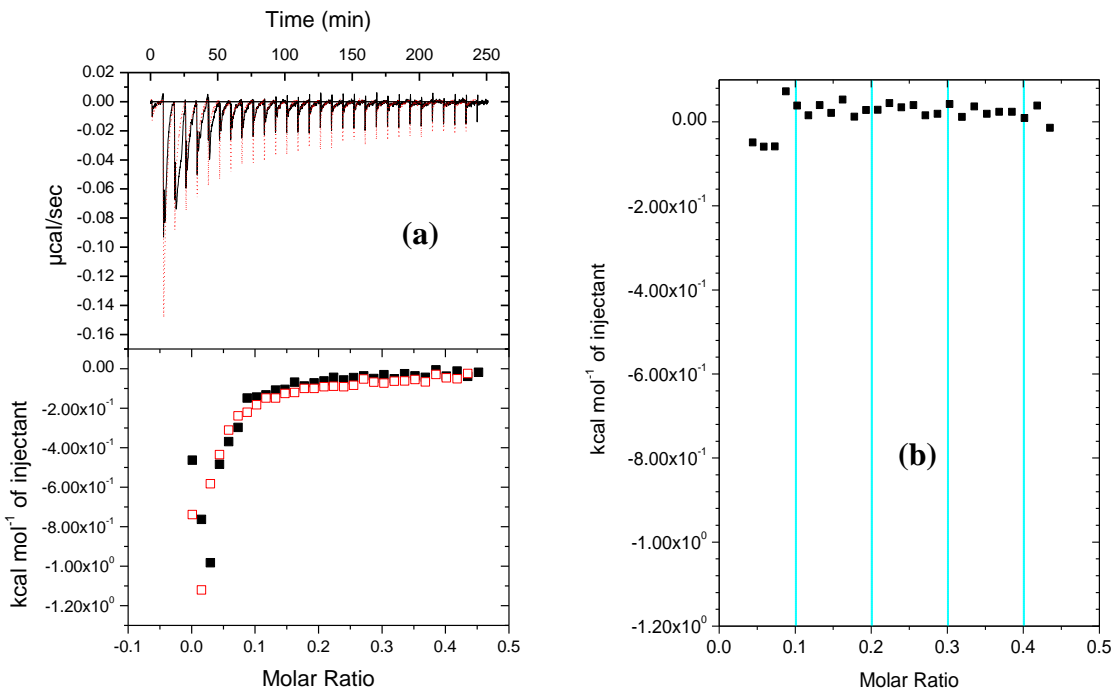


**Fig. 5.19.** Calorimetric binding studies showing (a) titration of 0.033 % w/v MET solution (pH 5) into 0.020 % w/v XG dispersion (pH 5) at 25 °C (red) and dilution of 0.033 % w/v MET (pH5) into water pH 5 (black): raw data (top) and integrated heats (bottom) as a function of molar ratio, and (b) integrated heats obtained upon subtraction of MET (0.033 % w/v) dilution in water from the data

#### 5.2.8.4.2. MET adsorption onto MAS-XG complex

Results obtained following titration of 0.080 % w/v MET into MAS and XG mixture (0.40 % w/v PEO dispersion mixed with 0.040 % w/v MAS dispersion at a 1 to 1 ratio v/v) at pH 5 and two different temperatures (25 and 37 °C) confirmed the adsorption of MET onto the MAS-XG mixture (Fig. 5.20.). The interaction was shown to be exothermic, and only one binding event could be observed, similarly to the previous binding experiments between MET and MAS (section 5.2.8.2.).

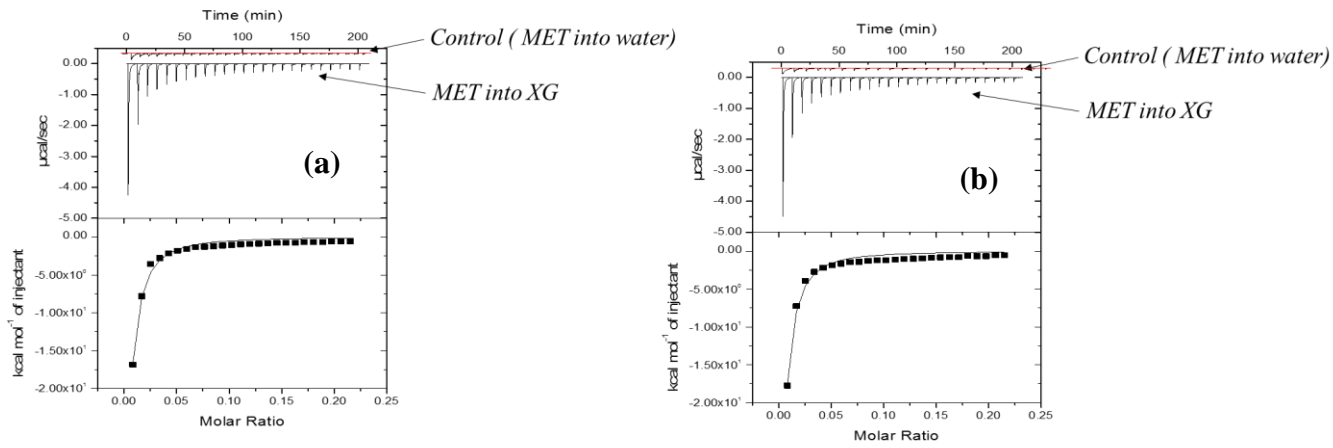


**Fig. 5.20.** Titration of 0.080 % w/v MET into MAS and XG mixture (0.020 % w/v XG; 0.020 % w/v MAS) at 25 °C (a) and 37 °C (b). Raw data (top) and integrated heats (bottom) as a function of molar ratio.

Integration of data to determine thermodynamics (affinity (K), changes in enthalpy ( $\Delta H$ ), entropy ( $\Delta S$ ) or Gibbs free energy ( $\Delta G$ )) is however difficult due to the absence of the first part of the sigmoidal binding curve, leading to inaccurate integration of the data when a “one set of sites model” is fitted (Fig. 5.21.).

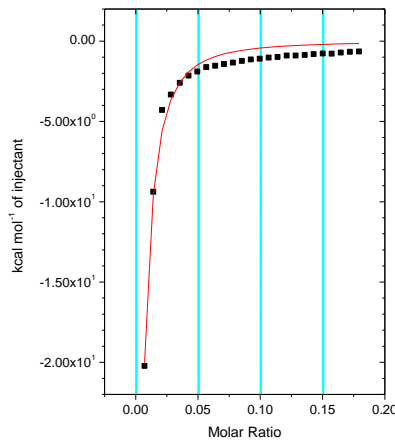


**Fig. 5.21.** Titration of 0.080 % w/v MET into MAS and XG mixture (0.40 % w/v XG dispersion mixed with 0.040 % w/v MAS dispersion at a 1 to 1 ratio v/v): integrated heats (bottom) as a function of molar ratio showing the erroneous fitting of a one set of sites model to the data

### **5.3. Conclusions**

Results confirmed the ability of the MAS to adsorb MET onto its surface and form flocculates in the MAS dispersion.

The flocculates were dried and characterised using a wide variety of techniques such as ATR-FTIR), PXRD, DSC, SEM/EDX, HPLC, SAXS which all confirmed changes as a result of the binding process which may have benefits for drug release.

The SIM and MIM ITC experiments revealed that the binding phenomenon between MET and MAS was predominantly enthalpically driven as high energy resulted from broken and created hydrogen bonds and electrostatic interactions. pH was shown to influence the speed of the reaction with the interaction between MAS and MET being faster at pH 5 compared to pH 7 and 9. The binding also became more exothermic and enthalpically driven upon increasing the temperature from 25 to 37° C. Binding was confirmed between PEO and MET. MET was also adsorbed onto MAS-PEO complex, results showing that MET adsorption onto MAS was influenced by the PEO in solution, which is most probably due to the competition of both MAS and PEO for MET. No interaction was observed between MET and XG. The adsorption of MET onto MAS-XG complex was shown to be similar to the binding between MAS and MET as only one binding event was observed. However further studies are needed for a better insight into these reactions.

#### **5.4. References**

- Bandyopadhyay, A. and Bose, S. (eds) (2013) *Characterization of Biomaterials Chapter 4*. Oxford, UK: Elsevier.
- Bohor, B. F. and Hughes, R. E. (1971) ‘Scanning Electron Microscopy of Clays and Clay Minerals’, *Clays and Clay Minerals*, 19(1969), pp. 49–54.
- Chatpalliwar, V. A., Porwal, P. K. and Upmanyu, N. (2012) ‘Validated gradient stability indicating HPLC method for determining Diltiazem Hydrochloride and related substances in bulk drug and novel tablet formulation’, *Journal of Pharmaceutical Analysis*, 2(3), pp. 226–237.
- Desai, D. *et al.* (2014) ‘Surfactant-mediated dissolution of metformin hydrochloride tablets: Wetting effects versus ion pairs diffusivity’, *Journal of Pharmaceutical Sciences*, 103(3), pp. 920–926.
- Ermer, J. and Ploss, H. J. (2005) ‘Validation in pharmaceutical analysis: Part II: Central importance of precision to establish acceptance criteria and for verifying and improving the quality of analytical data’, *Journal of Pharmaceutical and Biomedical Analysis*, 37(5), pp. 859–870.
- Gunasekaran, S. *et al.* (2006) ‘Vibrational spectra and thermodynamic analysis of metformin’, *Indian Journal of Pure and Applied Physics*, 44(7), pp. 495–500.
- Jagdale, S. C. *et al.* (2011) ‘Preparation and characterization of metformin hydrochloride-compritol 888 ATO solid dispersion’, *Journal of Young Pharmacists*, 3(3), pp. 197–204.
- Manoranjan, S. (2010) ‘Formulation of dual component drug delivery of glimepiride and metformin hydrochloride for immediate and sustain release’, *International Journal of Research in Ayurveda and Pharmacy*, 1(2), pp. 624–633.
- Milne, I. H. and Warhaw, C. M. (1955) ‘Methods of Preparation and Control of Clay Mineral Specimens in X-Ray Diffraction Analysis’, *Clays and Clay Minerals*, 4, pp. 22–30.
- Mita, A. R. A., Rupa, A. K. and Achowicz, R. J. (2010) ‘Preliminary Approach to Application of Modified Smectite Clay to Form Tablets in Direct Compression Process’, pp. 366–368.

Odo, E. A. *et al.* (2015) ‘SAXS Study of Silicon Nanocomposites’, 5(3), pp. 65–70.

Palmer, D. *et al.* (2013) ‘Mechanism of synergistic interactions and its influence on drug release from extended release matrices manufactured using binary mixtures of polyethylene oxide and sodium carboxymethylcellulose’, *Colloids and Surfaces B: Biointerfaces*, 104, pp. 174–180.

Pongjanyakul, T., Khunawattanakul, W. and Puttipipatkhachorn, S. (2009) ‘Physicochemical characterizations and release studies of nicotine-magnesium aluminum silicate complexes’, *Applied Clay Science*, 44(3–4), pp. 242–250.

Pongjanyakul, T. and Rojtanatanya, S. (2012) ‘Use of Propranolol-Magnesium Aluminium Silicate Intercalated Complexes as Drug Reservoirs in Polymeric Matrix Tablets’, *Indian Journal of Pharmaceutical Sciences*, 74(4), pp. 292–301.

Pongjanyakul, T. and Rongthong, T. (2010) ‘Enhanced entrapment efficiency and modulated drug release of alginate beads loaded with drug-clay intercalated complexes as microreservoirs’, *Carbohydrate Polymers*, 81(2), pp. 409–419.

Rojtanatanya, S. and Pongjanyakul, T. (2010) ‘Propranolol-magnesium aluminum silicate complex dispersions and particles: Characterization and factors influencing drug release’, *International Journal of Pharmaceutics*, 383(1–2), pp. 106–115.

Sheela, N. R., Muthu, S. and Krishnan, S. S. (2010) ‘FTIR , FT Raman and UV-Visible Spectroscopic Analysis on Metformin Hydrochloride’, *Asian Journal of Chemistry*, 22(7), pp. 5049–5056.

Totea, A. M. *et al.* (2019) ‘Real time calorimetric characterisation of clay – drug complex dispersions and particles’, *International Journal of Pharmaceutics: X*, 1(December 2018), p. 100003.

Totea, A. M. *et al.* (2019) ‘Thermodynamics of clay – Drug complex dispersions: Isothermal titration calorimetry and high-performance liquid chromatography’, *Journal of Pharmaceutical Analysis*. Xi'an Jiaotong University.

Vaingankar, P. and Amin, P. (2017) ‘Continuous melt granulation to develop high drug loaded sustained release tablet of Metformin HCl’, *Asian Journal of Pharmaceutical*

*Sciences*, 12(1), pp. 37–50.

# **Chapter 6:**

*Tablet formulation and dissolution testing studies*

## **Chapter 6: Tablet formulation and dissolution testing studies**

In this chapter, one of the model drugs, PPN, is selected as a candidate for further studies in tablet formulation and dissolution studies. Two very common hydrophilic polymers namely xanthan gum, XG, (anionic in nature) and polyethylene oxide, PEO, (non-ionic in nature) are used to aid in modulating drug release and their effect determined. A mechanism for the drug release is later proposed based on ITC results from chapter 3.

### **6.1. Methodology**

#### **6.1.1. Bulk compaction behaviour and tablet porosity**

Please refer to chapter 2, sections 2.2.3.1 and 2.2.3.2.

#### **6.1.2. Dissolution testing and kinetics of drug release**

Please refer to chapter 2, sections 2.2.3.3 and 2.2.3.4.

## **6.2. Results and discussion**

### **6.2.1. Formulation codes**

The formulation codes presented in Table 6.1 was used throughout this section. Each of the tablets prepared contained an equivalent of 40 mg PPN in the MAS-PPN complexes or MAS-PPN physical mixture, and had a final weight calculated according to the amount of polymer used (5 % w/w, 10 % w/w, 30 % w/w and 50 % w/w). The amount of MAS-PPN complex that contained 40 mg PPN was calculated using the assay described in chapter 3, section 3.2.5.2.

**Table. 6.1.** Formulation codes for tablets prepared using MAS-PPN complexes or MAS-PPN physical mixture (both containing an equivalent of 40 mg PPN), and PEO or XG in different amounts (5 % w/w, 10 % w/w, 30 % w/w and 50 % w/w)

<b>Formulation</b>	<b>Polymer amount in formulation (% w/w)</b>	<b>Formulation code</b>
<b>MAS-PPN (phys. mix) + PEO</b>	5	<i>PEO5%_PM</i>
	10	<i>PEO10%_PM</i>
	30	<i>PEO30%_PM</i>
	50	<i>PEO50%_PM</i>
<b>MAS-PPN (complex) + PEO</b>	5	<i>PEO5%_C</i>
	10	<i>PEO10%_C</i>
	30	<i>PEO30%_C</i>
	50	<i>PEO50%_C</i>
<b>MAS-PPN (phys. mix) + XG</b>	5	<i>XG5%_PM</i>
	10	<i>XG10%_PM</i>
	30	<i>XG30%_PM</i>
	50	<i>XG50%_PM</i>
<b>MAS-PPN (complex) + XG</b>	5	<i>XG5%_C</i>
	10	<i>XG10%_C</i>
	30	<i>XG30%_C</i>
	50	<i>XG50%_C</i>

### 6.2.2. Bulk compaction behaviour and tablet porosity

Bulk compaction behaviour was studied for the formulations prepared as plots of relative density vs. upper punch pressure measured during loading to 130 MPa (10 kN) and unloading. The compaction curves of all the samples tested followed roughly similar trends: the compaction behaviour was dominated by plastic recovery during the loading stage following non-reversible deformation, movement and fragmentation of the particles (Laity and Cameron, 2008; Han *et al.*, 2011; Laity *et al.*, 2015). Repeated experiments (n=3) overlapped closely, with small variations under  $\pm 2\%$  in the relative density during

compaction observed mainly in the smaller tablets (5% PEO/XG) which may be due to measurement variations of the tablet height and diameter after ejection.

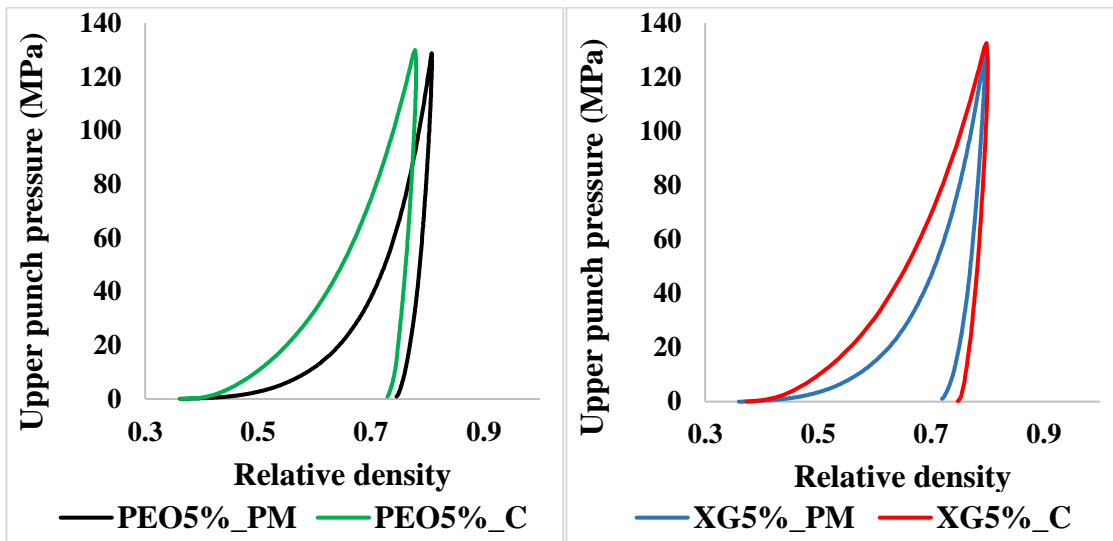


**Fig. 6.1.** Compaction behaviour of formulations containing MAS-PPN complexes or MAS-PPN physical mixture and 5% PEO (a) or XG (b) compacted to 130 MPa: plots of measured upper punch pressure vs. relative density

**Table 6.2.** Comparison of bulk compaction behaviour and porosity for formulations MAS-PPN complexes or MAS-PPN physical mixture and 5% w/w PEO or XG; all specimens compacted to 130 MPa average upper punch pressure

		PEO5%_PM	PEO5%_C	XG5%_PM	XG5%_C
<b>True density (kg/m<sup>3</sup>)</b>		1945.93 ± 1.45	1990.50 ± 22.71	2050.56 ± 12.40	1952.43 ± 1.02
<b>Relative density</b>	Uncompacted	0.37 ± 0.00	0.35 ± 0.01	0.35 ± 0.01	0.37 ± 0.01
	At maximum pressure	0.83 ± 0.01	0.80 ± 0.00	0.79 ± 0.02	0.81 ± 0.00
	After ejection	0.75 ± 0.01	0.75 ± 0.01	0.72 ± 0.01	0.74 ± 0.00
<b>Elastic recovery (%)</b>		9.10 ± 1.14	6.99 ± 0.54	8.35 ± 1.11	7.59 ± 0.82
<b>Diameter after ejection (mm)</b>		10.06 ± 0.01	10.05 ± 0.00	10.07 ± 0.01	10.03 ± 0.01
<b>Porosity (%)</b>		18.37 ± 1.20	22.50 ± 0.55	23.22 ± 1.07	20.50 ± 0.46

Following unloading, all the specimens exhibited significant elastic recovery showing reversible deformation of some of the structures in the tablets (Fig. 6.1. to 6.4.). Overall, the

elastic recovery was considerably higher for the specimens containing MAS-PPN physical mixture compared to those containing MAS-PPN complexes. An overall increase in elastic recovery during unloading was also observed upon the decrease of polymeric content in the tablets, suggesting that the MAS in the samples exhibits significant elastic recovery upon compaction. This behaviour was previously reported in literature by Laity *et al.* in 2015 (Laity *et al.*, 2015). The authors found that MAS exhibited significant elastic recovery upon compaction to 204 and 611 MPa. This behaviour was attributed to changes in the basal spacing of the clay upon compaction or to the bending of the clay platelets, theory which was not however further explored (Laity *et al.*, 2015).

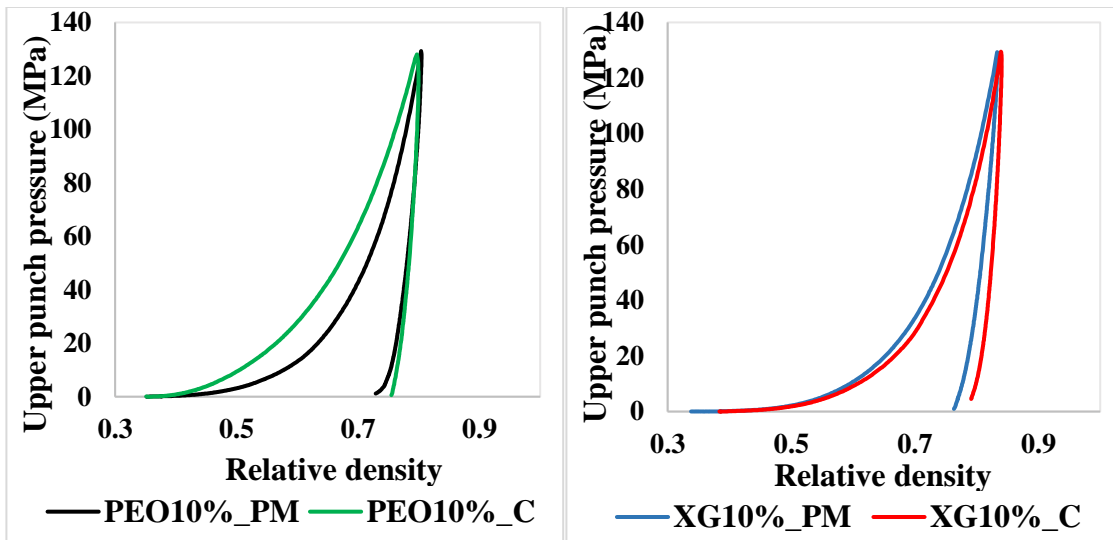


**Fig. 6.2.** Compaction behaviour of formulations containing MAS-PPN complexes or MAS-PPN physical mixture and 10 % PEO (a) or XG (b) compacted to 130 MPa: plots of measured upper punch pressure vs. relative density

**Table 6.3.** Comparison of bulk compaction behaviour and porosity for formulations MAS-PPN complexes or MAS-PPN physical mixture and 10 % PEO or XG; all specimens compacted to 130 MPa average upper punch pressure.

		PEO10%_PM	PEO10%_C	XG10%_PM	XG10%_C
<b>True density (kg/m<sup>3</sup>)</b>		1880.35 ± 5.78	1925.27 ± 3.92	1910.47 ± 2.97	1946.70 ± 1.87
<b>Relative density</b>	Uncompacted	0.36 ± 0.01	0.35 ± 0.01	0.36 ± 0.02	0.37 ± 0.01
	At maximum pressure	0.81 ± 0.02	0.79 ± 0.00	0.83 ± 0.01	0.81 ± 0.00
	After decompression	0.73 ± 0.01	0.75 ± 0.01	0.76 ± 0.02	0.76 ± 0.00
<b>Elastic recovery (%)</b>		9.18 ± 0.48	5.95 ± 0.78	7.93 ± 1.15	6.03 ± 0.33
<b>Diameter after ejection (mm)</b>		10.06 ± 0.01	10.04 ± 0.0	10.06 ± 0.0	10.05 ± 0.01
<b>Porosity (%)</b>		16.07 ± 0.62	20.19 ± 0.31	17.24 ± 0.72	20.31 ± 0.25

The reduction in elastic recovery during compaction upon use of MAS-PPN complexes in the tablets instead of MAS-PPN physical mixture is of high importance because it reduces the chances of tablets cracking or tooling wear (Laity *et al.*, 2015).

Furthermore, rather high ejection forces were observed when the specimens were expelled from the die, up to 200 N, which may be explained by the high elastic recovery of the tablets leading to high frictional forces between the tablets and the die walls (Laity *et al.*, 2015). During the prompt measurements of the ejected tablets it was observed that tablets had slightly larger diameters compared to that of the die used, observed as an increase in diameter from 10.00 mm (diameter of the tablet press) to 10.05 ± 0.02 mm. The diameter measured after ejection was also slightly higher for the tablets containing MAS-PPN physical mixture (10.05 ± 0.02 mm) compared to those containing MAS-PPN complexes (10.04 ± 0.12), suggesting a higher elastic recovery, hence the tablets being more prone to cracking and splitting (Laity *et al.*, 2015).

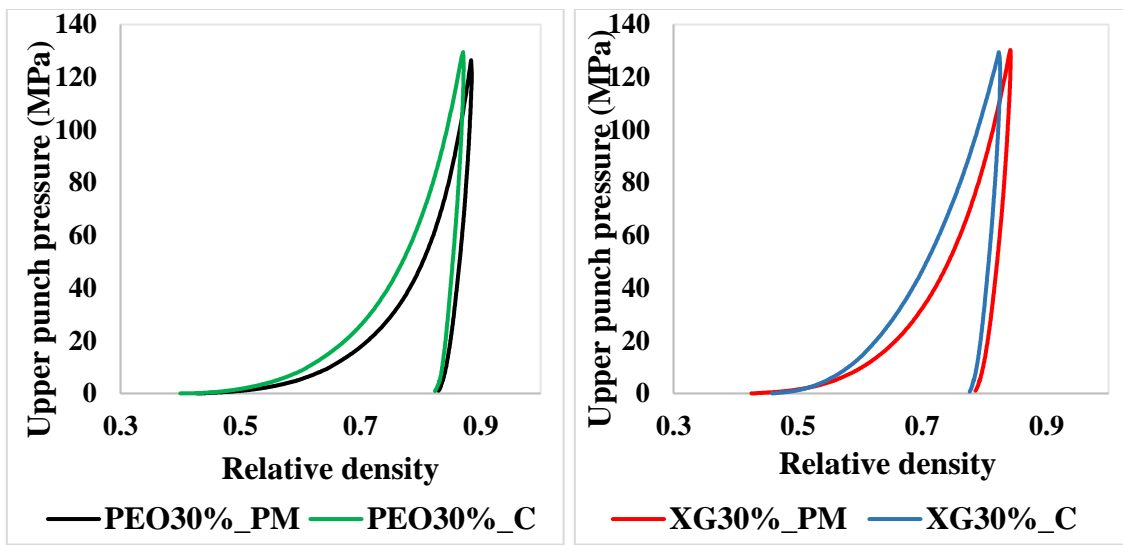


**Fig. 6.3.** Compaction behaviour of formulations containing MAS-PPN complexes or MAS-PPN physical mixture and 30 % PEO (a) or XG (b) compacted to 130 MPa: plots of measured upper punch pressure vs. relative density

**Table 6.4.** Comparison of bulk compaction behaviour and porosity for formulations MAS-PPN complexes or MAS-PPN physical mixture and 30 % PEO or XG; all specimens compacted to 130 MPa average upper punch pressure.

		PEO30%_PM	PEO30%_C	XG30%_PM	XG30%_C
<b>True density (kg/m<sup>3</sup>)</b>		1673.43 ± 2.99	1742.86 ± 12.38	1799.95 ± 5.77	1855.78 ± 2.26
<b>Relative density</b>	Uncompacted	0.42 ± 0.01	0.40 ± 0.00	0.43 ± 0.00	0.47 ± 0.01
	At maximum pressure	0.88 ± 0.00	0.87 ± 0.00	0.85 ± 0.01	0.83 ± 0.00
	After ejection	0.83 ± 0.01	0.83 ± 0.00	0.79 ± 0.01	0.78 ± 0.01
<b>Elastic recovery (%)</b>		6.38 ± 0.13	5.18 ± 0.27	6.78 ± 0.23	5.50 ± 0.41
<b>Diameter after ejection (mm)</b>		10.04 ± 0.02	10.04 ± 0.00	10.06 ± 0.04	10.06 ± 0.02
<b>Porosity (%)</b>		11.84 ± 0.49	12.64 ± 0.29	15.58 ± 0.57	17.84 ± 0.74

Porosity was calculated for all the tablets prepared. Overall, tablet porosity was shown to be slightly higher for the tablets containing MAS-PPN complexes which may offer additional benefits in controlling PPN release due to potential differences in water ingress. It is however important to note that other important tablet characteristics such as solubility, surface area and particle size can influence dissolution rates (Micrometrics, 1998; Riippi *et al.*, 1998). It

was also interesting to note that there was a significant reduction in the porosity of the tablets with an increase in the polymer content. This was particularly evident with regards to the PEO formulations e.g. the PEO5%\_PM had a porosity of 23% and this was significantly reduced to 8% in the PEO50% PM tablets.

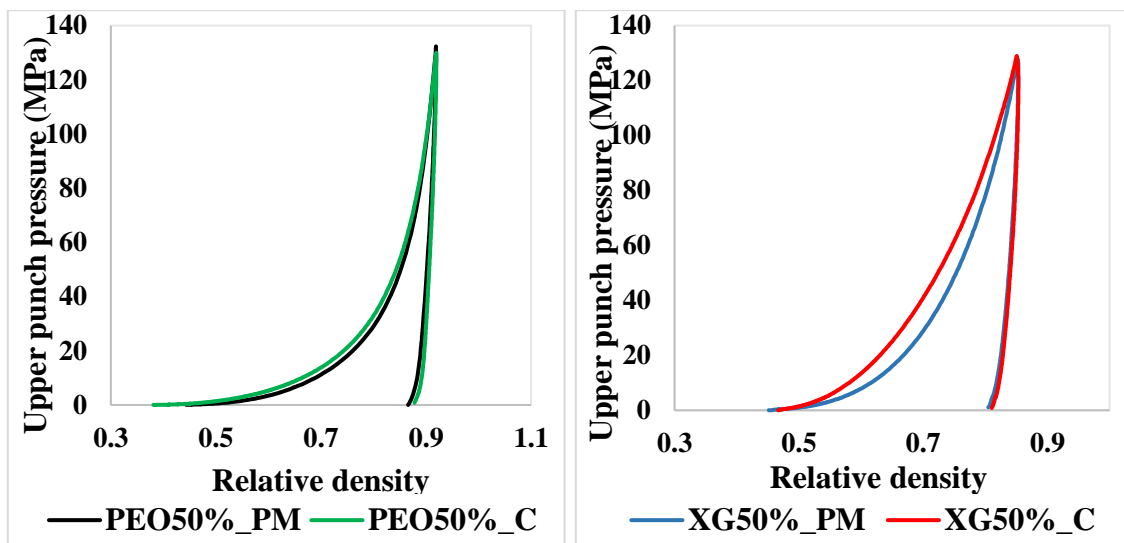


**Fig. 6.4.** Compaction behaviour of formulations containing MAS-PPN complexes or MAS-PPN physical mixture and 50 % PEO (a) or XG (b) compacted to 130 MPa: plots of measured upper punch pressure vs. relative density

**Table. 6.5.** Comparison of bulk compaction behaviour and porosity for formulations MAS-PPN complexes or MAS-PPN physical mixture and 50 % PEO or XG; all specimens compacted to 130 MPa average upper punch pressure.

		PEO50%_PM	PEO50%_C	XG50%_PM	XG50%_C
<b>True density (kg/m<sup>3</sup>)</b>		1507.83 ± 1.86	1515.72 ± 2.22	1718.95 ± 2.65	1731.33 ± 1.26
<b>Relative density</b>	Uncompacted	0.44 ± 0.01	0.47 ± 0.00	0.45 ± 0.02	0.47 ± 0.00
	At maximum pressure	0.92 ± 0.00	0.85 ± 0.00	0.85 ± 0.00	0.85 ± 0.00
	After ejection	0.86 ± 0.00	0.81 ± 0.00	0.80 ± 0.00	0.80 ± 0.00
<b>Elastic recovery (%)</b>		6.17 ± 0.48	4.23 ± 0.25	5.72 ± 0.08	5.10 ± 0.23
<b>Diameter after ejection (mm)</b>		10.06 ± 0.02	10.04 ± 0.00	10.02 ± 0.00	10.02 ± 0.00
<b>Porosity (%)</b>		7.89 ± 0.44	8.43 ± 0.96	13.50 ± 0.63	16.09 ± 1.17

The relative density values presented in this section depend on the true density of each formulation. Differences were observed between the true density of the formulations containing PEO and those containing XG, which can be attributed to the different particle sizes of the polymers. True powder density was similar for the formulations containing MAS-PPN complexes and those containing MAS-PPN physical mixture which was expected since the MAS and the MAS-PPN complex particles were sieved to a particle size between 63-125 µm (Table 6.2. to 6.5.). An increase in powder density was observed however upon a decrease in polymer content in the formulations due to the overall decrease of mean particle size in the samples.

Detailed results for each of the formulations compacted at 130 MPa can be found in Tables 6.2 - 6.5.

### **6.2.3. Dissolution testing and kinetics of drug release**

Dissolution studies evaluating drug release from MAS-PPN complexes/physical mixture in PEO or XG matrices show an overall superior capability of the compacts containing MAS-PPN complexes in modulating PPN release. However, these effects were less noticeable as the amount of polymer in tablets is increased to 30 % for PEO and 50 % for XG matrices. Results also demonstrate that the synergistic interactions between MAS and PEO/XG lead to a superior control of PPN release, when compared its release in control studies presented in literature from MAS-PPN complexes/physical mixture compacts (Rojtanatanya and Pongjanyakul, 2010). Here, the authors discuss the strong potential of the MAS-PPN complexes in controlling PPN release and the possibility of using these complexes in combination with polymers in future studies (Rojtanatanya and Pongjanyakul, 2010).

It should be noted that although XG and PEO can often be used in tablets in combination with other polymers or materials due to desired synergistic interactions leading to better control of drug release superior to that of the materials used on their own (Jian *et al.*, 2012; Pongjanyakul and Rojtanatanya, 2012; Palmer *et al.*, 2013; Rongthong *et al.*, 2013; Pappa *et al.*, 2018), there is no current study on their combination with MAS-PPN complexes/physical mixture.

### **6.2.3.1. Tablets containing PEO and MAS-PPN complexes/physical mixture**

Dissolution studies on tablets prepared using MAS-PPN complexes or MAS-PPN physical mixture (40 mg PPN) and different amounts of PEO (5 %, 10 %, 30 % and 50 % w/w) highlighted the ability of the MAS-PPN complexes to control drug release even at low polymer concentrations, in both pH 1.2 hydrochloric acid and pH 6.8 phosphate buffer. All tablets tested showed a controlled PPN release profile over the period tested. Overall, a higher PPN release was observed in pH 1.2 hydrochloric acid compared to pH 6.8 buffer. This behaviour also observed in recovery studies described in chapter 3, section 3.2.5.2.

#### **6.2.3.1.1. Tablets containing 5 % w/w PEO**

At 5 % PEO w/w, PPN release was controlled for all tablets containing MAS-PPN complexes or MAS-PPN physical mixture incorporated in the PEO matrix (Fig. 6.5.). Tablets containing 5 % PEO and MAS-PPN physical mixture gave sustained PPN release after an initial burst in both acid and buffer. However, this behaviour was not observed in the dissolution profiles of tablets containing 5 % PEO and MAS-PPN complexes which, in turn, demonstrate the efficacy of the MAS-PPN reservoirs in retarding drug release. A larger amount of PPN was released in acid from the tablets containing MAS-PPN complexes, up to 78 %, compared to those containing MAS-PPN physical mixture, up to 68 %. In buffer similar amounts of PPN were released from tablets containing MAS-PPN complexes (62 %) and MAS-PPN physical mixture (59 %) (Fig. 6.5. a and b).

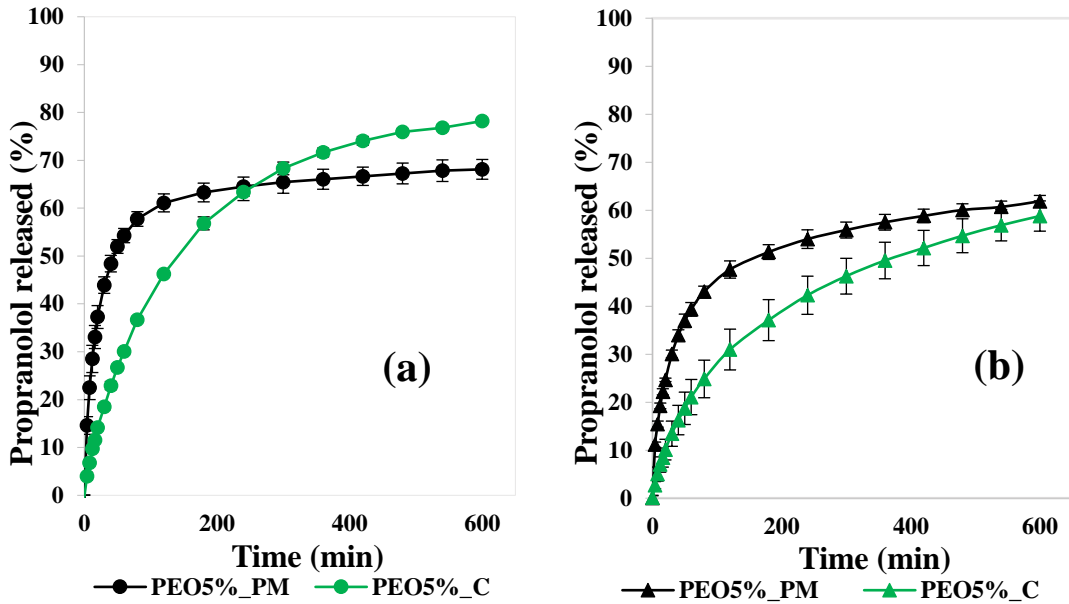


**Fig. 6.5.** PPN release profile from matrices made of MAS-PPN phys. mix and complex particles combined with PEO (5%) in (a) pH 1.2 hydrochloric acid and (b) pH 6.8 buffer over 10 h

Tablets had an anomalous (non-Fickian) diffusion occurring, with a value of  $n$  as 0.70 and 0.55 for formulations prepared using MAS-PPN complexes in acid and buffer respectively. For the tablets prepared using MAS-PPN physical mixture a value of  $n$  as 0.45 and 0.35 was observed in acid and buffer respectively, showing a rather Fickian diffusion mechanism, governed by PPN diffusion. Hence, it is clearly observed that the value of  $n$  was significantly increased upon the use of MAS-PPN complexes in the tablets, which shows that these have an impact on the mechanism of PPN release. MDT values changed considerably in acid and buffer, from 50 min (acid) and 98 min (buffer) respectively for tablets containing MAS-PPN physical mixture, to 135 min (acid) and 169 min (buffer) respectively for tablets containing MAS-PPN complexes suggesting a slower PPN release for MAS-PPN complexes in PEO matrices. DE was similar in acid for tablets containing MAS-PPN complexes (61 %) and tablets containing MAS-PPN physical mixture (62 %) showing their similarity and their capability in reducing PPN release. In buffer, DE values were considerably different, 52 % for tablets containing MAS-PPN physical mixture and 42% tablets containing MAS-PPN complexes, which is most probably an effect of the ions in solution. This can be explained

by the increase in ionic strength of the medium leading to a ‘salting out’ of the polymer. This causes the polymer to lose its water hydration properties and show a lower degree of swelling as ions present in solution compete for the available water of hydration (Kavanagh and Corrigan, 2004).

**Table. 6.6.** Kinetics of drug release of tablets prepared using MAS-PPN complexes of MAS-PPN physical mixture incorporated in 5 % PEO matrices

		<i>Formulation code</i>	$DE_{600\ min} (\%)$	MDT (min)	RSQ	<i>n</i> value
<i>pH</i>	<i>0.1M HCl</i>	<i>PEO5%_PM</i>	62.34	50.31	0.973	0.45
		<i>PEO5%_C</i>	60.57	134.75	0.996	0.70
<i>pH</i>	<i>6.8</i>	<i>PEO5%_PM</i>	52.44	91.58	0.956	0.35
		<i>PEO5%_C</i>	42.26	169.13	0.985	0.55

#### 6.2.3.1.2. Tablets containing 10 % w/w PEO

At 10 % PEO, PPN release was shown to be controlled for tablets containing MAS-PPN complexes and MAS-PPN physical mixture in both acid and buffer (Fig. 6.6.). In acid, a larger amount of PPN was released from the tablets containing MAS-PPN complexes, up to 74 %, compared to tablets containing MAS-PPN physical mixture, up to 63 %. In buffer, the amount of PPN released was similar, up to 52 % from tablets containing MAS-PPN physical mixture and up to 54% for the tablets containing MAS-PPN complexes.

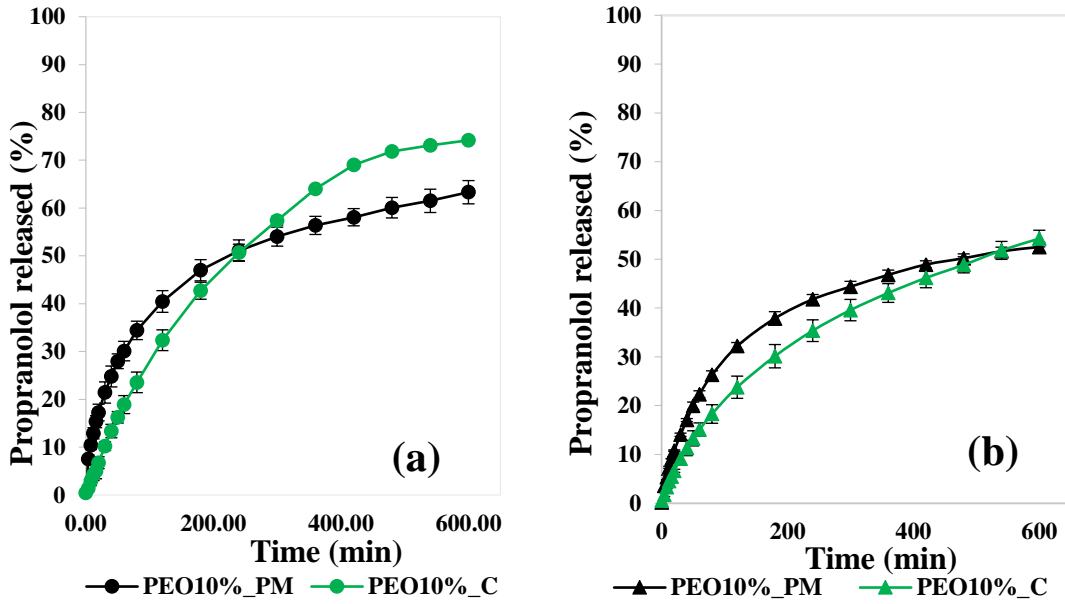


**Fig. 6.6.** PPN release profile from matrices made of MAS-PPN phys. mix and complex particles combined with PEO (10%) in (a) pH 1.2 hydrochloric acid and (b) pH 6.8 buffer over 10 h

However, in both acid and buffer PPN release was more controlled from the tablets containing MAS-PPN complexes, with a value of  $n$  as 0.83 and 0.63 respectively, compared to those containing MAS-PPN physical mixture, with a value of  $n$  as 0.45 and 0.51 respectively. The same behaviour was observed in the tablets containing 5 % PEO, although the increase in PEO content to 10% led to the tablets tested having anomalous (non-Fickian) diffusion to occur ( $n$  higher or equal to 0.45 but lower than 0.89) showing that both PEO erosion and PPN diffusion contributed to the overall drug release mechanisms (Siah-Shadbad *et al.*, 2011). It was also observed that  $n$  significantly increased upon dissolution of tablets containing MAS-PPN complexes compared to tablets containing MAS-PPN physical mixture in both acid and buffer, showing the ability of the MAS-PPN complexes to retard PPN release. DE had similar values for tablets containing MAS-PPN complexes and tablets containing MAS-PPN physical mixture in both acid (52 % and 50 % respectively) and buffer (36 % and 40 % respectively) showing their similarity and their capability in reducing PPN release. However, the MDT was considerably higher for tablets containing MAS-PPN complexes compared the tablets containing MAS-PPN physical mixture in acid (182 min

and 129 min respectively) and buffer (201 min and 138 min), suggesting a slower PPN release for MAS-PPN complexes in PEO matrices.

**Table 6.7.** Kinetics of drug release of tablets prepared using MAS-PPN complexes of MAS-PPN physical mixture incorporated in 10 % PEO matrices

	<i>Formulation code</i>	$DE_{600\text{ min}} (\%)$	MDT (min)	RSQ	<i>n</i> value
<i>pH</i> <b>0.1M HCl</b>	<i>PEO10%_PM</i>	49.57	129.24	0.987	0.45
	<i>PEO10%_C</i>	51.77	182.28	0.990	0.83
<i>pH</i> <b>6.8</b>	<i>PEO10%_PM</i>	40.49	137.84	0.971	0.51
	<i>PEO10%_C</i>	36.23	201.20	0.993	0.63

#### 6.2.3.1.3. Tablets containing 30 % w/w PEO

Tablets containing 30 % PEO were shown to be able to provide further controlled PPN release (Fig. 6.7.). However, the amount of PPN released was significantly lower when compared to previous formulations tested (5 % PEO and 10 % PEO), suggesting stronger effects of the PEO. In both acid and buffer a relatively higher amount of PPN was released from the tablets containing MAS-PPN complexes, up to 64 % and 57 % respectively, compared to tablets containing MAS-PPN physical mixture, up to 57 % and 50 % respectively, suggesting a reduction in PPN-MAS complexation rate upon dissolution of tablets containing MAS-PPN complexes compared to dissolution of tablets containing MAS-PPN physical mixtures.

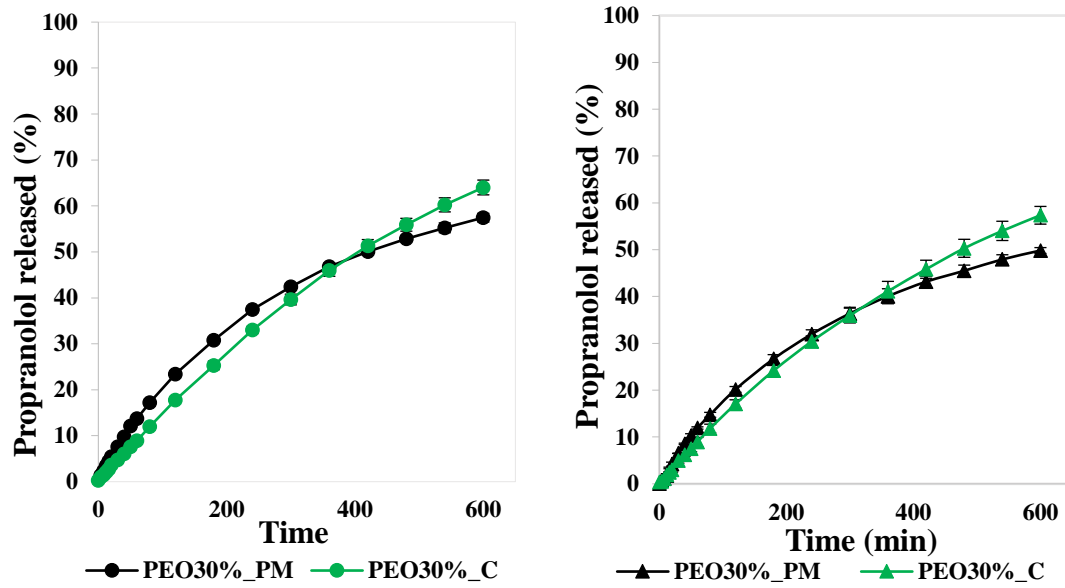


**Fig. 6.7.** PPN release profile from matrices made of MAS-PPN phys. mix and complex particles combined with PEO (30%) in (a) pH 1.2 hydrochloric acid and (b) pH 6.8 buffer over 10 h

In both acid and buffer, the kinetics of drug release shows the tablets containing MAS-PPN complexes to have a value of  $n$  as 0.91 and 0.83 respectively, compared to those containing MAS-PPN physical mixture, with a value of  $n$  as 0.70 and 0.68 respectively. This suggests that a ‘zero-order’ PPN release independent of time occurred from the tablets containing 30% PEO and MAS-PPN complexes in acid. The dissolution of tablets containing MAS-PPN complexes in buffer, as well as the dissolution of the tablets containing MAS-PPN physical mixture in acid and buffer showed an anomalous release, governed by both PPN diffusion and PEO erosion. DE had similar values for the tablets containing MAS-PPN complexes and tablets containing MAS-PPN physical mixture in both acid (37 % and 38 % respectively) and buffer (34 % and 33 % respectively) showing their similarity and their capability in slowing PPN release rate. However, the MDT was considerably higher for tablets containing MAS-PPN complexes compared the tablets containing MAS-PPN physical mixture in acid (254 min and 200 min respectively) and buffer (249 min and 204 min), suggesting a slower PPN release for MAS-PPN complexes in PEO matrices.

**Table. 6.8.** Kinetics of drug release of tablets prepared using MAS-PPN complexes of MAS-PPN physical mixture incorporated in 30 % PEO matrices

	<i>Formulation code</i>	$DE_{600\text{ min}} (\%)$	MDT (min)	RSQ	<i>n</i> value
<i>pH 6.8 Buffer</i>	<i>PEO30%_PM</i>	38.22	200.16	0.991	0.70
	<i>PEO30%_C</i>	37.04	254.06	0.999	0.91
<i>0.1M HCl</i>	<i>PEO30%_PM</i>	32.89	204.26	0.991	0.68
	<i>PEO30%_C</i>	33.67	249.41	0.998	0.83

#### 6.2.3.1.4. Tablets containing 50 % w/w PEO

Upon increasing the amount of PEO in the tablets to 50 % it was observed that the strong effects of the PEO led to almost identical release profile for tablets containing MAS-PPN complexes and MAS-PPN physical mixture in acid, as well as in buffer (Fig. 6.8.). Furthermore, the amount of PPN released was considerably lower than in previous studies where tablets were formulated with a lower PEO content (5, 10 and 30 %). In both acid and buffer a slightly larger amount of PPN was released from the tablets containing MAS-PPN complexes, up to 52 % and 44 % respectively, compared to tablets containing MAS-PPN physical mixture, up to 49 % and 42 % respectively. This suggests that at 50 % PEO in the tablets, approx.  $46 \pm 5$  % of PPN was released over 10 h. The high polymer content therefore masks the effects of the MAS-PPN complexes as well as the MAS effect in the physical mixtures.

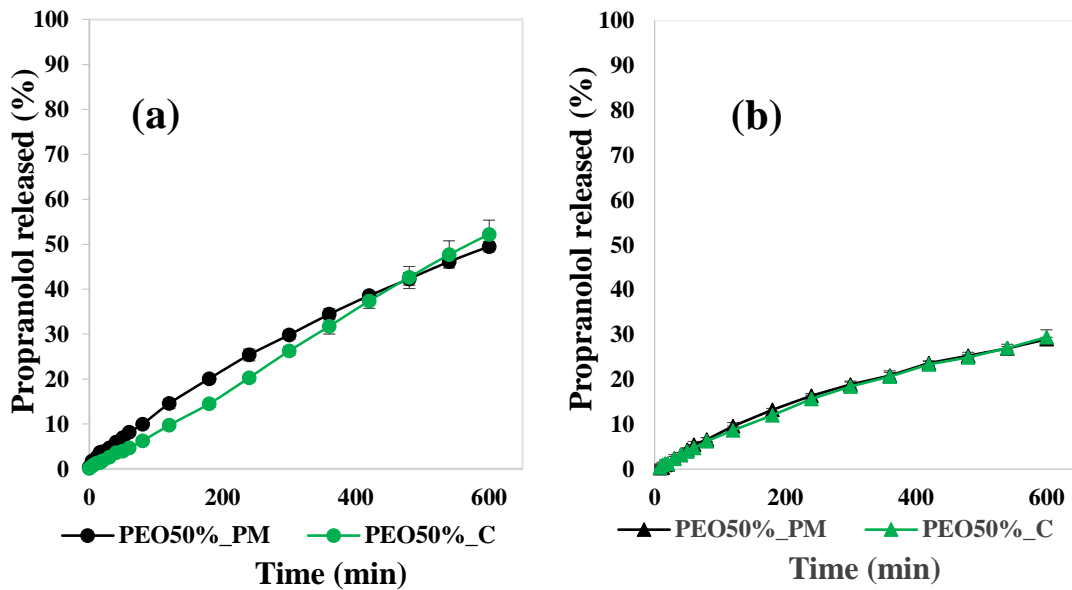


**Fig. 6.8.** PPN release profile from matrices made of MAS-PPN phys. mix and complex particles combined with PEO (50%) in (a) pH 1.2 hydrochloric acid and (b) pH 6.8 buffer over 10 h

Tablets containing MAS-PPN physical mixture had an anomalous (non-Fickian) diffusion, with a value of  $n$  as 0.80 and 0.77 in acid and buffer respectively. A super case II transport was observed for the tablets containing MAS-PPN complexes, with a value of  $n$  as 1.06 and 1.07 in acid and buffer respectively. It was clearly observed that the value of  $n$  was significantly increased upon the use of MAS-PPN complexes in the tablets, which demonstrates that these have an impact on the mechanism of PPN release. MDT values were similar in acid and buffer for tablets containing MAS-PPN complexes (301 min in acid and 291 min in buffer), as well as for the tablets containing MAS-PPN complexes (257 min in acid and 255 min in buffer), suggesting a slower PPN release from tablets containing MAS-PPN complexes in PEO matrices. DE was similar in acid and buffer for tablets containing MAS-PPN complexes (26 % in acid and 21 % in buffer) and tablets containing MAS-PPN physical mixture (28 % in acid and 25 % in buffer) showing their similarity and their capability in reducing PPN release.

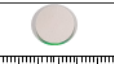
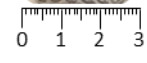
**Table. 6.9.** Kinetics of drug release of tablets prepared using MAS-PPN complexes of MAS-PPN physical mixture incorporated in 50 % PEO matrices

	<i>Formulation code</i>	$DE_{600\text{ min}} (\%)$	MDT (min)	RSQ	<i>n</i> value
<i>pH 6.8</i>	<i>HCl</i>	<i>PEO50%_PM</i>	28.47	256.99	0.999
		<i>PEO50%_C</i>	26.12	300.55	1.000
<i>Buffer</i>		<i>PEO50%_PM</i>	25.33	254.50	0.999
		<i>PEO50%_C</i>	21.33	291.03	0.997

#### 6.2.3.1.5. Evaluation of tablet appearance and conclusions

Evaluation of tablet appearance revealed that the tablets containing MAS-PPN complexes were a distinct light brown colour, darker than the tablets containing MAS-PPN physical mixture (Table. 6.10.). Furthermore, tablet erosion and growth were both observed. A higher amount of PPN released was observed in acid, which may be linked to the increased erosion of the tablets in acid compared to buffer as observed from the images in Table. 6.10. The increase in drug release in acid may also be explained by the hydrogen ions having a smaller size when compared to sodium ions (28 pm compared to 161 pm respectively), which may promote a deeper diffusion of the hydrogen ions inside the particles) (Rojtanatanya and Pongjanyakul, 2010). Furthermore, the increase in ionic strength of the medium causes the polymer to lose its water hydration properties and show a lower degree of swelling as ions present in solution compete for the available water of hydration (Kavanagh and Corrigan, 2004).

**Table. 6.10.** Tablets containing MAS-PPN complexes or MAS-PPN physical mixture in PEO matrix: appearance prior to dissolution studies and after dissolution in pH 1.2 hydrochloric acid and pH 6.8 buffer

<i>Formulation code</i>	Tablet	pH 1.2 HCl dissolution	pH 6.8 buffer dissolution	
<b>5%PEO_C</b>	 			
<b>5%PEO_PM</b>				
<b>10%PEO_C</b>				
<b>10%PEO_PM</b>				
<b>30%PEO_C</b>				
<b>30%PEO_PM</b>				
<b>50%PEO_C</b>				
<b>50%PEO_PM</b>				

These results obtained from the dissolution studies on the formulated tablets containing MAS-PPN complexes and MS-PPN physical mixture (40 mg PPN) in PEO matrices support the findings presented in previous publications (Rojtanatanya and Pongjanyakul, 2010; Pongjanyakul and Rojtanatanya, 2012). Here, the authors found more PPN to be released from MAS-PPN complexes in polymeric matrices compared to MAS-PPN physical mixtures in polymeric matrices due to a lower complexation rate between the MAS and PPN. Also, based on the findings described in chapter 3, section 3.2.8.3.1 suggesting that binding occurred between MAS and PEO, it is expected for some of the sites on the MAS to become saturated by the PEO during dissolution studies. This may further contribute to a reduction in PPN adsorption/reabsorption. Hence, a dissolution model may be proposed for PPN release from MAS-PPN complexes or physical mixture in PEO matrices (Fig. 6.9.).

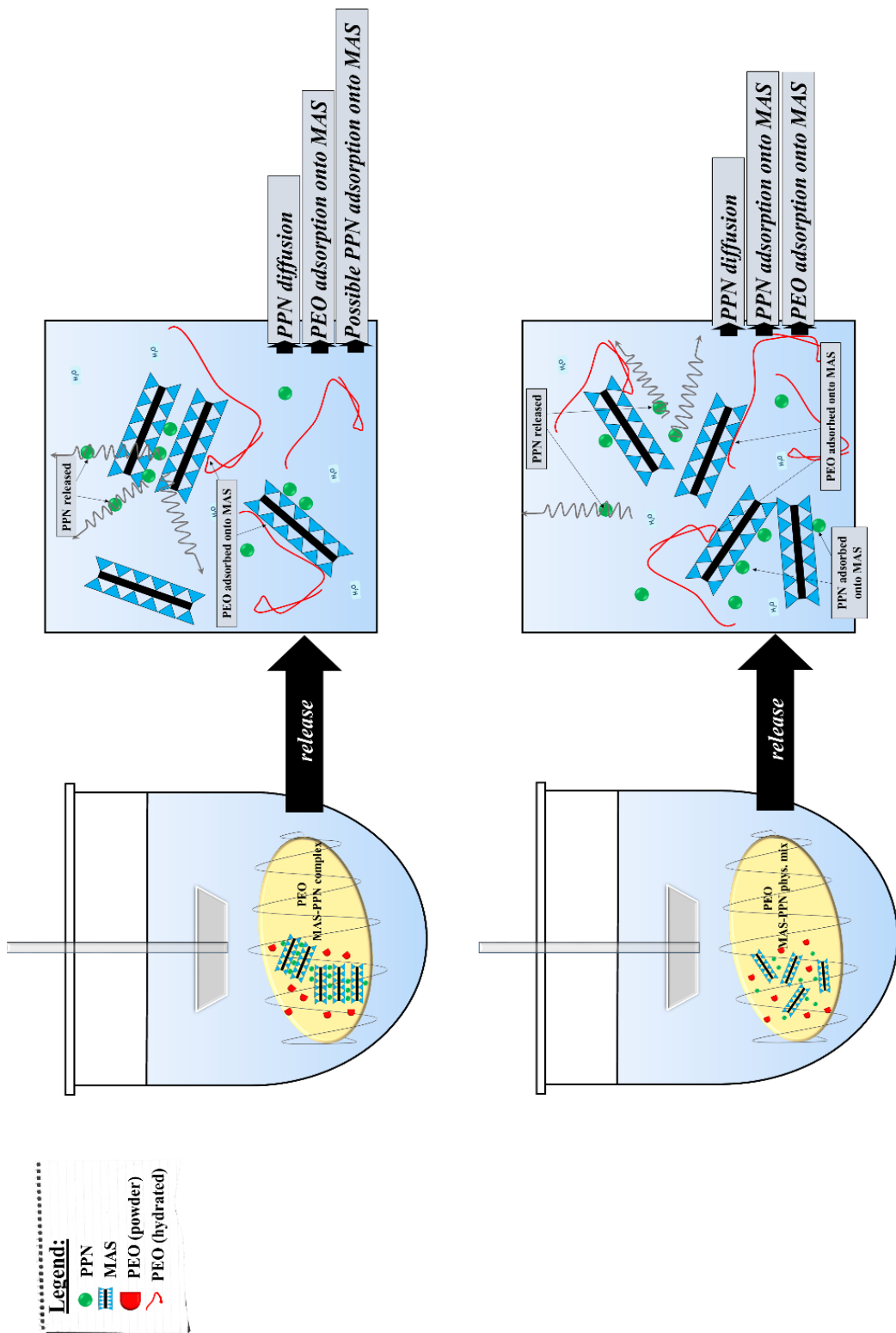


**Fig. 6.9.** Proposed release mechanism model of MAS-PPN complexes and MAS-PPN physical mixture in PEO matrix tablets

### **6.2.3.2. Tablets containing XG and MAS-PPN complexes/physical mixture**

The use of XG in tablets in different amounts (5, 10, 30, 50 % w/w) allowed the observation of MAS-PPN complexes and physical mixture behaviour in combination with XG and their overall effects on controlling PPN release.

#### **6.2.3.2.1. Tablets containing 5 % w/w XG**

At 5% XG w/w, PPN release was rapid for all the tablets tested (Fig. 6.10.). In acid, tablets containing MAS-PPN complexes and those containing MAS-PPN physical mixture were unable to retard PPN release, as they disintegrated within a few seconds. In buffer, the tablets containing MAS-PPN complexes were shown to be relatively controlled compared with its physical mixture counterpart with a significant decrease in the initial burst release. Overall, a larger amount of PPN was released from the tablets containing MAS-PPN complexes in both acid and buffer (82 % and 73 % respectively), compared to the tablets containing MAS-PPN physical mixture (69 % and 64 % respectively). This behaviour can be linked to a lower complexation rate between PPN and MAS when PPN is released from an already formed MAS-PPN complexes. What is advantageous however, is its ability in reducing the burst release. What can also be observed here is the influence of ions in the dissolution media. It is important to note the XG is an anionic polymer. This therefore means the pH does have an influence on its behaviour. XG has a pKa of 3.1 and hence, becomes less soluble at lower pH leading to a lower solubility and hence, a lower matrix swelling (Mu, Tobyn and Staniforth, 2003). Furthermore, the increase in ionic strength of the medium leading to a ‘salting out’ of the polymer causes the polymer to lose its water hydration properties and show a lower degree of swelling and erosion and form a more rigid structure (Kavanagh and Corrigan, 2004; Baumgartner, Pavli and Kristl, 2008).

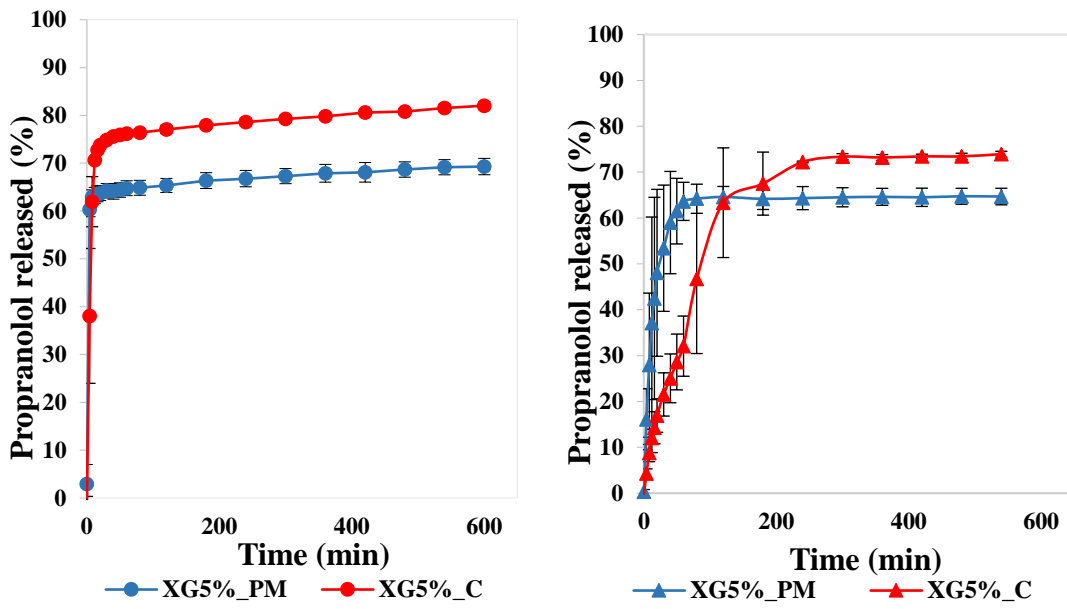


**Fig. 6.10.** PPN release profile from matrices made of MAS-PPN phys. mix and complex particles combined with XG (5%) in (a) pH 1.2 hydrochloric acid and (b) pH 6.8 buffer over 10 h

The calculation of  $n$  value was not possible for the dissolution of tablets containing 5 % w/w XG and MAS-PPN complexes/ physical mixture in acid due to the rapid PPN release. In buffer, the tablets had an anomalous (non-Fickian) diffusion, with a value of  $n$  as 0.73 for tablets containing MAS-PPN complexes and 0.56 for tablets containing MAS-PPN physical mixture (Table 6.11.). Hence,  $n$  value was significantly higher upon the use of MAS-PPN complexes in the tablets, which demonstrates their impact on the mechanism of PPN release. MDT values were similar in acid for tablets containing MAS-PPN complexes (27 min) and those containing MAS-PPN physical mixture (22 min) (Table 6.11.). In buffer, tablets containing MAS-PPN complexes had a considerably higher MDT (76 min), while the tablets containing MAS-PPN physical mixture had a low MDT (19 min). DE values in acid and buffer for tablets containing MAS-PPN physical mixture (67 % in acid and 63 % in buffer) and for the tablets containing MAS-PPN complexes (78 % acid and 67 % buffer) suggest the low capability of the tested tablets to modulate PPN release.

**Table. 6.11.** Kinetics of drug release of tablets prepared using MAS-PPN complexes of MAS-PPN physical mixture incorporated in 5 % XG matrices

	<i>Formulation code</i>	$DE_{600\ min} (\%)$	MDT (min)	RSQ	<i>n</i> value
<i>0.1M HCl</i>	XG5%_PM	66.84	22.26	-	-
	XG5%_C	78.36	26.86	-	-
<i>pH 6.8 Buffer</i>	XG5%_PM	62.87	18.85	0.958	0.56
	XG5%_C	64.53	76.37	0.985	0.73

- Indicates PPN release was too rapid for n values to be calculated

### 6.2.3.2.2. Tablets containing 10 % w/w XG

Tablets containing 10 % w/w XG and MAS-PPN complexes/ physical mixture were shown to be able to provide controlled PPN release in both acid and buffer (Fig. 6.11.). PPN release from tablets containing MAS-PPN complexes was shown to be more controlled in both acid and buffer, compared to PPN release from tablets containing MAS-PPN physical mixture. However, the amount of PPN released from the MAS-PPN complex containing tablets and MAS-PPN physical mixture containing tablets was very similar in acid (72 % and 73 % respectively) and in buffer (44 % and 46 % respectively). Also, as observed, a lower amount of PPN was released upon tablets dissolution in buffer compared to the acidic media, which is due to the effects of the ions in solution, behaviour also observed in recovery studies chapter 3, section 3.2.5.2.

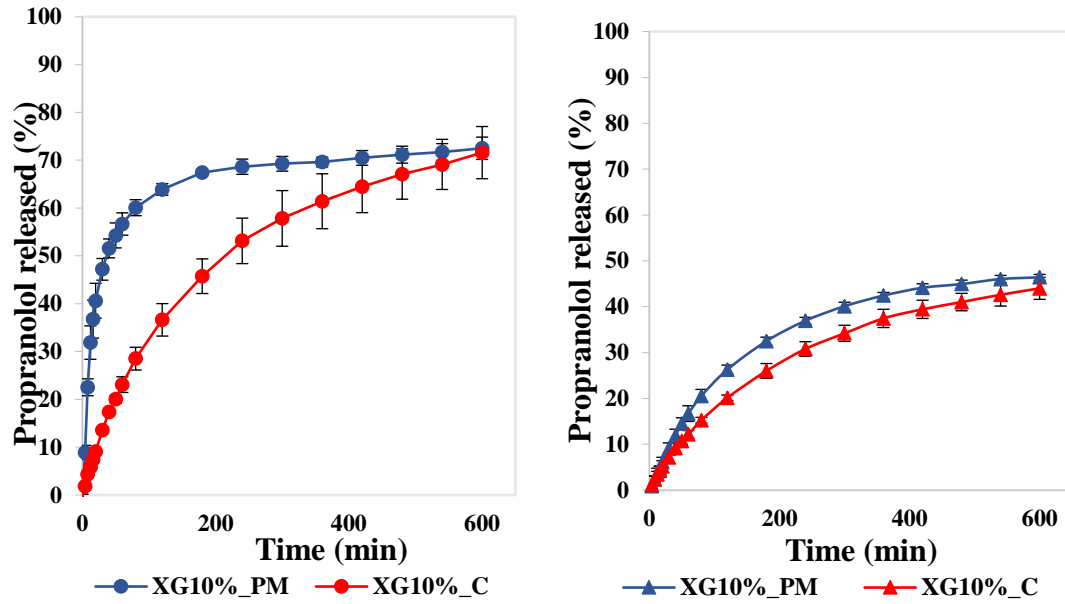


**Fig. 6.11.** PPN release profile from matrices made of MAS-PPN phys. mix and complex particles combined with XG (10%) in (a) pH 1.2 hydrochloric acid and (b) pH 6.8 buffer over 10 h

Analysis of kinetics of drug release (Table 6.12.) showed that  $n$  had a value lower than 0.89 and higher than 0.45 for all the tablets tested suggesting anomalous transport, governed by both PPN diffusion and XG matrix relaxation.  $n$  value was slightly higher for the tablets containing MAS-PPN complexes compared to tablets containing MAS-PPN physical mixture in both acid (0.74 compared to 0.62) and buffer (0.63 compared to 0.57). MDT was considerably lower in acid for the tablets containing MAS-PPN physical mixture (54 min), compared to the tablets containing MAS-PPN complexes (166 min), proving the efficiency of the MAS-PPN complexes in controlling the release rate of PPN. In buffer, the MDT of the tablets containing MAS-PPN complexes (180 min) was also slightly higher than the MDT of the tablets containing MAS-PPN physical mixture (142 min). DE was slightly higher for the tablets containing MAS-PPN physical mixture compared to the tablets containing MAS-PPN complexes in both acid (66 % compared to 51 %) and buffer (31 % compared to 35 %). This mainly suggests that more PPN was released from the tablets containing MAS-PPN physical mixture which is in contrast with the data collected from dissolution of tablets containing PEO (section 6.2.3.1.) and may be due to the compatibility between XG, PPN and MAS. Hence, this behaviour may be explained by the ITC findings

that showed both XG and MAS to compete for the binding with PPN, possibly leading to a reduction in drug released from the MAS-PPN complexes as it is potentially rebinding with XG.

**Table. 6.12.** Kinetics of drug release of tablets prepared using MAS-PPN complexes of MAS-PPN physical mixture incorporated in 10 % XG matrices

		<i>Formulation code</i>	$DE_{600\text{ min}} (\%)$	MDT (min)	RSQ	<i>n</i> value
<i>pH 6.8</i>	<i>0.1M HCl</i>	XG10%_PM	65.89	54.62	0.883	0.62
		XG10%_C	51.61	166.96	0.988	0.74
<i>Buffer</i>		XG10%_PM	35.41	141.58	0.960	0.57
		XG10%_C	30.69	180.77	0.988	0.63

#### 6.2.3.2.3. Tablets containing 30 % w/w XG

At 30% XG, PPN release was controlled for all the tablets tested which contained either MAS-PPN complexes or MAS-PPN physical mixture (Fig. 6.12.). Analysis showed that a considerably higher amount of PPN was released in acidic media compared to buffer from both MAS-PPN complex containing tablets (55 % in acid and 37 % in buffer) and MAS-PPN physical mixture containing tablets (46 % in acid and 38 % in buffer).

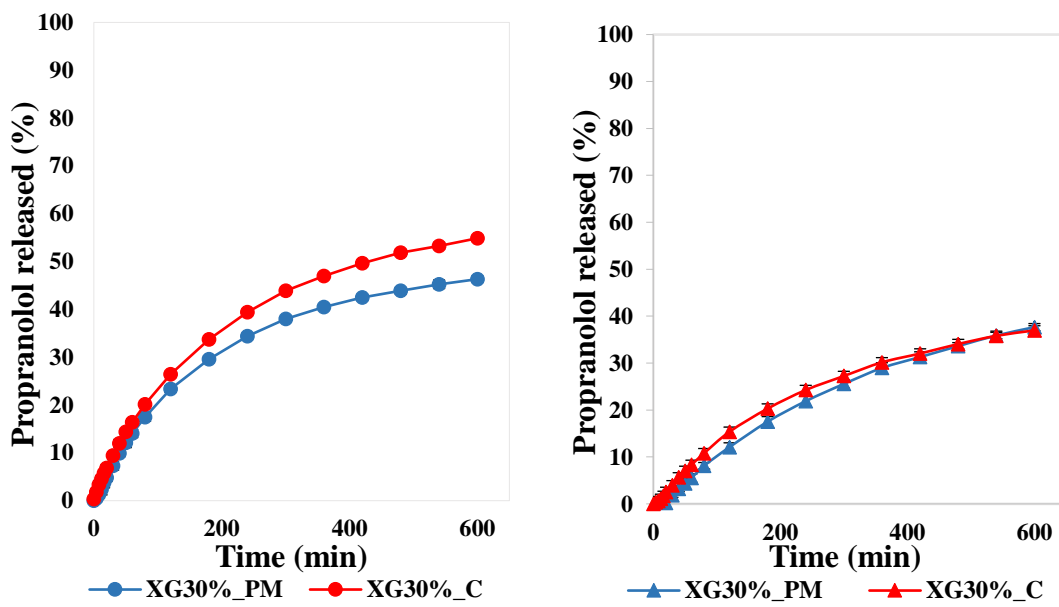


**Fig. 6.12.** PPN release profile from matrices made of MAS-PPN phys. mix and complex particles combined with XG (30%) in (a) pH 1.2 hydrochloric acid and (b) pH 6.8 buffer over 10 h

All tablets had anomalous (non-Fickian) diffusion occurring (Table 6.13.). A value of  $n$  as 0.63 and 0.69 was found for the tablets prepared using MAS-PPN complexes in acid and buffer respectively. For the tablets prepared using MAS-PPN physical mixture a value of  $n$  as 0.60 and 0.81 was observed in acid and buffer respectively. MDT values were similar for the tablets containing MAS-PPN complexes and MAS-PPN physical mixture in acid (174 min compared to 166 min) and in buffer (200 min and 219 min) suggesting the similarity between the tablets and their greater capability to reduce PPN release in buffer. Similarly, DE was comparable for tablets containing MAS-PPN complexes and tablets containing MAS-PPN physical mixture in acid (39 % and 33 % respectively) and buffer (25 % and 23 % respectively) suggesting tablets similarity and their great capability in controlling PPN release.

**Table. 6.13.** Kinetics of drug release of tablets prepared using MAS-PPN complexes of MAS-PPN physical mixture incorporated in 30 % XG matrices

	<i>Formulation code</i>	$DE_{600\text{ min}} (\%)$	MDT (min)	RSQ	<i>n</i> value
<i>pH 1.2 HCl</i>	XG30%_PM	33.49	166.23	0.973	0.60
	XG30%_C	39.02	174.31	0.985	0.63
<i>pH 6.8 Buffer</i>	XG30%_PM	23.02	219.43	0.982	0.81
	XG30%_C	24.59	200.68	0.984	0.69

#### 6.2.3.2.4. Tablets containing 50 % w/w XG

The release profiles of the tablets containing 50 % XG and MAS-PPN complexes/ physical mixture looked very similar in acid and in buffer, most probably due to the strong effects of the XG (Fig. 6.13). Release of PPN was controlled, however the amount of PPN released was relatively low for tablets containing MAS-PPN complexes and MAS-PPN physical mixture in both acid (41 % and 37 % respectively) and buffer (30 % and 29 % respectively).

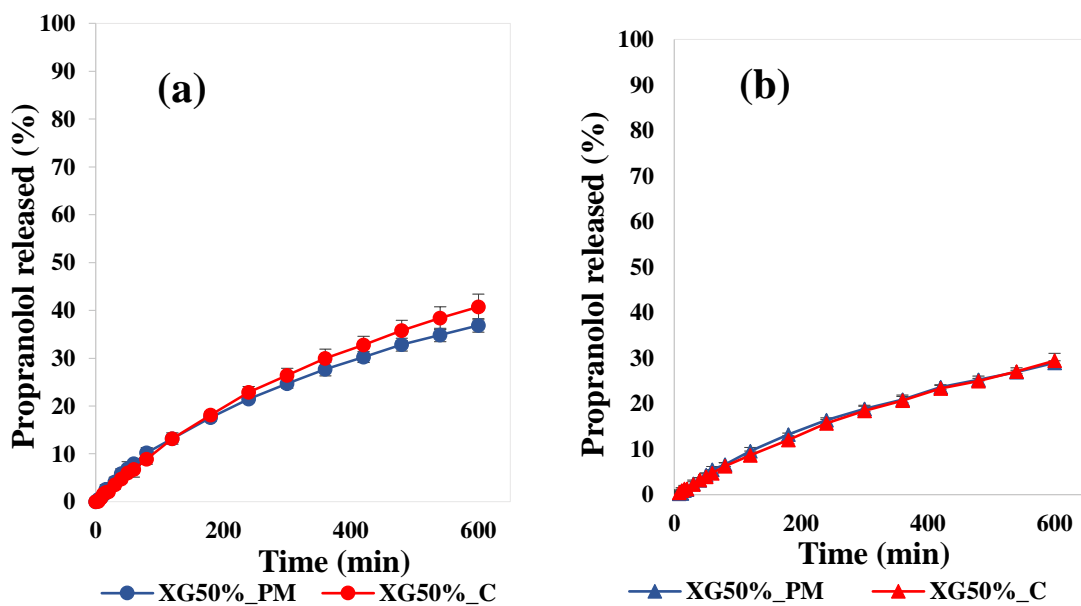


**Fig. 6.13.** PPN release profile from matrices made of MAS-PPN phys. mix and complex particles combined with XG (50%) in (a) pH 1.2 hydrochloric acid and (b) pH 6.8 buffer over 10 h

Tablets had an anomalous (non-Fickian) diffusion with a value of  $n$  as 0.80 and 0.79 for the tablets containing MAS-PPN complexes and 0.68 and 0.73 for the tablets containing MAS-PPN physical mixture in acid and buffer respectively (Table 6.14.). Hence, the value of  $n$  was significantly increased upon the use of MAS-PPN complexes in the tablets, which shows their impact on the mechanism of PPN release. MDT values were very similar in acid and buffer for all the tablets tested: 239 and 252 min respectively for tablets containing MAS-PPN physical mixture, and 226 min and 237 min respectively for tablets containing MAS-PPN complexes. The similarity between the MDT values outlines the similarity between the tablets tested and the strong effects of the XG in the tablets at 50% w/w. DE was similar in acid for tablets containing MAS-PPN complexes (24 %) and tablets containing MAS-PPN physical mixture (23 %) showing their similarity and their capability in reducing PPN release. In buffer, DE values were also similar, 17 % for both tablets containing MAS-PPN physical mixture and those containing MAS-PPN complexes (Table 6.14.).

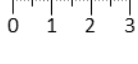
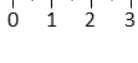
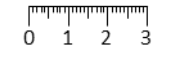
**Table. 6.14.** Kinetics of drug release of tablets prepared using MAS-PPN complexes of MAS-PPN physical mixture incorporated in 50 % XG matrices

	<i>Formulation code</i>	$DE_{600\text{ min}} (\%)$	MDT (min)	RSQ	<i>n</i> value
<i>0.1M HCl</i>	XG50%_PM	22.93	226.67	0.998	0.68
	XG50%_C	24.47	239.51	0.995	0.80
<i>pH 6.8 Buffer</i>	XG50%_PM	17.42	237.94	0.996	0.73
	XG50%_C	17.02	252.01	0.997	0.79

### 6.2.3.2.5. Evaluation of tablets appearance and conclusions

Analysis of tablet appearance showed the tablets containing MAS-PPN complexes were a distinct light brown colour, darker than the tablets containing MAS-PPN physical mixture (Table 6.15.). Furthermore, tablet growth can easily be observed, as the tablets doubled in volume. Tablet erosion was also observed, which was shown to be more likely to occur during dissolution in acid, compared to buffer dissolution, which may be the effects of smaller hydrogen ions in acid promoting a deeper diffusion inside the particles and faster polymer disentanglement. (Rojtanatanya and Pongjanyakul, 2010)

**Table. 6.15.** Tablets containing MAS-PPN complexes or MAS-PPN physical mixture in XG matrix: appearance prior to dissolution studies and after dissolution in pH 1.2 hydrochloric acid and pH 6.8 buffer

<i>Formulation code</i>	Tablet	pH 1.2 HCl dissolution	pH 6.8 buffer dissolution
<b>5%XG_C</b>	 		
<b>5%XG_PM</b>	 		
<b>10%XG_C</b>	 	 	 
<b>10%XG_PM</b>	 	 	 
<b>30%XG_C</b>	 	 	 
<b>30%XG_PM</b>	 	 	 
<b>50%XG_C</b>	 	 	 
<b>50%XG_PM</b>	 	 	 

Based on the findings presented, a dissolution model was proposed for MAS-PPN complexes and MAS-PPN physical mixture in XG matrix tablets (Fig. 6.13.). The model is in agreement with previous studies by Pongjanyakul and Rojtanatanya (2010 and 2012) (Rojtanatanya and Pongjanyakul, 2010; Pongjanyakul and Rojtanatanya, 2012). Also, based on the findings described in chapter 3, section 3.2.8.4.2 suggesting that binding occurred between PPN and XG it was also expected that both MAS and XG to compete for the binding with PPN, which can contribute to a reduction in PPN released.

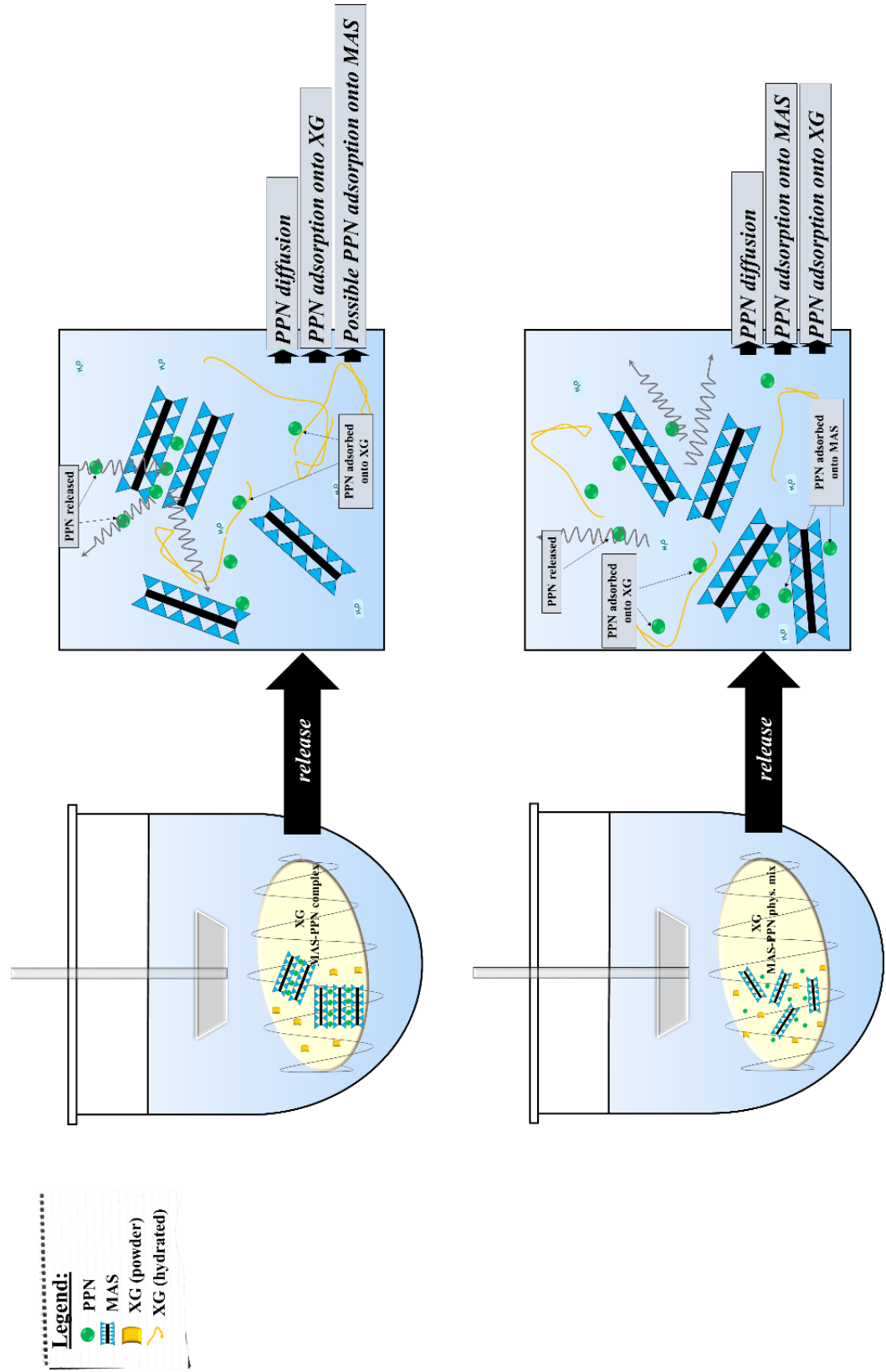


**Fig. 6.13.** Proposed release mechanism model of MAS-PPN complexes and MAS-PPN physical mixture in XG matrix tablets

### **6.3. Conclusions**

Compacts were prepared using MAS-PPN complexes or physical mixture, dispersed in either XG or PEO polymers. Bulk compaction behaviour was studied for the formulations prepared as plots of relative density vs. upper punch pressure measured during loading to 130 MPa (10 kN) and unloading. The compaction curves of all the samples tested followed roughly similar trends: the compaction behaviour was dominated by plastic recovery during the loading stage following non-reversible deformation, movement and fragmentation of the particles. Compacts were further tested for their dissolution properties in pH 1.2 hydrochloric acid and pH 6.8 buffer. Results showed that PEO was able to provide controlled PPN release in both acid and buffer at very low polymer concentrations in tablets (5% w/w), whereas burst effects were observed upon dissolution of compacts containing same amount of XG. Overall, a more controlled PPN release rate from the tablets containing MAS-PPN complexes compared to those containing MAS-PPN physical mixture was observed which is as a result of the MAS-PPN binding and adds important benefits to drug release.

#### **6.4. References**

- Baumgartner, S., Pavli, M. and Kristl, J. (2008) ‘Effect of calcium ions on the gelling and drug release characteristics of xanthan matrix tablets’, *European Journal of Pharmaceutics and Biopharmaceutics*, 69(2), pp. 698–707.
- Han, L. H. *et al.* (2011) ‘Density and plastic strain evaluations using small-angle X-ray scattering and finite element simulations for powder compacts of complex shape’, pp. 5977–5990. doi: 10.1007/s10853-011-5559-8.
- Jian, H. *et al.* (2012) ‘Galactomannan (from Gleditsia sinensis Lam.) and xanthan gum matrix tablets for controlled delivery of theophylline: In vitro drug release and swelling behavior’, *Carbohydrate Polymers*, 87(3), pp. 2176–2182.
- Kavanagh, N. and Corrigan, O. I. (2004) ‘Swelling and erosion properties of hydroxypropylmethylcellulose (Hypromellose) matrices - Influence of agitation rate and dissolution medium composition’, *International Journal of Pharmaceutics*, 279(1–2), pp. 141–152.
- Laity, P. R. *et al.* (2015) ‘Using small-angle X-ray scattering to investigate the compaction behaviour of a granulated clay’, *Applied Clay Science*, 108, pp. 149–164.
- Laity, P. R. and Cameron, R. E. (2008) ‘A small-angle X-ray scattering study of powder compaction’, *Powder Technology*, pp. 119–127.
- Micrometrics (1998) ‘Porosity and Its Influence on Pharmaceutical Tablet Dissolution Profiles’.
- Mu, X., Tobyn, M. J. and Staniforth, J. N. (2003) ‘Influence of Physiological Variables on the In Vitro Drug-Release Behavior of a Polysaccharide Matrix Controlled-Release System’, *Drug Development and Industrial Pharmacy*, 29(1), pp. 19–29.
- Palmer, D. *et al.* (2013) ‘Mechanism of synergistic interactions and its influence on drug release from extended release matrices manufactured using binary mixtures of polyethylene oxide and sodium carboxymethylcellulose’, *Colloids and Surfaces B: Biointerfaces*, 104, pp. 174–180.
- Pappa, C. *et al.* (2018) ‘Nanostructured Composites of Sodium Montmorillonite Clay and

PEO Used in Dissolution Improvement of Aprepitant Drug by Melt Mixing', *Applied Sciences*, 8(5), p. 786.

Pongjanyakul, T. and Rojtanatanya, S. (2012) 'Use of Propranolol-Magnesium Aluminium Silicate Intercalated Complexes as Drug Reservoirs in Polymeric Matrix Tablets', *Indian Journal of Pharmaceutical Sciences*, 74(4), pp. 292–301.

Riippi, M. et al. (1998) 'Dependence between dissolution rate and porosity of compressed erythromycin acistrate tablets', 46, pp. 169–175.

Rojtanatanya, S. and Pongjanyakul, T. (2010) 'Propranolol-magnesium aluminum silicate complex dispersions and particles: Characterization and factors influencing drug release', *International Journal of Pharmaceutics*, 383(1–2), pp. 106–115.

Rongthong, T. et al. (2013) 'Quaternary polymethacrylate-magnesium aluminum silicate films: Molecular interactions, mechanical properties and tackiness', *International Journal of Pharmaceutics*, 458(1), pp. 57–64.

Siahi-Shabdar, M. R. et al. (2011) 'Release Behaviour of Propranolol HCl from Hydrophilic Matrix Tablets Containing Psyllium Powder in Combination with Hydrophilic Polymers', *AAPS PharmSciTech*, 12(4), pp. 1176–1182.

# *Chapter 7:*

## *General discussions and conclusions*

## **Chapter 7: General discussions and conclusions**

### **7.1. Introduction**

Minerals are widely used in the pharmaceutical industry and in medicine. Minerals are easily available in nature and are used for their nutritional, cosmetic and therapeutic properties due to their safety and physicochemical properties. Novel practices involve the use of minerals as drug carriers in the formulation of pharmaceutical dosage forms through their capacity to adsorb or reversibly fixate polar compounds onto their structure and form complex dispersions and particles (Carretero and Pozo, 2009). These complexes can modify the release of drugs upon administration, which is desirable for drugs having a short half-life and require frequent administration to maintain adequate drug plasma levels that are used to treat chronic conditions (Rojtanatanya and Pongjanyakul, 2010). However, the physicochemical characteristics of the formed complexes are not entirely understood and understanding them is essential to establishing a successful formulation. Therefore, the purpose of the presented research was to understand the process of adsorption of cationic drugs onto a smectite clay magnesium aluminium silicate (MAS) and the effects of this process on extending the release of such drugs. The adsorption onto MAS of three model drugs having different therapeutic effects was studied: propranolol hydrochloride (PPN), diltiazem hydrochloride (DIL) and metformin hydrochloride (MET). Furthermore, two different polymers were used in the study in combination with the formulated clay-drug complexes: xanthan gum (XG) and polyethylene oxide (PEO).

### **7.2. Binding between Propranolol hydrochloride (PPN) and Magnesium Aluminium Silicate (MAS)**

The single injection mode (SIM) and multiple injection mode (MIM) isothermal titration calorimetry (ITC) experiments revealed that the binding phenomenon was predominantly enthalpically driven as high energy resulted from broken and created hydrogen bonds and electrostatic interactions. pH was shown to have no effects on the binding process (pH 5, 7 and 9 tested), while upon increasing temperature from 25 to 37 °C the binding became more exothermic and enthalpically driven. Additional ITC experiments were carried out to explore the effects that two different polymers PEO and XG may have on the PPN adsorption onto

MAS. The experiments showed no interaction taking place between PEO and PPN and confirmed binding between MAS and PEO. Differences between PPN adsorption onto MAS-PEO mixture, compared to PPN adsorption onto MAS dispersion were observed, which may likely be due to the addition of the PEO polymer to the reaction. These findings imply that PEO can interfere with the amount of PPN adsorbed onto MAS and with the strength of the binding. This may also influence PPN release from tablets made of MAS-PPN complex particles and PEO (added as physical mixture) as the polymer may saturate the available sites onto the clay preventing the drug to be readsorbed once released. Experiments were carried out to find the effects of XG on the MAS and PPN binding. These showed no interaction between MAS and XG and confirmed binding between PPN and XG. The binding phenomenon between PPN and MAS was shown to be more enthalpy driven and had a higher affinity in the presence of XG. This may be due to the competition of MAS and XG for the PPN which affects the binding. MAS and XG competition for the binding with PPN may potentially reduce the amount of PPN released from tablets made of MAS-PPN complex particles.

Results hence confirmed the ability of the MAS to adsorb PPN (propranolol) onto its surface and form flocculates in the MAS dispersion. The flocculates were further dried and characterised using a wide variety of techniques such as attenuated total reflectance Fourier transform infrared spectroscopy (ATR-FTIR), powder X-ray diffractometry (PXRD), differential scanning calorimetry (DSC), scanning electron microscopy with energy dispersive X-ray spectroscopy (SEM/EDX), high performance liquid chromatography (HPLC) and small angle X-Ray scattering (SAXS) which all confirmed changes as a result of the binding process which may have benefits for drug release. The basal spacing of the MAS was calculated from the PXRD data and was shown to be variable not only upon drug adsorption, but also upon fluctuations in storage temperature leading to dehydration and rehydration of the MAS. The PPN drug was shown to have a melting point of 167.221 °C. The drug was also found to be molecularly dispersed into the MAS-PPN complexes. Images and atomic distribution profiles obtained using SEM/EDX allowed the observation of the structural difference between raw materials PPN and MAS and the structural similarity between the MAS and the prepared MAS-PPN complex particles. Elements belonging to the PPN were observed in the atomic distribution profiles of the MAS-PPN complex particles.

PPN content in the MAS-PPN complexes was determined using HPLC in 2M HCl, pH 5.0 ultra-pure water and pH 6.8 phosphate buffer. For this assay a new method was developed and validated for linearity range, intermediate and intra assay precision, LOD and LOQ. PPN content was shown to be highly variable depending on the dissolution media. Results showed that a higher amount on PPN was recovered by dispersing the MAS-PPN particles in 2M HCl and pH 6.8 buffer compared to ultra-pure water, suggesting that the polydispersity of MAS particles was influenced by the increased ions present in the dissolution media used. PPN content also varied in the single and double drug loaded complexes and it was concluded that the increase in the PPN content observed in the MAS-PPN double drug loaded complexes suggests that there were still available binding sites onto MAS after adsorption equilibrium was reached following the single drug loading which allowed further adsorption of PPN particles. The results of ATR-FTIR experiments agree with the data obtained from the ITC experiments, as the disappearance of peaks belonging to both MAS and PPN when MAS-PPN single and double drug loaded complexes tested were observed, suggesting that the PPN adsorption onto MAS may occur via hydrogen bonds formation between the silanol groups of MAS with the amine and/or hydroxyl groups of PPN.

SAXS studies on the raw MAS and MAS-PPN complex particles revealed MAS which is a mixture of montmorillonite and saponite clays, to have a rough and irregular morphology at nanometre scale. Furthermore, the MAS-PPN complex was also shown to have a rough and irregular nanometre scale morphology, being only slightly different from that of MAS. The results obtained following SAXS analysis of the MAS dispersion and MAS-PPN complex dispersion revealed that the MAS-PPN complex dispersion had a more complex structure compared to the MAS dispersion, which was expected since the MAS flocculated upon the addition of the PPN solution.

The capacity of the formed MAS-PPN complexes combined with XG and PEO, compared to MAS-PPN physical mix combined with the same polymers to control the release of PPN was also studied. Bulk compaction behaviour was studied for the formulations prepared as plots of relative density vs. upper punch pressure measured during loading to 130 MPa (10 kN) and unloading. The compaction curves of all the samples tested followed roughly similar

trends: the compaction behaviour was dominated by plastic recovery during the loading stage following non-reversible deformation, movement and fragmentation of the particles. Compacts were further tested for their dissolution properties in pH 1.2 hydrochloric acid and pH 6.8 buffer. Results showed that PEO was able to provide controlled PPN release in both acid and buffer at very low polymer concentrations in tablets (5% w/w), whereas burst effects were observed upon dissolution of compacts containing the same amount of XG. Overall, a more controlled PPN release rate from the tablets containing MAS-PPN complexes compared to those containing MAS-PPN physical mixture was observed which is a result of the MAS-PPN binding and adds important benefits to drug release.

### **7.3. Binding between Diltiazem hydrochloride (DIL) and Magnesium Aluminium Silicate (MAS)**

Results confirmed the ability of the MAS to adsorb DIL onto its surface and form flocculates in the MAS dispersion.

The MAS basal spacing in the MAS-DIL complexes was calculated from the PXRD data and was shown to increase upon drug adsorption. Images and atomic distribution profiles obtained using SEM/EDX allowed the observation of the structural difference between raw materials DIL and MAS and the structural similarity between the MAS and the prepared MAS-DIL complex particles. DIL content in the MAS-DIL complexes was determined using HPLC in 2M HCl, pH 5.0 ultra-pure water and pH 6.8 phosphate buffer. A degradant of DIL, desacetyl diltiazem was observed on the chromatograms during analysis (occurring via DIL hydrolysis). DIL and desacetyldiltiazem content was shown to be highly variable depending on the dissolution media used.

Microscopy studies allowed the observation of the MAS dispersion and the flocs formed upon DIL addition to the MAS dispersion. Flocs were shown to get porous and spread out as the particles clustered together and then decrease in size due to loosely bound aggregates “breaking off” and reattaching to other aggregates in a more stable form. Following SAXS studies, the MAS-DIL complex particles were shown to have a rough and irregular nanometre scale morphology, being only slightly different from that of MAS. The analysis of the MAS-DIL complex dispersion revealed that the MAS-DIL complex dispersion had a

more complex structure compared to that of MAS dispersion, which was expected since the MAS flocculated upon the addition of the DIL solution.

The single injection mode (SIM) and multiple injection mode (MIM) ITC experiments revealed that the binding phenomenon was predominantly enthalpically driven as high energy resulted from broken and created hydrogen bonds and electrostatic interactions, with a slight entropic contribution. Multiple binding events upon MAS and DIL binding were observed in the ITC MIM experiments, which could not be seen in the ITC SIM experiments. A competitor binding model was fitted to the data to determine the thermodynamic parameters of the reaction assuming that the two different types of clay within MAS (montmorillonite and saponite) placed into the sample cell may potentially interact differently upon the addition of DIL (assumption was made based on the isomorphic substitution of a limited number of octahedral  $\text{Al}^{3+}$  with  $\text{Mg}^{2+}$  in montmorillonite and the substitution of a limited number of tetrahedral  $\text{Si}^{4+}$  by  $\text{Al}^{3+}$  in saponite, naturally balanced by exchangeable  $\text{Na}^+$  ions that can be easily displaced and replaced, giving the clay the ability to act like a reservoir). The results agree with the data obtained from the ATR-FTIR experiments which revealed the disappearance of peaks belonging to both MAS and DIL when MAS-DIL single and double drug loaded complexes were tested, suggesting that the DIL adsorption onto MAS may occur via hydrogen bonds formation between the silanol groups of MAS with the amine and/or hydroxyl groups of DIL.

Additional ITC experiments were carried out to evaluate the effects of polyethylene oxide (PEO) and xanthan gum (XG) on DIL adsorption onto MAS. Results showed that the binding between DIL and PEO was enthalpy and entropy driven. Furthermore, the binding between MAS and DIL in the presence of PEO was shown to be enthalpy driven and entropically unfavourable, which was also the case for the binding between MAS and PEO. This behaviour suggests that the slight entropic effects observed in the simple MAS and DIL binding experiments were reduced upon the addition of the polymer to the mixture. The adsorption of DIL onto MAS in the presence of XG was shown to be highly exothermic. Two binding events were observed and a competitor binding model was fitted to the data to determine the thermodynamic parameters of the reaction, considering that the two different types of clay within MAS (montmorillonite and saponite) placed into the sample cell may potentially interact differently upon the addition of DIL. The binding was shown to be

enthalpy driven and entropically unfavourable. No binding was shown to occur between XG and DIL.

#### **7.4. Binding between Metformin hydrochloride (MET) and Magnesium Aluminium Silicate (MAS)**

The SIM and MIM isothermal titration calorimetry (ITC) experiments revealed that the binding phenomenon between MET (metformin) and MAS was predominantly enthalpically driven as high energy resulted from broken and created hydrogen bonds and electrostatic interactions. pH was shown to influence the speed of the reaction, the interaction between MAS and MET being faster at pH 5 compared to pH 7 and 9. The binding also became more exothermic and enthalpically driven upon increasing the temperature from 25 to 37° C. Results confirmed the ability of the MAS to adsorb MET onto its surface and form flocculates in the MAS dispersion. The flocculates were further dried and characterised using a wide variety of techniques. The MAS basal spacing in the MAS-MET complexes was calculated from the PXRD data and was shown to increase upon drug adsorption. However, the extent of the increase was similar for the single and double drug loaded MAS-PPN complexes, hence changes in basal distance may not accurately reflect the intercalation of a drug within clay platelets when humidity is not controlled to allow for comparisons. Images and atomic distribution profiles obtained using SEM/EDX allowed the observation of the structural difference between raw materials MET and MAS and the structural similarity between the MAS and the prepared MAS-MET complex particles. MET content in the MAS-MET complexes was determined using HPLC in 2M HCl, pH 5.0 ultra-pure water and pH 6.8 phosphate buffer and was shown to be highest in 2M HCl. No degradants were observed on the chromatograms. Following SAXS studies, the MAS-MET complex particles were shown to have a rough and irregular nanometre scale morphology, being only slightly different from that of MAS. The analysis of the MAS-MET complex dispersion revealed that the MAS-MET complex dispersion had a more complex structure compared to that of MAS dispersion, which was expected since the MAS flocculated upon the addition of the MET solution.

## **7.5. Challenges of current study**

The findings presented in this study add novelty to the already existing studies by focusing on the ITC studies to understand the clay drug-complexation at a molecular level and use the acquired information to explain the release of a model drug PPN from clay-drug-polymer matrices. ITC was found to be a useful technique in characterising the adsorption onto the MAS of PPN, DIL and MET. However, the ITC data interpretation was quite challenging due to the lack of molecular weight for the MAS. In conventional ITC studies, models are fit to the data by the input of the molecular weight for both the ligand in the syringe and the macromolecule in the sample cell in a designated software, which allows for the calculation of thermodynamic parameters and stoichiometry. When the molecular weight for the macromolecule in the sample cell is unknown, one can only determine the thermodynamic parameters correctly, but not the stoichiometry. There are however studies where data analysis was approached differently, by using the CEC (cation exchange capacity) for the clay as the molecular weight, along with the ligand molecular weight. The authors of such publications still do not report values for the stoichiometry. An example is a report written by Morrissey and Cheicante, where the authors describe the sorption of a chemical warfare agent VX (O-ethyl-S-[2-N,N-(diisopropylamino)ethyl] methylphosphonothioate) onto clay minerals and soils using isothermal titration calorimetry (Morrissey, Schenning and Cheicante, 2012).

The present study also focused on the effects of humidity on the MAS and on the MAS-drug complexes formulated. The effects of humidity were mainly observed during XRD analysis, leading to inconsistency in the results and basal distance variation which, in turn, created challenges during data analysis. Similar findings were also reported in literature for different types for clays such as montmorillonite, kaolinite and bentonite (Milne and Warhaw, 1955). However, the work presented in this thesis draws attention to the accuracy of using basal distance increases to confirm clay-drug intercalation when samples are not dried, which was not taken into account in previous similar studies (Pongjanyakul and Rojtanatanya, 2012). Samples and raw material (clay) tested should always be dried and humidity should be minimised to allow for comparisons.

## **7.6. Future work**

Formulation of clay-polymer-drug nanocomposites may be a challenging area to further explore, which may offer additional capabilities to the modulation of drug release as multi-functional systems. A study by published in by Datta in 2013 demonstrates the efficiency of PPN loaded Montmorillonite–Poly lactic-co-glycolic acid (Mt–PLGA) nanocomposites as a controlled drug delivery system for PPN (Datta, 2013). Compacts may also be formulated and tested using SAXS and tomography to evaluate content uniformity and cracking (Laity *et al.*, 2015), as well as dissolution testing to determine their capability to modulate drug release. The clay-drug-polymer nanocomposites should additionally be formulated using a polymer combination, as synergistic interactions between polymers were shown to have benefits in controlling drug release (Palmer *et al.*, 2013). Freeze drying, spray drying, and plasma treatment should further be incorporated in the formulation method. Previous publications showed promising mechanical and physicochemical behaviour of the nanocomposites when such techniques were used, such as being good candidates for extrusion which would be promising for 3D printing of tablets to modulate drug release (Scaffaro and Maio, 2012; Shang *et al.*, 2016; Almansoori, Majewski and Rodenburg, 2017).

## 7.7. References

- Almansoori, A., Majewski, C. and Rodenburg, C. (2017) ‘Nanoclay/Polymer Composite Powders for Use in Laser Sintering Applications: Effects of Nanoclay Plasma Treatment’, *Jom*. Springer US, 69(11), pp. 2278–2285.
- Carretero, M. I. and Pozo, M. (2009) ‘Clay and non-clay minerals in the pharmaceutical industry. Part I. Excipients and medical applications’, *Applied Clay Science*. Elsevier B.V., 46(1), pp. 73–80.
- Datta, S. M. (2013) ‘Clay-polymer nanocomposites as a novel drug carrier: Synthesis, characterization and controlled release study of Propranolol Hydrochloride’, *Applied Clay Science*, 80–81, pp. 85–92.
- Laity, P. R. *et al.* (2015) ‘Using small-angle X-ray scattering to investigate the compaction behaviour of a granulated clay’, *Applied Clay Science*, 108, pp. 149–164.
- Milne, I. H. and Warhaw, C. M. (1955) ‘Methods of Preparation and Control of Clay Mineral Specimens in X-Ray Diffraction Analysis’, *Clays and Clay Minerals*, 4, pp. 22–30.
- Morrissey, K. M., Schenning, A. M. and Cheicante, R. L. (2012) *Sorption of VX to clay minerals and soils: thermodynamic and kinetic studies*.
- Palmer, D. *et al.* (2013) ‘Mechanism of synergistic interactions and its influence on drug release from extended release matrices manufactured using binary mixtures of polyethylene oxide and sodium carboxymethylcellulose’, *Colloids and Surfaces B: Biointerfaces*, 104, pp. 174–180.
- Pongjanyakul, T. and Rojtanatanya, S. (2012) ‘Use of Propranolol-Magnesium Aluminium Silicate Intercalated Complexes as Drug Reservoirs in Polymeric Matrix Tablets’, *Indian Journal of Pharmaceutical Sciences*, 74(4), pp. 292–301.
- Rojtanatanya, S. and Pongjanyakul, T. (2010) ‘Propranolol-magnesium aluminum silicate complex dispersions and particles: Characterization and factors influencing drug release’, *International Journal of Pharmaceutics*, 383(1–2), pp. 106–115.
- Scaffaro, R. and Maio, A. (2012) ‘Enhancing the mechanical performance of polymer based nanocomposites by plasma-modification of nanoparticles’, *Polymer Testing*, 31(7), pp. 889–894.
- Shang, K. *et al.* (2016) ‘Nonflammable Alginate Nanocomposite Aerogels Prepared by a Simple Freeze-Drying and Post-Cross-Linking Method’, *ACS Applied Materials and Interfaces*, 8(1), pp. 643–650.